The collapse of linear polyelectrolyte chains in a poor solvent:

When does a collapsing polyelectrolyte collect its counter ions?

Dissertation
zur Erlangung des Grades
„Doktor der Naturwissenschaften"
im Promotionsfach Chemie

am Fachbereich Chemie, Pharmazie und Geowissenschaften
der Johannes Gutenberg-Universität in Mainz.

Peter Loh
geboren in Lippstadt

Mainz, 2008

Dekan:

1. Berichterstatter:

2. Berichterstatter:

Tag der mündlichen Prüfung: 16. Dezember 2008

The collapse of linear polyelectrolyte chains in a poor solvent:
When does a collapsing polyelectrolyte collect its counter ions?

The collapse of polyions in a poor solvent is a complex system and is an active research subject in the theoretical polyelectrolyte community. The complexity is due to the subtle interplay between hydrophobic effects, electrostatic interactions, entropy elasticity, intrinsic excluded volume as well as specific counter-ion and co-ion properties.

Long range Coulomb forces can obscure single molecule properties. The here presented approach is to use just a small amount of screening salt in combination with a very high sample dilution in order to screen intermolecular interaction whereas keeping intramolecular interaction as much as possible (polyelectrolyte concentration $c_p \leq 12$ mg/L, salt concentration; $C_s = 10^{-5}$ mol/L). This is so far not described in literature. During collapse, the polyion is subject to a drastic change in size along with strong reduction of free counterions in solution. Therefore light scattering was utilized to obtain the size of the polyion whereas a conductivity setup was developed to monitor the proceeding of counterion collection by the polyion.

Partially quaternized PVP's below and above the Manning limit were investigated and compared to the collapse of their uncharged precursor. The collapses were induced by an isorefractive solvent/non-solvent mixture consisting of 1-propanol and 2-pentanone, with nearly constant dielectric constant. The solvent quality for the uncharged polyion could be quantified which, for the first time, allowed the experimental investigation of the effect of electrostatic interaction prior and during polyion collapse.

Given that the Manning parameter ξ_M for QPVP$_{4.3}$ is as low as $l_B / c = 0.6$ (l_B the Bjerrum length and c the mean contour distance between two charges), no counterion binding should occur. However the Walden product reduces with first addition of non solvent and accelerates when the structural collapse sets in. Since the dielectric constant of the solvent remains virtually constant during the chain collapse, the counterion binding is entirely caused by the reduction in the polyion chain dimension. The collapse is shifted to lower w_{ns} with higher degrees of quaternization as the samples QPVP$_{20}$ and QPVP$_{35}$ show ($\xi_M = 2.8$ respectively 4.9). The combination of light scattering and conductivity measurement revealed for the first time that polyion chains already collect their counter ions well above the θ-dimension when the dimensions start to shrink.

Due to only small amounts of screening salt, strong electrostatic interactions bias dynamic as well as static light scattering measurements. An extended Zimm formula was derived to account for this interaction and to obtain the real chain dimensions. The effective degree of dissociation γ could be obtained semi quantitatively using this extrapolated static in combination with conductivity measurements. One can conclude the expansion factor α_g and the effective degree of ionization of the polyion to be mutually dependent. In the good solvent regime γ of QPVP$_{4.3}$, QPVP$_{20}$ and QPVP$_{35}$ exhibited a decreasing value in the order $1 > \gamma_{4.3} > \gamma_{20} > \gamma_{35}$. The low values of γ for QPVP$_{20}$ and QPVP$_{35}$ are assumed to be responsible for the prior collapse of the higher quaternized samples. Collapse theory predicts dipole-dipole attraction to increase accordingly and even predicts a collapse in the good solvent regime. This could be exactly observed for the QPVP$_{35}$-sample.

The experimental results were compared to a newly developed theory of uniform spherical collapse induced by concomitant counterion binding developed by M. Muthukumar and A. Kundagrami. The theory agrees qualitatively with the location of the phase boundary as well as the trend of an increasing expansion with an increase of the degree of quaternization. However experimental determined γ for the samples QPVP$_{4.3}$, QPVP$_{20}$ and QPVP$_{35}$ decreases linearly with the degree of quaternization whereas this theory predicts an almost constant value.

Der Kollaps eines linearen Polyelektrolyten in einem schlechten Lösungsmittel: Wann sammelt der Polyelektrolyt seine Gegenionen ein?

Der Kollaps von Polyionen in schlechten Lösungsmitteln ist ein komplexes System welches aktiv in der theoretischen Polyelektrolytforschung untersucht wird. Die Komplexität resultiert aus dem subtilen Wechselspiel der Hydrophobie, elektrostatischer Effekte, Entropieelastizität der Kette, intrinsischem Ausschlussvolumen sowie spezifischer Gegen- und Co-ioneneigenschaften.

Langreichweitige Coulomb-Kräfte können die Einzelmoleküleigenschaften verdecken. Der in dieser Arbeit gewählte Ansatz ist es, in Verbindung mit geringen Probenkonzentrationen nur geringe Mengen Salz zur Abschirmung zu verwenden. Hierdurch können intermolekulare Wechselwirkungen abgeschirmt werden, während intramolekulare Kräfte so weit wie möglich beibehalten werden (Polyelektrolytkonzentration $c_p \leq 12$ mg/L, Salzkonzentration; $C_s = 10^{-5}$ mol/L). Während des Kollapses ändert sich sowohl die Größe des Polyelektrolyten als auch die Anzahl an freien Ionen in Lösung drastisch. Daher wurde die Lichtstreuung verwendet um die Größe des Polyions zu ermitteln und ein Leitfähigkeitsaufbau entwickelt um das Einsammeln der Gegenionen zu monitorisieren.

Partiell quaternisierte PVP's unterhalb und oberhalb des Manning-Limits wurden untersucht und mit dem Kollaps des ungeladenen Precursors verglichen. Der Kollaps wurde induziert durch ein isorefraktivieves Lösungsmittel/Nichtlösungsmittelgemisch aus 1-Propanol und 2-Pentanon, die zudem beide eine ähnliche Permittivität aufweisen. Die Lösungmittelqualität des ungeladenen Polyions konnte quantifiziert werden, so dass es zum ersten Mal möglich war die experimentelle Untersuchung des Effektes der Elektrostatik vor und während des Kollaps zu verfolgen.

In Anbetracht des Manning Parameters ξ_M von QPVP$_{4.3}$ mit lediglich $l_B / c = 0.6$ (l_B Bjerrumlänge und c der durchschnittliche Konturlängenabstand zwischen zwei Ladungen), sollte keinerlei Gegenionenkondensation auftreten. Jedoch verringert sich das Walden-Produkt von der ersten Zugabe von Nichtlösungsmittel an und diese Abnahme beschleunigt sich mit Eintreten des strukturellen Kollapses. Da die Dielektrizitätskonstante des Lösungsmittels während des Kollapses quasi konstant bleibt, kann die Gegenionenkondensation nur durch die Verringerung der Polyionengröße motiviert sein. Die Proben QPVP$_{20}$ und QPVP$_{35}$ zeigen ($\xi_M = 2.8$ bzw. 4.9), dass der Kollapspunkt zu immer größeren Nichtlösemittelanteilen w_{ns} verschoben wird. Die Kombination aus Lichtstreuung und Leitfähigkeit zeigte zum ersten Mal, dass die Polyionenkette Gegenionen einsammelt deutlich bevor sie θ-Dimensionen erreicht.

In Folge der geringen Menge Abschirmsalz verfälschen elektrostatische Interaktionen die dynamischen als auch statischen Lichtstreumessungen. Eine erweiterte Zimm-Gleichung wurde abgeleitet, um diesen Effekten Rechnung zu tragen und die tatsächlichen Dimensionen zu erhalten. Durch Verwendung dieser extrapolierten Daten und den Leitfähigkeitsmessungen konnte der effektive Dissoziationsgrad γ semiquantitativ ermittelt werden. Man kann schlussfolgern, dass der Expansionskoeffizient α_g und der effektive Dissoziantiongrad des Polyions sich wechselseitig bedingen. Im Bereich des guten Lösungsmittels weist γ der QPVP$_{4.3}$-, QPVP$_{20}$- und QPVP$_{35}$–Probe einen kleiner werdenden Wert auf: $1 > \gamma_{4.3} > \gamma_{20} > \gamma_{35}$. Ferner kann man davon ausgehen, dass die niedrigen γ-Werte der QPVP$_{20}$ und der QPVP$_{35}$-Probe für den früheren Kollaps höher Quaternisierungen verantwortlich sind. Kollapstheorien gehen analog von sich verstärkenden Dipol-Dipol-Attraktionen aus und sagen sogar einen Kollaps in guten Lösungsmitteln voraus, was auch bei der vermessenen QPVP$_{35}$-Probe beobachtet werden konnte.

Die experimentellen Resultate wurden zusätzlich verglichen mit einer neu entwickelten Theorie des uniformen sphärischen Kollapses, induziert durch wechselseitige Gegenionenbindung, entwickelt von M. Muthukumar und A. Kundagrami. Die Theorie stimmt qualitative mit der Phasengrenze überein, ebenso der Trend der ansteigenden Expansion mit ansteigendem Grad der Quaternisierung. Jedoch nehmen die experimentell bestimmten γ-Werte der QPVP$_{4.3}$-, QPVP$_{20}$- und der QPVP$_{35}$-Probe linear mit dem Quaternisierungsgrad ab, während die Theorie einen nahezu konstanten Wert voraussagt.

Contents

1 Motivation

1.1 Polyelectrolytes in Solution

Polyelectrolytes are chainlike macromolecules made of discrete building blocks that contain a defined number of ionizable functional groups along their contour. Dissolving a polyelectrolyte in a proper solvent leads to dissociation of the ion pairs. In contrast to the localized charges along the chain, the counterions may redistribute in the whole sample volume thereby charging the polyelectrolyte (Figure 1.1).
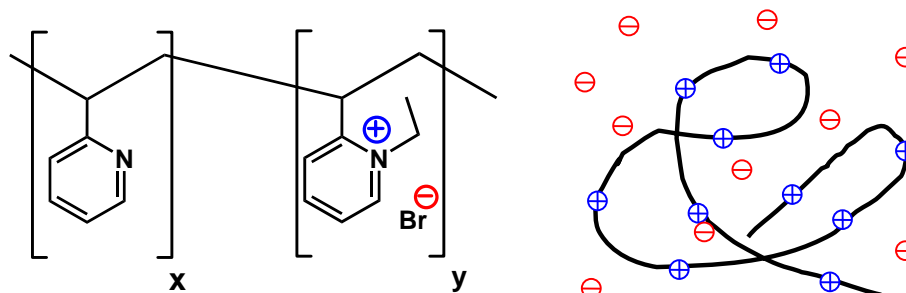
Figure 1.1 Chemical structure of quaternized polyvinylpyridine (QPVP) and scheme of the solvated polyion

Due to hydrophobic interactions uncharged polymers with their hydrocarbon-backbone usually do not dissolve in polar solvents whereas addition of charges along the chain increases solubility drastically. By attaching enough charged groups to a hydrophobic backbone, even water with its high dielectric constant can act as a solvent. Polyelectrolytes exhibit various structures although the number of chemically different charge carrying groups is rather small:
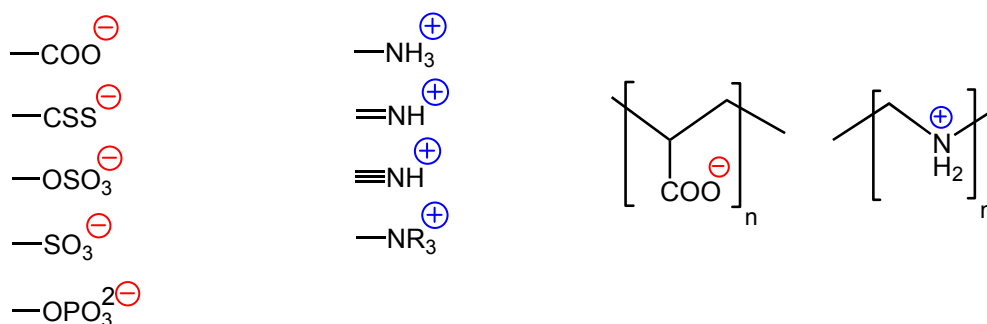
Figure 1.2 Left: structures of negative and positive ionic groups; right: examples for different structures of polyelectrolytes: polyacrylic acid and polyethyleneimine

In water sulphonate- and tetraalkylammonium-groups are dissociated over the whole ph-range and therefore called strong electrolytes. On the other hand, for weak or annealed polyelectrolytes the dissociation of charges depends on pH-value. The ionic group can be an integral part of the repeating unit itself as well as it can be covalently bound onto the polyelectrolyte backbone whereas the position of the group along the chain is fixed by chemical synthesis (Figure 1.2).

There are natural as well as synthetic polyelectrolytes, appearing in a huge variety of different shapes and classes and they play a major part in everyday life. The complexity arises from a competition between solvent quality, entropy elasticity of the backbone, long-range Coulomb

interaction as well as entropic energy of dissociated counterions, determining the structure on the molecular-scale and up to the bulk-phase.

For organisms the synthesis of defined strings made of building blocks that then further assemble into bigger structures is an effective procedure. These biopolymers act as structural elements e.g. cellulose or pectin, as energy storage e.g. starch, as "metabolism-machines" like proteins or as carrier of information like DNA and RNA. Nucleic acids and proteins (Figure 1.3) are polyelectrolytes and exploit their solubility characteristics in a complex manner. Superstructures of proteins are highly impressive: Strings consisting of monomers with different solubility properties are further folded into hydrophobic and hydrophilic domains, stabilized by myriads of local interactions, electrostatic interplay and osmotic pressure (Figure 1.3). The important role of proteins in our metabolism is defined by this superstructure.
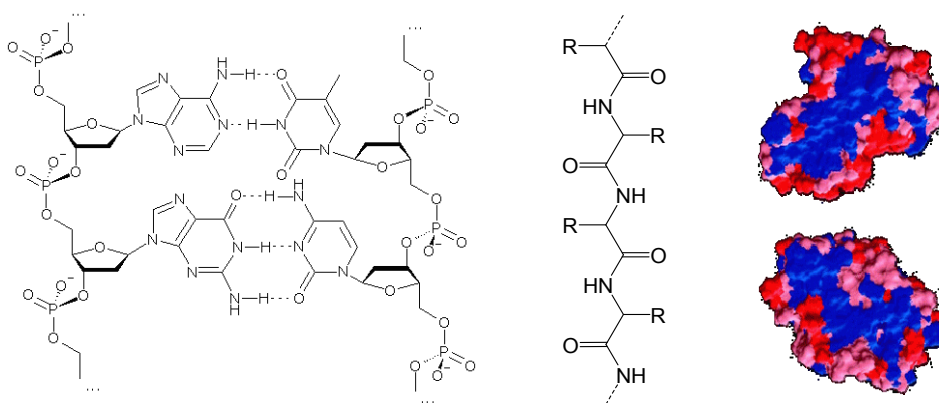
Figure 1.3 From left to right: chemical structure of DNA; peptide backbone; simulation snapshot of superstructure of the two domain protein BphC enzyme; hydrophobic regions are marked in blue and strong hydrophilic in red [Ruhong Zhou 2004]. DNA is an example for a polyelectrolyte with charged repeating units as an integral part of the backbone whereas proteins may bear a charge on their 22 different side chains R.

Therefore deeper understanding of structure and important parameters for polyelectrolyte collapse is of high interest, even more as polyelectrolytes have a wide application field. They are used in food and cosmetics industry as thickening agent for puddings or creamy low fat milk products, all kinds of hair products, creams and ointments. Furthermore they are applied as flocking agents for cellulose/paper production, for waste water processing or for the precipitation of colloids from solution in various processes. Other applications are the usage as additives for spinning fibers in textile industry, as viscosity modifier to reduce drag in oil pipelines, as superabsorbent polymers used in hygiene products, or the production of ion exchange resins.

1.2   Aim of this Thesis

The conformation of linear polyelectrolytes in a good solvent is frequently investigated but the results are still controversially discussed, despite some progress in analytical theory as well as in computer simulation.[1,2] Problems are originated from the subtle interplay between electrostatic interactions, entropy elasticity, intrinsic excluded volume and hydrophobic effects as well as from frequently ignored contributions of specific counter-ion and co-ion properties,[2,3] empirically expressed in the Hofmeister series.[4]

As compared to polyelectrolytes in a good solvent, the collapse of polyions in a poor solvent is even more complex and is an active research subject in the theoretical polyelectrolyte community. It is assumed that a poor solvent environment adds an effective attraction between monomers. The competition between attraction and repulsion is supposed to govern the shape of the polyion in a poor solvent.[5-22] Starting from the theoretical work of Khokhlov as early as 1980,[5-9] several papers based on analytical theory[10-16] and computer simulations can be found.[17-22] In particular the postulation of the "string of spheres" conformation close to the precipitation point by Dobrynin and Rubinstein[10-12] has been intriguing. Although few experimental studies on the collapse of polyelectrolytes supporting the "string of spheres" picture have been published so far, a solid experimental proof is still missing.[23-30]
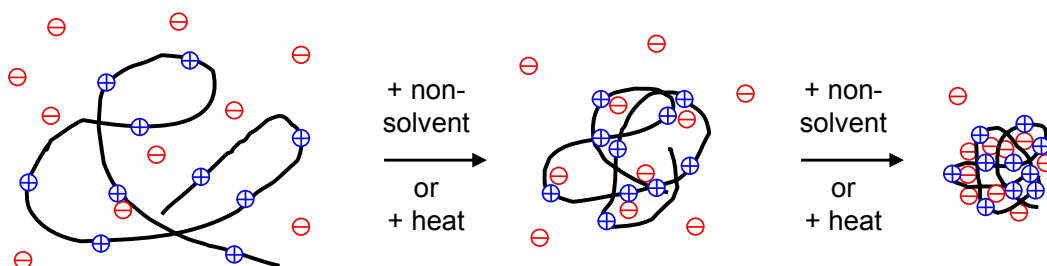
Figure 1.4 Scheme of polyelectrolyte collapse induced by addition of non-solvent or by heating; the initial configuration in a good solvent is a coil, expanded by electrostatic and solvent interactions, the final shape is a collapsed globule due to unfavorable solvent interactions. The configuration during the collapse is subject of this dissertation.

A reason for the lack of convincing data is given by the fact that long range Coulomb forces obscure the single molecule properties which are actually the point of interest. To circumvent these ensemble properties the addition of big amounts of screening salt to the solution can reduce those long range interactions but inescapable blurs the polyelectrolyte properties as well. The here presented approach is to use just a small amount of screening salt in combination with a very high dilution of the sample, so far not described in literature.[1-30] During my Diploma-thesis[31] I was able to conduct LS-measurements on two sufficient low diluted QPVP-samples. However we showed that light scattering measurements at these required conditions are systematically biased by the mentioned Coulomb interactions if evaluated with conventional approaches. Only few useful attempts to evaluate this kind of systems are described in literature.[32-34] First approaches for evaluation from my diploma thesis had to be further developed to yield a convincing tool for light scattering of polyelectrolytes at low amounts of screening salt. The developed LS-technique should be applied systematically to quaternized polyvinyl pyridines with different charge fractions. Concomitant with the configurationally change, answer to the question "when does a collapsing polyelectrolyte collect its counter ions?" ought to be answered. Therefore a conductivity measurement setup had to be developed, that would be able to produce and measure solvent compositions at the same sample dilution as measured with the light scattering setup. Due to simultaneous utilization of light scattering and conductivity measurements at very high dilution, this thesis should provide data of nonbiased single molecule behavior. Furthermore the results should be compared with a newly developed theory by M. Muthukumar and A. Kundagrami.[36]

1   [Förster, Schmidt 1995]
2   [Schmidt, Huber, Kremer et al. 2004]

[3]   [Beer, Schmidt, Muthukumar 1997]
[4]   [Collins, Washabaugh 1985]
[5]   [Khokhlov 1980]
[6]   [Kramarenko, Khokhlov, Yoshikawa 1997]
[7]   [Kramarenko, Khokhlov, Yoshikawa 2000]
[8]   [Vasilevskaya, Khokhlov, Yoshikawa 2000]
[9]   [Krmarenko, Erukhimovich, Khokhlov 2002]
[10] [Dobrynin, Rubinstein 1996]
[11] [Dobrynin, Rubinstein 1999]
[12] [Dobrynin, Rubinstein 2001]
[13] [Bordi, Cametti, Sennato, Zuzzi, Dou, Colby 2006]
[14] [Schweins, Huber 2004]
[15] [Schiessel 1999]
[16] [Manning 2007]
[17] [Chodanowski, Stoll 1999]
[18] [Limbach, Holm, 2003]
[19] [Liao, Dobrynin, Rubinstein 2006]
[20] [Jeon, Dobrynin2007]
[21] [Chang, Yethiraj 2006]
[22] [Reddy, Yethiraj 2006]
[23] [Williams, Carbajal-Tinoco 2000]
[24] [Williams et al. 2002]
[25] [Spiteri, Williams, Boue 2007]
[26] [Aseyev, Klenin, Tenhu 1998]
[27] [Aseyev, Klenin, Tenhu 1999]
[28] [Aseyev, Klenin, Tenhu, Grillo, Geissler 2001]
[29] [Lee, Green, Mikes, Morawetz 2002]
[30] [Bordi, Cametti, Gili, Sennato, Zuzzi, Dou, Colby 2006]
[31] [Loh 2005]
[32] [Bodycomb, Hara 1994]
[33] [Sorci, Reed 2002]
[34] [Koyama 1986]
[35] [Gröhn, Antonietti 2000]
[36] [Loh, Deen, Vollmer, Fischer, Schmidt, Kundagrami Muthukumar 2008]

2 Polyelectrolyte Theory

2.1 Polyelectrolyte Features

To understand polyelectrolyte behavior two simple approaches are presented: a model for the osmotic pressure and for the formation of intermolecular structures. Furthermore the so far "spooky" slow mode is discussed.

2.1.1 Osmotic Pressure

Measuring the osmotic pressure of uncharged or charged polymers, deviations of the ideal behavior will occur. The experimental data can be described by a virial series:

$$\frac{\Pi}{c_p} = RT\left(\frac{1}{M_n} + A_2 c_p + A_3 c_p^2 + ...\right)$$

2.1

Π	*osmotic pressure in Pa*
c_p	*polymer concentration in g/L*
R	*gas constant in J/Kmol*
T	*absolute Temperature in K*
M_n	*number average molar mass*
A_2, A_3	*second, third virial coefficient*

In salt free polyelectrolyte solutions due to the electro-neutrality law the counter ions cannot move through the semipermeable membrane. Assuming complete dissociation and neglecting solvent-solute interactions (that are the source of non-ideal behavior for uncharged polymers), the total molar concentration of particles is given by $c_p/M_n \cdot (z+1)$, with c_p/M_n the molar concentration of the polyelectrolyte and z_p the number of charges along the chain. The ideal osmotic pressure Π_{id} is therefore given by:

$$\frac{\Pi_{id}}{c_p} = RT \frac{1}{M_n}\left(z_p + 1\right)$$

2.2

The osmotic coefficient ϕ is defined as the ratio of the measured osmotic pressure divided by Π_{id}. Alternatively the osmotic pressure can be defined by the ratio of an effective charge number z_{eff} and z_p:

$$\phi = \frac{\Pi}{\Pi_{id}} = \frac{z_{eff}}{z_p}$$

2.3

Therefore the osmotic coefficient is a measure for the deviation from ideal behavior due to solvation and Coulomb effects. Measuring the osmotic pressure with membrane osmometry gives:

$$\frac{\Pi}{c_p} = \phi RT \frac{1}{M_n}\left(z_p + 1\right)$$

2.4

where ϕ includes solvation as well as ionic interactions. The number of charges of a polyelectrolyte is quite big and according to eq. 2.4 only the fraction $1/z_p+1$ of the osmotic pressure can be attributed to the polyelectrolyte itself. Even knowing the ratio of $1/z_p+1$, e.g. by elemental analysis, a determination of M_n in salt free solution is not possible due to the unknown ϕ which furthermore depends on c_p.
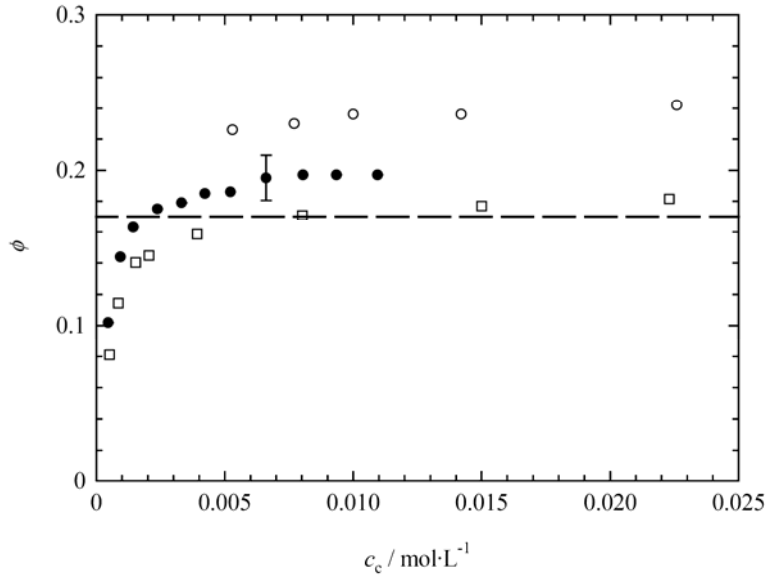
Figure 2.1 [Blaul 2001] Osmotic coefficient ϕ vs. concentration of polystyrene sulfonate in water from three different sources; the dashed line indicates the Manning limiting law given by eq. 2.25.

Nevertheless in principle a M_n determination of polyelectrolytes by osmometry is possible by adding an excess of salt. This screening salt leads to decoupling of macro-ions and its counterions and eq. 2.1 can be rewritten as [Dautzenberg 1994] (compare chapter 2.2):

$$\frac{\Pi}{c_p} = RT\left(\frac{1}{M_n} + \frac{z_{eff}^2}{4M_n^2 c_s}c_p + ...\right)$$

$$2.5$$

c_s *salt concentration in g/L*

whereas the deviation of the linear dependency is interpreted by the Donnan-effect and the big electrostatic motivated second virial coefficient is given by:

$$A_2 = \frac{z_{eff}^2}{4M_n^2 c_s}$$

$$2.6$$

2.1.2 Intermolecular Structure in Solution

In polyelectrolyte solutions containing only small or no additional salt, Coulomb interactions between polyions are screened only weakly, leading to a huge interaction range (compare chapter 2.2). If the resulting repulsion is equal or bigger than $k_B T$ the polyions order into a lattice-like structure in solution with an average inter particle distance $\bar{d}$. Assuming a cubic lattice, $\bar{d}$ can be calculated by:

$$\bar{d} = \left(\frac{M}{N_A c_p}\right)^{1/3}$$

$$2.7$$

with M the molecular weight of the particle, N_A the Avogadro constant and c_p the polyelectrolyte concentration in g/L. A preferential distance $\bar{d}$ leads to a maximum q_{max} in the angle-dependent intensity in scattering experiments. The maximum can be calculated using the Bragg-equation:

$$\overline{d} = \frac{2\pi}{q_{max}}$$

2.8

Therefore q_{max} is proportional to $c_p^{1/3}$ as verified by experiments [Förster, Schmidt 1995]. However it is known that the order is not perfect due to the Brownian motion of the latex particles as well as lattice defects. As a result, the scattering curve exhibits no sharp reflexes as for crystals, but rather a broad first maximum with a few smaller higher order peaks (compare Figure 4.5). An increase of salt content leads to a reduction of the peak intensity, however the peak position is unchanged.

Similar to light scattering the reduced specific viscosity in highly diluted polyelectrolyte solutions exhibit a concentration dependent maxima, too. Structure formation is used in the explanation of these results as well [Förster, Schmidt 1995].

2.1.3 Influence of Salt on the Diffusion Coefficient

Static as well as dynamic properties of polyelectrolytes are strongly influenced by the presence of added low molecular salt [Beer 1997]. In literature the influence of salt on the diffusion coefficient D has been examined in detail [Förster, Schmidt 1995]. It turned out that in dilute solutions it is not the absolute value of salt concentration that is decisive but the polymer to salt ratio. This is taken into account by the parameter $\lambda_R = C_p / C_s$ with C_p the equivalent polyelectrolyte concentration in *mol functionalized monomers per liter* and C_s the molar salt concentration.
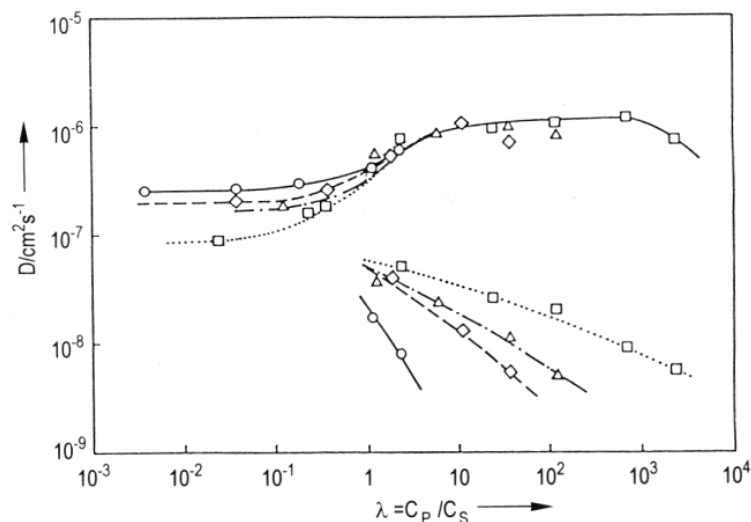
Figure 2.2 [Förster, Schmidt 1995]: Diffusion coefficients of quaternized polyvinyl-pyridines vs. the λ_R-parameter. Different symbols indicate different absolute salt concentrations.

Figure 2.2 shows a quite intriguing behavior and in fact it is not specific to the used sample but common for linear polyelectrolytes: polyelectrolytes exhibit different behavior at different salt concentration primarily governed by different λ_R-values. Three regions can be distinguished phenomenologically:

I $\lambda_R < 1$
        D stays constant with increasing λ_R

II   *1 < λ_R < 10*
        D increases strongly with an increase of λ_R, leading to a so called fast mode. Furthermore many samples feature the onset of a secondary slower relaxation time the so called slow mode but usually with smaller amplitude compared to the Fast-Mode [Förster, Schmidt 1995; Wilcoxon, Schurr 1983; Drifford, Dalbiez 1985, Förster, Schmidt, Anonietti 1990].

III   *10 < λ_R*
        The fast diffusion mode now exhibits a constant value, like in region **I**, but is usually two orders of magnitude faster. The slow diffusion mode continues to drop with increasing amount of salt.

Coupled–Mode Theory

The occurrence of the fast mode in regions **II** and **III** is described straightforward by the Coupled-Mode Theory, where electrostatic interactions couple the movement of the fast low molecular weight ions to the slow polyion. This leads to an acceleration of the polyelectrolytes:

I   High salt content in region **I** leads to screening of Coulomb forces and therefore coupling is weak in this area. All ions move independently and routine measurements are conducted with these conditions → 'measurements at salt-excess'

II   The degree of coupling increases with an increase of λ_R accelerating the polyions via the counterions.

III   The polyions are completely coupled to the coions resulting in a constant diffusion coefficient.

Slow Mode

The slow mode can occur in regions **II** and **III**. Slow mode means that the amplitude autocorrelation function $F_s^A(q, \tau)$ from dynamic light scattering (see chapter 4.2) can be fitted well by a biexponential fit whereas the two resulting diffusion coefficients differ by two orders of magnitude. Typically this can be visualized by a plot of $F_s^A(q, \tau)$ vs. $\log(\tau)$, exhibiting two step functions, although the small amplitude of the slow mode can make it hard to recognize.
It was argued that the slow mode might be dust or kinetically trapped aggregates. In contrast a coexistence of solved polyelectrolytes and its aggregates are proposed as well. Reed et al found that using a suitable filtration technique the slow mode could be suppressed [Reed et al. 1992, 1994]. Furthermore they found that the amplitude of the slow mode gets smaller with time (minutes till days) till it eventually vanishes and concluded that slow modes are the result of kinetically trapped aggregates formed during synthesis [Ricardo, Michel, Reed 2000]. These findings are in contradiction to measurements of Sedlák who could not remove the aggregates by filter techniques but found a systematic C_p and C_s dependence [Sedlák 1996] in line with the theory of Muthukumar of thermodynamic stable aggregates in coexistence with the fully solvated polyelectrolytes [Muthukumar 2007]. One might argue that the measurements of Reed et al. were conducted in a regime exhibiting only kinetically trapped aggregates but no thermodynamically stable slow mode but so far no bottom line has been agreed on.

2.2 Debye–Hückel Theory

The Debye-Hückel-Theory is the basic model to describe non-polymeric electrolytes in a solvent. In this model particles are regarded as point charges and the solvent is treated as a continuum only characterized by its permittivity $\varepsilon_0\varepsilon_r$ with ε_0 the permittivity of vacuum and ε_r the relative dielectric constant.

The coulomb potential of a test charge in the solution volume at a vector $\boldsymbol{r}$ is given by the sum of the potentials of all Z ions in the solution (throughout this thesis vectors will be printed bold whereas scalars will be non-bold). The extent of this potential $\phi_c(\boldsymbol{r})$ depends on the charges Q_j of the respective particles and their distances towards the considered point $\boldsymbol{r} - \boldsymbol{r}_j$:

$$\phi_c\left(\boldsymbol{r}\right) = \frac{1}{4\pi\varepsilon_0\varepsilon_r} \sum_{j=1}^{Z} \frac{Q_j}{\left|\boldsymbol{r} - \boldsymbol{r}_j\right|} \tag{2.9}$$

Z	number of charges in solution
$\left\|\boldsymbol{r} - \boldsymbol{r}_j\right\|$	distance of test charge and ion
$Q_j = z_k \cdot e$	charge with valency z_k and elementary charge e

In this theory the concomitant charge density $\rho_c(\boldsymbol{r})$ is given by the local ion density in an infinitesimal small volume element at any given vector $\boldsymbol{r}$:

$$\rho_c\left(\boldsymbol{r}\right) = e\sum_{k} z_k n_k\left(\boldsymbol{r}\right) \tag{2.10}$$

k	index of ion species
z_k	valency of ion species k
$n_k(\boldsymbol{r})$	number of ions of ion species k in infinitesimal volume at $\boldsymbol{r}$ (constituting the local concentration)

A constraint is given by the law of charge neutrality:

$$\sum_{k} z_k n_k^{\infty} = 0 \tag{2.11}$$

n_k^{∞}	bulk concentration of the solution

The potential energy of a cation at $\boldsymbol{r}$ is given by $z_k\, e\, \phi_c(\boldsymbol{r})$ whereas the occupation probability of different energy levels is described by the Boltzmann distribution. Neglecting the fluctuation of the local potential, therefore introducing a mean field approximation one can describe the local ion distribution by:

$$n_k\left(\boldsymbol{r}\right) = n_k^{\infty} \exp\left(-\frac{z_k e \left\langle \phi_c\left(\boldsymbol{r}\right)\right\rangle}{k_B T}\right) \tag{2.12}$$

Starting from one of the Maxwell equations the Poisson equation can be derived, relating the charge density to the Coulomb potential:

$$\Delta\phi_c\left(\boldsymbol{r}\right) = \frac{\rho_c\left(\boldsymbol{r}\right)}{\varepsilon_0\varepsilon_r} \tag{2.13}$$

Δ	$\dfrac{\partial^2}{x^2} + \dfrac{\partial^2}{y^2} + \dfrac{\partial^2}{z^2}$ Laplace operator

Therefore the Poisson equation connects equation 2.9 with 2.10 leading to the so called Poisson-Boltzmann equation:

$$\Delta\langle\phi_c(\mathbf{r})\rangle = -\frac{e}{\varepsilon_0\varepsilon_r}\sum_k z_k n_k^\infty \exp\left(-\frac{z_k e\langle\phi_c(\mathbf{r})\rangle}{k_B T}\right)$$

(2.14)

Its solution gives the time averaged electrostatic potential $\langle\phi_c(\mathbf{r})\rangle$. Equation 2.14 is a non linear differential equation that cannot be solved analytically for the considered radial symmetry. However assuming that the electrostatic energy $z_k e\,\phi_c(\mathbf{r})$ between the ions is much smaller than the thermal energy $k_B T$ ($z_k e\,\phi_c(\mathbf{r})\,/\,k_B T$ << 1) the exponential can be developed into a series expansion. This approximation is valid for low valencies and low concentrations and it is the main drawback if applied to polymeric systems, see below. Breaking off after the linear term one gets a simple linear relation where the term of the 0-order vanishes due to electro neutrality constraints, yielding the Debye-Hückel approximation:

$$\Delta\langle\phi_c(\mathbf{r})\rangle = \frac{e^2\sum_k z_k^2 n_k^\infty}{\varepsilon_0\varepsilon_r k_B T}\langle\phi_c(\mathbf{r})\rangle$$

(2.15)

For convenient handling the Debye-length λ_D, or respectively its inverse the screening constant κ_D is introduced as:

$$\lambda_D = \kappa_D^{-1} = \sqrt{\frac{\varepsilon_0\varepsilon_r k_B T}{e^2\sum_k z_k^2 n_k^\infty}}$$

(2.16)

and equation 2.15 can be rewritten as:

$$\Delta\langle\phi_c(\mathbf{r})\rangle = \frac{\langle\phi_c(\mathbf{r})\rangle}{\lambda_D^2} = \kappa_D^2\langle\phi_c(\mathbf{r})\rangle$$

(2.17)

The solution of this differential equation is

$$\langle\phi_c(\mathbf{r})\rangle = \frac{1}{4\pi\varepsilon_0\varepsilon_r}\frac{z_k e}{r}\exp\left(-\frac{r}{\lambda_D}\right)$$

(2.18)

$$\langle\rho_c(\mathbf{r})\rangle = -\varepsilon_0\varepsilon_r\lambda_D^{-2}\langle\phi_c(\mathbf{r})\rangle = -\frac{1}{4\pi\lambda_D^2}\frac{z_k e}{r}\exp\left(-\frac{r}{\lambda_D}\right)$$

(2.19)

One can summarize that the Coulomb potential of an isolated point charge is proportional to the inverse distance of the test charge ($\phi_c(r)\sim 1/r$), whereas in the presence of additional charges the potential is additionally screened: $\phi(r)\sim 1/r\,\exp(-r/\lambda_D)$ and the length scale of attenuation is given by the Debye length. Defining the ion strength as:

$$I \equiv \frac{1}{2}\sum_k z_k^2 n_k^\infty$$

(2.20)

The Debye length can be rewritten as:

$$\lambda_D = \sqrt{\frac{\varepsilon_0\varepsilon_r k_B T}{2e^2 I}}$$

(2.21)

The Debye length has a physical meaning, it represents the radius of the ion cloud of opposite charge surrounding any ion. (e.g. at I = 1.0 M, λ_D is about 0.3 nm, and at I = 10^{-3} M, λ_D is about 10 nm). Therefore integrating the charge density within a hollow sphere with radius r

and thickness *dr* surrounding any ion, the charge passes through a maximum at λ_D: ($q = 4\pi r^2 \, \rho_c(r)dr \sim r\,e^{-r}$):
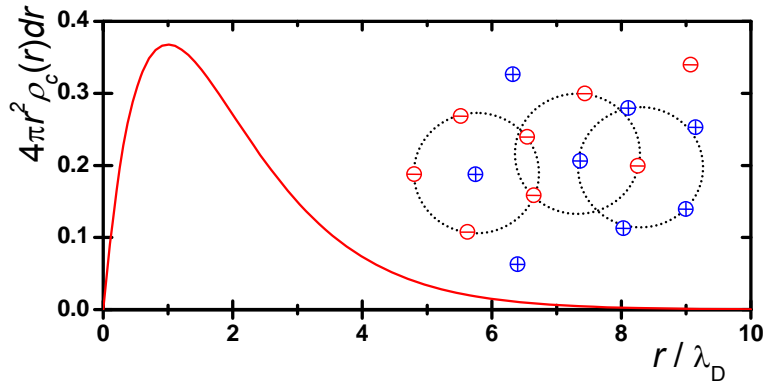
Figure 2.3 Spherical charge density in dependence of r / λ_D; sketch of ion atmosphere

The interaction of two charges surrounded by a solvent that is characterized by its permittivity, introduces a fundamental length scale, the Bjerrum length l_B. This is the length over which two charges of magnitude e experience electrostatic interaction energy equal to the medium's thermal energy k_BT:

$$l_B = \frac{e^2}{4\pi\varepsilon_0\varepsilon_r k_BT} \tag{2.22}$$

For a solvent with a high ε_r like water ($\varepsilon_r = 78$) the Bjerrum length is quite small (0.7 nm) whereas for non-polar solvents like 2-pentanone ($\varepsilon_r = 16$) the Bjerrum length is 3.5nm.

2.2.1 Lattice Model

Assuming the dimension of the polyion as small compared to the intermolecular distances, the application of the Debye Hückel theory to polyion-solutions might give a first approximation of the resulting forces. Therefore polyions are treated like ions with valency z_P. According to eq. 2.18 and 2.22 the interaction energy of two macroions at distance $\overline{d}$, each with number of charges z_P, in units of k_BT is given by:

$$\frac{U(\kappa_D, r)}{k_BT} = \frac{\phi_c(r)ez_p}{k_BT} = z_p^2 l_B \frac{1}{\overline{d}}\exp\left(-\kappa_D\overline{d}\right) \tag{2.23}$$

The distance of two ions can be approximated by eq. 2.8. The screening constant has two contributions: the added salt and the counterions of the polyelectrolyte itself (see chapter 5.4.3). Figure 2.4 shows the interaction energy in units of k_BT for a low charged polyelectrolyte. The polymer concentration influences $\overline{d}$ as well as κ_D, starting from $c_p = 0$ an increase of c_p leads to higher interaction but then counterion-screening exceeds the interaction term and U / k_BT goes down (c_p-axis). The salt influence is only incorporated in κ_D and an increase of C_s only strengthens the screening term by reducing the interaction energy (C_s-axis).

For high dilution but strong enough long range electrostatic interactions a lattice-like structure is formed visible on a smaller q-scale than the particle form factor $P(q)$ (compare chapter 2.1.2 and Figure 4.6b).
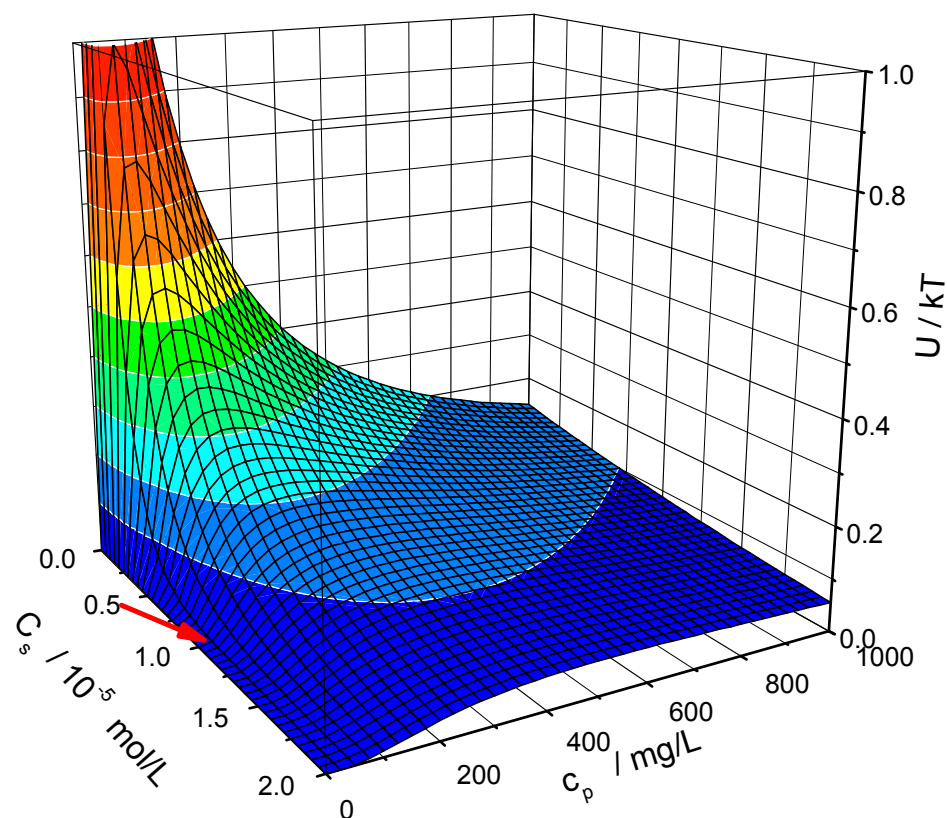
**Figure 2.4** Interaction energy U in units of k_BT is plotted vs. the salt concentration C_s and the polyelectrolyte concentration c_p. The Bjerrum length is set to the value of 1-propanol l_B = 2.7 nm; the number of charges of per polyelectrolyte is that $QPVP_{4.3}$ with z_p = 295; complete charge dissociation is assumed; the molar mass is M = 8.9*10^5 g/mol for the $QPVP_{4.3}$. The red arrow indicates the point of the measurement series at C_s = 10^{-5} mol/L and c_p = 12 mg/L.

2.2.2 Manning Counterion Condensation

Application of the Poisson-Boltzmann theory (PB theory) for a cylinder-like geometry leads to the PB cell model for infinite long rods with counterions. In case of no additional salt the PB equation can be solved analytically. The polyelectrolyte backbone is assumed as a long rod with a defined radius and a line-charge-density ρ_L. With respect to the electric fields the cylinders are assumed to be infinitely long. The 'cigar' is incorporated lengthwise in another cylinder (see Figure 2.4). The outer cylinder contains the counterions for charge neutrality. The sub volume respectively the length of each cylinder is determined by the bulk concentration. Intermolecular interactions as well as backbone entropy are neglected in this model, reducing the problem to a single particle problem. An analytical description of the polyelectrolyte solution with all individual counter ions is analytically not feasible; therefore the single species are substituted by a cylindrical counterion-density $n(r)$, with r the radial distance from the centerline. This is analogue to the mean-field approximation of the PB theory whereas the three degrees of freedom of the counter ions change from former spherical-symmetric to a cylindrical-symmetric geometry.
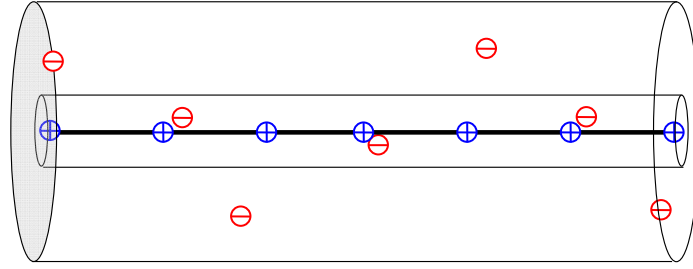
Figure 2.4 Scheme for condensation according to Manning. In this case the spacing of the charges is "too small" and a fraction of the counterions has condensed respectively has remained on the backbone.

According to the cell model a fraction of the counterions in the vicinity of the backbone is considered as condensed. These condensed ions reduce the line-charge-density to γ the effective degree of dissociation. The extent of the condensation is given by the interplay of the electrostatic attraction of the line charge and the counter ions and the loss of entropy in case of condensation. Special about the line charge model is the logarithmic scaling of its electric potential with distance r from the axis. This coincides with the logarithmic scaling of the Entropy S with volume per ion V: $T\delta S \propto k_B T \ln V \propto k_B T \ln r$. Thereby the PB cell model predicts partial condensation for line-charges even at infinite dilution. In contrast for spheres or planes the model predicts total loss respectively full condensation [Manning 2007].

According to Manning a critical charge-distance along the backbone exists: If a polyelectrolyte contains more functional units per length than this critical value a fraction of the dissociated counterions will condense to reduce the line charge density. For monovalent counterions the critical distance is simply given by the Bjerrum length l_B. This is usually expressed by the Manning parameter ξ_M:

$$\xi_M = \frac{l_B}{c} \tag{2.24}$$

with c the distance of two charges along the chain. For $\xi_M > 1$ condensation occurs till the effective contour length per charge c_{eff} is increased to l_B, and accordingly the fraction of the condensed ions is given by $(1 - 1/\xi_M)$. Furthermore the so called Manning limiting law makes a prediction for the osmotic coefficient ϕ at infinite dilution; for monovalent ions it should be given by:

$$\phi = \frac{1}{2\xi_M} \tag{2.25}$$

The concept of counterion condensation was originally developed for a line charge with infinite length [Manning, Zimm 1965] and then further developed by Oosawa and Manning to the more elaborated cell-model [Oosawa 1971; Manning 1969-2007]. In principal the PB-cell-model is only valid without any added salt and assumes the polyelectrolyte as stiff (although in [Manning 1981] he applies his counterion condensation concept to conditions with added salt as well). The important feature of the cell model is the prediction that counterions remain condensed even at infinite dilution which has been verified in experiments [Mandel 1988]. Nevertheless besides the mean field approach that neglects attraction due to charge fluctuations, the idea of polyelectrolytes being rigid rods is the main drawback of this model and is probably the source of discrepancies with experiments; see [Blaul 2001] as review. Furthermore deviations occur even if compared to stiff polyelectrolytes like DNA or rigid synthetic polyelectrolytes [Blaul 2001].

2.3   Wormlike Chain

For the characterization of semi flexible polymers the wormlike chain model developed by Kratky and Porod is used quite often [Kratky, Porod 1949]. This model can be used for polyelectrolytes in good solvents as done by Beer [Beer 1997]. The polymer is assumed as a chain with step length a and the correlation of two successive segment-tangent-vectors is characterized by the parameter λ_{corr}. The correlation between any two segments $\boldsymbol{Q}_j$ and $\boldsymbol{Q}_k$ can therefore be written as:

$$\left\langle \boldsymbol{Q}_j \bullet \boldsymbol{Q}_k \right\rangle = a^2 \lambda_{corr}^{|j-k|} = a^2 \exp-\left(\frac{|j-k|a}{l_p} \right) \tag{2.26}$$

$$
\begin{aligned}
&\lambda_{corr} = 0 && \textit{ideal flexible coil} \\
&\lambda_{corr} = 1 && \textit{rigid rod} \\
&a && \textit{monomer length} \\
&l_p && \textit{persistence length}
\end{aligned}
$$

Defining the contour length as $L_{cont} := N \cdot a$ and $l_p := a/(1-\lambda_{corr})$ the radius of gyration R_g of the wormlike chain model can be described by only two parameters:

$$R_g = \left\{ \frac{L l_p}{3} - l_p^2 + 2\frac{l_p^3}{L} - 2\frac{l_p^4}{L^2}\left[1 - \exp\left(-\frac{L}{l_p} \right) \right] \right\}^{1/2} \tag{2.27}$$

The two limiting cases of very big ($l_p \gg L$) and very small persistence lengths ($l_p \ll L_{cont}$) correspond to the conformation of a rigid rod or a Gaussian coil. Therefore l_p marks the crossover between rod-like behavior at length scales smaller than l_p and flexible chain behavior at length scales larger than l_p. The orientation correlation function for a worm-like chain follows an exponential decay and l_p is defined as the contour-length for which the orientation correlation (eq. 2.26) has decayed to $1/e$. Polymer textbooks usually define the Kuhn length l_K that is an imaginary step length for which the relations of a random-flight respectively a Gaussian-coil hold true, e.g. $R_g^2 \sim l_K L_{cont}/6$ ($\sim a \bullet aN$, compare eq. 2.36). Now setting $l_K := 2l_p$ and $N_K := L_{cont} / l_K$, R_g^2 can be rewritten as:

$$R_g^2 = \frac{2l_p L_{cont}}{6}\left\{ 1 - \frac{3}{2N_K} + \frac{3}{2N_K^2} - \frac{3}{4N_K^3}\left[1 - \exp\left(-2N_K \right) \right] \right\} \tag{2.28}$$

Therefore in the limit of $N_K \to \infty$ the square of the radius of gyration is proportional to $2l_p L_{cont}/6$ whereas a random flight model would give $R_g^2 = l_K L_{cont}/6$. Therefore the wormlike chain can be interpreted as a random-flight-model with step width $2l_p$.

2.3.1 Theory of Skolnick–Fixman–Odijk

The simplest way to introduce the concept of the persistence length into polyelectrolytes is the so-called SFO-Theory [Odijk 1977, 1978, Skolnick 1977]. Compared to the wormlike chain an alternative description of a semi flexible polymer is used: the bending of a wire-spring. First, entropy elasticity counteracts any backbone rigidity (compare chapter 2.4.2), therefore a continuously bend rod for the uncharged backbone is assumed and bending energy is of the form:

$$E_0 = \frac{1}{2} s \upsilon_{mod} \left(\frac{\beta_{end}}{s} \right)^2 = \upsilon_{mod} \frac{\beta_{end}^2}{2s} \tag{2.29}$$

s	*bended segment length*
υ_{mod}	*bending modulus*
β_{end}	*bending-angle*
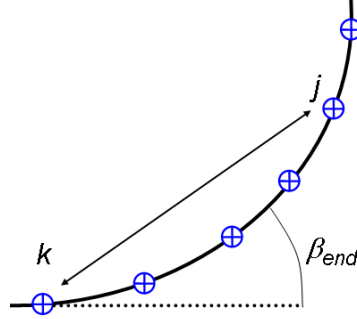
Figure 2.5 The electrostatic contribution to the persistence stems from charging of an already curved backbone via a screened Coulomb potential. The deformation of a segment with length s is given by β_{end} / s. β_{end} can be interpreted as the valence angle (e.g. 71.5° for a sp³-hybridization).

According to eq. 2.29 the elastic bending energy for a wire-spring is assumed as proportional to the bending modulus υ_{mod}, its length s and the square of the deformation β_{end} / s. The intrinsic persistence length of the uncharged backbone is simply given by:

$$l_0 = \frac{\upsilon_{mod}}{k_B T} \tag{2.30}$$

In case of polyelectrolytes the electrostatic contribution to the persistence stems from the charging of an already curved backbone as depicted in Figure 2.5. The bending energy is given accordingly by two contributions:

$$
\begin{aligned}
E &= E_0 + E_e \\
&= \frac{1}{2} k_B T l_0 \frac{\beta_{end}^2}{s} + \frac{1}{2} k_B T l_e \frac{\beta_{end}^2}{s}
\end{aligned}
\tag{2.31}
$$

whereas E_e is given by the sum of screened Debye-Hückel potentials of the form $1/r_{jk} \exp(-r_{jk} / \lambda_D)$ (compare Figure 2.5 and eq. 2.19). Due to electrostatic repulsion that counteracts the bending of the backbone, polyelectrolytes exhibit an enhanced persistence length compared to uncharged linear polymers. Accordingly l_p can be split into two contributions:

$$l_p = l_0 + l_e \tag{2.32}$$

with l_0 the intrinsic persistence length of the uncharged and l_e an additional persistence due to electrostatic repulsion. The electrostatic persistence length is given by:

$$l_e = \frac{1}{12} \frac{(z_p e)^2}{4\pi\varepsilon_0\varepsilon_r k_B T} N^2 h(\kappa_D L_{cont}) \tag{2.33}$$

$$
\begin{aligned}
h(\kappa_D L_{cont}) = {} & 3(\kappa_D L) L_{cont}^{-2} - 8(\kappa_D L_{cont})^{-3} \\
& + \left[(\kappa_D L_{cont})^{-1} + 5(\kappa_D L_{cont})^{-2} + 8(\kappa_D L_{cont})^{-3} \right] \exp(\kappa_D L_{cont})
\end{aligned}
$$

For high ionic strength and concomitant big values of $\kappa_D \, L_{cont}$ ($L_{cont}/\lambda_D > 25$) the higher terms of $h(\kappa_D \, L_{cont})$ can be neglected and furthermore accounting for counterion condensation one gets:

$$l_e = \frac{l_B}{4\kappa_D^2 c^2} \qquad\qquad\qquad l_B < c$$

$$l_e = \frac{1}{4\kappa_D^2 l_B} \qquad\qquad\qquad l_B > c \qquad\qquad\qquad (2.34)$$

with c the charge spacing along the chain. The main result of this calculation is that at short length scales the chain keeps its original characteristics despite the electrostatic interactions. This approach is therefore consistent only for chains with an intrinsic rigidity $l_0 > l_e$, for example, for DNA molecules that have a quite stiff backbone ($l_p \approx 50$ nm). However Odijk [Odijk 1978] later pointed out that in the case of $c \ll \lambda_D \ll L_{cont}$ eq. 2.33 could be applicable to flexible polyions as well, as the many charged segments on a local scale cause a weak bend rod again.

2.4   Solvent Solute Interactions

2.4.1 Single Chain in a Good Solvent – Flory Theory

Using simple arguments Flory could describe the scaling of a self avoiding random walk: The Gaussian probability distribution of an ideal chain with no self-avoidance is given by:

$$p(\boldsymbol{R_E}, N) = \left(\frac{3}{2\pi \langle R_E^2 \rangle} \right)^{3/2} exp\left(-\frac{3 R_E^2}{2 \langle R_E^2 \rangle} \right) \qquad\qquad (2.35)$$

$$R_E^2 = \boldsymbol{R_E} \cdot \boldsymbol{R_E} \qquad\qquad \textit{square of the end-to-end-distance-vector}$$

An important feature of this model is the scaling of R_E and the radius of gyration R_g with the number of segments N and the segment-length a:

$$\langle R_E^2 \rangle = 6 \langle R_g^2 \rangle = N a^2 \qquad\qquad (2.36)$$

The fundamental relation of entropy and microstates Ω is given by:

$$S = k_B \, ln \, \Omega \qquad\qquad (2.37)$$

Therefore the entropy of a Gauss-chain can be rewritten as a function of $\boldsymbol{R_E}$:

$$S(\boldsymbol{R_E}) = S(0) - \frac{3}{2} k_B \frac{R_E^2}{Na^2} \qquad\qquad (2.38)$$

The derivative of eq. 2.38 with respect to $\boldsymbol{R_E}$ yields a force that is attractive as indicated by its negative sign, and is the origin of the so called entropy elasticity in its most simple form. The 'elasticity' stems from the free energy change associated with alteration in the molecular configuration towards improbable states.
On the other hand the energy of a chain with end-to-end-distance $\overline{R_E}$ is given by the repulsion of its monomers. The average density of N monomers of size a in a Volume $\overline{R_E}^3$ is:

$$\phi_{int} = \frac{Na^3}{\overline{R_E}^3} \qquad\qquad (2.39)$$

The numerator correlates to the filled volume and the denominator to the whole volume. To calculate the number of interactions, ϕ_{int} is multiplied by the number of segments N. Furthermore defining ω_{Int} as the energy per interaction, the free energy can be calculated straight forward to yield:

$$F = E - TS = \omega_{Int} \frac{N^2 a^3}{\overline{R_E}^3} + \frac{3}{2} \frac{k_B T}{Na^2} \overline{R_E}^2$$

(2.40)

Minimizing E with respect to $\overline{R_E}$ gives:

$$\overline{R_E} = a \left(\frac{\omega_{int}}{k_B T} \right)^{1/5} N^{3/5}$$

(2.41)

Therefore independent of the size of the monomer (= exclusion volume) the end-to-end-distance scales with $N^{3/5}$. This value is very close to the exponent evaluated from renormalization theory and computer simulations (0.588). Furthermore whereas the most probable end to end distance for a random walk is $\overline{R_E} = 0$ (see eq. 2.35), it is obvious that in case of a self-avoiding random walk $\overline{R_E} = 0$ is very unlikely.

2.4.2 Flory–Huggins Theory

In his book "Principles of Polymer Chemistry" Flory describes the thermodynamics of polymer solutions based on a liquid lattice theory. Using statistical mechanics and mean field arguments for a diluted polymer solution with 'clouds of polymers' surrounded by pure solvent, he calculated the Gibbs free energy:

$$G_m = RT \left[ln(1 - \phi_2) + \phi_2 + \chi_1 \phi_2^2 \right]$$

(2.42)

G_m	*chemical potential*
ϕ_1, ϕ_2	*volume fraction of solvent 1 and polymer 2*
χ_1	*Flory-Huggins parameter*

The χ_1-parameter represents the interaction energy of the solvent-solute pair. Three different configurations of solvent-solute interactions are distinguished and in case of solvation the interaction-difference per contact is given by:

$$w = w_{12} - \frac{1}{2}(w_{11} + w_{22})$$

(2.43)

w_{11}	*polymer-polymer-interaction*
w_{12}	*polymer-solvent-interaction*
w_{22}	*solvent-solvent-interaction*

Using a mean field approximation the energy difference of the mixture on a lattice with coordination number y is given by:

$$\chi_1 = (y - 2)w / k_B T$$

(2.44)

This theory can be applied to evaluate the miscibility of mixtures or the osmotic pressure Π, e.g. Π times the molar solvent volume v_{solv} is given by:

$$\Pi v_{solv} = RT \left[\frac{\phi_2}{N} + \left(\frac{1}{2} - \chi_1 \right) \phi_2^2 + ... \right]$$

(2.45)

According to eq. 2.45 three different values of χ_1 should be distinguished:

$\chi_1 < \frac{1}{2}$ *The osmotic pressure is higher than that of an ideal chain. The solvent is good in this regime. The end-to-end-distances of the coils behave as discussed in chapter 2.4.1.*

$\chi_1 > \frac{1}{2}$ *The osmotic pressure is lower than that of an ideal chain and it may stay solvated only if the entropy exceeds the attractive forces.*

$\chi_1 = \frac{1}{2}$ *The chain behaves ideal. This condition is called θ-condition.*

Comparison of eq. 2.45 with 2.1 gives:

$$A_2 = \left(0.5 - \chi_1\right) \rho_{poly}^{-2} \, v_{solv}^{-1} \tag{2.46}$$

ρ_{poly} *density of the solid polymer*
v_{solv} *molar volume of the solvent*

If χ_1 would be purely enthalpic according to eq. 2.44, it should simply be proportional to *1/T* and one would expect an increase of solvent quality with an increase of temperature. This is usually not the case. Much more complex characteristics were found experimentally, e.g. in this dissertation the lower critical solution temperature (LCST) is probed, meaning an increase of *T* reduces solvent quality. Therefore χ_1 can incorporate entropic contributions, too. For example a molecular weight dependence is not captured by eq. 2.45 respectively 2.46. Independent of any assumed model, it can be shown that the excess chemical potential of the solvent must vary with the square and higher powers of the solute concentration, whereas for diluted systems higher terms usually are neglected. Therefore the ϕ_2^2 terms in equation 2.42 and 2.45 can alternatively be interpreted as excess terms accounting for non-ideality ($G_m^E = H_m^E - T S_m^E$). For dilute solutions Flory split the χ_1–parameter into an enthalpic and an entropic contribution according to:

$$\kappa_1 - \psi_1 = \chi_1 - \frac{1}{2} \tag{2.47}$$

κ_1 *enthalpy-parameter according to* $H_m^E = RT \kappa_1 \phi_2^2$
ψ_1 *entropy-parameter according to* $S_m^E = R \psi_1 \phi_2^2$

Within experimental conditions one may find a temperature for which entropic and enthalpic contributions cancel each other. The system is called to behave pseudo-ideal and the corresponding temperature is called θ- or Flory temperature:

$$\theta = \frac{\kappa_1 T}{\psi_1} \tag{2.48}$$

Expressing κ_1 in terms of the Flory temperature yields for the excess Gibbs free energy:

$$G_m^E = RT \psi_1 \left(\frac{\theta}{T} - 1 \right) \phi_2^2 \tag{2.49}$$

Therefore deviations from ideality vanish at the θ-temperature.

Solvent Solute Interactions in Terms of the θ–Temperature

Whereas in chapter 2.4.1 a quite simple approach was sufficient for the basic features of a coil with self-avoidance, Flory derived a more elaborated expression based on the osmotic action

of the solvent. Furthermore using the excess chemical potential for enthalpic interactions (eq. 2.49), he could formulate a more elaborated free energy expression. Minimizing with respect to the expansion factor α (= $R_g/R_{g,\theta}$, with $R_{g,\theta}$ the radius of gyration at θ-conditions) he derived the following equation (analogue to eq. 2.40):

$$\alpha^5 - \alpha^3 = 2C_M\psi_1\left(1-\frac{\theta}{T}\right)M^{1/2}$$

$$C_M = \left(3^3/2^{5/2}\,\pi^{3/2}\right)\left(\upsilon_p{}^2/v_1N\right)\left(M/\overline{R_{E,\theta}}\right)^{3/2}$$

(2.50)

υ_p	*specific volume of polymer*
v_1	*volume fraction of solvent*

More elaborated theories [Grosberg, Kuznetsov 1992; Birshtein, Pryamitsyn 1991; Muthukumar 1987] often refer or extrapolate their theory to the relation of eq. '2.50 left hand side' but give new expressions for the right hand side of eq. 2.50.

2.5 Blob–model and Scaling

Whereas a random walk of a polymer coil without any excluded volume ($A_2 = 0$) gives a scaling of $R_g \sim M^{1/2} \sim N^{1/2}$, a self-avoiding random walk with positive A_2 yields $R_g \sim M^{3/5} \sim N^{3/5}$. According to the so called blob-model every self-avoiding random walk has a length scale called blob on which monomers do not interfere with each other but behave like a common Gauss distribution. The blob size is given by a correlation length that sets the distance below which a certain interaction is suppressed by thermal fluctuations (Figure 2.6 bottom left).
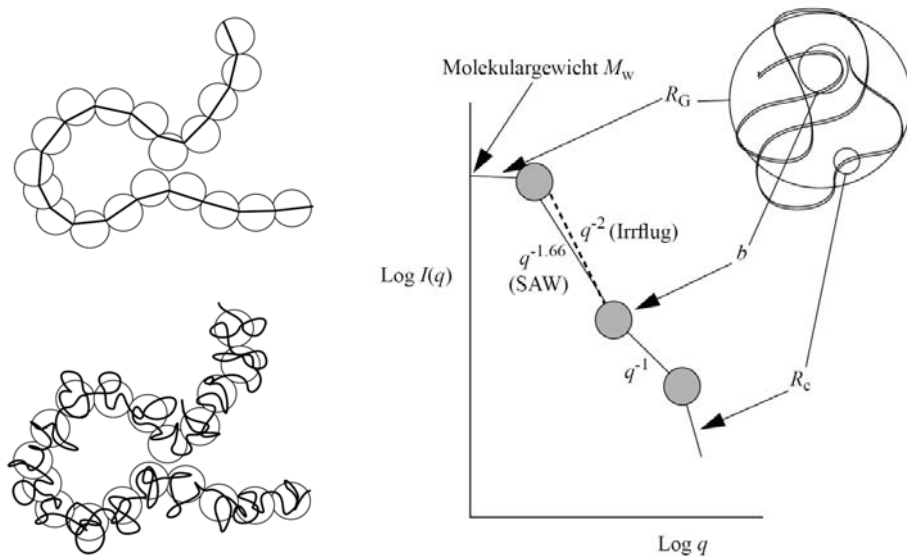
Figure 2.6 [Oettinger] Left top: blobs assembled of sufficient correlated monomers till correlation amongst them is lost; bottom: self-avoiding walk assembled of random flight blobs; right: The different length scales can be probed in scattering experiments; starting at small q one can evaluate the molecular weight, the size in terms of R_g, the inner structure - here a coil with a self-avoiding walk or a random flight; the length of a stiff unit and lastly a monomer cross section.

Similar the persistence may be visualized, too (Figure 2.6 left top). Steps that are correlated may be combined into one blob whereas the blobs themselves behave like a (self-avoiding) random walk. The blob-picture is motivated by the scaling of the measured intensity in scattering experiments, probing different length scales as depicted in Figure 2.6 and is explained in detail in chapter 4.1.The blob concept for polyelectrolytes without screening salt in different concentration regimes can be derived as follows. For a fully dissociated polyelectrolyte the coulomb interaction for the size R_{sc} is of the order:

$$E_C \simeq \frac{1}{4\pi\varepsilon_0\varepsilon_r}\frac{(Ne)^2}{R_{sc}} \tag{2.51}$$

According to eq. 2.38 the elastic energy can be written as:

$$E_{el} \simeq k_B T \frac{R_{sc}^2}{Na^2} \tag{2.52}$$

Minimizing the total energy $E = E_C + E_{el}$ with respect to R_{sc} gives:

$$R_{sc} \simeq N a^{2/3} l_B^{1/3} \tag{2.53}$$

Defining a new step width $\tilde{a}$ as:

$$\tilde{a} = \left(a^2 l_B\right)^{1/3} \tag{2.54}$$

a new scaling of N^1 instead of $N^{3/5}$ is found:

$$R_{sc} \simeq N\tilde{a} \tag{2.55}$$

For annealed polyelectrolytes the number of charges g within one blob is assumed to be in the order of $k_B T$ (compare chapter 2.2.2). With the size of the blob R_B one can write:

$$\frac{1}{4\pi\varepsilon_0\varepsilon_r}\frac{(ge)^2}{R_B} \sim k_B T \tag{2.56}$$

Furthermore for a θ-solvent R_B should be given by:

$$R_B \sim aN_B^{1/2} \sim a\left(\frac{g}{\gamma}\right)^{1/2} \tag{2.57}$$

$N_B = g / \gamma$	*number of monomers per blob*
$\gamma = z_p/N$	*degree of dissociation*
z_p	*number of charges along chain*
N	*number of monomers*

The number of charges within one blob can be calculated according to:

$$g \sim l_B^{-2/3} a^{2/3} \gamma^{-1/3} \tag{2.58}$$

Due to their mutual repulsion the blobs in turn are assumed to line up as a stiff rod, to yield an elongation in the order of:

$$R_{\parallel} \sim \frac{N}{N_B} R_B \sim \frac{N\gamma}{g} R_B \sim Na^{2/3} l_B^{1/3} \gamma^{2/3} \sim N \tag{2.59}$$

These approximations may work as a rule of thumb for some conditions. In contrast more complex scaling approaches as imagined by Schiessel [Schiessel 1999] or the pearl-necklace-model by Dobrynin and Rubinstein [Dobrynin 1996-2007] use many approximation steps till they comprehensively predict a whole sets of states (see next chapter.

2.6 Pearl Necklace Structure

The conformation of a polyelectrolyte in solution is determined by the minimum of free energy. To reduce the number of unfavorable polymer-solvent-contacts, uncharged chains collapse to dense globules which is equivalent to a minimization of the surface tension. In contrast the conformation of a charged polymer is determined by the balance of electrostatic repulsion, entropy elasticity of the chain, entropic energy of the counterions and solvent-solute interactions. The repulsion of ionic groups along the backbone can cause different structures than the collapsed sphere.

2.6.1 Pearl Necklace – Blob Concept

Khokhlov was the first to propose a distortion from the spherical shape and assumed a cylinder shape or 'cigar-like structure' using scaling models. He showed that the free energy was reduced compared to the spherical globule. Rayleigh showed [Rayleigh 1882] that due to the ratio of surface tension and coulomb repulsion, a charged droplet will split into many smaller droplets thereby decreasing the free energy. Kantor and Kardar [Kantor, Kardar 1994, 1995] performed Monte Carlo simulations and were the first to find at least a dumbbell-shaped configuration (they only could simulate 64 monomers due to limited computational power at that time). They explained their findings with a blob-model of a charged chain with short range attraction and long range repulsion.
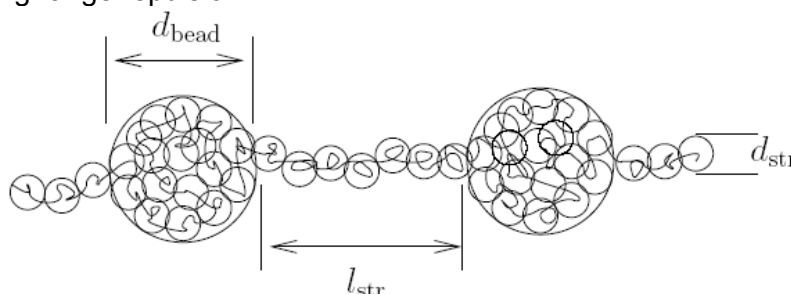
Figure 2.7 [Dobrynin 1998] Pearl necklace structure of thermal-blobs, explanation see text.

Dobrynin and Rubinstein refined this scaling-model in their paper series lastly even claiming pearl necklace structures to appear in a good solvent regime [Dobrynin 2007] (They argue that polyelectrolytes with a high Manning parameter have a high fraction of condensed counterions, leading to an effective potential that is attractive even if the good-solvent induced effective potential is repulsive). Using scaling arguments their pearl necklace model predicts the bead number N_{bead}, the size of the beads d_{bead}, the number of monomers per m_{bead}, and the length of the connecting strings l_{str} with their cross-section d_{str} and number of monomers m_{str}. According to their blob-concept the free energy of the necklace E_{nec} is lower than that of a cylinder and given by:

$$\frac{E_{nec}}{k_B T} \approx N\gamma \left(\tau \xi_M\right)^{1/2} \tag{2.60}$$

$$d_{bead} \approx a\left(\xi_M \gamma^2\right)^{-1/3} \qquad l_{str} \approx a\left(\frac{\tau}{\xi_M \gamma^2}\right)^{1/2} \qquad \gamma \approx \left(\frac{\tau}{\xi_M}\frac{N_{bead}}{N}\right)^{1/2} \tag{2.61}$$

$$\tau = \frac{\theta - T}{\theta} \qquad\qquad \text{relative deviation from } \theta\text{-temperature}$$

whereas the solvent quality is characterized by the parameter τ. Figure 2.7 shows the pearl necklace structure composed of thermal-blobs as imagined by Dobrynin and Rubinstein. Within a thermal blob the effective attraction of the segments is suppressed due to thermal motion and a random walk is assumed whereas on a larger scale the pearl necklace is assembled. A further thinning of the strings would increase the free energy due to entropy elasticity. A change of the charge on the chain via γ or the solvent quality via τ should force the polyelectrolyte to undergo a cascade of abrupt transitions with different number of beads.

2.6.2 Pearl Necklace – Computer Simulations

Not at least due to its intriguing structure there are many computer simulations of polyelectrolytes in poor solvents that support the pearl necklace structure [e.g. Chodanowski, Stoll 1999; Limbach, Holm, 2003; Liao, Dobrynin, Rubinstein 2006; Jeon, Dobrynin2007]. Almost all of the newer pearl necklace simulations are coarse grained molecular dynamics simulations (MD-simulation) in which atoms are combined to more crucial, bigger units like monomers or Kuhn steps. The backbone with its discrete charges along the chain as well as the counterions are simulated explicitly whereas the solvent is only accounted for by its dielectric constant. The trajectories of all particles are evaluated solving the Newtonian equations and the solvent is simulated by a random noise term called Langevin thermostat:

$$m_i \frac{d^2 r_i}{dt^2} = -f_i v_i + \nabla_{r_i} U + F_i(t) \tag{2.62}$$

m_i, f_i	mass and friction coefficient of particle i
r_i, v_i	position and velocity vector of particle i
t	time
$\nabla_{r_i} U$	force field acting on particle i due to potential U
F_i	stochastic force term → noise of the bath acting on particle i

During a research stay in Muthukumar's theory group (he does not believe in pearl necklaces) using their MD-simulation code and the help of the group member Zhaoyang Ou, I could reproduce the various types of pearl necklaces.

In case of my simulation study the polyelectrolyte was assumed as composed of Kuhn steps, therefore a freely jointed chain without bond-angle-penalties was used and three potentials were necessary to characterize the system. A conventional Lennard-Jones potential was used to mimic the effective attraction of any two units of the backbone which is the net result of unfavorable interactions with the solvent molecules:

$$U_{LJ} = \begin{cases} \varepsilon_{LJ}\left[\left(\dfrac{r_0}{r}\right)^{12} - 2\left(\dfrac{r_0}{r}\right)^6 + 1\right] & r \leq r_0 \\[2mm] 0 & r \geq r_0 \end{cases} \tag{2.63}$$

$$\varepsilon_{LJ} \qquad\qquad\qquad \text{\textit{strength of the LJ-potential with unit } } k_B T$$

$$r_0, r \qquad\qquad\qquad \text{\textit{hardcore distance, distance between two units}}$$

The energy associated with bond stretching of each bond of the chain is taken as:

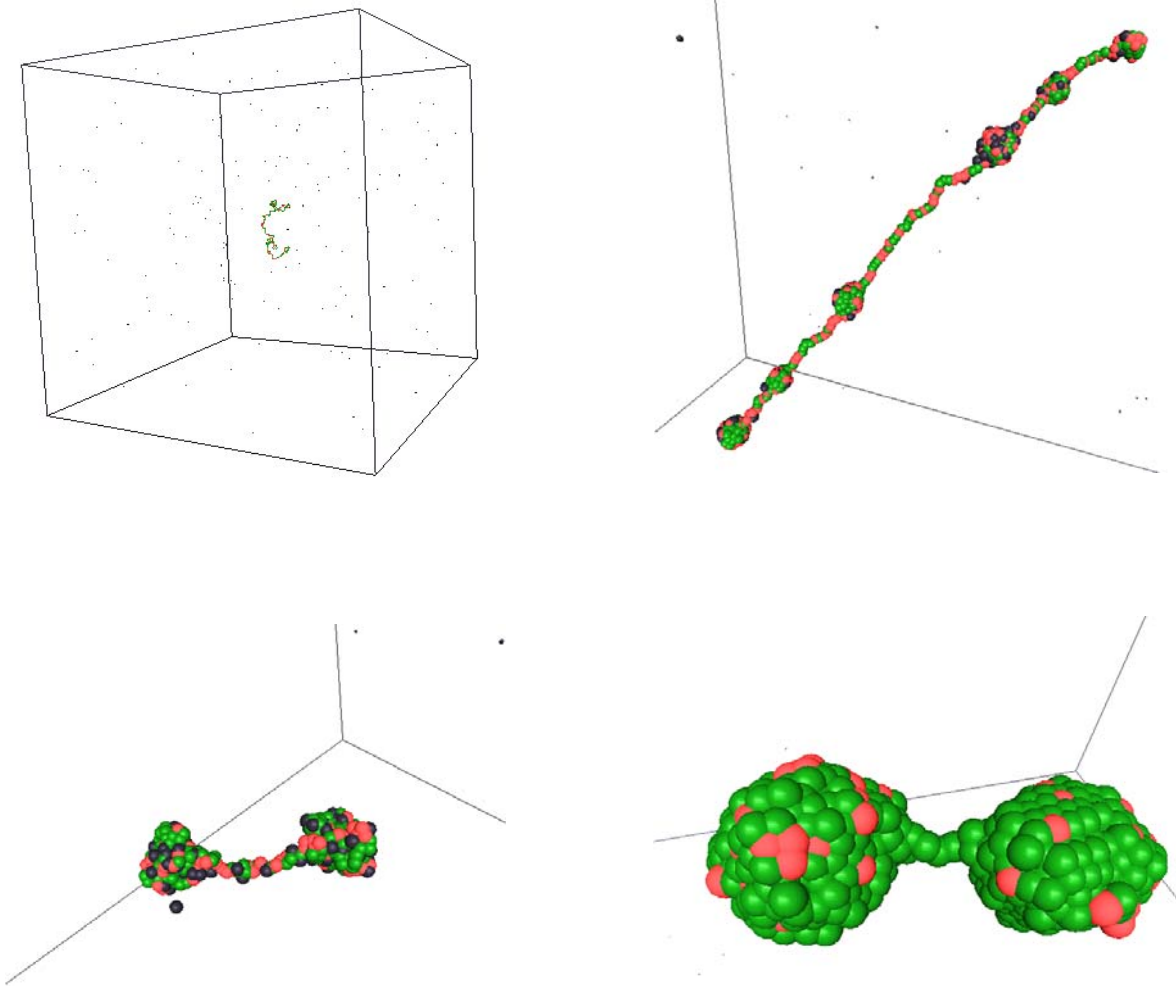$$U_{bond} = k \left(l - l_0 \right)^2 \tag{2.64}$$

$$l, l_0 \qquad\qquad\qquad \text{\textit{bond length and equilibrium bond length}}$$

The electrostatic energy among the charged monomers and counterions is given by:

$$U_c \left(r_{ij} \right) = \frac{e^2}{4\pi\varepsilon_0\varepsilon_r r_{ij}} \tag{2.65}$$

More details of the simulation method are given in [Liu 2003]. Figure 2.8 shows some snapshots of different simulations.

Figure 2.8 Snapshots of MD-simulations; 500 monomers with uncharged units in green, charged in red and counterions in black; within constraints all particles were placed randomly in a medium of uniform ε_r and one polymer per simulation-box was simulated with cubic boundary conditions – mirrored at the planes; top left shows a starting configuration whereas the other snapshots show equilibrated structures with different charge fractions and LJ-strengths.

Although pearl necklace structures form easily in coarse grained MD-simulations, whether these conformations occur in reality is not save. Yethiraj and coworkers simulated polyelectrolytes in poor solvents with explicit simulation of the solvent molecules [Reddy Yethiraj 2006] and surprisingly they did not find signatures of pearls but found sausage like structures. They claimed that the LJ-potential (eq. 2.63) that all other groups used is not valid in the inner part of a 'pearl'. They argued that a unit within a collapsed globule is only surrounded by other polymer units therefore will not experience an effective attractive LJ-pair-potential but a weaker or even repulsive one. To test this assumption Yethiraj et al. devised a new potential for implicit solvent simulation that is not static but based on the solvent accessible surface area (SASA) of a chain segment. With this potential they could reproduce their previous findings with the explicit solvent simulation (which is much slower and therefore unpopular). One should note that in contrast to MD-simulations experiments show that collapsed beads still contain solvent molecules of about 50 volume percent [Chi Vu 1998]. Nevertheless it is obvious that the common used LJ-potential at least overestimates attraction due to hydrophobic interaction and the experiments so far trying to proof pearl necklaces should be watched critically.

2.7   Muthukumar-Kundagrami Theory

Muthukumar developed a theory of counter-ion condensation on flexible polyelectrolytes giving self consistently all necessary contributions to the free energy F in terms of analytical expressions [Muthukumar 2004 + 1987]. In this theory F is minimized with respect to two parameters: the expansion coefficient α_{Rg} and the degree of dissociation γ. By calculation and subsequent minimization of F he simulated α_{Rg} and γ for three experimental available variables: salt concentration, Bjerrum length and dielectric mismatch parameter (see below). Two distinctions compared to the Manning theory should be emphasized: Muthukumar's approach yields no 'kink' for the degree of dissociation with respect to the Bjerrum length (compare chapter 2.2.2). Polyelectrolytes are not assumed to be rigid but have a configurational free energy. Muthukumar's theory is aimed to replace Manning's theory in favor of quantitative agreement with experiment respectively molecular-dynamics simulation, whereas it lacks any 'rule of thumb' for the degree of dissociation nor the osmotic coefficient.

In [Muthukumar 2004] the coupling among polyelectrolyte conformations, counterion adsorption, and translational entropy and electrostatic correlations of small ions is treated self-consistently. However only the progressive accumulation of counterions as the polymer coil continues to shrink due to an increasing number of ion-pair formation has been addressed. Following the theoretical explanations of Muthukumar [Loh, Schmidt, Kundagrami Muthukumar 2008] the theory is now extended for the self-consistent determination of counterion accumulation as the polymer collapses due to hydrophobic forces. One should note that hydrophobic effects are not covered in Manning's theory at all. To differentiate between experiment and theory the notation of Muthukumar and Kundagrami is used for all theoretical considerations throughout this thesis.

When a flexible polyelectrolyte chain is present in a solution containing its counterions and dissociated electrolyte ions, the effective charge of the polymer is modulated by adsorption of counterions. The extent of this adsorption is controlled by an optimization between attractive energies associated with the formation of ion pairs (among polymer segments and counterions) and the loss in translational entropy of the counterions, which would otherwise be free to explore the whole solution. Further, the distribution of counterions around the polymer

depends on the polymer conformations, which in turn depend on how many counter-ions are adsorbing on the polymer molecule. Thus a self-consistent procedure is necessitated to calculate the size and the effective charge of the polyelectrolyte molecule.

Several computer simulations [Chang, Yethiraj 2006; Reddy, Yethiraj 2006; Severin 1993; Stevens, Kremer 1993 + 1995, Winkler, Gold, Reineker 1998; Liu, Muthukumar 2002], where counterions are accounted for explicitly, clearly demonstrate that the effective charge indeed depends uniquely on the polymer size. Within the same context, there has recently been another model [Vasilevskaya, Khokhlov 2000; Kramarenko, Erukhimovich, Khokhlov 2002] where the polyelectrolyte chain and the background solution is treated as a three-state system. In this model, the unadsorbed counterions are presumed to partition into two domains, with one domain being the volume within the coil and the other domain outside the coil. In addition, the entropic part of chain fluctuations is not explicitly accounted for. The major prediction of the three-state model is that the polymer collapse induced by intra-chain hydrophobic attraction occurs in two stages with the accompanying two levels of counterion condensation. In contrast, in our theory, there is only one collapsed state and the extent of counterion adsorption follows the shrinkage of the polymer size. The key steps of the theory are given as follows (for more details see [Muthukumar 2004]).

The size and shape of a polyelectrolyte molecule in solutions are controlled by the binding energy of counterions onto the chain backbone, the translational entropy of counterions in the solution, and the concomitant changes in polymer conformations. The complete free energy F of the system consisting of a flexible polyelectrolyte chain with ionizable groups assumed to be uniformly distributed along the chain backbone, its counterions and the added salt ions in high dilution is a sum of 6 contributions ($F = \sum_{i=1}^{6} F_i$) [Muthukumar 2004], and the components are given as follows.

F_1, related to the **entropy of mobility of the condensed counterions on the chain backbone**, is given by:

$$\frac{F_1}{Nk_BT} = (f_m - \alpha_1)\log\left(1 - \frac{\alpha_1}{f_m}\right) + \alpha_1\log\left(\frac{\alpha_1}{f_m}\right) \tag{2.66}$$

N	number of Kuhn segments in the chain
k_B	Boltzmann constant
T	absolute temperature
f_m	number of ionizable groups per Kuhn segment
α_1	number of ionizable groups with condensed counterions per Kuhn segment

F_2, related to the **translational entropy of the uncondensed counterions and the salt ions** (i.e., the free and mobile ions in the solution), is given by

$$\frac{F_2}{Nk_BT} = \left(f_m - \alpha_1 + \frac{\tilde{c}_s}{\tilde{c}_p}\right)\log\left\{\tilde{c}_p\left(f_m - \alpha_1\right) + \tilde{c}_s\right\} + \frac{\tilde{c}_s}{\tilde{c}_p}\log\tilde{c}_s - \left(f_m - \alpha_1 + \frac{2\tilde{c}_s}{\tilde{c}_p}\right) \tag{2.67}$$

$\tilde{c}_p = c_p l_0^3$,	dimensionless number density of the monomers
$\tilde{c}_s = c_s l_0^3$	dimensionless number density of the monovalent saltions
l_0	Kuhn segment length

F_3, related to the **fluctuations arising from the electrostatic interactions among all mobile ions**, is given by the Debye-Hückel form,

$$\frac{F_3}{Nk_BT} = -\frac{2}{3}\sqrt{\pi}\tilde{l}_B^{3/2}\frac{1}{\tilde{c}_p}\left\{\tilde{c}_p\left(f_m - \alpha_1\right) + 2\tilde{c}_s\right\}^{3/2}$$

(2.68)

$\tilde{l}_B = e^2 / 4\pi\varepsilon\varepsilon_0 k_BT l_0$	*dimensionless Bjerrum length*
e	*electron charge*
$\varepsilon, \varepsilon_0$	*solvent dielectric constant and vacuum permittivity*

F_4, the **adsorption energy gain due to ion-pairs formation with condensation**, is given by:

$$\frac{F_4}{Nk_BT} = -\tilde{l}_B\delta\alpha_1$$

(2.69)

$\delta = \left(\varepsilon/\varepsilon_I\right)\left(l_0/d\right) \equiv C\varepsilon l_0$	*mismatch parameter, reflecting the disparity between bulk dielectric constant and local dielectric constant close to the chain backbone*
$C = 1/\varepsilon_I d$	*system specific parameter*
ε_I	*'local' dielectric constant related to the material of the polymer backbone*
d	*dipole length of the ion-pairs*

The free energy of the polymer chain considers the interaction energy $V(r)$ between the Kuhn segments separated by a distance r, where

$$\frac{V(r)}{k_BT} = w\delta(r) + f^2 l_B\frac{e^{-\kappa r}}{r}$$

(2.70)

w	*strength of the excluded volume interaction,*
$f = f_m - \alpha_1$	*degree of ionization, maximum degree of ionization, fraction of condensed ions*
$\kappa = \sqrt{4\pi l_B\left\{c_p f + 2c_s\right\}}$	*inverse Debye length*

is valid for monovalent ionic groups. The first and second terms of the potential represent the excluded volume (non-electrostatic) and electrostatic interactions, respectively. Using a well-known variational method [Muthukumar 2004 + 1987] F_5, the **chain free energy**, is obtained as

$$\frac{F_5}{k_BT} = \frac{3}{2}\left(\tilde{l}_1 - 1 - \log\tilde{l}_1\right) + \frac{4}{3}\left(\frac{3}{2\pi}\right)^{3/2}\left[w + w_1\alpha_1^2\delta^2\tilde{l}_B^2\right]\sqrt{N}\frac{1}{\tilde{l}_1^{3/2}}$$
$$+ \frac{w_3}{N\tilde{l}_1^3} + 2\sqrt{\frac{6}{\pi}}f^2\tilde{l}_B\frac{N^{3/2}}{\tilde{l}_1^{1/2}}\Theta_0\left(\kappa\right)$$

(2.71)

$\tilde{l}_1 = 6R_g^2 / Nl_0^2 = \alpha_{Rg}^2$	*effective expansion factor*
R_g	*radius of gyration*
N, l_0	*number of Kuhn segments, Kuhn length*
$w = 1/2 - \chi$	*excluded volume parameter*
χ	*Flory-Huggins chemical mismatch parameter*
$w_1 < 0,$	*temperature dependent parameter*
w_3	*three-body interaction parameter*

Here

$$\Theta_0(a) = \frac{\sqrt{\pi}}{2}\left(\frac{2}{a^{5/2}} - \frac{1}{a^{3/2}}\right)\exp(a)\,\mathrm{erfc}\left(\sqrt{a}\right) + \frac{1}{3a} + \frac{2}{a^2} - \frac{\sqrt{\pi}}{a^{5/2}} - \frac{\sqrt{\pi}}{2a^{3/2}} \tag{2.72}$$

is a cross-over function with $a = \tilde{\kappa}^2 N\tilde{l}_1/6$, where $\tilde{\kappa} = \kappa l_0$ is a dimensionless inverse Debye length. A major assumption to derive eq. 2.71 is that of uniform swelling of the chain with spherical symmetry. Note that a positive and non-zero w_3 is required to stabilize the free energy in the case of a chain collapse below the Gaussian dimension ($\tilde{l}_1 = 1$) for negative values of w. The four major terms of eq. 2.71 represent the contributions to the free energy of the backbone: entropy, two body interaction, three body interaction and electrostatic interaction.

F_6, the **free energy contribution arising from interactions among ion-pairs** can be obtained by modifying the expression for short ranged excluded volume effect to be:

$$\frac{F_6}{k_B T} = \frac{4}{3}\left(\frac{3}{2\pi}\right)^{3/2} w_1 \alpha_1^2 \delta^2 \tilde{l}_B^2 \alpha_1^2 \sqrt{N}\tilde{l}_1^{-3/2} \tag{2.73}$$

F_6 is short-ranged and attractive. It introduces an additional parameter w_1 that leads to a reduction of the value of the excluded volume parameter w as it accounts for the attractive nature of interacting dipoles. In case of low degrees of quaternization F_6 has only a minor influence on the conformation and may be neglected, thereby canceling the contribution to the chain free energy accordingly [Loh, Schmidt, Kundagrami Muthukumar 2008]. Including F_6 the theory is able to cover the whole experimental range of the degree of quaternization as used in this thesis (1.2 to 35%).

The optimum radius of gyration R_g and the degree of ionization f of an isolated chain are derived by simultaneous minimization of the free energy of the system (chain, counterions, salt ions, and the solvent) with respect to R_g and f. Numerically, F is minimized self-consistently with respect to f and $\tilde{l}_1$ to obtain the equilibrium values of the respective quantities in specific physical conditions stipulated by T, ε, and $\tilde{c}_s$. It must be remarked that the free energy described above is for a single polyelectrolyte chain in a dilute solution, and it is valid for concentrations of salt not too high (so that $\kappa^{-1} \geq l_B$ or $c_s \leq (8\pi l_B^3)^{-1}$ for a monovalent salt). It is valid, however, for all temperatures, and for any degree of ionization (or ionizability) of the polymer. In addition, the above free energy is equally applicable for multi-chain systems in infinitely dilute solutions in which the chains have negligible inter-chain interaction (either excluded volume or electrostatic). Qualitative analysis of the free energy shows that the size and charge of the polyelectrolyte chain are primarily determined by the energy gain of ion-pairs (which is linearly proportional to an effective Coulomb strength ($\tilde{l}_B \delta$)) relative to the translational entropy of the mobile ions in the expanded state and by the relative strength of w to w_3 in the collapsed state. The parameters C in eq. (2.69) and w_3 in eq. 2.71 are the the only adjustable parameters taken to fit the experimental data (In case of low degree of quaternization, QPVP4.3, see below, w_3 is negligible and only one parameter is sufficient to describe the data). One notes that calibration of w by the respective uncharged chain is necessary to eliminate the uncertainty in determining the non-electrostatic interactions in charged polymers and that can be performed by setting $w_3 = w_1 = f = 0$ in eq. (2.71). Minimizing F_5 with respect to $\tilde{l}_1$, in this case, yields the familiar formula for chain expansion

$$\alpha^5 - \alpha^3 = \frac{4}{3}\left(\frac{3}{2\pi}\right)^{3/2} w\sqrt{N} \tag{2.74}$$

where $\alpha^2 = \tilde{l}_1$. The functional dependence of the non-electrostatic parameter w on the solvent composition is established first by using eq. 2.74 to determine w from the expansion factor of the uncharged polymer chain. Later, by performing the double minimization of the free energy of the charged polymer, α and f were determined with C as a parameter, and then compared with the experimental data.

3 Electrolyte–Conductivity

The response of a medium to an external electrical field generally depends on the frequency of the alternating current. This frequency dependence reflects the fact that the material's polarization does not respond instantaneously to an applied field. To account for potential frequency dependence, the impedance is generally used to describe a system. The impedance is a complex quantity with a real part, the resistance and an imaginary part, the reactance. Measuring the impedance of a polyelectrolyte solution at increasing frequencies, various relaxations are expected to occur: polyion dipolar orientation, polarization of condensed counterions, polarization of the ionic atmosphere and at higher frequencies orientational polarization of the solvent molecules. In low frequency electro magnetic fields the molecular dipoles of a sample follow the polarity changes without measurable lag. However it is not possible to measure at low frequencies due to electrode polarization effects [Bordi et al 2006].
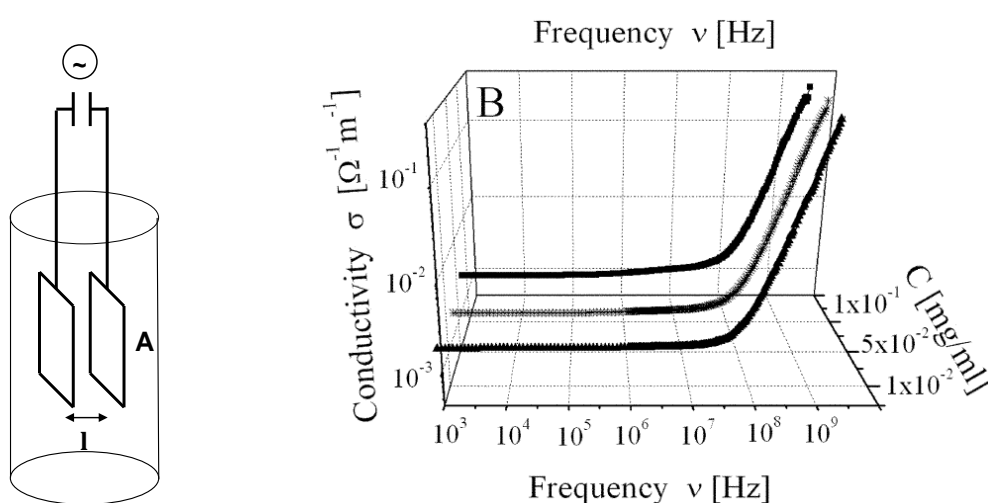
Figure 3.1 Left: sketch of a conductivity setup. The cell constant K_{cell} is given by the ratio l / A however it is practical determined with a conductivity standard. Right [Bordi et al 2006]: electrical conductivity of 55% functionalized poly(N-methyl-2-vinyl pyridinium chloride) polyion in water (poor solvent condition) as a function of frequency of the applied external electric field, at three different polyion concentrations: 'front': 0.01 mg/ml; 'middle': 0.03 mg/ml; 'back': 0.06 mg/ml.

In his paper series Colby et al. deduced polyelectrolyte configurations from relaxation time measurements of various polyelectrolytes in good and poor solvent conditions (amongst others quaternized 2PVP in ethylene-glycol/water mixtures, see [Bordi et al 2006] as review). They found the frequency range from 10^2 to 10^4 Hz to be unbiased by relaxation from polarization respectively electrode polarization effects (see Figure 3.1; However his conclusion to have pearl necklace structures, drawn from relaxation time measurements and fitted with 'blob-theory', is highly questionable). All measurements of this thesis have been conducted at 2.4 kHz, therefore are not expected to be biased by those two effects. Therefore Ohm's law can be assumed as valid to give a relation between the current I, the resistance R and the potential U:

$$I = \frac{1}{R} U \tag{3.1}$$

The resistance depends on the probe used and is characterized by the parameter K_{Cell}. In principal K_{Cell} is given by the distance l of the two electrodes divided by the area A (see Figure 3.1). One can define a normalized resistance ω that accounts for the probe used:

$$\omega = \frac{1}{\kappa_{el}} = R \cdot \frac{A}{l} = \frac{R}{K_{Cell}} \tag{3.2}$$

with κ_{el} the electrolytic conductivity (in S/cm).

3.1   Low Molecular Strong Electrolyte

Dividing κ_{el} by the molar concentration C_s (in mol/mL) gives the molar conductivity Λ (in S cm^2/equiv):

$$\Lambda = \frac{\kappa_{el}}{C_s} \tag{3.3}$$

Λ is a function of the concentration. The concentration dependency is given by the empirical Kohlrausch law:

$$\Lambda = \Lambda^0 - \mathcal{K} C_s^{1/2} \tag{3.4}$$

The constant Λ^0 is the limiting molar conductivity, when the ions are infinitely far apart and do not interact with each other. This empirical law was validated by the Debye-Hückel-Onsager theory that furthermore determines $\mathcal{K}$ as:

$$\mathcal{K} = A + B \Lambda^0 \tag{3.5}$$

with A and B consisting of only molecular parameters, see [Atkins 1998] for details. This influence is explained with two pictures, the relaxation effect and the electrophoretic effect. These introduce the effect of motion to the picture of a static ionic atmosphere as a spherical shell of nearest neighbors (see Figure 2.3).
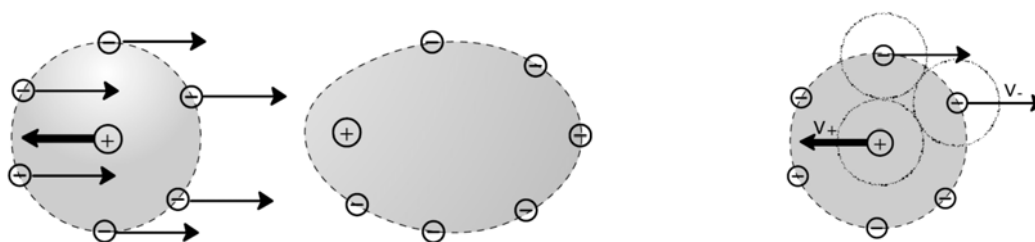
Figure 3.2 Left: sketch of relaxation effect; right sketch of electrophoretic effect.

Relaxation Effect: The ions forming the atmosphere do not adjust to the moving ion infinitely quickly, and the counterion cloud is distorted. The center of charge of the 'atmosphere-circle' is displaced a short distance behind the moving ion, thereby retarding the moving ion (see Figure 3.2).

Electrophoretic Effect: The ionic atmosphere has another effect on the motion of the ions. Moving particles change the speed of solvent molecules in their vicinity. Since opposite charged particles move in opposite directions the viscous drag experienced by the moving central ion is enhanced accordingly (see Figure 3.2).

The limiting molar conductivity Λ^0 can be expressed as the sum of contributions from its individual ions:

$$\Lambda^0 = F\,v^+z^+u^{0+} + F\,v^-z^-u^{0-} = v^+\lambda^{0+} + v^-\lambda^{0-}$$

(3.6)

F	*Faraday constant*
v^+, v^-	*stoichiometric numbers*
z^+, z^-	*number of charges of the ions*
u^{0+}, u^{0-}	*limiting mobility of the ions*
$\lambda^{0+}, \lambda^{0-}$	*limiting equivalent mobility of the ions*

As a first approximation, the mobility u_i^0 of any ion is given by its velocity v_i at a given electrical field E which is equivalent to the dragging charge divided by Stokes friction f_i:

$$u_i = \frac{v_i}{E} = \frac{z_i e}{f_i} = \frac{z_i e}{6\pi r_i \eta}$$

(3.7)

Combining equation 3.6 and 3.7 one gets the Walden rule:

$$\Lambda_{0i}^{\pm}\,\eta = \frac{F\,z_i^2\,e}{6\,\pi\,r_i}$$

(3.8)

It states that the product of the viscosity and molar conductivity has to be constant with respect to temperature and solvent composition whereas the microstructure of solvent and ions is neglected.

3.2 Polyelectrolyte Conductivity

Generally the equivalent conductivity of a polyelectrolyte solution without addition of low molecular salt is given by:

$$\Lambda = f_c\left(\lambda_p + \lambda_c^0\right)$$

(3.9)

Where λ_c^0 is the equivalent conductivity of the counterion in an infinitely diluted solution in the absence of polyions, λ_p is the equivalent conductivity of the polyion, and f_c is the interaction parameter which includes the electrostatic interactions between the polyion and the counterions as well as the degree of ionization.

3.2.1 'Monomer–Theory–model'

For high ionic strength, the polyion may be assumed as fully drained due to vanishing interactions. In this case the polyion is expected to approach the mobility of a charge carrying segment. This idea is motivated by the experimental finding that for various conditions λ_p does not depend very much on the molecular mass of the polyion but it has values in the same order of magnitude as small ions. In this most simple model the friction of successive units adds up linearly with increasing degree of polymerization:

$$\lambda_p = \frac{z_i e}{f_p} = \frac{z_i e}{z_i f_{segment}}$$

(3.10)

f_p	*friction coefficient of polyion*
$f_{segment}$	*friction coefficient of subunit with one charge*

However the good agreement with experiments is believed to be a cancellation of errors [Muthukumar 1997, Manning 1981] and for many cases the 'monomer-theory' is too rough. It ignores association of counterions and hydrodynamic interactions between different monomers, leading to an overestimation of the mobility

3.2.2 Manning's Line Charge Model

In salt-free solutions Manning's line charge model (compare chapter 2.2.2) [Manning 1975] gives expressions for λ_p as well as f_c. For the spacing of chemical charges along the chain c less than the Bjerrum length l_B and consequently $l_B/c = \xi_M > 1$, f_c was calculated as:

$$f_c = 0.866\, \xi_M \tag{3.11}$$

Manning's line charge model in salt free solution was compared to experimental data by Wandrey [Wandrey 1999]. She found that if applying Manning's line charge model, f_c is not a constant but rather a function of the empiric parameter λ_D / L.

Whereas in frictional formalism (chapter 3.2.4) friction coefficients of the ionic species (poly-, counter-, coions) are the result of mutual interaction, Manning [Manning 1981] focused on the evaluation of the friction coefficient of the polyion f_p. Starting from 'monomer Theory' (eqn. 3.10) he added consecutively to f_p: the hydrodynamic interactions (wind-shielding), the electrophoretic effect and lastly the relaxation field. His model is applicable for the addition of screening salt as long as $\kappa_D\, c \ll 1$, with c. Manning assumed the polyion as composed of rigid segments (at least) of the length of λ_D due to unscreened electrostatic repulsions among polymeric charges within this length (he did not allow coiling neither due to entropy elasticity nor due to poor solvent interactions). In irreversible thermodynamics (chapter 3.2.4) the friction coefficients are empirical entities. In contrast Manning could break them down to involve only molecular parameters, e.g. those of line charge model, respectively DH-Theory. However his model does not incorporate solute-solvent-interactions in any kind thereby it can not explain the data of this thesis.

3.2.3 The Porous Sphere Model

In case of a coiled polyion, the conductivity is a complex property since small ions penetrate the coil. In case of negligible drainage of the coil, the mobility of the polyelectrolyte is primarily determined by a classical Stokes type of friction coefficient $6\pi\eta R$. The migration in an external field is described in the colloid chemical literature on the electrophoresis of charged spheres (see [Deggelmann 1992] as review). The mobility of the polyelectrolyte u_p is related to the zeta potential ζ_{zeta} according to:

$$u_p = F\left(\kappa_D, R\right) \frac{\varepsilon_0 \varepsilon_r \zeta_{zeta}}{\eta_0} \tag{3.12}$$

Where the function $F\left(\kappa_D, R\right)$ accounts for the electrophoretic retardation as well as the relaxation effect and has the limits:

$$F\left(\kappa_D, R\right) = \begin{cases} 1 & \kappa_D\, R \to \infty \\ \dfrac{2}{3} & \kappa_D\, R \to 1 \end{cases} \tag{3.13}$$

In this particular case the charge Q_e is a net result of the structural polyionic charge and the counterions/co-ions contained within the sphere. For this spherical geometry the PB equation can be solved to yield:

$$Q_e = 4\pi\varepsilon_0\varepsilon_r R\left(1 + \kappa_D R\right)\zeta_{zeta} \qquad (3.14)$$

3.2.4 Frictional Formalism of Non-Equilibrium Thermodynamics

Schmitt and coworkers were the first to apply irreversible thermodynamics to polyelectrolyte solutions by assigning friction coefficients to all possible collision-pairs of ionic species in the solution [Varoqui 1972, Schmitt 1978]. In particular they could show that the relaxation field and the electrophoretic effect from Debye-Hückel-Onsager theory inevitable are incorporated in the frictional formalism. They calculated the extent of those two effects onto the mobility of the polyion in terms of friction properties. In the case of added salt they showed, that the coin drifting into the same direction as the polyion, enhances λ_D whereas the coions themselves are slowed down. Frictional formalism is of great experimental use because in principal it does not need the assumption of any certain topology of the polyion (coil, rod, wormlike chain…). Vink reused friction formalism [Vink 1984] and deduced that the electrophoretic and relaxation effect is equal to the fraction of total hydrodynamic energy dissipation due to interionic friction. He could express the electrolytic conductivity in a clear manner:

$$\kappa_{el} = \left(1-\beta\right)\left[\left(\lambda_1 + \lambda_2\right)C_s + \gamma\left(\lambda_1 + \lambda_p\right)C_p\right] \qquad (3.15)$$

$$\lambda_1 = \frac{F^2\left|z_1\right|}{f_1} \qquad \lambda_2 = \frac{F^2\left|z_2\right|}{f_2} \qquad \lambda_p = \frac{F^2\gamma\left|z_p\right|}{f_p} \qquad (3.16 - 3.18)$$

β	*fraction of total energy dissipation due to interionic friction*
$\lambda_1, \lambda_2, \lambda_p$	*free-ion equivalent conductivities of counter-, co- and polyion*
C_s, C_p	*equivalent concentrations of salt and polyion*
γ	*apparent degree of dissociation of the polyion*
z_1, z_2, z_p	*charge numbers of counter-, co- and polyion*
f_1, f_2, f_p	*hydrodynamic molar friction coefficients of counter-, co- and polyion*

In preliminary measurements he could show that in dilute solutions hydrodynamic friction properties of small ions are very little affected by the presence of polymeric solutes [Vink 1981, 1982]. Therefore λ_1 and λ_2 in eq. 3.15 may be replaced by λ_1^0 and λ_2^0 the free-ion equivalent conductivities at infinite dilution. In contrast the equivalent conductivity of the polyion depends on C_p. This is indicated in eq. 3.18 as γ is a function of C_p. Vink could further break down polyion mobility by assuming f_p to contain friction contributions from the fraction of the counterions forming a kinetic unit with the polyion $(1-\gamma)$, leading to:

$$\lambda_p = \frac{F^2\gamma\left|z_p\right|}{f_p^* + \left(1-\gamma\right)\vartheta\dfrac{F^2\left|z_p\right|}{\lambda_1^0}} \qquad (3.19)$$

with f_p^* the friction coefficient of the polyion chain and ϑ an adjustable parameter accounting for hydrodynamic shielding effects within the polyion domain. For a free-draining counterion

atmosphere $\vartheta = 1$, whereas $\vartheta \ll 1$ holds for counterions closely condensed onto the polyion chain thereby indicating that λ_p depends on the nature of the counterion. Therefore in dilute solutions eqn. 3.15 can be rewritten as:

$$\kappa_{el} = (1 - \beta)\left[\Lambda_s^0 C_s + \gamma\left(\lambda_1^0 + \lambda_p\right)C_p\right]$$ (3.20)

The factor $(1-\beta)$ in eqn. 3.15 shows that all ions are equally affected by interionic friction, a direct consequence of the Onsager reciprocity law and the electroneutrality conditions.

4   Light Scattering

An electromagnetic wave hitting weak bound electric charges will accelerate these with oscillating motion according to the Maxwell equations. Steadily accelerated charges create electromagnetic waves that oscillate in phase with the primary radiation and leave the oscillator as a secondary electromagnetic wave. For light scattering with its big wavelength, depending on the molecule size this translates into parts of the molecule acting as classical dipole antennas. The superposition of scattered light from many positions of the molecule or from different molecules at the detector leads to the intrinsic scattering characteristics of the sample. A light scattering setup basically consists of a vertically polarized light beam passing through a solvated sample, and a detector that measures the scattered intensity angle dependent. By evaluation of the scattering radiation one can obtain information of the structure and the dynamics of the solvated samples.
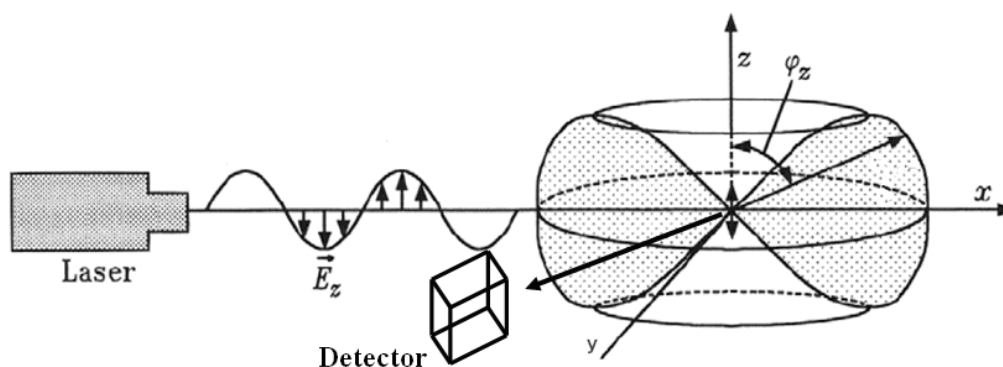
Figure 4.1 Scheme of the relation between the polarized incident beam and the scattered intensity from a hertz dipole.

In **static light scattering** (SLS) one collects the radiation angle dependent in the horizontal x-y plane, typically between 30-150° in 5° steps. For a given angle the intensity over a period of i. e. 30s is averaged. By evaluation of the angle dependent intensity one can obtain up to three characteristics of the static features of the sample:

radius of gyration – essentially a z-average $\left\langle R_g^2 \right\rangle_z^{0.5}$

molecular weight as weight average M_w

second virial coefficient of the osmotic pressure A_2

In **dynamic light scattering** (DLS) one observes the time dependent fluctuation of the intensity signal with a very fast sampling time down to tens of nanoseconds. The time scale of the intensity fluctuations are governed by the diffusion coefficient D_z of all particles inside the scattering volume. From this value one can calculate the sphere equivalent hydrodynamic radius as:

hydrodynamic radius – essentially an inverse z-average $\left\langle R_h^{-1} \right\rangle_z^{-1}$

In case of polydisperse samples DLS needs to be measured angle dependent, too (see below).

4.1   Static Light Scattering

A laser beam can be adequately described as a monochromatic, polarized plane wave with field vector E, maximum field vector E_0, wave vector k_0, angular frequency ω and phase offset δ:

$$E = E_0 \exp\left[i\left(k_0 R - \omega t + \delta\right)\right],$$ (4.1)

whereas R describes the position of interest. It will turn out that the absolute phase is not of interest and concomitant the phase offset δ is obsolete and will be neglected in the following description. Furthermore in the case of a defined setup with two polarizers before and after the sample with an vertical-vertical or vertical-horizontal alignment (see Fig. 4.1) the absolute value of the field vector E, the scalar E is sufficient to describe the system. If this plane wave hits a point scatterer, the scatterer will originate a spherical wave as sketched in figure 4.2.
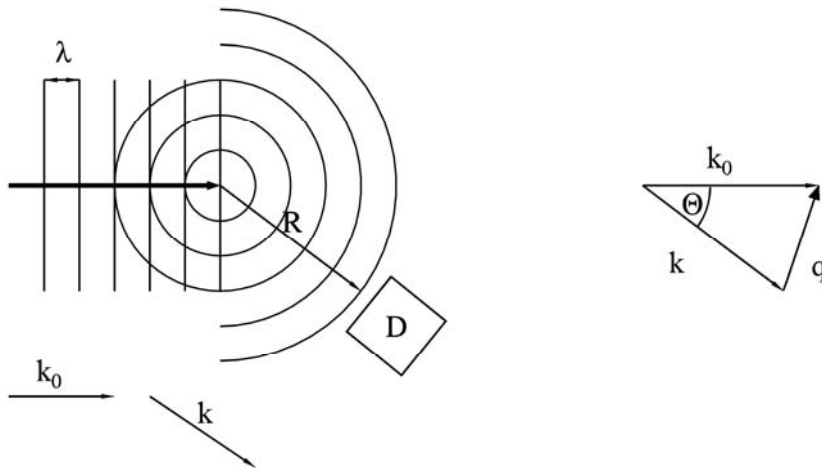
Figure 4.2 [Bartsch] Left: A monochromatic wave hits a point scatterer. The outgoing wave vector is set to be parallel to the vector R pointing towards the detector. Right: The difference vector of initial and scattered wave vector is called the scattering vector q.

For the theory of SLS the scattering-process is assumed as fully elastic which is not correct but due to the used avalanche-detection-system that counts photons and is not photon-energy-sensitive, no error is introduced as explained in detail in the next chapter. The absolute value of the initial wave vector therefore can be set equal to the scattered one: $\left|k_0\right| = \left|k\right| = 2\pi n_D / \lambda_0$. The refractive index n_D accounts for the reduced wavelength of the beam in a medium compared to λ_0 the wavelength of the radiation in vacuum. The absolute value of the difference vector between in- and outgoing wave vectors is called q and is given by:

$$\left|k_0 - k\right| = \left|q\right| = q = \frac{4\pi n_D}{\lambda_0} \sin\left(\frac{\theta}{2}\right)$$ (4.2)

Using the notation from eq. 4.1 the amplitude at R is given by:

$$E_s\left(R, k, t\right) = \frac{E_0 b}{R} \exp\left(-i\omega t\right) \exp\left(ikR\right)$$ (4.3)

b is called scattering length and is proportional to the polarization ability of parts of the molecule. For simplification this factor can be imagined as the polarization ability of a monomer. The next step is to superimpose two scattered waves at the detector which is set at an arbitrary position. Figure 4.3 exemplifies the phase difference of a pair of scatterers for one

arrangement at the detector, simply given by the scalar product of their distance vector *r* times the scattering-vector *q*.
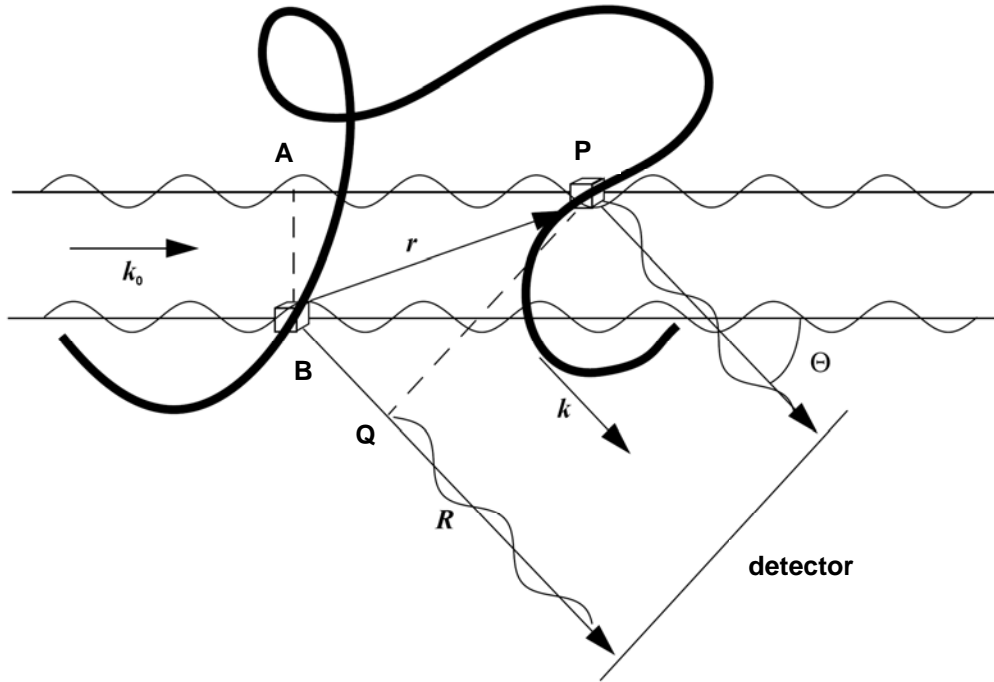
Figure 4.3. [Öttinger et. al] Scattering scheme of polymer-coil to evaluate the resulting phase difference at the detector – for convenience an x-ray wave length is shown; the path difference $\Delta = \overline{AP} - \overline{BQ}$ is given by $\Delta = \dfrac{\mathbf{k_o} \cdot \mathbf{r}}{|\mathbf{k_o}|} - \dfrac{\mathbf{k} \cdot \mathbf{r}}{|\mathbf{k}|} = \dfrac{\mathbf{q} \cdot \mathbf{r}}{|\mathbf{k_o}|}$ and therefore the phase difference by $\Phi = \Delta |\mathbf{k_o}| = \mathbf{q}\mathbf{r}$.

Therefore the phase difference only depends on the reciprocal of the wavelength inside the solvent, the distance of the origins of the point scatterers, and the angle between initial and scattered wave vector. The inverse of the wavelength and the trigonometric scaling with the angle can be merged into a single variable the scattering vector *q*. This variable is used throughout the literature as abscissa. Applying this principle the superimposed amplitude of E_B and E_P at *R* is given by:

$$E_B + E_P = E_S\left(\mathbf{R}, \mathbf{k}, t, \mathbf{q}, \mathbf{r}\right) = \frac{E_0 b}{R} \exp\left[i\left(\mathbf{k}\mathbf{R} - \omega t\right)\right]\left[1 + \exp\left(i\mathbf{q}\mathbf{r}\right)\right] \tag{4.4}$$

Scatterer B is defined as the point of origin. The phase offset due to the arbitrarily chosen point of origin and time is represented by the first exponential term in eq. 4.4. This term is the same for both particles thus neglected in the further discussion. By taking the sum over all scattering particles S, allowing different scattering lengths and movements for those scatterers one gets:

$$E_{S,\,sum}\left(\mathbf{q}\mathbf{r_k}(t)\right) = \frac{E_0}{R} \sum_{k=0}^{S} b_k \exp\left[i\mathbf{q}\mathbf{r_k}(t)\right] \tag{4.5}$$

The sum notation does not specify the explicit distribution function of the scattering particles *g(r)* as would be necessary by using the more precise integral notation. Integral notation and *g(r)* will be introduced when needed. The detector detects the time average of the intensity of a scattering volume over a relative long period of time. The intensity from two scatterers

located at $\boldsymbol{0}$ and $\boldsymbol{r}$ (eq. 4.4) is given by $2E_0^2 b^2/R^2 [1 + \cos(\boldsymbol{q}r)]$ and accordingly the resulting intensity for S scatterers (eq. 4.5) is given by:

$$I(\boldsymbol{q}) = \langle E(q)E*(q) \rangle = \frac{E_0^2}{R^2} \left\langle \sum_{k=1}^{S} b_k \exp\left[i\boldsymbol{q}\boldsymbol{r}_k(t)\right] \sum_{j=1}^{S} b_j \exp\left[i\boldsymbol{q}\boldsymbol{r}_j(t)\right] \right\rangle_t \qquad (4.6)$$

Movements like rotation, translation and vibration or change of conformation happen on a very short time scale, therefore they are not resolved in SLS but are included in the time averaging $\langle \ \rangle_t$. This average can be taken either over the whole sum or over each term of the sum, yielding:

$$I(\boldsymbol{q}) = \frac{E_0^2}{R^2} \sum_{k=1}^{S} \sum_{j=1}^{S} \left\langle b_k b_j \exp\left[i\boldsymbol{q}\left(\boldsymbol{r}_k - \boldsymbol{r}_j\right)\right] \right\rangle \qquad (4.7)$$

By rearranging eq. 4.7 one can distinguish between the incoherent and coherent scattering [Benoit and Higgins 1994]:

$$I(\boldsymbol{q}) = \underbrace{\frac{E_0^2}{R^2} S\left(\langle b^2 \rangle - \langle b \rangle^2\right)}_{incoherent} + \underbrace{\frac{E_0^2}{R^2} \langle b \rangle^2 \sum_{j=1}^{S} \sum_{k=1}^{S} \left\langle \exp\left[i\boldsymbol{q}\left(\boldsymbol{r}_k - \boldsymbol{r}_j\right)\right] \right\rangle}_{coherent} \qquad (4.8)$$

The incoherent part is due to differences in the scattering length of the scatterers and is q-independent – just a constant. This term is important for neutron scattering where the nuclei are the scattering centres and their scattering length differs up to a factor of ten. In static light scattering the "dipole antenna" constitutes of hundreds of monomers and the sum of all these scattering lengths are representing one dipole antenna therefore is essentially constant [Benoit and Higgins 1994]. Therefore the incoherent term can be neglected in the further discussion. Although for SLS big parts of a polymer are scattering in phase it would be clumsy to define a part of a molecule as a scattering centre. It is easier to use a monomer instead, as done in the following. This approach is appropriate as long as the used scatterer is smaller than the resolution of the light scattering setup, that is roughly the reciprocal of the absolute value of the scattering vector.

The detected scattering intensity $I(\boldsymbol{q})$ depends on the intensity E_0^2 inside the scattering volume, on the distance from the scattering volume to the detector R^2 as well as on the scattering volume V itself. Dividing eq. 4.8 by $I_0 V$ and multiplying it with R^2 gives a setup independent quantity, the Rayleigh Ratio $R(\boldsymbol{q})$ with the unit cm^{-1} (not to be confused with the distance to the detector R). In principal the particles are immersed in a solvent which scatters, too. This is treated straightforward by simply subtracting the scattering intensity of the solvent – see experimental methods:

$$\frac{I(\boldsymbol{q})R^2}{I_0 V} = R(\boldsymbol{q}) = \frac{b^2}{V} \sum_{j=1}^{S} \sum_{k=1}^{S} \left\langle \exp\left[i\boldsymbol{q}\left(\boldsymbol{r}_k - \boldsymbol{r}_j\right)\right] \right\rangle \qquad (4.9)$$
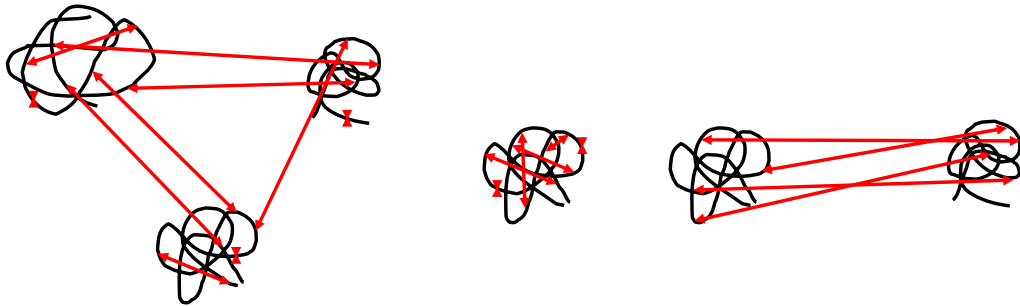
Equation 4.9 depends on the position of all scattering centres and it is responsible for the angular dependency of the scattering. As shown in figure 4.4 the S particles in the scattering volume can be split into $L*N$ scatterers, with L the number of polymers with degree of polymerization N. For the sake of simplicity they are assumed to be uniform. In a field of $L*N$ scatterers there are $(L*N)^2-L*N$ distance vectors. Adding the pure constructive contribution of each scatterer leads to $L^2*N^2=S^2$ pair combinations of scattered waves. Every scatterer will thus have two indices p and q each for the number of the molecule (going from 1 to L) resp. j

and k for the segment number within one polymer (going from *1 to N*). This leads to a fourfold sum:

$$R(\boldsymbol{q}) = \frac{b^2}{V} \sum_{p=1}^{L} \sum_{q=1}^{L} \sum_{j=1}^{N} \sum_{k=1}^{N} \left\langle \exp\left[i\boldsymbol{q}\left(\boldsymbol{r}_{p,j} - \boldsymbol{r}_{q,k} \right) \right] \right\rangle \tag{4.10}$$

The Rayleigh Ratio is now divided into inter- and intra-molecular scattering. Within one molecule there are N^2 scattering waves (whereas *j=k* is valid, too) and on time average these N^2 scattering waves are identical for all L molecules. Therefore these $L*N^2$ intra-molecular scattering waves can be separated from the rest:

$$R(\boldsymbol{q}) = \frac{b^2}{V} \left\{ L \sum_{j_1=1}^{N} \sum_{k_1=1}^{N} \left\langle \exp\left[-i\boldsymbol{q}\left(\boldsymbol{r}_{j_1} - \boldsymbol{r}_{k_1} \right) \right] \right\rangle + L(L-1) \sum_{j_1=1}^{N} \sum_{k_2=1}^{N} \left\langle \exp\left[-i\boldsymbol{q}\left(\boldsymbol{r}_{j_1} - \boldsymbol{r}_{k_2} \right) \right] \right\rangle \right\} \tag{4.11}$$

Figure 4.4 Representation of unsorted eq. 4.10 (left); representation of eq. 4.12 (middle) respectively eq. 4.13 (right); intra-particle vectors (eq. 4.12) are indexed by the same index → $_1$ and include $j_1=k_1$ whereas inter-particle vectors (eq. 4.13) exhibit two indices: j_1 and k_2

The first term of eq. 4.11 only depends on the size and the shape of the macromolecule. The expression between the angled brackets in this term is formed of N^2 terms. If divided by N^2 one obtains what is called the form factor of the molecules $P(\boldsymbol{q})$. It is normalized to unity for $q = 0$:

$$P(\boldsymbol{q}) = \frac{1}{N^2} \sum_{j_1=1}^{N} \sum_{k_1=1}^{N} \left\langle \exp\left[-i\boldsymbol{q}\left(\boldsymbol{r}_{j_1} - \boldsymbol{r}_{k_1} \right) \right] \right\rangle \tag{4.12}$$

The second term also contains N^2 pair-combinations. Therefore the inter-particle contribution is divided by N^2, too:

$$Q(\boldsymbol{q}) = \frac{1}{N^2} \sum_{j_1=1}^{N} \sum_{k_2=1}^{N} \left\langle \exp\left[-i\boldsymbol{q}\left(\boldsymbol{r}_{j_1} - \boldsymbol{r}_{k_2} \right) \right] \right\rangle \tag{4.13}$$

Therefore the Rayleigh Ratio is given by

$$R(\boldsymbol{q}) = \frac{b^2}{V} LN^2 \left[P(\boldsymbol{q}) + LQ(\boldsymbol{q}) \right] \tag{4.14}$$

Whereas (L-1) has been substituted by L since L is always large. This equation shows that $P(q)$ and $Q(q)$ are essentially different: $P(q)$ is a dimensionless intensive property whereas $Q(q)$ is inversely proportional to L. In isotropic media the absolute value of $\boldsymbol{q}$ has all relevant information to describe the system. Therefore using polar coordinates and integration over all

possible angles (from $\phi = 0$ to 2π and $\varphi = 0$ to π) reduces the form factor to be only dependent on scalars:

$$P(q) = \frac{1}{N^2} \sum_{j_1=1}^{N} \sum_{k_1=1}^{N} \left\langle \frac{\sin\left(qr_{j_1 k_1}\right)}{qr_{j_1 k_1}} \right\rangle \qquad Q(q) = \frac{1}{N^2} \sum_{j_1=1}^{N} \sum_{k_2=1}^{N} \left\langle \frac{\sin\left(qr_{j_1 k_2}\right)}{qr_{j_1 k_2}} \right\rangle \qquad (4.15)$$

The fluctuation theory developed by Einstein and Smoluchowski [Benoit and Higgins 1994] gives the connection of the scattering length b to macroscopic observables, namely the refractive index n_D and the refractive index increment dn_D/dc and it can be shown to yield [Oettinger]:

$$b = \frac{2\pi}{\lambda^2} \frac{m}{N_A} n_D \left(\frac{dn_D}{dc}\right)_{Donnan-Equilibrium} \qquad (4.16)$$

with m the molecular weight of a monomer and the refractive index increment ideally measured in Donnan-Equilibrium (see below). Defining the contrast factor K as $b^2 N_A/m^2$ we get:

$$\frac{4\pi^2}{\lambda_0^4} \frac{n_{Lsm}^2}{N_A} \left(\frac{dn}{dc}\right)_{Donnan-Equilibrium}^2 \frac{LN^2 m^2}{N_A V} \equiv K\ c_p M \qquad (4.17)$$

With the molecular weight in g/mol and the polymer concentration in g/L. In favor of an multiplicative scattering equation instead of an additive one the inter particle structure factor $S(q)$ is defined as:

$$S(q) = 1 + \frac{LQ(q)}{P(q)} \qquad (4.18)$$

to yield:

$$R(q) = Kc_p M P(q) S(q) \qquad (4.19)$$
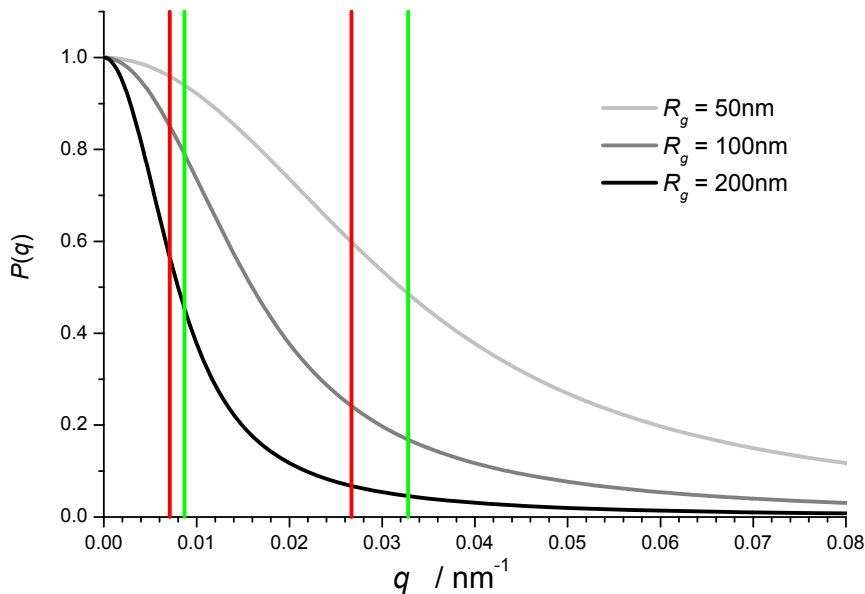
Figure 4.5 Particle form factor $P(q)$ of a random coil called Debye function with $R_g^2 = 50$, 100 and 200nm. Vertical lines indicate the q-range of the two laser wavelength' used for this thesis ($\lambda_{red} = 632$nm, $\lambda_{green} = 514$nm).
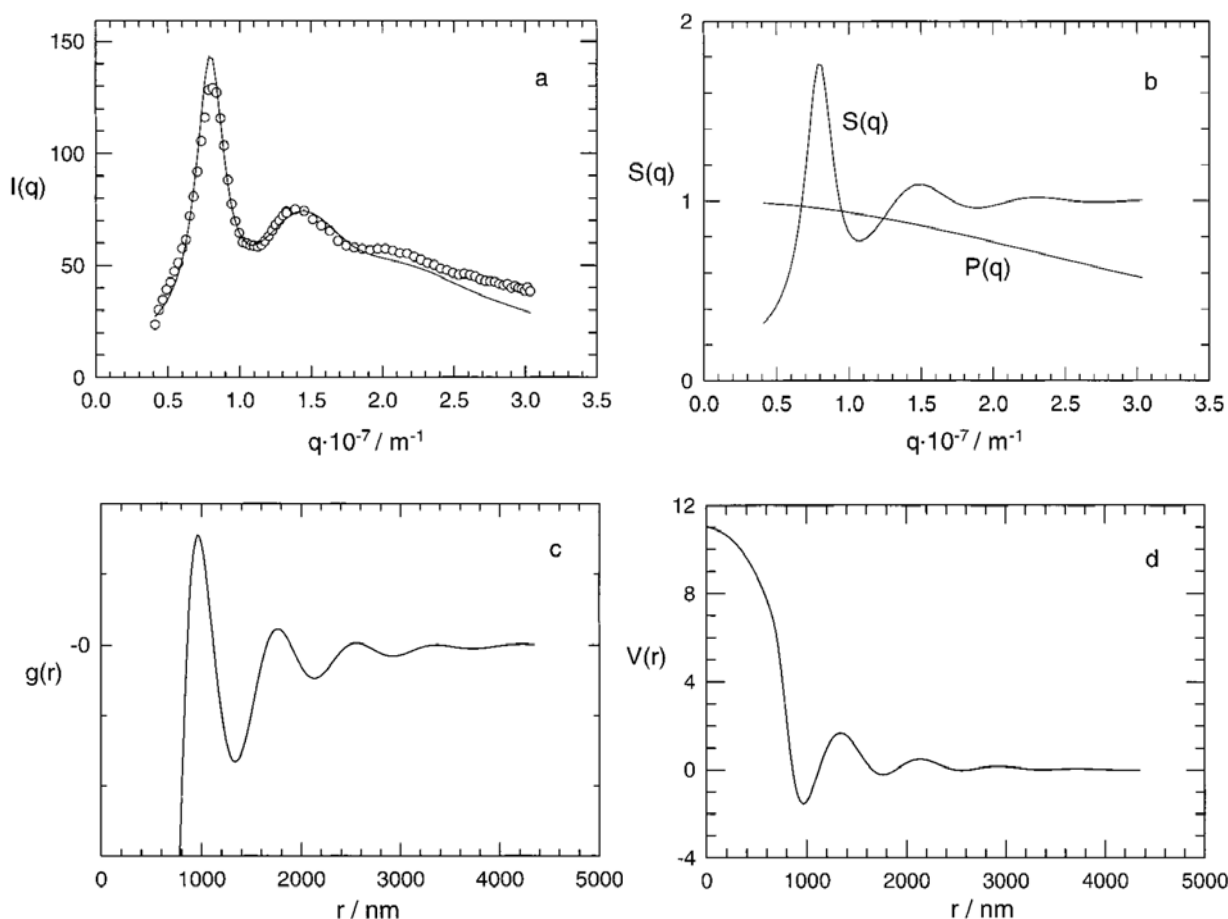
Figure 4.6 [Gröhn 2000] Light scattering on spherical polyelectrolyte microgels in dilute salt free aqueous solution. Long range electrostatic interactions lead to the formation of a lattice-like structure in solution visible on a smaller q-scale than the particle form factor $P(q)$. The measured intensity and its fit is given in a. It's contributions $P(q)$ and $S(q)$ are given in b. $P(q)$ was fitted by the form factor for spheres

$$P(q) = \left[\left(3\sin(qr) - 3(qr)\cos(qr) \right) / (qr)^3 \right]^2$$ and $S(q)$ by a rather elaborated fit

function, see original literature. Fourier transformation of $S(q)$ leads to $g(r)$ the radial distribution function of particle centers shown in c. Fourier transformation of $P(q)$ gives the full sphere radial density distribution $n(r)dr = 4\pi r^2 dr$. The resulting inter-particle potential $V(r)$ is given in d.

4.1.1 The Extended Zimm Formula

Owing to the subtle interplay of long range Coulomb forces, counter ion condensation as well as Donnan-equilibrium [Donnan 1924], light scattering on polyelectrolytes is still not an established technique. The two extremes: no added salt as well as excess added salt can be considered as fairly understood (compare Figure 4.5 and eq. 4.19). For the crossover region with low screening salt contents only few attempts for quantitative evaluation of real meaurements can be found in literature [Koyama 1984, 1986; Bodycomb, Hara 1994; Sorci, Reed 2002]. An elegant approach was derived by Bodycomb and Hara which is essentially an extended Zimm formula [Zimm 1948]. For laser light scattering with its low q-values, plotting $P(q)$ versus q^2, at least for $R_g q < 1$ the particle form factor drops proportional to the square of the radius of gyration R_g^2 [Benoit and Higgins 1994]:

$$P(q) \approx 1 - \frac{1}{3} R_g{}^2 q^2 \tag{4.20}$$

Bodycomb and Hara used a similar convenient expansion for the description of the inter particle structure factor $S(q)$. Their equation for $R(q)$ reduces in case of weak long range interactions (equal to high salt contents) to the well established Zimm formula. For the derivation of the inter-particle structure factor they started with the Zernicke-Prins equation [Zernicke, Prins 1927] which is one of the most general used equations among light scattering literature:

$$S(q) = \left\{ 1 - \frac{L}{V} \int_0^\infty [1 - g(r)] \frac{\sin qr}{qr} dv \right\} \qquad \text{with} \quad dv = 4\pi r^2 dr \tag{4.21}$$

Where $g(r)$ is the radial distribution function corresponding to the probability to find a particle at distance r if another one is at $r = 0$. In principal eq. 4.21 evaluates all inter-particle configurations that are forbidden due to steric overlapping. $S(q)$ gets important for high concentrations or in case of big exclusion volumes like electrostatic motivated repulsion. To develop more general relations, the reciprocal of eq. 4.19 is used and $S(q)$ is rewritten using the Born-Green method, introducing the inter-particle potential $V(r)$:

$$\frac{Kc_p}{R(q)} = \frac{1}{MP(q)} \left\{ 1 + \frac{L}{V} \int_0^\infty \left[1 - \exp\left(-\frac{V(r)}{kT} \right) \right] \frac{\sin qr}{qr} dv \right\} \tag{4.22}$$

By assuming a proper potential function $V(r)$, as done by Gröhn [Gröhn 2000], $Kc_p/R(q)$ can be fitted to evaluate the radial distribution function $g(r)$. However for weak interaction one can derive general relations without assuming any potential functions at all. To develop general relations $\sin(qr)/qr$ is expanded similar to the approximation of $P(q)$ in power series of qr, leading to the following equation:

$$\frac{Kc_p}{R(q)} = \frac{1}{MP(q)} \left\{ 1 + \frac{L}{V} m_0 - \frac{q^2}{3} \frac{L}{V} m_2 + ... \right\}$$

$$m_0 = \int_0^\infty \left[1 - \exp\left(-\frac{V(r)}{kT} \right) \right] dv \qquad m_2 = \int_0^\infty \left[1 - \exp\left(-\frac{V(r)}{kT} \right) \right] r^2 dv \tag{4.23}$$

The integrals in the square brackets of eq. 4.23 are the zero- and second moment of $\{ 1 - \exp(-V(r)/kT) \}$; m_0 is considered as the intermolecular excluded volume of the scatterer. The ratio m_2/m_0 is considered as a radius of gyration of the excluded volume $\xi_g{}^2$, which is also a measure for the dimension of the region around a scattering particle, that is unoccupied by other particles (i.e. exclusion zones). For $q = 0$ we get a simple relation that can be compared to fluctuation theory to yield the well known relation [Benoit and Higgins 1994]:

$$\frac{Kc_p}{R(q=0)} = \frac{1}{M} \left(1 + \frac{L}{V} m_0 \right) = \frac{1}{RT} (d\Pi/dc_p) = \frac{1}{M} + 2A_2 c_p + 3A_3 c_p{}^2 \equiv \frac{1}{M_{app}} \tag{4.24}$$

Defining the apparent molecular weight M_{app} as $R(q=0)/Kc_p$ one obtains:

$$S(q)^{-1} = \frac{M}{M_{app}} \left[1 - q^2 \frac{\xi_g{}^2}{6} \left(1 - \frac{M_{app}}{M} \right) \right] \tag{4.25}$$

Using eq. 4.22 one finally arrives at an extended Zimm formula:

$$\frac{Kc_p}{R(q)} = \frac{1}{M_{app}}\left\{1 + q^2\left[\frac{R_g^2}{3} - \frac{\xi_g^2}{6}\left(1 - \frac{M_{app}}{M}\right)\right]\right\}$$

(4.26)

Because now both intramolecular and intermolecular scattering is expressed in a series of q^2, the initial slope normalized against the intercept yields an apparent R_g that is given by:

$$R_{g\,app} = \left[R_g^2 - \frac{\xi_g^2}{2}\left(1 - \frac{M_{app}}{M}\right)\right]^{0.5}$$

(4.27)

In the case of weak inter-particle potentials $V(r)$ one gets $M_{app} \approx M$ and equation 4.26 reduces to the common Zimm formula:

$$\frac{Kc_p}{R(q)} = \frac{1}{M}\left(1 + \frac{R_g^2}{3}q^2\right) + 2A_2c_p$$

(4.28)

4.1.2 The Effect of Polydispersity

For measuring techniques like membrane osmosis that exploit colligative effects the number average molecular weight $\langle M \rangle_n \equiv M_n$ respectively the number average degree of polymerization $\langle N \rangle_n$ is evaluated. In contrast light scattering evaluates the weight average M_w. For $q = 0$ eq. 4.14 yields:

$$I(q=0) = b^2\sum L_iN_i^2 = b^2c\frac{\sum L_iN_i^2}{\sum L_iN_i} = b^2c\langle N \rangle_w = cM_w$$

(4.29)

The same formalism can be used to determine the polydispersity of the radius of gyration R_g, using eq. 4.14 and 4.20 yields:

$$I(q) \approx b^2\sum L_iN_i^2 - b^2\frac{q^2}{3}\sum L_iN_i^2R_i^2$$

(4.30)

This defines the radius of gyration as:

$$\langle R_i^2 \rangle = \frac{\sum L_iN_i^2R_i^2}{\sum L_iN_i^2}$$

(4.31)

In polymer chemistry eq. 4.31 is the definition of a z-average and accordingly light scattering yields the z-average. To compare the average to other measuring techniques like viscosity or gel permeation chromatography one may further break down eq. 4.31. According to chapter 2.4 R_g is given by:

$$R_g^2 = a^2N^{2\nu} = const \cdot N^{2\nu}$$

(4.32)

and eq. 4.31 can be rewritten as:

$$\left[\frac{const \cdot \sum L_iN_i^{2+2\nu}}{\sum L_iN_i^2}\right]^{\frac{1}{2\nu}}$$

(4.33)

In case of a random walk with $v = 0.5$ eq. 4.33 resembles the third moment of the distribution of species N_i divided by its second moment:

$$const \cdot \frac{\sum L_i N_i^3}{\sum L_i N_i^2} \qquad\qquad (4.34)$$

4.2   Dynamic Light Scattering

4.2.1 DLS – Fundamentals and Fourier Transformation
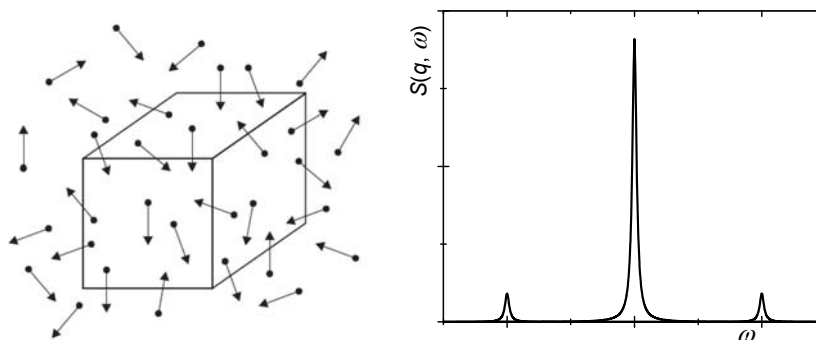
Figure 4.7 Scattering particles move in and out of the scattering volume – sketched as a cube (left). This movement leads to a peak broadening of the scattered intensity characterized by the power spectrum $S(q, \omega)$ at constant q. The two satellites are the result of a change in vibrational mode (right).

Inelastic scattering means energy loss or gain compared to the initial photon. Inelastic scattering occurs due to thermal motion as well as shifts in vibrational mode. Thermal motion leads to peak broadening but does not change the average energy and is therefore called quasielastic scattering, as well. In contrast, changes in the vibrational mode, called Raman scattering, shift the average energy up or down. However, due to its strict selection rules Raman scattering is 10^7 times more infrequent than an elastic scattering process [Levine 2000], making inelastic scattering negligible when counting photons as done in LS. Figure 4.7 demonstrates a typical power spectrum $S(q, \omega)$ as observed by a detector at fixed q. In this plot the two satellites from the main peak represent energy gain or loss due to changes in the vibrational mode. The main peak as well as the satellites are broadened by translational and rotational modes. Taking only translational diffusion into account, the peaks can be described by a Lorentzian function which is the common equation for a spectral line subjected to homogenous peak broadening [Berne and Pecora 2000]:

$$S_s(q, \omega) = \pi^{-1} \frac{\Gamma}{\Gamma^2 + (\omega - \omega_0)^2} \qquad\qquad \Gamma = q^2 D \qquad\qquad (4.35)$$

In principal, for strong peak broadening it is possible to obtain the diffusion coefficient just by fitting the data to eq. 4.35. The photon spectral density can be obtained by an adequate detector as well as by a Fabry-Perot interferometer which can be used at least for fast diffusive processes as they occur in gasses. For slow diffusive processes like big molecules in a solvent, line broadening is vanishing compared to the absolute frequency of the laser and therefore can't be utilized.

The Wiener-Khintchine theorem [Wiener 1930] states that the power spectral density $S(q, \omega)$ (frequency domain) of a stationary random process is the Fourier transform of the corresponding autocorrelation function $F_s^A(q, \tau)$ (time domain). $F_s^A(q, \tau)$ is the amplitude autocorrelation function ($I = |EE^*| = |E|^2$) and in turn is the Fourier transform of the diffusive particle movement of the van Hove self correlation function $G_s(r, \tau)$. Therefore $S(q, \omega)$ is the actual result of many random walks described by a function $G_s(r, \tau)$. So the "first" Fourier transformation of these random walks with the q-r-Fourier-pair gives the dynamic structure factor $F_s^A(q, \tau)$ which is utilized in DLS. $G_s(r, \tau)$ describes the probability to find a given scattering particle at time $t+\tau$ and distance r if the same particle previously was at 0. For isotropic media only the distance is decisive, as is true in SLS $\rightarrow r = |r|$:

$$F_s^A(q, \tau) = \int_{r=-\infty}^{r=\infty} G_s(r, \tau) \exp(iqr) dr = \left\langle E_s(q, t) E_s^*(q, t+\tau) \right\rangle \tag{4.36}$$

$$G_s(r, \tau) = \left\langle n(0, t) n(0, t+\tau) \right\rangle_E \tag{4.37}$$

$n(r, t)$ is the local number density of scattering particles at a given time t and at distance r. The average $\langle...\rangle_E$ is an ensemble-average meaning that every subsystem can represent the whole system. In case of only diffusive translational motion the van Hove self correlation function $G_s(r, \tau)$ is a Gaussian function with its half width given by the self diffusion coefficient D_s. The index s means self diffusion in contrast to cooperative motion. Self diffusion can only be obtained in very dilute solutions when interactions among particles can be safely ruled out [Schärtl 2007]. $G_s(r, \tau)$ is given by [Benoit and Higgins 1994] (compare eq. 2.35):

$$G_s(r, \tau) = \left[\frac{2\pi}{3} \left\langle \Delta R(\tau)^2 \right\rangle \right]^{3/2} \exp\left(-\frac{3r(\tau)^2}{2\left\langle \Delta R(\tau)^2 \right\rangle} \right) \tag{4.38}$$

With $\left\langle \Delta R(\tau)^2 \right\rangle$ the mean-square displacement of the scattering particle traveled during time τ. The Brownian particle motion is caused by the solvent molecules hitting the molecule and thereby moving it along. The scattering particle therefore exhibits a random walk through the scattering volume, and the mean-square displacement is given as [Benoit and Higgins 1994]:

$$\left\langle \Delta R(\tau)^2 \right\rangle = 6D_s\tau \tag{4.39}$$

$$F_s^A(q, \tau) = \exp\left(-\frac{q^2}{6} \left\langle \Delta R(\tau)^2 \right\rangle \right) = \exp\left(-q^2 D_s \tau \right) \tag{4.40}$$

The equations 4.35 – 4.40 only cover translational motion. Bigger particles exhibit several scattering units which do not move freely but are correlated as governed by the rotational motion. Eq. 4.40 can be modified to include rotational motion, too [Berne and Pecora 2000]:

$$F_s^A(q, \tau) = \exp\left(-\frac{q^2}{6} \left\langle \Delta R(\tau)^2 \right\rangle \right) \left[1 + \alpha(\tau) \left\langle \Delta R(\tau)^2 \right\rangle^2 q^4 + ... \right] \tag{4.41}$$

$\alpha(\tau)$ includes higher moments of the scatterer movement distribution; for $t \rightarrow 0$ $\alpha(\tau)$ goes to 0. This means deviations from eq. 4.40 may occur for big, anisotropic particles in high LS-q-regime. Anyway evaluating only the appropriate q-regime the sphere equivalent hydrodynamic Radius can be calculated according to the Stokes-Einstein-law:

$$R_H = \frac{kT}{6\pi\eta D_s} \tag{4.42}$$

4.2.2 DLS – Evaluation of the Intensity-Autocorrelation-Function

In DLS one observes the time dependent fluctuation of the scattering intensity at a given angle respectively q-value. This intensity fluctuation of the intensity can be imagined as the drifting of particles in and out of the detection volume inside the sample cuvette. Whereas in SLS the intensity is averaged over a period of i.e. 30s in DLS the intensity is self-correlated with a sampling time $\Delta\tau$ down to tens of nanoseconds. The diffusion coefficient of small particles is bigger than that of big ones and the speed of the intensity fluctuation changes accordingly. So storing the whole intensity trace, and magnifying it, one could judge how big the particles are. However this is not feasible due to the huge amount of produced data (using a sampling time of 30ns and 5 Byte per value one needs 166MB per second). Therefore only a correlation function $g_s^I(q, \tau)$ is computed by a commercial hardware correlator in between the output of the photo-multiplier and the computer and finally saved. $g_s^I(q, \tau)$ is computed on-line during data acquisition and is given by:

$$g_s^{I}\left(q,\tau\right)=\frac{\left\langle I\left(q,t\right)I\left(q,t+\tau\right)\right\rangle_{T}}{\left\langle I\left(q,t\right)\right\rangle_{T}^{2}} \tag{4.43}$$

$$\left\langle I\left(q,t\right)I\left(q,t+\tau\right)\right\rangle_{T}=\lim_{T\to\infty}\frac{1}{T}\int_{0}^{T}I\left(q,t\right)I\left(q,t+\tau\right)dt \tag{4.44}$$
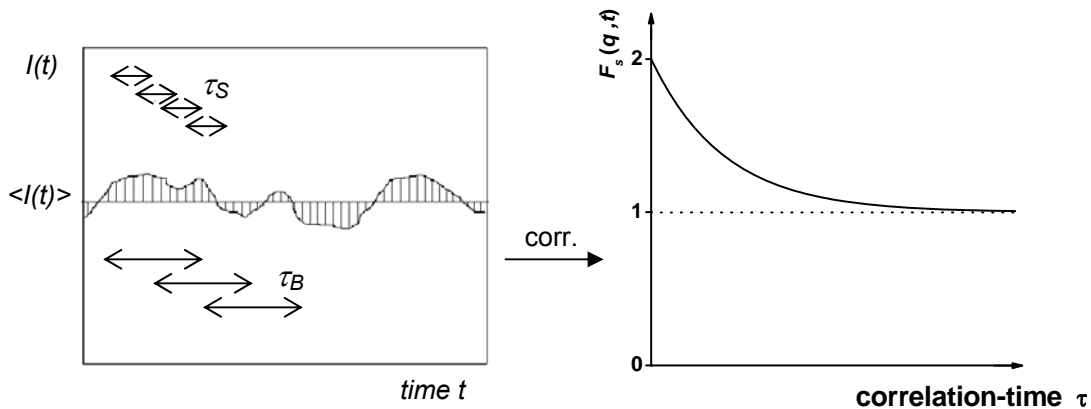
Figure 4.8 Principle of the hardware correlator: sketched are the intensity fluctuations as measured by a photo detector at constant q (left) and the procedure to calculate the intensity autocorrelation function (right).

whereas the finite interval of averaging $\langle...\rangle_T$ has to be bigger than the time scale of the fluctuations. The principle of the intensity-auto-correlation-function as computed by the hardware correlator can be summarized as follows:

A time-test-point t_1 is chosen and the intensity at this time is multiplied with the intensity at time $t_1 + \tau_S$ to yield $I\left(q,t_1\right)I\left(q,t_1+\tau_S\right)$. Then another test-point t_2 is taken to calculate $I\left(q,t_2\right)I\left(q,t_2+\tau_S\right)$ and so on. Averaging over all pairs each using the shift τ_S, one point of the intensity correlation function $g_s^I(q, \tau)$ is obtained as sketched in figure 4.8 (right). By changing τ to different values the whole run of $g_s^I(q, \tau)$ is established which is sketched in figure 4.8 (left). Whereas older hardware correlators increase the correlation time linearly a correlator with 1000 channels can span over a window of 3 orders of magnitude (1000 * τ_{Minimum}). Using these linear correlators the operator has to set the smallest correlation time according to the process to be monitored. Modern correlators increase their τ exponentially to scan the full time-range starting from the sampling time of the detector and ranging up to measurement

time. This technique called "multitau-correlation" screens over the whole spectrum and therefore avoids the risk to miss unexpected processes of bigger or smaller particles or dust, and was used for this PhD-thesis. Neglecting the uncorrelated scattering intensity of the solvent one can expect the correlation function to decrease continuously from two to one. A value of two represents full correlation which means that the particles have not moved and this is obviously achieved for $\tau \to 0$. A value of one means no correlation at all, so the particle configuration has nothing to do with the initial configuration it is compared too. This happens for $\tau \to \infty$. Values in between represent partially correlated particle configurations.

$$\lim_{\tau \to 0} g_s^I(q, \tau) = \frac{\left\langle I(q, t)^2 \right\rangle_T}{\left\langle I(q, t) \right\rangle_T^2} = 2 \qquad\qquad \text{full correlation} \qquad\qquad (4.45)$$

$$\lim_{\tau \to \infty} g_s^I(q, \tau) = \frac{\left\langle I(q, t) \right\rangle_T \left\langle I(q, t) \right\rangle_T}{\left\langle I(q, t) \right\rangle_T^2} = 1 \qquad\qquad \text{no correlation} \qquad\qquad (4.46)$$

One gets a decreasing function and its decay constant is a measure of the dynamics of the particle movements. In theory the time dependent fluctuations of particles in a volume are given by the amplitude-autocorrelation-function $F_s^A(q, \tau)$ which is connected to $g_s^I(q, \tau)$ via the Siegert-relation [Berne and Pecora 2000]:

$$F_s^A(q, \tau) = 1 + c_{coh} \left| g_s^A(q, \tau) \right|^2 \qquad\qquad (4.47)$$

In old LS-setups pinholes were used and c_{coh}, the reciprocal of the number of coherent areas from the detected volume was in between 0 and 1. As $c_{coh} = 1$ gives the best signal to noise ratio, the setup was calibrated to a c value as close to 1 as possible. In recent LS-setups as the one used for this PhD-thesis, the detected light is first coupled into an optical fiber which automatically "selects" only coherent photons making $c_{coh} \equiv 1$ and thereby allowing comparatively huge sample volumes which boosts the signal to noise ratio even further. Therefore $F_s^A(q, \tau)$ is simply obtained by:

$$F_s^A(q, \tau) = \sqrt{\frac{\left\langle I(q, t) I(q, t + \tau) \right\rangle_T - \left\langle I(q, t) \right\rangle_T^2}{\left\langle I(q, t) \right\rangle_T^2}} \qquad\qquad (4.48)$$

For small mono-disperse particles $F_s(q, \tau)$ drops mono-exponential according to:

$$F_s^A(q, \tau) = B \exp\left(-q^2 D t\right) \qquad\qquad (4.49)$$

$\quad B$ *signal-noise ratio*
$\quad D$ *translational diffusion coefficient*

Equation 4.49 is only valid if neglecting the velocity distribution, and only for long time movement as valid for diffusive motion of macromolecules [Berne and Pecora 2000]. For small polydisperse samples $F_s^A(q, \tau)$ is given by the sum of exponentials of the different species:

$$F_s^A(q, \tau) = B \frac{\sum m_i M_i \exp\left(-q^2 D_i t\right)}{\sum m_i M_i} \qquad\qquad (4.50)$$

$\quad D_i$ *translational diffusion coefficient of particle i*
$\quad m_i$ *mass fraction of particle i*
$\quad M_i$ *molecular weight of particle i*

For particles bigger than 10nm additionally the particle form factor $P(q)$ (eq. 4.12) has to be taken into account:

$$F_S^A(q, \tau) = B \frac{\sum m_i M_i P_i(q) \exp(-q^2 D_i t)}{\sum m_i M_i P_i(q)}$$ (4.51)

Figure 4.6 shows that the particle form factor decays faster for bigger particles. In combination with eq. 4.51 this means the bigger q, the smaller $F_s^A(q, \tau)$. However from the starting slope of a logarithmic plot of $F_s^A(q, \tau)$ vs. q^2 one gets a defined diffusion coefficient that in case of a random coil resembles a z-average D_z (see discussion of polydispersity in SLS):

$$\ln\left(F_S^A(q, \tau)\right) = -q^2 \frac{\sum m_i M_i P_i(q) D_i(q)}{\sum m_i M_i P_i(q)} = -q^2 D_{app}(q)$$ (4.52)

$$\lim_{q \to 0} D_{app}(q) = D_z$$ (4.53)

The deviations from a single exponential decay can be accounted for by a cumulant analysis of a logarithmic $F_s^A(q, \tau)$ -plot:

$$\ln\left(F_s^A(q, \tau)\right) = -\Gamma\tau + \frac{\mu_2}{2!}\Gamma^3\tau^2 - \frac{\mu_3}{3!}\Gamma^3 t^3 + ...$$ (4.54)

The starting slope $\Gamma = q^2 D_{app}$ defines an apparent diffusion coefficient D_{app}, which depends on q. In case of molecules with $\langle R_g^2 \rangle_z \cdot q^2 < 1$ higher cumulants represent a qualitative measure of the polydispersity, whereas with increasing value of $\langle R_g^2 \rangle_z \cdot q^2$ rotational as well as configurational motion give contributions as well. Therefore in analogy to the Zimm-plot one gets:

$$D_{app}(q) = D_{s, z}\left(1 + K_{DLS}\langle R_g \rangle^2 q^2 + ...\right)$$ (4.55)

K_{DLS} *constant depending on size and topology
as well as on polydispersity*

In case of higher concentrations the particle movement is not independent anymore but cooperative which leads to a further increase of D_{app}:

$$D_{app}(q, c) = D_{s, z}\left(1 + K_{DLS}\langle R_g \rangle^2 q^2 + ...\right)\left(1 + k_D c_p + ...\right)$$ (4.56)

The concentration dependence can be described by:

$$k_D = 2A_2 M - k_f - \upsilon_p$$ (4.57)

with A_2 the second virial coefficient, k_f friction virial coefficient of the scatterer and υ_p the partial molar volume.

Applying the Stokes-Einstein-law with stick-boundary-conditions finally gives a sphere-equivalent hydrodynamic radius that is usually referred to as the reciprocal of the inverse of a z-average (compare discussion chapter 4.1.2):

$$R_h = \left\langle \frac{1}{R_h} \right\rangle_z^{-1} = \frac{kT}{6\pi\eta_0 D_z}$$ (4.58)

4.3   The ρ–Ratio

In the q-regime where $P(q)$ versus q^2 scales with R_g (particles in the size regime of 10-100nm), the topology is not evaluable from SLS alone. Yet by combination of SLS with DLS an estimate of the shape is possible. In the case of R_g all scattering parts of a particle are responsible for the resulting R_g-value. In the case of DLS only the size of the outer shell determines the evaluated R_h. Therefore a kind of volume to surface ratio is given by the ratio of R_g over R_h called ρ-ratio.

$$\rho = \frac{R_g}{R_h} \tag{4.59}$$

Theoretically calculated ρ-ratios for the most important particle-topologies are summarized in Tab 4.1.

Table 4.1 ρ-ratio for the most-typical particle topologies [Schärtl 2007]

Topology	ρ−ratio Theory
Homogeneous sphere	0.775
Hollow sphere	1
Ellipsoid	0.775 - 4
Random coil, monodisperse, θ-conditions	1.505
Random coil, polydisperse, θ-conditions	1.73
Random coil, monodisperse, good solvent	1.78
Random coil, polydisperse, good solvent	2.05
Cylinder of length l, diameter D	$\frac{1}{\sqrt{3}} \cdot \ln\left(\frac{l}{D} - 0.5\right)$

5   Materials & Methods

5.1   Characterization of PVP$_{851}$–Precursor

The unquaternized poly(2-vinylpyridine) was bought from Polymer Standard Services, Mainz (PSS), Lot No: vp13058. The molar mass distribution evaluated by PSS is given in Figure 5.1 with M_w/M_n = 1.18. Zimm plots were conducted over the whole 1-propanol/2-pentanone regime, for examples see Figures 5.14 - 5.16, respectively chapter 6. The M_w as evaluated by SLS is 8.51*10^5 g/mol and has been used throughout this thesis. A Zimm plot conducted using our very accurate LS-setup with an ALV-SP86 goniometer is given in Figure 5.2. M_w, R_g and A_2 are in agreement with the measurements of the faster ALV-1800 setup (compare Figure 5.14) used for the many measurements in dependence on the fraction of non solvent w_{ns}.
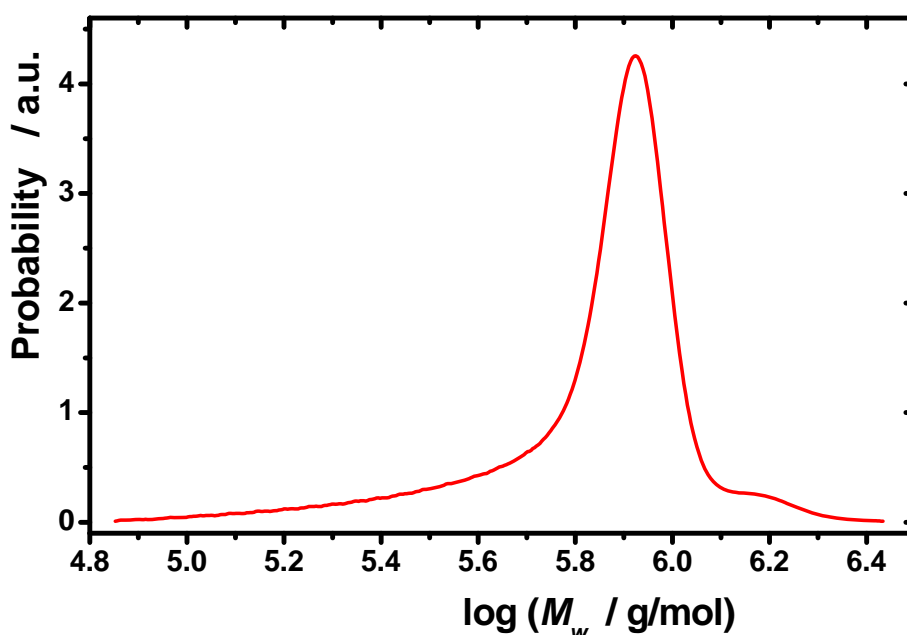
Figure 5.1 Original GPC data of PVP$_{851}$ conducted by PSS; Solvent: THF/0.1Vol% Diethylaminoethylamine; M_w = 8.60*10^5 g/mol; M_n = 7.28*10^5 g/mol; M_w/M_n was evaluated to 1.18.
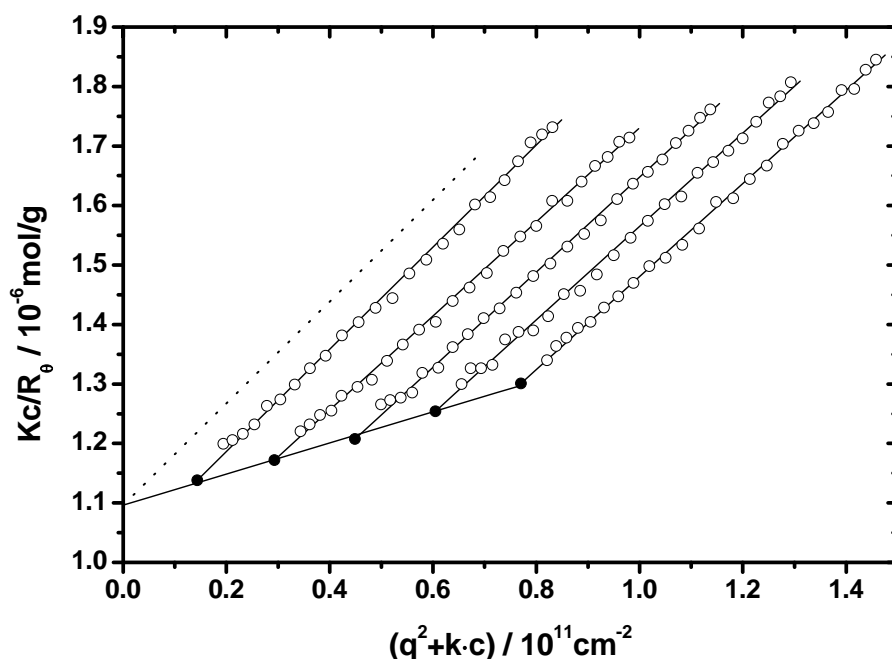
Figure 5.2 Zimm plot for PVP_{851} using an ALV-SP86 goniometer; solvent: 1-propanol with 10^{-5} M TBAB; $A_2 = 3.4*10^{-4}$ mol*cm^3/g^2; $R_g = 48.2$ nm; $M_w = 9.14*10^5$ g/mol

5.2 Quaternization of PVP

1 g of the poly-2-vinylpyridine (PVP_{851}) was dissolved at 60°C in 100 ml nitromethane. A fourfold excess of ethyl bromide (analytical grade, Sigma-Aldrich) was added. The solution was then stirred under argon at 60°C for different time periods. Depending on the degree of quaternization ranging from 24 h ($QPVP_{1.2}$) to 2 weeks ($QPVP_{35}$). After cooling to room temperature, the solution was added to 1L of diethyl ether at -30°C. The resulting precipitate was washed, vacuum dried at room temperature and depending on the degree of quaternization freeze dried in benzene; benzene with a few drops of methanol; or pure water. For all samples the degree of quaternization was determined by double-elemental-analysis of the Br/N-ratio at a professional elemental-analysis-lab: 'Mikroanalytisches Labor Pascher, Remagen'. In literature usually the degree of quaternization is determined by UV-absorption, this method was tested but gave no reliable results at least for the low quaternized samples, therefore not used for characterization.

Five samples were prepared for this thesis; the percentage of quaternization is given as index: $QPVP_{1.2}$; $QPVP_{2.4}$, $QPVP_{4.3}$, $QPVP_{20}$, $QPVP_{35}$
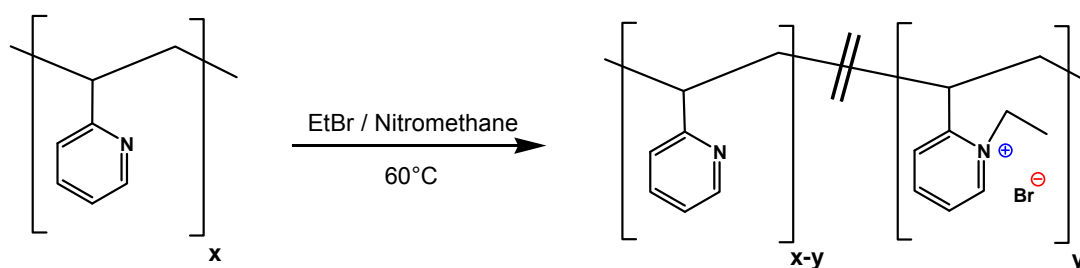
Figure 5.6 Quaternization of PVP with ethyl bromide. The quaternization occurs randomly along the chain.

5.3   Screening Salt

Screening salt was added to the polyelectrolyte solution in order to simplify light scattering data evaluation by avoiding structuring of the polyions (chapter 5.4.3). Tetra-n-butylammonium bromide (TBAB; Figure 5.7) was chosen for our system due to its high solubility in 1-propanol as well as 2-pentanone, respectively their mixtures (> 1 mol/L).
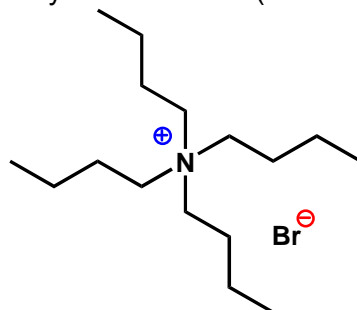
Figure 5.7 Chemical structure of Tetra-n-butylammonium bromide – TBAB

5.4   Solvents

Whereas 1-propanol represents a good solvent for uncharged PVP and QPVP$_{4.3}$, 2-pentanone is a non-solvent for both. The solvents are essentially isorefractive: 1-propanol n_D = 1.385; 2-pentanone n_D = 1.390. Thus complications in the interpretation of the light scattering data arising from preferential absorption are avoided. Density measurements on mixtures showed that no volume contraction due to mixing occurred, compare Figure 5.11. Furthermore the density of both solvents is equal, the value of 0.802 g/ml at 20 °C was used throughout the thesis for the calculation of volume-concentrations from weight using a precise balance within the glove-box.

Table 5.1 Solvent characteristics

solvent		ε_r	$n_D{}^{20}$	η_0 /Pas
solvent	1 - propanol	21.3	1.385	0.488
non-solvent	2 - pentanone	16.0	1.390	2.256

5.4.1 Drying and Purification

HPLC-grade 2-pentanone and 1-propanol (CHROMASOLV) were bought from Sigma-Aldrich. The solvents were dried over 3Å molecular sieve (freshly reactivated for 48 h at 280 °C with applied vacuum) for at least 2 days and then distilled over argon to get rid of molecular sieve dust. The handling of the solvents and all further preparation were conducted in a glove box with nitrogen atmosphere (MBraun/Unilab).

5.4.2 Relative Permittivity and Bjerrum Length

The dielectric constants of the solvent mixtures range from ε_r = 21 (1-propanol) to ε_r = 16 (2-pentanone) (Figure 5.8), and accordingly, the Bjerrum length l_B varies from 2.7 nm to 3.5 nm

for 0% and 100% 2-pentanone content, respectively (eq. 2.22; Figure 5.9). Given the contour distance between two vinyl-pyridine-monomers along the chain, a = 2.5Å, no counter-ion condensation is expected to occur for the 1.2, 2.4 and 4.3% quaternized PVPs according to Manning (eq. 2.24, Figure 5.9).
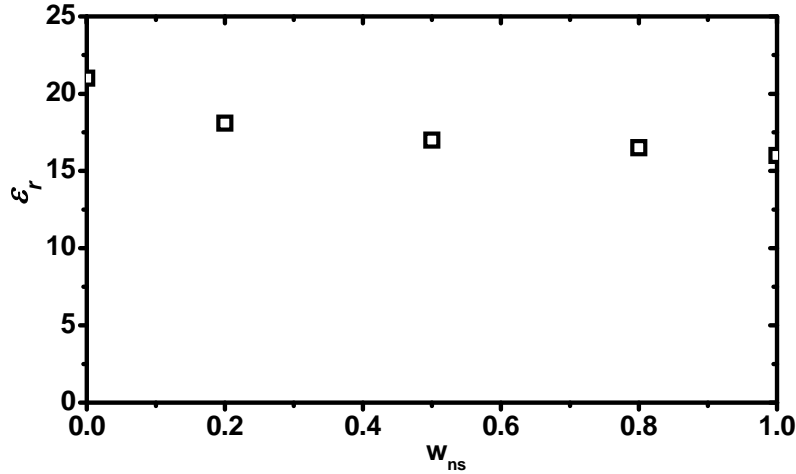
Figure 5.8 Dielectric constant ε_r as function of the fraction of the non-solvent w_{ns}.
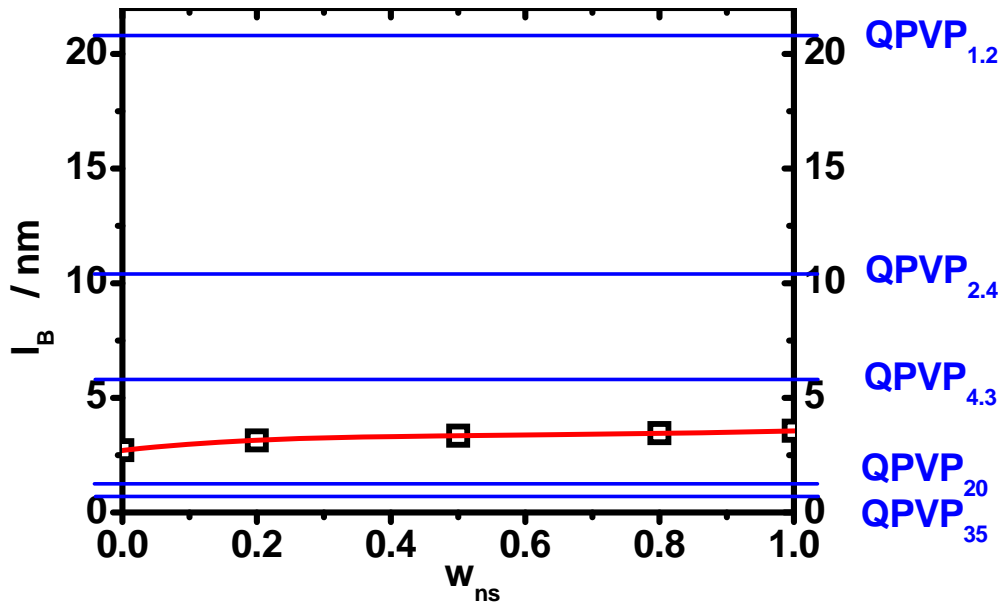
Figure 5.9 Bjerrum length as function of the fraction of the non-solvent w_{ns}. The blue lines represent the mean contour distances between the chemical charges of the QPVPs.

5.4.3 Debye Length

Whereas the Bjerrum length l_B characterizes pure solvents or solvent mixtures, the Debye length λ_D additionally incorporates the impact of the ion strength (eq. 2.20). Comparison of eq. 2.21 and 2.22 yields the connection of l_B and λ_D as:

$$\lambda_D = \left(8\pi l_B I\right)^{-1/2} = \left(4\pi l_B \sum_k z_k^2 n_k^\infty\right)^{-1/2} \tag{5.1}$$

The sum $\sum z_k^2 n_k^\infty$ is composed of two contributions: added salt and the polyelectrolyte itself. The salt contribution is given accordingly:

$$2 * C_s = 2 * 1^{2} * 10^{-5} \text{ mol/L} \tag{5.2}$$

The polyelectrolyte contribution is given by the polyion itself and its counterions. However the polyions are usually neglected due to their comparatively small number [Förster, Schmidt 1995, Muthukumar 2004]. The concentration of counterions depends on the degree of quaternization yielding for the Debye length:

$$\lambda_D = (4 \pi l_B \bullet (2C_s + \gamma C_p))^{-1/2} \tag{5.3}$$

Depending on the solvent composition the Debye screening length ranges from about 40 nm to 50 nm (Figure 5.10). At this added salt and polyion concentrations no "slow mode" (chapter 2.1.3) could be detected. Thus, the amount of salt addition was chosen such that the known problems arising from intermolecular electrostatic interaction are minimized and that intramolecular electrostatic interactions are kept as large as possible (compare chapter 2.2.1 and 2.6.3). Given the experimental conditions for the utilized concentrations and samples used in this thesis, the centers of mass of the polyions are separated by a mean distance bigger than 300 nm and one can summarize:

$$l_B \ll \lambda_D \ll \overline{d} \tag{5.4}$$
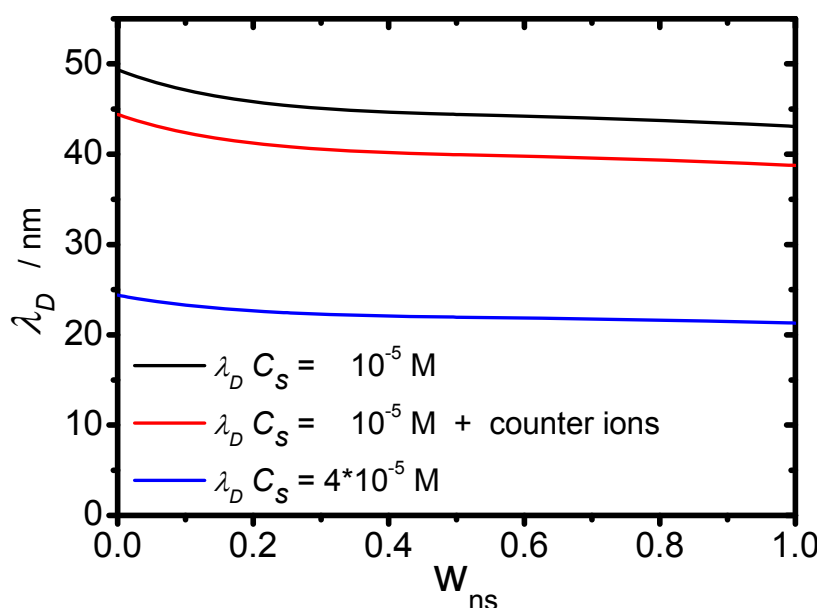
Figure 5.10 Debye length as function of the fraction of non-solvent w_{ns}. The black and the blue line represents λ_D taking only added salt ions into account. The red line is the Debye length for the QPVP$_{4.3}$ sample with full ion dissociation. QPVP$_{4.3}$ and in particular the samples with higher degrees of quaternization exhibit increasing counter ion condensation. Therefore the red line can be assumed as a lower limit for a combined screening at $C_s = 10^{-5}$ M.

5.4.4 Viscosity Measurements

Viscosity measurements have been conducted using an automated Ubbelohde Micro-Viscometer (Schott AVS 300, with a CT 1150/2 Thermostat). For measurements two capillaries (with calibration constants of c_{calib} = 3.0655 respectively 2.68731 * 10^{-6} cp m^3 kg^{-1} s^{-1}) were used yielding a retention time of about 160 – 230 s. Values of pure 1-propanol and

pure 2-pentanone matched literature data and standard deviations of the measurements were smaller than 0.1%. The addition of 10^{-5} mol/L TBAB to the solvents or solvent mixtures did not change the viscosity within this high measurement accuracy.

Dependence on w_{ns}

To evaluate the hydrodynamic radius according to eq. 4.58 the solvent viscosity η_0 is needed. Therefore η_0 was measured in dependence of w_{ns}, the fraction of the non-solvent (Figure 5.11). The run of the viscosity can be fitted by a biexponential decay which is typical for a binary mixture:

$$\eta_0 = A_1 \exp\left(-\frac{w_{ns}}{t_1}\right) + A_2 \exp\left(-\frac{w_{ns}}{t_2}\right) + \eta_0^{\ 0} \tag{5.5}$$

$\eta_0^{\ 0}$	0.37682 Pas
A_1	1.38214 Pas
t_1	0.39595
A_2	0.49703 Pas
t_2	0.14820
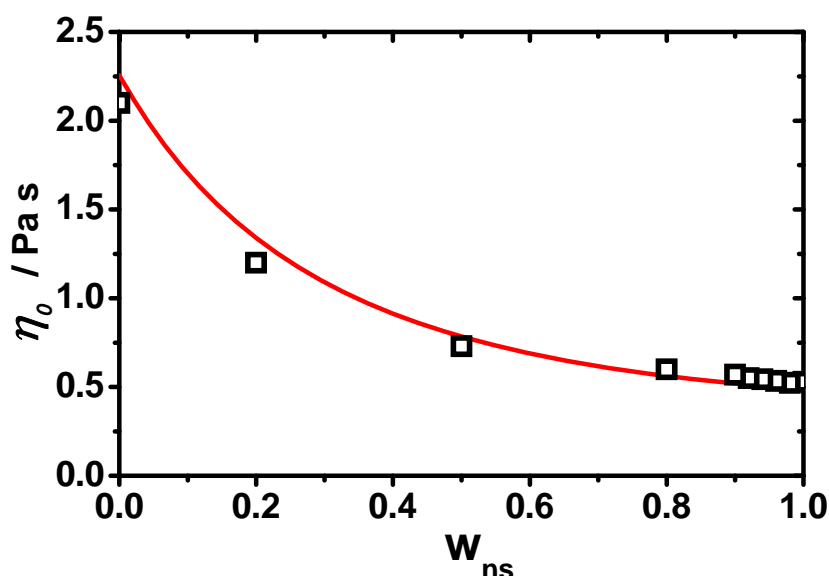
Figure 5.11 Solvent viscosity as function of w_{ns}, squares: measurement data; red line fit according to eq. 5.5.

Dependence on Temperature

The collapse was induced by increasing the temperature, too. Whereas the solvent/non-solvent mixtures could probe in good-, θ- and poor solvent conditions, only a smaller regime of solvent-quality could be monitored due to the experimental limited temperature regime. The temperature dependence for the solvent viscosity was determined for the two compositions w_{ns} = 0.875 and 0.915 which is close to the precipitation point of the PVP_{851} and $QPVP_{20}$. As Figure 5.12 shows, the temperature dependence can be described by an exponential relation. Therefore the temperature-dependence of solvent-viscosity can be described by two parameters:

$$\eta_0 = 10^{\left(P_1 + P_2 \frac{1000}{T}\right)} \tag{5.6}$$

P_1 viscosity-parameter 1
P_2 viscosity-parameter 2
T Temperature in Kelvin

Additionally using the temperature dependency of pure 2-pentanone (literature values) all other viscosities were extrapolated. The used viscosity parameters are given in Table 5.2.

Table 5.2 Viscosity-parameters characterizing the temperature depen-dence

w_{ns}	P_1	P_2 /K^{-1}
0.875	-1.80711	0.4515
0.915	-1.80556	0.44748
1.000	-1.80081	0.43816
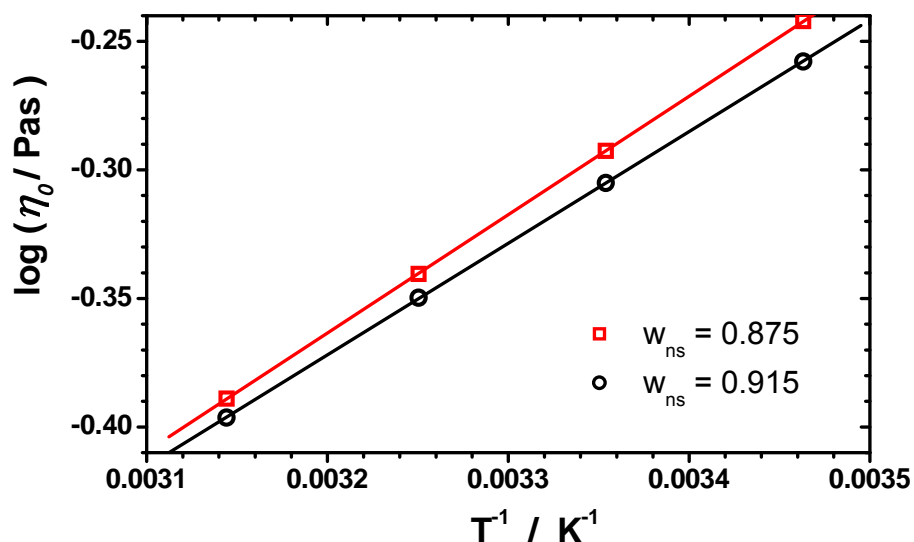
Figure 5.12 Solvent viscosity as function of w_{ns}, symbols: measurement data; straight lines: fits according to eq. 5.6.

5.4.5 Refractive Index

Dependence on w_{ns}

The change of refractive index in dependence on w_{ns} is neglected as they are essentially isorefractive (Table 5.1). The value n_D =1.390 was taken for all w_{ns} at 20°C. According to Table 5.1 and eq. 4.17 and 4.19 this may lead to an error in the determination of M_W of up to 1%. However due to the high dilution of the samples, light scattering solvent calibration for every solution with identical solvent composition was inevitable, e. g. using a w_{ns} = 0 calibration for a w_{ns} = 0.95 sample even resulted in a negative Rayleigh ratio.

Dependence on Temperature

Temperature dependent measurements were conducted with DLS. Therefore a change in n_D affects only q according to eq. 4.2. Refractive index measurements of the used solvent-pair do not exist in literature. The change of n_D shall be approximated as follows. The use of refractive-index-data for 3-pentanone from various sources [Liessmann 1995, Marras 1994, Govindan1988] yielded a change of n_D to be within 1.2% for the temperature interval of 20-50°C. The refractive index of DMF [Marchetti 1991] yielded a change of 0.9% within 20-50°C. Using a relation of n_D and the temperature dependence of the solvent density ρ_0 the temperature dependence of n_D can be determined very accurate. The Lorentz-Lorenz formula describes the relation of n_D, ρ_0, molecular weight M and the polarizability of the solvent α_{pol} :

$$\frac{n_D^2 - 1}{n_D^2 + 2} = \frac{N_a \alpha}{3\varepsilon_0 M} \rho_0 \tag{5.7}$$

The polarizability usually does not depend on the temperature. However with a change in temperature the density changes due to thermal expansion of the solvent and therefore the refractive index according to eq. 5.7 as well:

$$\frac{n_D^2 - 1}{n_D^2 + 2} = c_{LL} \rho_0 \tag{5.8}$$

Knowing the density and refractive index at reference temperature 20°C one can calculate the constant c_{LL}, that is 0.2931ml/g for n_D =1.390. With this formula one can calculate the temperature-dependent refractive index by knowing ρ_0 temperature dependent [Cowan 1940]. Changing the temperature from 20 to 50°C, the refractive index of 2-Pentanone will shift by 0.0165 that is 1.2%.

Density measurements were conducted using a DMA 60 density meter with a DMA 602 external measurement cell. The temperature dependency for the solvent density was determined for the two compositions w_{ns} = 0.875 and 0.915 which is close to the precipitation point of the PVP and QPVP$_{20}$. As Figure 5.13 shows, the temperature dependence can be described by a linear dependency. Therefore the temperature dependence of ρ_0 is described by two parameters according to:

$$\rho_0 = D_1 + D_2 T \tag{5.9}$$

$$D_1 \qquad\qquad\qquad density\text{-}parameter\ 1$$
$$D_2 \qquad\qquad\qquad density\text{-}parameter\ 2$$

Additionally using the temperature dependency of pure 2-pentanone (literature values) all other densities were extrapolated. The used density parameters are given in Table 5.3.

Table 5.3 Viscosity-parameters characterizing the temperature dependence

w_{ns}	D_1 / g/ml	D_2 / g/ml*K
0.875	1.08654	-9.591E-04
0.915	1.09567	-9.864E-04
1.000	1.11507	-1.044E-03
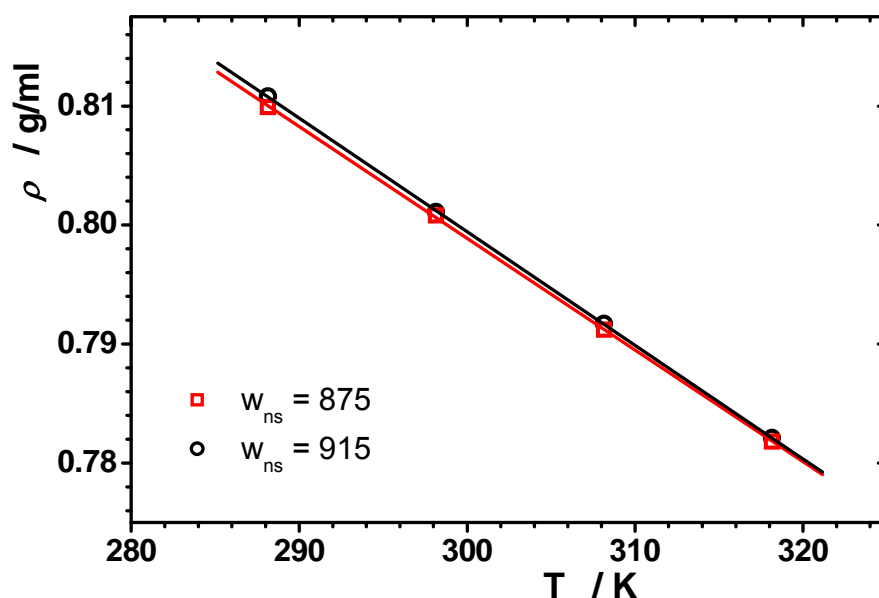
Figure 5.13 Solvent density ρ_0 as function of w_{ns}; symbols: measurement data; straight lines: fits according to eq. 5.5.

Dependence on Salt Concentration

Due to condensation of counterions close to the precipitation point, the concentration of salt is reduced. Therefore the influence of this condensation onto n_D should be approximated. Whereas for our solvent pair no literature is available, the system NaCl in H_2O shall be used instead [Mandel 1982]. Data show that the influence is small. Using concentrations of 4.6 to 36 g/L the refractive index change with respect to the salt concentration is given by:

$$\frac{\Delta n}{c_s} = 1{,}735 * 10^{-3} - 2{,}7 * 10^{-5} c_s + 10^{-6} c_s{}^2 \tag{5.10}$$

Assuming full dissociation and full condensation and the concentrations used for the samples of this thesis, due to the very dilute solutions the influence is vanishing small, about 10^{-5} % and therefore neglected.

5.5   Refractive Index Increment

dn_D/dc_p values were determined with a home built [Becker 1995] Michelson interferometer at various 2-pentanone fractions and TBAB concentrations (Table. 5.4). In general dn_D/dc_p values had no trend regarding the 2-pentanone content or TBAB concentration (reverse: PVP showed a constant M_w for different w_{ns}-values but constant dn_D/dc_p). For QPVP$_{4.3}$ and QPVP$_{20}$ averages were used for LS-measurements: 0.1880 ml/g, respectively 0.1948 ml/g. Due to the similarity of dn_D/dc_p values of PVP and QPVP$_{4.3}$ and the measurement accuracy, no dn_D/dc_p measurements were done for QPVP$_{1.2}$ and QPVP$_{2.4}$. For both samples dn_D/dc_p = 0.1880 ml/g was used. The determined dn_D/dc_p-values were applied to all measurements at different solvent compositions.

Table 5.4 dn_D/dc_p values for PVP and QPVPs, measured at different solvent compositions and added salt concentrations.

Polymer	w_{ns}	c_{TBAB} / mol/L	dn/dc_p / ml/g
PVP	0	10^{-5}	0.1902
QPVP$_{4.3}$	0	10^{-1}	0.1891
QPVP$_{4.3}$	0	10^{-4}	0.1918
QPVP$_{4.3}$	0	10^{-5}	0.1894
QPVP$_{4.3}$	0.90	10^{-1}	0.1851
QPVP$_{4.3}$	0.90	10^{-4}	0.1870
QPVP$_{4.3}$	0.99	10^{-5}	0.1852
QPVP$_{20}$	0.20	10^{-5}	0.1966
QPVP$_{20}$	0.80	10^{-5}	0.1930
QPVP$_{35}$	0	10^{-5}	0.1910

Dependence of dn_D/dc_p on Temperature

The change of the refractive index increment with temperature can be approximated as follows: Solving eq. 5.8 for n_D gives:

$$n_D(\rho_0) = +\sqrt{\frac{2c_{LL}\rho_0 + 1}{1 - c_{LL}\rho_0}} \tag{5.11}$$

The concentration is connected to the density as:

$$c_p = \frac{m_{poly}}{m_{solv}} \rho_0 \tag{5.12}$$

m_{poly} *polymer mass*
m_{solv} *solvent mass*

To yield for the increment:

$$\frac{dn_D}{dc_p} = \frac{m_{solv}}{m_{poly}} \frac{dn_D}{d\rho_0} \tag{5.13}$$

Derivation of eq. 5.11 with respect to ρ_0 yields the expression:

$$n_D'(\rho_0) = \left(\frac{2c_{LL}\rho_0 + 1}{1 - c_{LL}\rho_0}\right)^{0,5} \frac{3c_{LL}}{2(1 - c_{LL}\rho_0)^2} \tag{5.14}$$

Using the density data for the temperature interval 20 to 50°C gives a change in the increment of 3.5%. To verify this relation and to enable unbiased LS-data, the increment was measured at different temperatures for the QPVP$_{20}$-system, however measured refractive indexes were within experimental error.

5.6   Conductivity

The conductivity was measured in a homemade PTFE container equipped with a stirring bar inside. Tightness was assured using O-seals for all connectors. The container was wrapped into a rubber envelope and placed into a temperature bath located on a shaker. The water bath was attached to a thermostat (HAAKE Phoenix II P1).

The conductivity probe with a built in Pt 1000 temperature sensor from Metrohm is made out of stainless steel and especially designed for measurements of low conductivities with a cell constant of 0.105 cm^{-1}. The cell constant was determined using a low conductivity standard from Metrohm. The Metrohm 712 conductometer was utilized for all measurements. The temperature inside the container was kept constant at 20°C ± 0.1 °C. A typical measurement with successive addition of solutions took about 16 h. The vessel was absolutely air tight and the measured conductivities were stable for at least 24 h in the order of ± 0.002 μS. In contrast to light scattering measurements (glass cuvette) no change in conductivity with time was observed for the Teflon container whereas a decrease of conductance with time was observed for measurements in a glass container.

A series of measurements was performed for various w_{ns} at a constant polyelectrolyte concentration. For this purpose solutions at different w_{ns} were prepared by two titration units, one with a stock solution of PVP in a good solvent mixture (or plain 1-propanol) and a second one with a poor solvent mixture (or even plain 2-pentanone). The titration units (Metrohm S-Titrino 719 with a 5ml cylinder for the poor solvent and a 702 SM Titrino for the polyelectrolyte solution with a 1 ml cylinder) have an accuracy of 0.5 and 0.1 μL, respectively. The starting volume was at least 10 ml and the maximum 150ml. Due to the very small diameter of the capillaries in the micro burette tips, no apparent effect due to diffusion in and out of the burette tips being immersed into the solution could be detected. The conductometer as well as the titration units were connected to a PC and controlled by homemade software written with Testpoint. After addition of calculated amounts of solutions the software collected always four values while waiting. The measurement values taken for evaluation were at least 10 minutes after addition of the solutions, whereas the solution was stirred and shaken. Collecting successively data while waiting the values could be checked with respect to a potential drift. After the measurement the vessel was cleaned in an ultrasonic bath and rinsed thoroughly in a flow box with dust free solvents. It turned out that the cleaning process of the probe was essential to avoid aging. The vessel was then transported back into the glove box for refilling.

Figure 5.14 Conductivity vessel, completely made out of PTFE, Probe made out of steel.
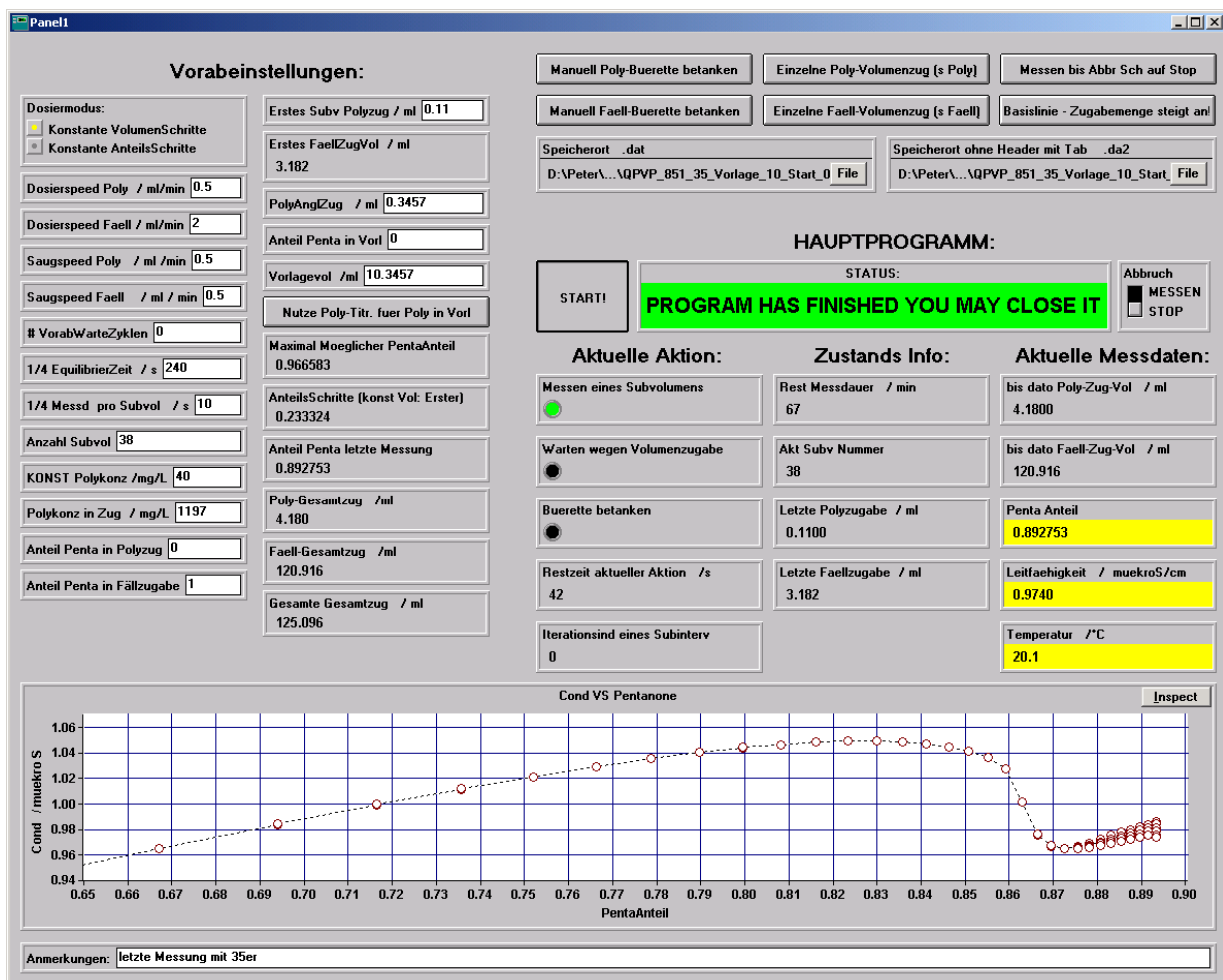
Figure 5.15 The Software drives the two titration units and collects data and parameters from the conductometer. Two different programs can be chosen, constant volume or constant fraction-steps (upper left) with various parameters (left). The devices can be used manually as well (upper right). The ongoing data is displayed and stored in two files with and without a header (middle right). A graph displays the so far collected data (bottom).

5.7 Light Scattering

The light scattering cuvettes were cleaned in an acetone fountain and then transported into the glove box in a nitrogen counter flow. The polyion concentration for a measurement series was kept constant at c_p = 6, 8, 10 or 12 mg/L. 6 mg/L was the lowest concentration where a reliable scattering signal could be obtained. In order to avoid filtration losses of solutions close to the phase boundary a three syringe system (each having a 200 nm pore size Millipore Dimex LG filter at the outlet) was used. One syringe contained a polyelectrolyte stock solution at w_{ns} ≤ 0.9 (which is not critical in respect to concentration losses), a second syringe with high 1-propanol and a third one with low 1-propanol content, or pure pentanone. The precalculated volumes of the respective components were filtered into the LS cuvettes. In order to minimize the loss of concentration due to adsorption of the QPVP on glass surfaces the concentration of the stock solution was relatively high (c_p = 240 mg/L). This solution was never kept longer than one week. Exact final concentrations were determined by a balance inside the glove box. Measurements were performed at T = 20°C.

5.7.1 Adsorption of QPVP on Glass Surfaces

A time dependent decrease of the intensity could be observed for the final low QPVP concentration in the poor solvent regime (w_{ns} ≤ 0.9). The intensity loss amounted to 10% a week depending in detail on the respective solvent composition. This intensity loss is attributed to the adsorption of the positively charged QPVP onto the negatively charged glass surface. Because with increasing time bright spots developed at the inner surface of the light scattering cell due to stronger reflections/scattering of the primary laser beam. Therefore all samples were measured directly after preparation (except temperature dependent measurements), the duration never exceeding three hours.

Temperature dependent measurements took up to two days. Therefore to reduce the intensity-loss due to adsorption processes onto the glass surface, measurements were carried out in hydrophobized cuvettes:

Preparation of Hydrophobic Cuvettes

The cuvettes were cleaned using piranha-solution (H_2SO_4/H_2O_2; 75/25; v/v) and afterwards treated with Hellmanex solution (alkaline solution with detergents; 7/93 v/v). The cuvettes were then rinsed with Milli-Q-water and dried in an oven. A chloromethylsilane/toluene solution (2/98 v/v) was prepared and poured into the hot cuvettes. Protected from humidity by a stopper the solution was kept in the cuvettes for one day. Cuvettes with longer hydrophobic tales than methylsilane were investigated, too, however these cuvettes showed reflexes when set into the laser beam, and were therefore not used.

5.7.2 Static Light Scattering Measurements

The influence of the Donnan equilibrium

Neither light scattering nor dn_D/dc_p measurements were performed under Donnan equilibrium which could introduce errors in the molar mass determination of polyelectrolytes according to [Vrij 1962]:

$$M_{w,app} = M_w \left[1 + \frac{dn/dc_S}{dn/dc_P} \left(\frac{dc_S}{dc_P} \right)_{\mu_2} \right]^2 \tag{5.15}$$

c_s denotes the added salt concentration, c_p the polyelectrolyte concentration and μ_2 constant chemical potential at Donnan equilibrium. The measured dn_D/dc_p values were observed to be constant within experimental error over a broad range of salt concentrations and different 2-pentanone contents (see Table 5.4). This suggests that dn_D/dc_p is not very different from zero (which can also be deduced by comparison of the refractive indices of TBAB and 1-propanol) and therefore the light scattering molar mass $M_{w,app}$ for the used system should not be affected significantly by the Donnan effect.

Unquaternized PVP

For the determination of M_w, A_2 and R_g of PVP$_{851}$ as function of the solvent composition w_{ns}, Zimm plots were measured for $0 \leq w_{ns} \leq 0.954$. Measurements were performed in a concentration regime 100 mg/L $\leq c_p \leq$ 450 mg/L, and the scattering intensity was recorded at 19 angles ranging from 26 to 154°. A multi-angle light scattering setup (ALV-1800) was utilized in combination with a Kr-ion laser operating at a wavelength of λ = 647 nm as described in detail elsewhere [Becker, Schmidt 1991]. Some representative Zimm plots are shown in Figures 5.16 - 5.18 for good, θ and poor solvent conditions.
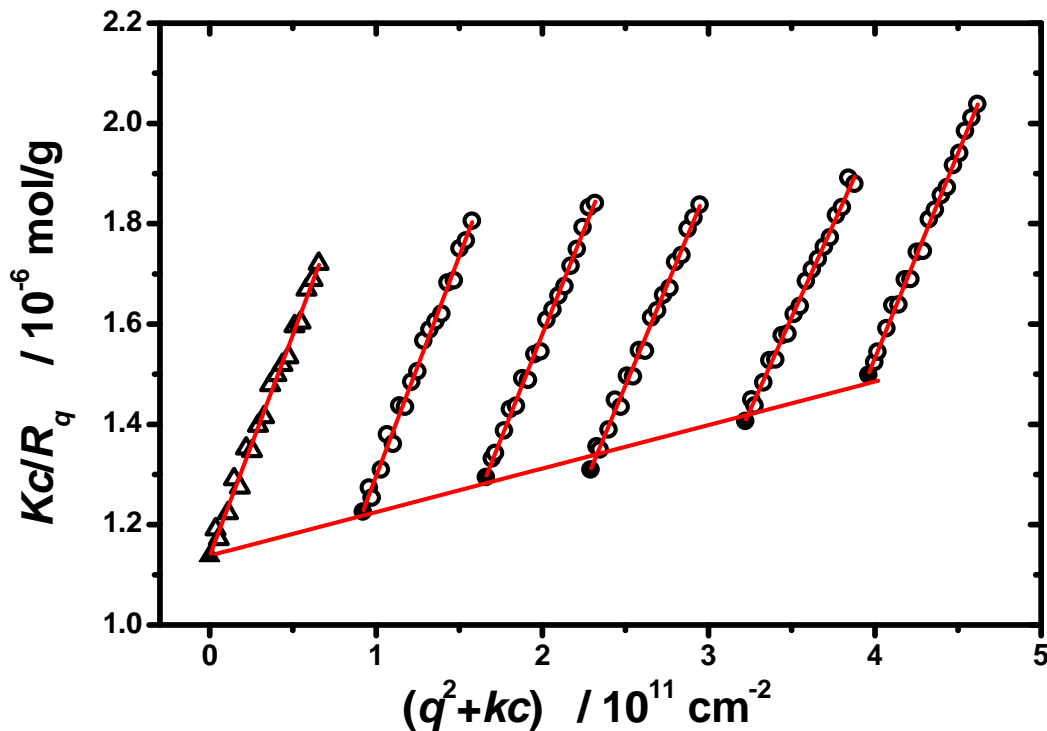
Figure 5.16 Zimm plot for PVP$_{851}$; w_{ns} = 0: A_2 = 4.3*10^{-4} mol*cm^3/g^2; R_g = 48.2 nm; M_w = 8.8*10^5 g/mol
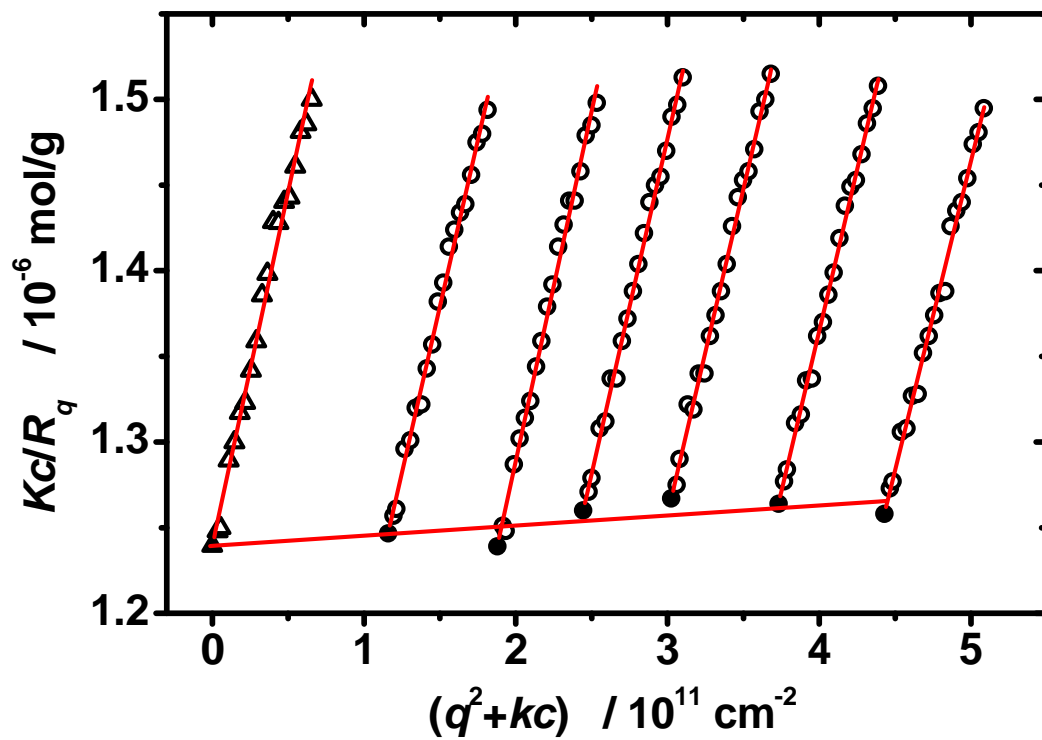
Figure 5.17 Zimm plot for PVP_{851}; w_{ns} = 0.909: A_2 = 0.3*10^{-4} mol*cm^3/g^2; R_g = 30.6 nm; 8.8*10^5 g/mol
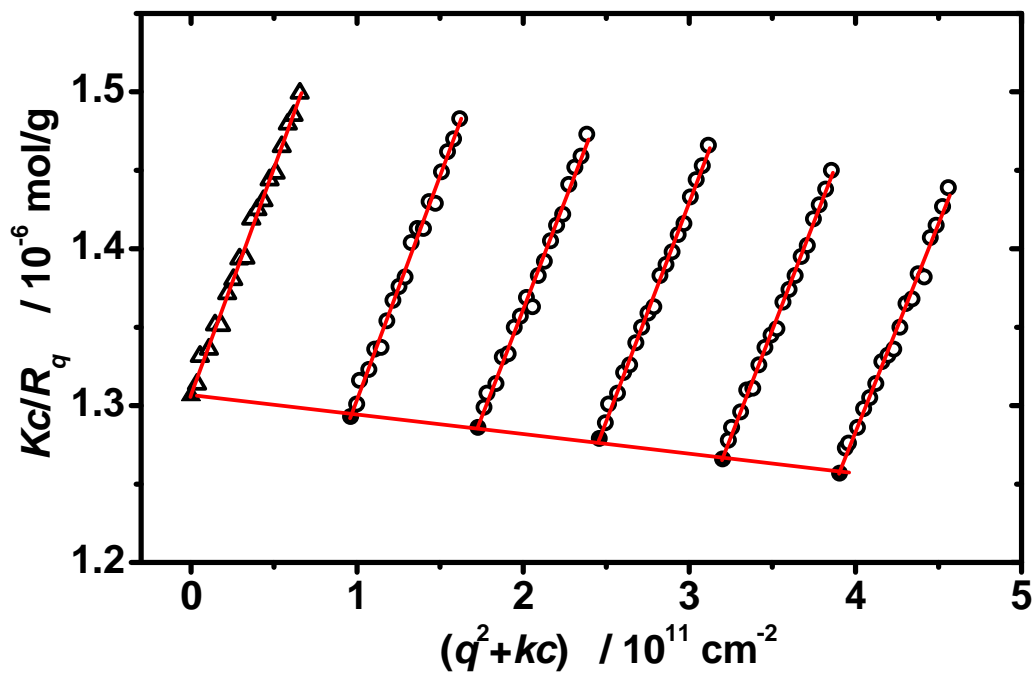
Figure 5.18 Zimm plot for PVP_{851}; w_{ns} = 0.931: A_2 = -0.5*10^{-4} mol*cm^3/g^2; R_g = 26.7 nm; M_w = 7.8*10^5 g/mol

Quaternized QPVP

Static light scattering measurements were performed with an ALV-SP86 goniometer, an ALV-3000 correlator, a Uniphase HeNe Laser (25mW output power at λ = 632.8nm wavelength) and ALV/High QE APD avalanche diode fiber optic detection system. Due to the low concentration the excess scattering intensity amounted to typically 25% of the solvent scattering. The measurements were conducted at scattering angles from 30° to 150° in steps of 3°, examples are shown in Figures 5.19 - 5.22 and A.1-A.6.

5.7.3 Dynamic Light Scattering Measurements

Dynamic measurements were conducted with an ALV-SP125 goniometer equipped with a fiber optical detection unit. The scattering intensity is divided in two parts by a beam splitter (approximately 50:50) and detected by two photomultipliers connected to an ALV-5000 correlator. The two signals were cross correlated in order to eliminate non random electronic noise which could originate from the detector electronics leading to correlation signals in the time regime below 1 µs. An Ar-ion laser operating at 514 nm wavelength and 500 mW output power was used as the light source. For small scattering angles the probed sample volume is bigger than for big angles. Therefore the signal to noise ratio is better for small angles and correlation functions were typically measured from 20° to 30° in steps of 2° and each angle for about 10 runs * 100 s (see Figures 5.19-5.23 and A.1-A.6 for some examples). Due to the low excess count rate besides the cooperative diffusion of the polyelectrolyte the solvent self-diffusion arising from density fluctuations could be observed [Stepanek, Kadlec 2007] at small times for the smallest q-values. Accordingly, only the long time decay of the correlation functions were fitted with two exponentials utilizing the simplex algorithm from which the initial decay constant, i.e. the first cumulant was derived. The resulting apparent diffusion coefficients showed no q-dependency and therefore the average of all angles was calculated and utilized for the determination of the hydrodynamic radius.
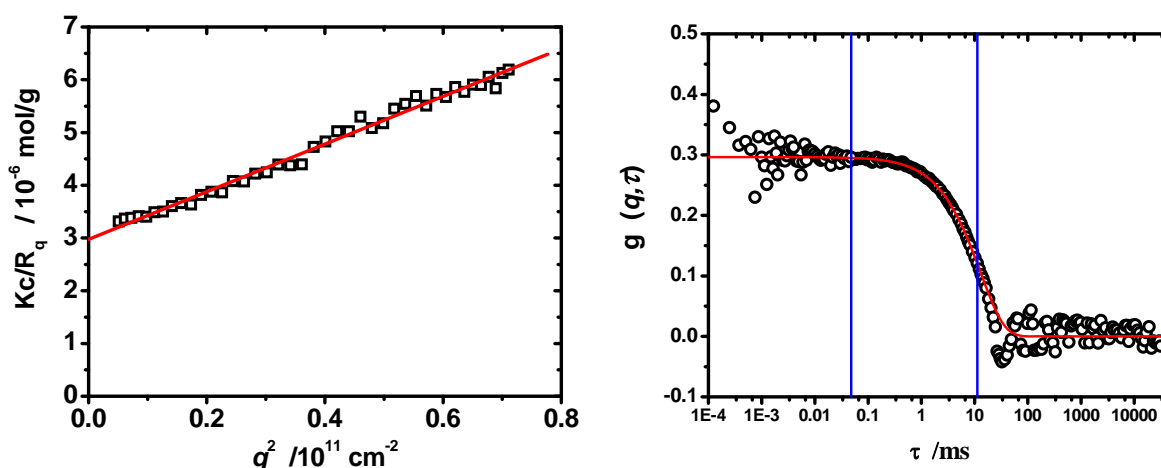
Figure 5.19 Static and dynamic light scattering on QPVP$_{4.3}$ at w_{ns} = 0; Reduced scattering intensity vs. q^2 yielding R_g^{app} = 68.7 nm and M_w^{app} = 3.4 * 10^5 g/mol and a correlation function measured at 22° scattering angle, data were fitted with a second order exponential decay within the blue borders. The average over all measured angles yields R_h^{app} = 37.5 nm.
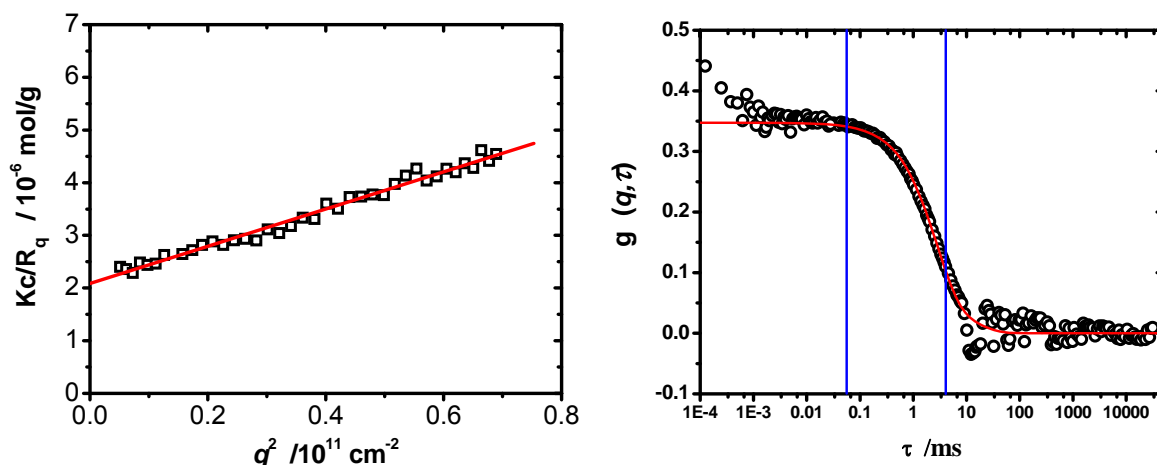
Figure 5.20 Static and dynamic light scattering on QPVP$_{4.3}$ at w$_{ns}$ = 0.902; Reduced scattering intensity vs. q^2 yielding R_g^{app} = 70.3 nm and M_w^{app} = 4.8 * 10^5 g/mol and a correlation function measured at 22° scattering angle, data were fitted with a second order exponential decay within the blue borders. The average over all measured angles yields R_h^{app} = 36.7 nm.
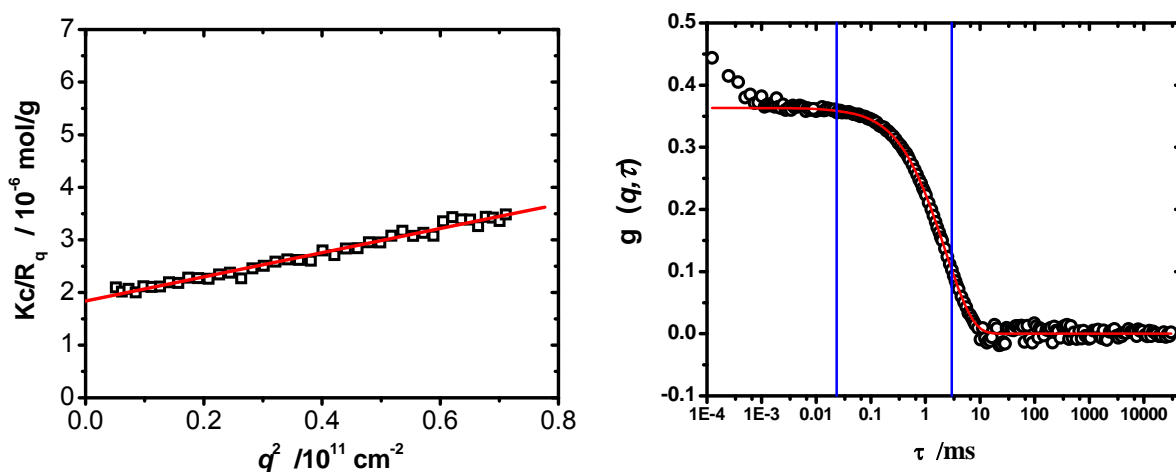
Figure 5.21 Static and dynamic light scattering on QPVP$_{4.3}$ at w$_{ns}$ = 0.980; Reduced scattering intensity vs. q^2 yielding R_g^{app} = 56.9 nm and M_w^{app} = 5.4 * 10^5 g/mol a correlation function measured at 22° scattering angle, data were fitted with a second order exponential decay within the blue borders. The average over all measured angles yields R_h^{app} = 31.0 nm.
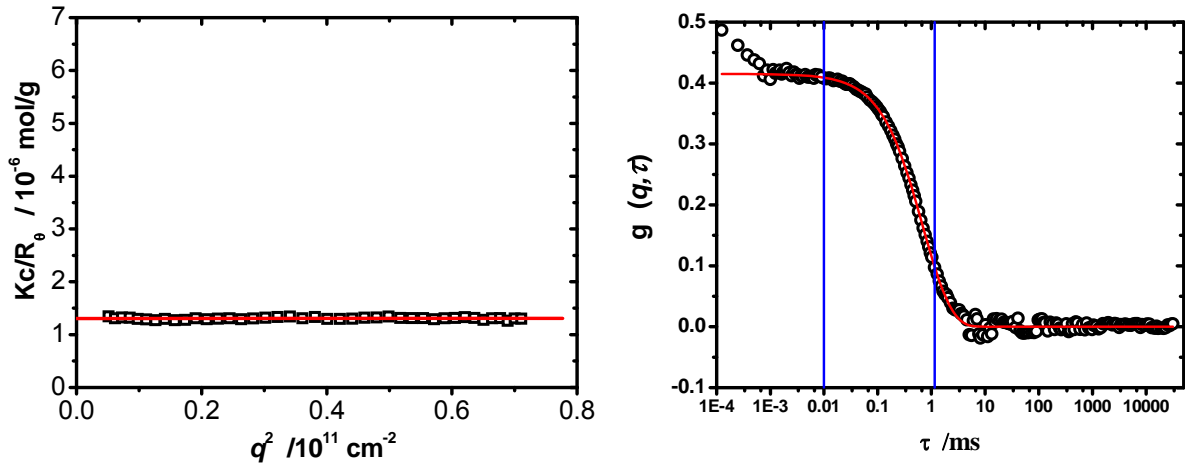
Figure 5.22 Static and dynamic light scattering on QPVP$_{4.3}$ at w$_{ns}$ = 0.994; Reduced scattering intensity vs. q^2 yielding $M_w{}^{app}$ = 7.7 * 10^5 g/mol (R$_g$ too small to be determined) and a correlation function measured at 22° scattering angle, data were fitted with a second order exponential decay within the blue borders. The average over all measured angles yields $R_h{}^{app}$ = 12.5 nm
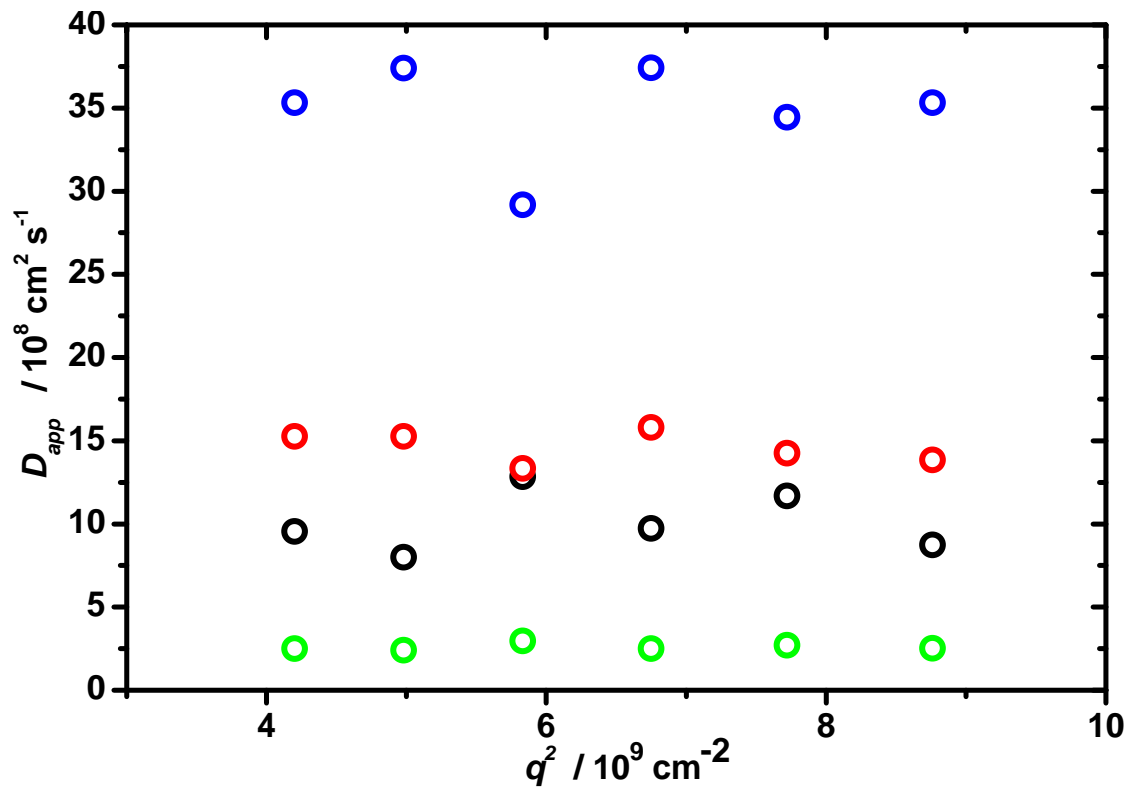
Figure 5.23 Apparent diffusion coefficient D_{app} vs. q^2 for QPVP$_{4.3}$. Correlation functions were measured from 22° to 32° in steps of 2° at w$_{ns}$ = 0 (blue), w$_{ns}$ = 0902 (red), w$_{ns}$ = 0.980 (black), w$_{ns}$ = 0.994 (green). Note that the solvent viscosity changes with w$_{ns}$ according to eq. 5.5

6 Measurement – Results

6.1 The Coil-Globule Transition of Unquaternized PVP$_{851}$

In order to quantify the solvent quality of the uncharged polyvinylpyridine PVP$_{851}$, Zimm plots (eq. 4.28) were conducted over the whole experimental accessible solvent quality regime (0 < w$_{ns}$ < 0.954), covering good, theta and poor conditions. The polymer conformation characterized by the three characteristics mean square radius of gyration $R_g \equiv \langle R_g^2 \rangle_z^{1/2}$, second virial coefficient A_2 and molecular weight M_w, is plotted as a function of the non-solvent 2-pentanone, w$_{ns}$ in Figure 6.1 - 6.4. The Flory solvent quality parameter χ_1 is related to the second virial coefficient according to eq. 2.46 and is plotted in Figure 6.2, too. θ-dimensions ($A_2 = 0$, $R_{g,\theta} = 29$ nm, $R_{h,\theta} = 22$ nm) were observed at w$_{ns} = 0.91$ (see Figure 6.2 and 6.3). As expected the decrease of R_g is reflected in a decrease of the second virial coefficient. Moreover as A_2 is a direct measure of solvent quality its decrease causes the coil to reduce the number of solvent-solute contacts in favor of more and more backbone-backbone contacts, reflected in the R_g decrease. The R_g / R_h ratio is 1.4 that is close to the theoretical value of 1.5 for a coil with low polydispersity.
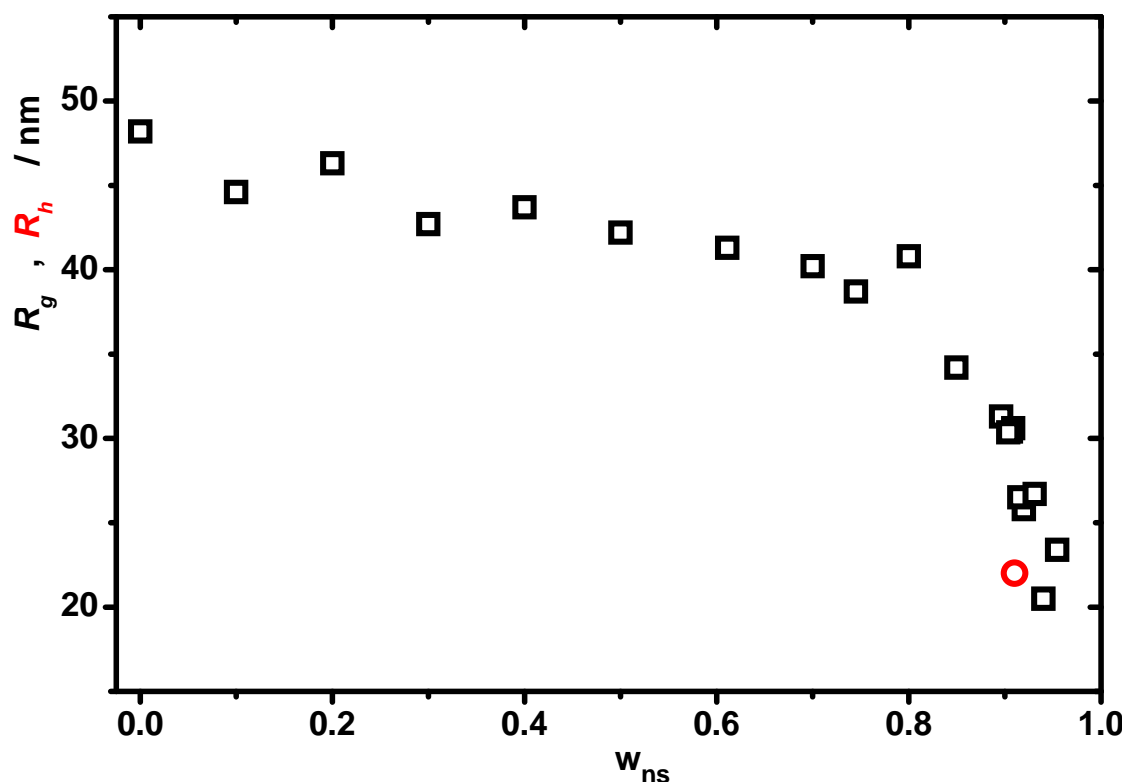
Figure 6.1 The radius of gyration R_g (black squares) and the hydrodynamic radius R_h (red circle, only at θ-condition: w$_{ns}$=0.91) are plotted against the volume fraction of the non-solvent, w$_{ns}$, for the neutral polyvinylpyridine PVP$_{851}$.
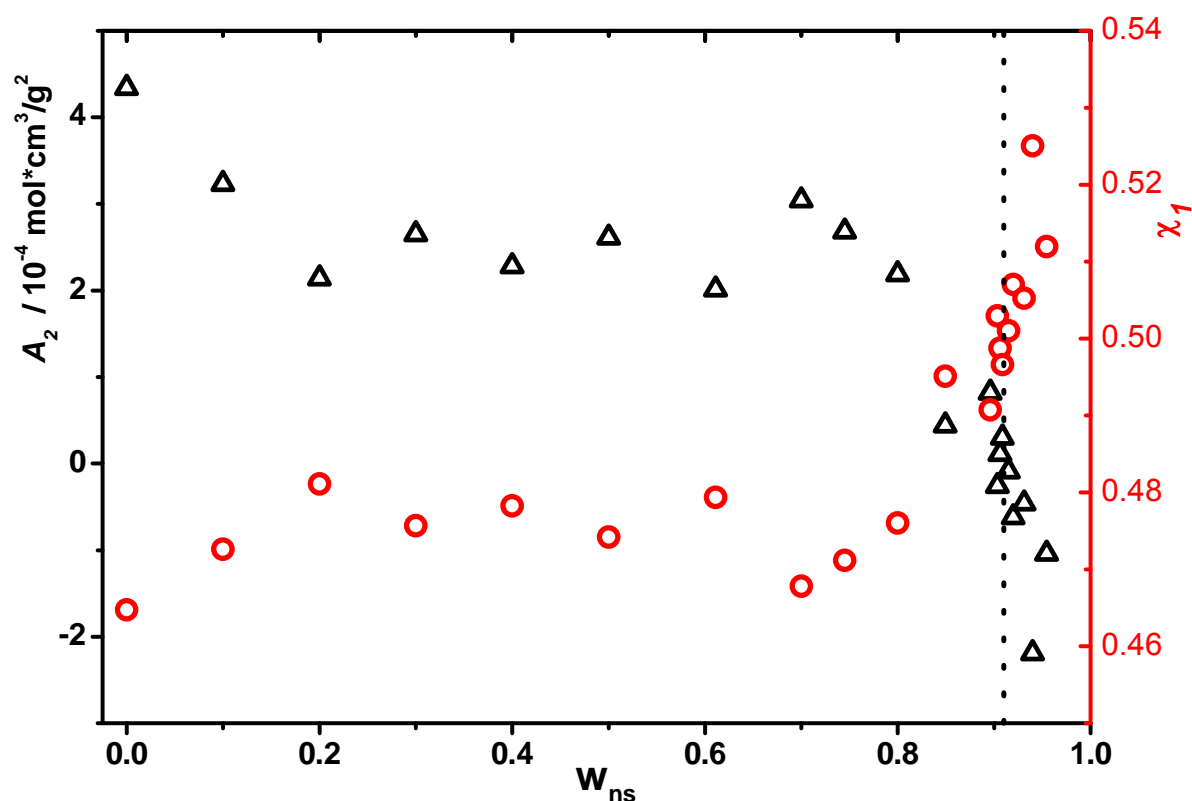
Figure 6.2 The second virial coefficient A_2 and the χ_1 parameter (according to eq. 2.46) for the neutral polyvinylpyridine are plotted against the volume fraction of the non-solvent, w_{ns}. θ-conditions are marked by the dotted vertical line at $w_{ns} = 0.91$
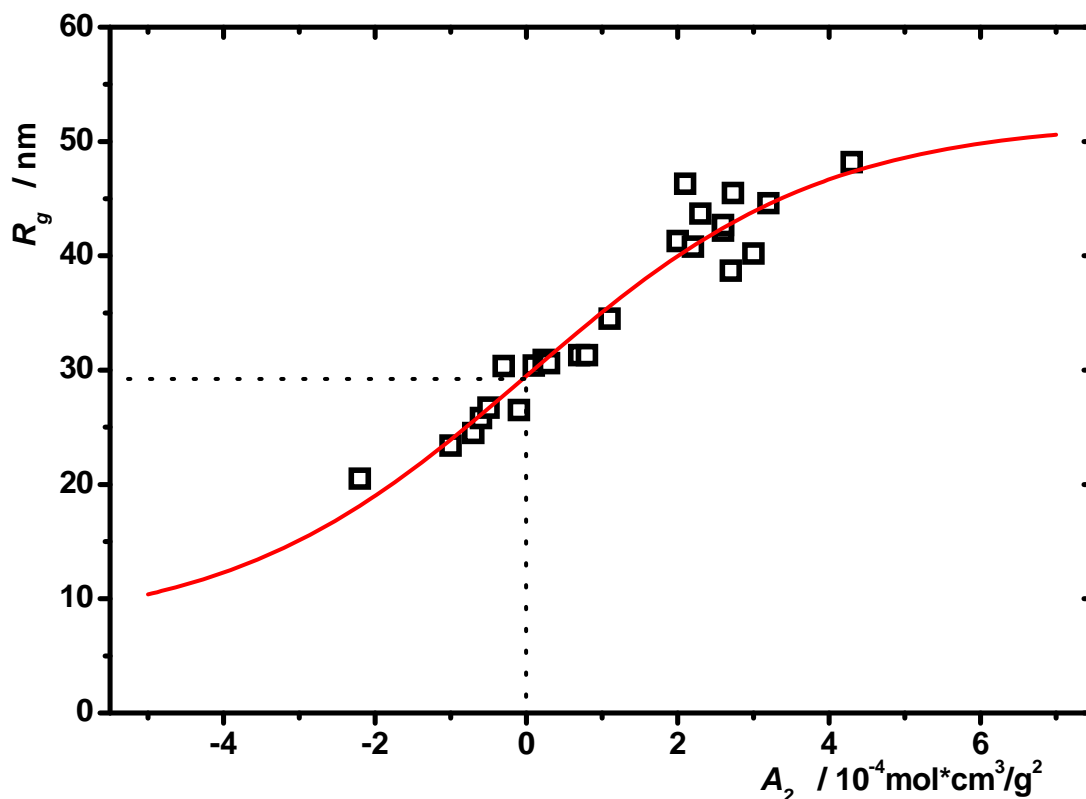
Figure 6.3 The radius of gyration for the neutral polyvinylpyridine PVP$_{851}$ is plotted versus its second virial coefficient, A_2, determined at different w_{ns}. A sigmoidal fit (red line) having its inflection point set to $A_2 = 0$ describes the data satisfactorily and yields the θ-dimensions marked by the two dotted lines ($A_2 = 0$, $R_{g\,\theta} = 29$ nm)
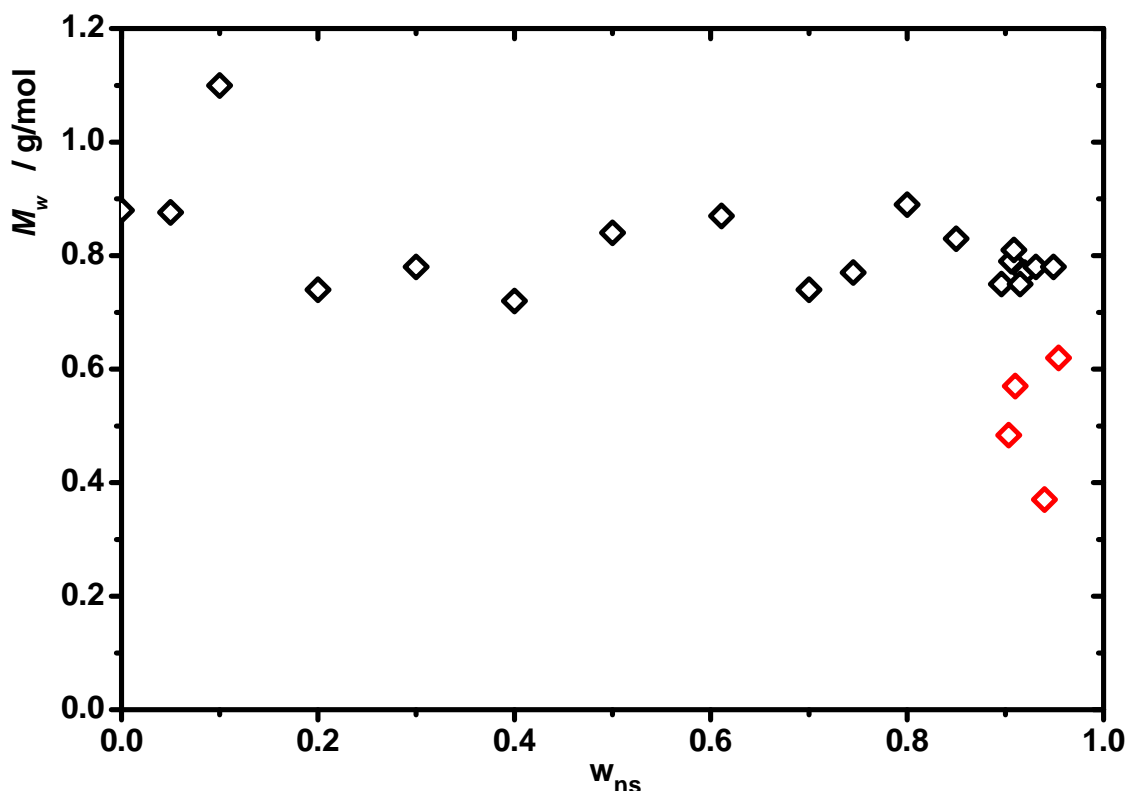
Figure 6.4 The molecular weight M_w is plotted against w_{ns}. For bigger non-solvent fractions the polymer tends to aggregate. Those aggregates are filtered out due to standard preparation procedure, thereby reducing the evaluated molar mass (red).

For linear uncharged homopolymers the expanded "coil" and the dense "globule" are two theoretically defined thermodynamically stable states. The two states can be distinguished by the scaling behavior of their size with the degree of polymerization N. For the coil $R_g \sim N^{3/5}$ and for the globule $R_g \sim N^{1/3}$. In between these two states is the θ-point where $R_g \sim N^{1/2}$ and the polymer is said to behave ideally.

Theories predict for flexible polymers the coil-globule transition to be a smooth second order process, which has been confirmed by various experiments [Itaya et al. 1982; Park et al.1987; Chu et al. 1987; Wu et al. 1995+1998; Zhou et al. 2008]. In contrast theories predict that with increasing stiffness the transition gets more abrupt even predicting a first order transition for sufficient rigid polymers [Grosberg, Kuznetsov 1992; Birshtein, Pryamitsyn 1991], which however hasn't been observed in experiments so far.

In all mentioned experiments, light scattering was utilized to monitor the coil-to-globule transition and the collapse was induced by increasing or decreasing the temperature. From good to poor solvent conditions a sigmoidal shaped collapse transition of R_g vs. τ respectively R_h vs. τ was observed (τ is the relative deviation from the θ-temperature, see eq. 2.61). From an experimental point of view it is hard to observe single collapsed coils due to the fact that aggregation may further reduce the Gibbs free energy. Going from good to poor solvent conditions, high molar masses will precipitate first. Chi Wu argued that in case of polydisperse systems close to the precipitation point already collapsed coils may act as a pattern for aggregation [Wu, Wang 1998]. The aggregation tendency is hard to predict and depends on the system studied. A low polydispersity is assumed to avoid early aggregation. Chi Wu was able to monitor the coil globule transition of non aggregating chains in high dilution using two different very low polydispersity samples: PNIPAM (poly(N-isopropylacrylamide) [Wu, Wang

1998] and PDEAM poly(N,N-diethylacrylamide) [Wu, Wang 2008]. He found that PDEAM was apparently hysteresis free whereas PNIPAM showed a hysteresis. Wu argued that formation of hydrogen-bonding in the collapsed state may be responsible for the hysteresis.

6.2   Collapse of QPVP$_{4.3}$

The collapse of QPVP$_{4.3}$ at c_p = 12mg/L has been monitored in very small w_{ns} steps and will be discussed first. The Manning parameter for this system is ξ_M = l_B/c = 0.6 (l_B the Bjerrum length and c the mean contour distance between two charges), i.e. no counterion binding should occur according to Manning. Data evaluation procedure is identical for all samples and will be presented only in this chapter. Comparing the QPVP$_{4.3}$ to the uncharged backbone it is obvious that i) the coil is expanded due to electrostatic expansion, ii) the collapse proceeds at much higher non-solvent fractions, iii) the polyion collects its counterions continually during shrinkage. Therefore even 4.3% of quaternized units along the chain are sufficient to change the dissolving behavior drastically.

6.2.1 QPVP$_{4.3}$ – Light Scattering Data

One should note that measurements have not been conducted in Donnan equilibrium but at constant added salt concentration. Measurements at Donnan equilibrium were not established in favor of well defined highly diluted concentration regimes at different solvent/non-solvent compositions with defined salt concentration. Therefore measurements at different polyion concentrations c_p but constant c_s will change the λ_R-value (= c_p/c_s) thereby changing the polyelectrolyte species a little. For example lower λ_R will lead to contraction of the polyelectrolyte (see Figure 2.2). Therefore a Zimm concentration extrapolation according to eq. 4.28 can not yield a nonbiased A_2 value. Although the concentration of the measured solution is extremely small, long range electrostatic interactions due to only a small amount of screening salt are supposed to influence both, dynamic and static light scattering measurements. They should be falsified by an intermolecular structure factor as will be discussed in chapter 6.3.1. They are marked as "apparent" quantities, accordingly. The $R_{g\,app}$-values shown in Figure 6.1 were derived from the slopes of the reduced scattering intensity versus q^2 at c_p = 12 mg/L (eq. 4.28), omitting the concentration dependent term, i.e. without extrapolation to infinite dilution.

$$\frac{Kc_p}{R(q)} = \frac{1}{M_{w\,app}}\left(1+\frac{R_{g\,app}{}^2}{3}q^2\right)$$

(6.1)

The slopes vs. q^2 were strictly linear for all solvent compositions (see chapter 5.7.3 for some examples). However, the experimentally observed linearity does not necessarily prove the slope to be unaffected by intermolecular interference effects as will be discussed in chapter 7.1 and 7.2. The hydrodynamic radius should be affected by the static structure factor as well. Intermolecular electrostatic interactions should always lead to smaller $R_{g\,app}$- and $R_{h\,app}$-values as compared to interaction-free values, the effect on R_h being more pronounced than on R_g as will be discussed in chapter 6.8.

The polyion conformation characterized by the square root of the apparent mean square radius of gyration, $R_{g\,app} \equiv \left\langle R_{g\,app}{}^2 \right\rangle_z^{1/2}$, the apparent hydrodynamic radius, $R_{h\,app} \equiv \left\langle 1/R_{h\,app} \right\rangle_z^{-1}$, and the apparent molecular weight $M_{w\,app}$ are shown in Figure 6.5 as functions of the weight

fraction of the non-solvent 2-pentanone, w_{ns} (which is equivalent to the volume fraction due to almost equal densities).

The apparent molar mass at $w_{ns} < 0.8$ is observed to be less than half of the true molar mass which is $8.9*10^5$ g/mol, as calculated from the precursor molar mass and the degree of quaternization. Chain degradation during the quaternization reaction can be safely ruled out, as for larger amounts of added salt ($c_s = 0.1$ M) the true molar mass is obtained within experimental error. Alternatively, one might misinterpret the increase of the apparent molar mass of the polyelectrolyte in the collapse regime in terms of a true increase of molar mass caused by inter chain aggregation. However aggregation can be safely ruled out because i) the apparent molar mass for all w_{ns}-values is smaller than the true molar mass, ii) the increasing molar mass in the collapse regime approaches the true molar mass and iii) the correlation functions measured in the collapse regime do not exhibit broader relaxation time distributions than those at small 2-pentanone content. Uncertainties in the determination of the refractive index increments, dn_D/dc_p, are also not likely to influence $M_{w\,app}$ as discussed in chapter 5.5.

Rather, the disparity between the apparent molar mass M_{app} (respectively $M_{w\,app}$) and the true molar mass M (respectively M_w) is governed by the dissociated counterions and by the osmotic coefficient ϕ defined as [Katchalsky et al. 1966; Mandel 1974] (compare eq. 2.3):

$$\phi = \Pi \,/\, \Pi^{id} = M^{id} \,/\, M_{app} \tag{6.2}$$

Π *measured osmotic pressure*
Π^{id} *ideal osmotic pressure*

For most polyion solutions the ideal osmotic pressure in volume V is dominated by the very many dissociated counterions

$$\Pi^{id} = RTn_p\left(1 + fN\right)/V \tag{6.3}$$

n_p *number of polyions*
f *degree of dissociation*

Since $fN \gg 1$, the ideal osmotic pressure does not yield the true polyion molar mass but represents a measure for counterion dissociation according to

$$M^{id} = M \,/\left(1 + fN\right) \approx M \,/\, fN \tag{6.4}$$

In practice, eq. 6.4 cannot be utilized for the determination of counterion dissociation due to the non ideal behavior leading to the osmotic coefficient in eq. 6.2. However, since the scattering intensity extrapolated to $q = 0$ is inversely proportional to the osmotic compressibility, the ratio $M_w / M_{w\,app}$ is proportional to the product $(\phi\gamma)_{LS}$ according to:

$$\left(\phi\gamma\right)_{LS} = M_w \,/\left(M_{w\,app}fN\right) \tag{6.5}$$

with γ the fraction of dissociated counterions $f\,/\,f_m$. According to eq. 6.5 $M_{w\,app}$ shown in Figure 6.5 is inversely related to the number of dissociated counterions. Consequently the effective charge density is observed to decrease with decreasing solvent quality.

Keeping these uncertainties in mind, the measured R_g- as well as the R_h-values remain constant for $0 < w_{ns} < 0.8$, followed by a slight decrease until $w_{ns} \approx 0.988$, above which the polyelectrolyte chains collapse and eventually aggregate and phase separate at $w_{ns} > 0.994$. The regime close to the phase boundary, $0.95 < w_{ns} < 1$, is enlarged in Fig. 6.5b for better clarity.
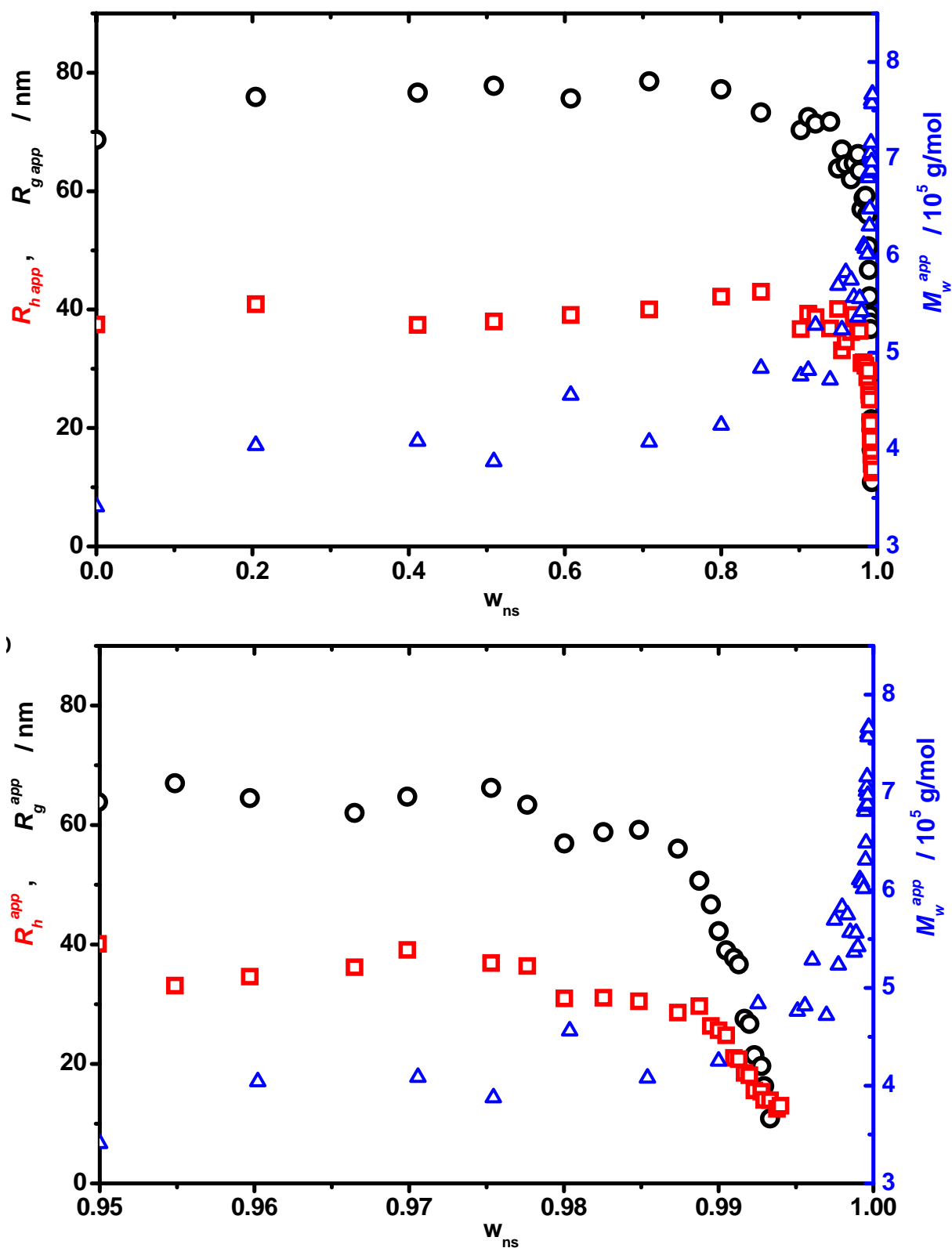
Figure 6.5 QPVP$_{4.3}$: (a) Apparent radius of gyration, $R_{g\,app}$, (circles, left axis), the apparent hydrodynamic radius $R_{h\,app}$, (squares, left axis) and the apparent molar mass, $M_{w\,app}$, (crosses, right axis) are plotted as functions of the weight fraction of non-solvent, w_{ns}. (b) Magnification of the collapse regime, same symbols as in (a)

6.2.2 QPVP$_{4.3}$ – Conductivity Data

Following the general conductivity theory based on non-equilibrium thermodynamics (chapter 3.2.4), and ignoring interionic friction effects, the electrolytic conductivity of a polyelectrolyte solution in the presence of added salt κ_{el} (in S/cm), is given by

$$\kappa_{el} = \kappa_{el\,s} + \kappa_{el\,p} = \kappa_{el\,s} + \gamma \left(\lambda_{br} + \lambda_p \right) C_p \qquad (6.6)$$

where $\kappa_{el\,s}$ represents the conductivity of the bare salt solution, $\kappa_{el\,p}$ the polyion contribution, λ_{br} and λ_p are the equivalent electrophoretic mobilities (in S cm^2/equiv) of the bromide ion and the polyion, respectively and C_p is the equivalent concentration of the polyelectrolyte (in equiv/L). The equivalent conductivity of a polyelectrolyte solution,

$$\Lambda_p = \left(\kappa_{el} - \kappa_{el\,s} \right) \big/ C_p \qquad (6.7)$$

may then be expressed as

$$\Lambda_p = \gamma \left(\lambda_{br} + \lambda_p \right) \qquad (6.8)$$

γ *effective degree of dissociation*

Figure 6.6 shows the raw conductivity of the polyion solutions with c_p = 6, 8, 10 and 12 mg/L, whereas each series includes the conductivity of the pure salt. The molar concentration of the salt is C_s = 10^{-5} mol/L and the polyion equivalent concentrations (= concentrations of chemical units) are respectively C_p = 2.4, 3.1, 3.9, and 4.7 * 10^{-6} mol/L. Therefore from Figure 6.6 it is obvious that the electrolytic conductivity per functional unit of the salt Λ_s is bigger than that for the polyion Λ_p. Counterion condensation must occur in different extents to explain the course of the conductivity data. Counterion condensation must occur even if $\lambda_p \approx 0$. However even in case of low functionalized polyions, experiments agree that λ_p features a notable contribution to polyelectrolyte conductivity [MacFarlane, Fuoss 1957; Katchalsky et al. 1966; Vink 1981].

Figure 6.7 shows the net conductivity of the polyion $\kappa_{el\,p}$ evaluated by subtracting the bare salt conductivity $\kappa_{el\,s}$ from the gross conductivity κ_{el}. $\kappa_{el\,s}$ is an average from separated measurements containing only the salt. As expected the highest polyelectrolyte concentration (12 mg/L) exhibits the highest conductivity for all w$_{ns}$ values. A sharp decrease from w$_{ns}$ = 0.9 on hints the onset of strong counterion binding due to hydrophobic effects. This decrease reflects the continuous structural collapse as monitored by light scattering (Figure 6.5 b). One may already conclude that both are mutually dependent. Another feature of Figure 6.7 is the increase of the electrolytic conductivity from w$_{ns}$ = 0 to w$_{ns}$ ≈ 0.9 for each concentration series. This clearly reflects the run of the viscosity which is high for 1-propanol and low for 2-pentanone (Figure 5.11).

a

b
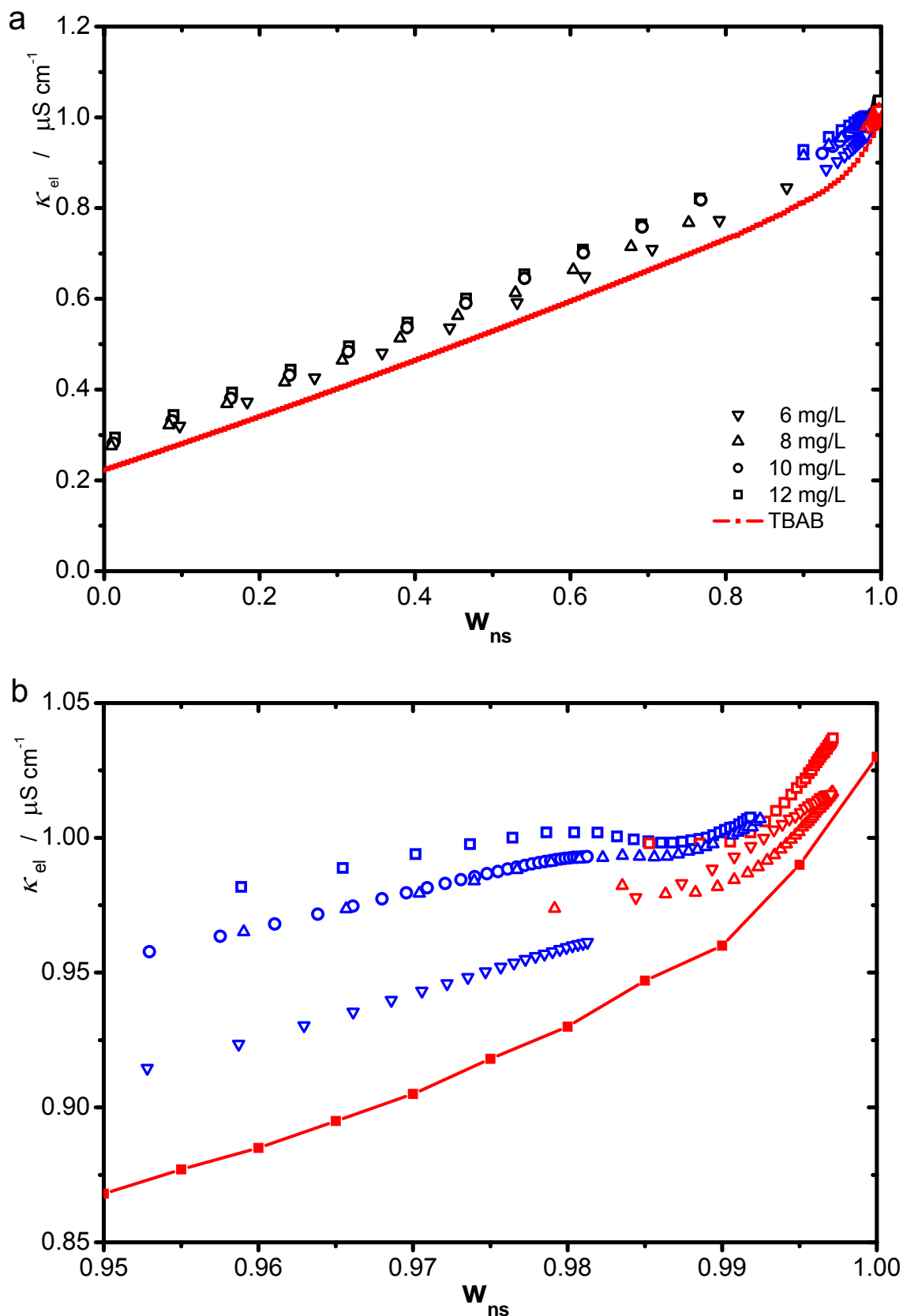
Figure 6.6 QPVP$_{4.3}$: (a) Raw conductivity data of QPVP$_{4.3}$; bare salt solution (average of many series; red curve) and of the polyelectrolyte solution for different concentrations. The different colors indicate different dilution series. (b) Magnification, symbols as in (a)
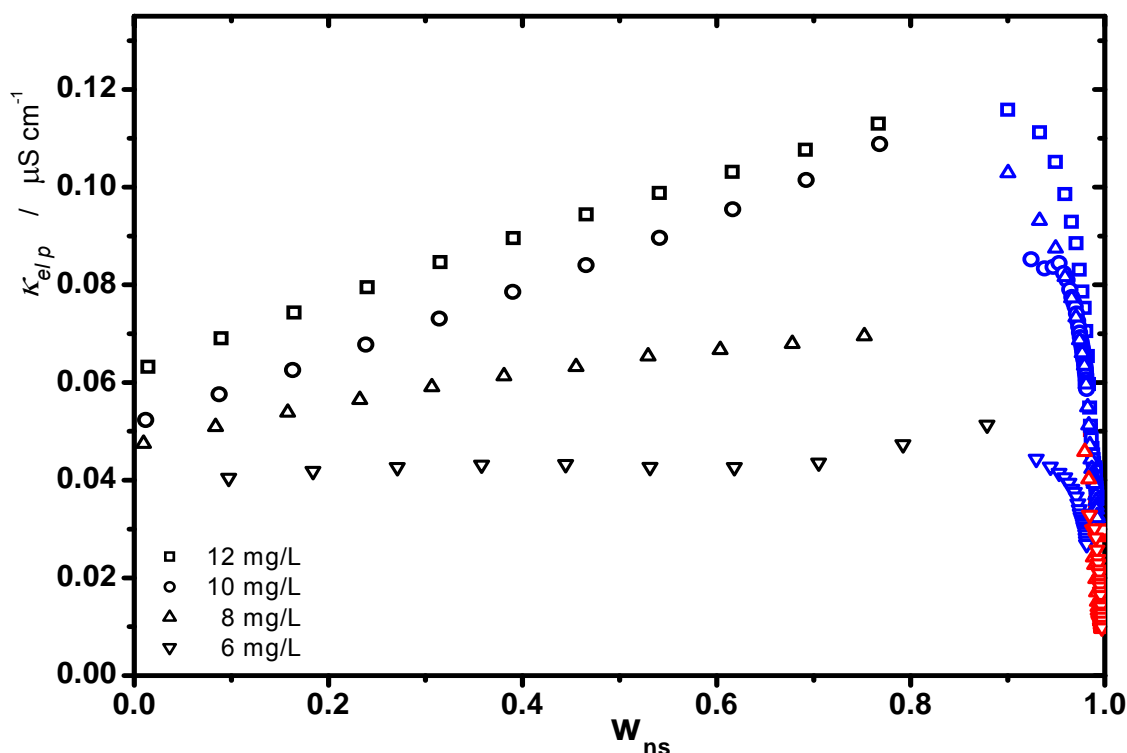
Figure 6.7 QPVP$_{4.3}$: Net conductivity: from each gross data point (Figure 6.6) the "salt-baseline" was subtracted, symbols as in Figure 6.6; The different colors indicate different dilution series.

To account for the change of viscosity according to eq. 3.7 and 3.8 as a first approximation multiplying the conductivity respectively the equivalent conductivity by the viscosity yields a normalized quantity. The equivalent conductivity corrected by the solvent viscosity $\Lambda\eta_0$, the so-called Walden product, is shown for the bare salt solution and for the polyion solutions in Fig. 6.8. For the bare salt solution the Walden product is expected to be independent of solvent composition; however, the $\Lambda\eta_0$ values for the TBAB depend on w_{ns} as shown by the red curve in Fig. 6.8 in qualitative agreement with literature data [Fennell Evans et al. 1968+1971; de Lisi, Gofredi 1973; Hughes 1967, Huie 2003]. Specific ion solvation effects, microviscosity and liquid dynamics were postulated to cause the non-ideal behavior of the conductivity data. For TBAB in mixtures of 1-propanol (forming hydrogen bonds) and acetone (solvating cations strongly) it was concluded [Fennell Evans et al. 1971] that preferential solvation of both the tetrabutylammonium-cation as well as the bromide cause the peculiar dependence of the Walden product on solvent composition.

Compared to the TBAB, the Walden products of the polyion solutions decrease in a similar fashion with increasing pentanone content but a bit more pronounced in the regime $0 < w_{ns} < 0.7$. However, for $w_{ns} > 0.9$ the Walden products of the polyion strongly decrease to very small values whereas the bare salt mobility even increases. The Walden product as a function of solvent composition is qualitatively similar to measurements of QPVP in mixtures of methanol/2-butanone [MacFarlane, Fuoss 1957] and of poly(methacryloylethyl trimethylammonium methylsulfate) in mixtures of water/acetone [Aseyev et al. 1998]. Obviously this strong decrease cannot be explained by subtle ion solvation effects as discussed above but rather reflects the association or binding of counter ions onto the polyion chain. It should be noted that the concentration dependence of the Walden product is very small which indicates that for the concentration regime of $6 < c_p < 12$ mg/L the conductivity of the solvent is not significantly influenced by the polyions and that interionic dynamic coupling

effects are small. (However the other samples exhibit a noticeable increase of the Walden product from 6 to 12 mg/L which will be discussed in the according chapters). Approaching the phase transition the polyion chain starts to collect and bind its counter-ions as the chain dimensions become successively smaller. Eventually, the collapsed polyion chain preserves a few charges only, most probably some surface charges known from colloids. This experimental observation is in remarkable qualitative agreement with the results of explicit solvent simulations [Reddy, Yethiraj 2006]. Interestingly, the polyion mobility is already significantly reduced well before the unperturbed θ-dimension is reached (see Figure 6.8 b). The obvious strong charge reduction in a regime where the Bjerrum length changes by 5% only, questions the applicability of the Manning condensation concept [Manning 1969+1981] to flexible polyelectrolyte chains at least for poor solvent conditions.

a

b
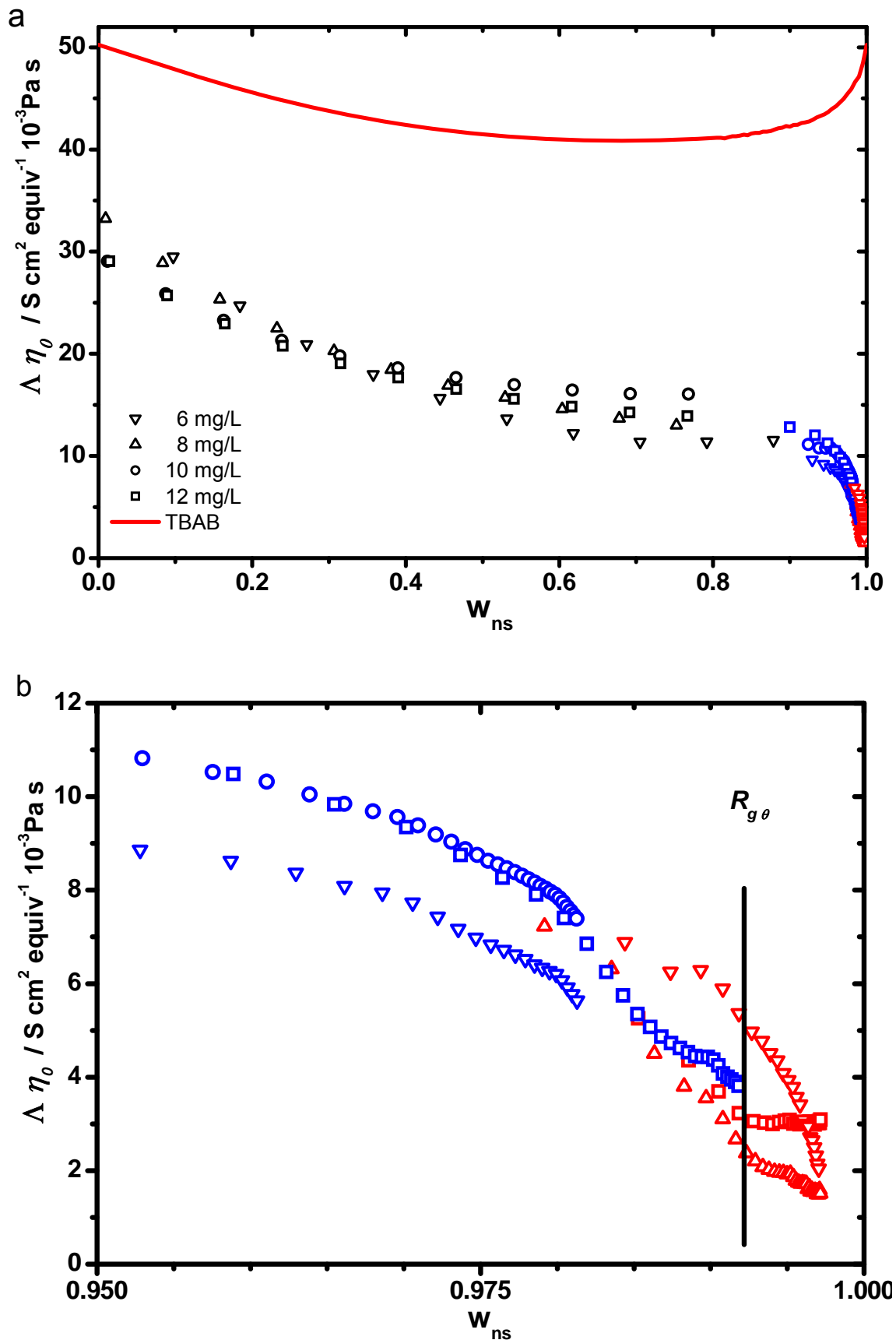
Figure 6.8 $QPVP_{4.3}$: (a) Walden product of the bare salt solution (curve) and of the polyelectrolyte solution for different concentrations; (b) Magnification; the vertical line indicates the non-solvent fraction for which θ-dimensions ($R_{g\,app}$ = 29nm) are reached for the uncharged PVP (see Figure 6.5), symbols as in (a).

6.3 Collapse of QPVP$_{20}$

In the following it is presumed that enthalpic monomer-solvent interactions are unchanged compared to the uncharged polymer. Enthalpic monomer-solvent interactions of the quaternization agent ethyl bromide are neglected and classification into poor-, θ-, and good-solvent condition is adopted from PVP$_{851}$. Whereas QPVP$_{4.3}$ has a Manning parameter of ξ_M = 0.6 ($\xi_M = l_B$ / c with l_B the Bjerrum length and c the mean contour distance between two charges), QPVP$_{20}$ features ξ_M = 2.8 (compare Figure 5.9). Therefore QPVP$_{20}$ is expected to exhibit counterion condensation even in the good solvent regime. However although bearing more chemical charges, QPVP$_{20}$ precipitates at lower fraction of non-solvent compared to QPVP$_{4.3}$ (from w$_{ns}$ = 0.995 to w$_{ns}$ = 0.93). The major part of the QPVP$_{20}$-collapse still proceeds in the bad solvent regime (θ-conditions at w$_{ns}$ = 0.91). QPVP$_{35}$ (next chapter) follows the trend towards lower w$_{ns}$ and a collapse well in the good solvent regime occurs (w$_{ns}$ = 0.87, see next chapter). This behavior can be ascribed to interactions among condensed ion-pairs. The concomitant free energy contribution (F_6 as captured by eq. 2.73) is short-ranged and attractive [Muthukumar 2004]. Phase separation in the good solvent regime due to ion-pair formation is incorporated in polyelectrolyte collapse theories only recently [Kramarenko, Erukhimovich, Khokhlov 2002]. Dobrynin's pearl-necklace scaling arguments now capture phase separation proceeding in the good solvent regime as well, which he demonstrated by MD-simulations, too [Jeon, Dobrynin 2007] (compare chapter 2.6.1).

6.3.1 QPVP$_{20}$ – Light Scattering Data

QPVP$_{20}$ was measured at different polyion concentrations c_p: 6, 8, 10, 12 mg/L at C_s = 10^{-5} mol/L and an additional series with c_p = 8 mg/L at C_s = 4*10^{-5} mol/L. Basically the run of $R_{g\,app}$, $R_{h\,app}$ and $M_{w\,app}$ are comparable to the data of QPVP$_{4.3}$. At equal salt concentration the apparent molar masses are even lower than those of QPVP$_{4.3}$ although the true molar mass of QPVP$_{20}$ is higher than that of QPVP$_{4.3}$ (1.03 * 10^6 g/mol compared to 8.9 * 10^5 g/mol). An increased number of dissociated counterions would increase the inter-polyelectrolyte repulsion due to charging of the backbone. This charging should lead to an increased exclusion zone around the coils as depicted in Figure 6.9, left. However the interaction energy obviously is not strong enough to structure the polyions into an ordered lattice (compare chapter 2.2.1). For example using the evaluated radii of gyration in pure propanol ($\approx$ 80 nm) and the distance of the centers of mass ($\approx$ 350 nm), a signature of the lattice ordering length scale would appear at small q-values as an overlay to the steadily decreasing particle form factor (see Figure 4.6 b and 6.9, right). A detailed study on the mutually influence of particle form factor and structure factor in static light scattering was carried out by Gröhn [Gröhn, Antonietti 2000]. Figure 6.9 right shows the influence of salt concentration on the ordering. By increasing the salt concentration C_s, the C_p/C_s-ratio is lowered. Below a certain value the lattice structure is lost and a continuously decreasing particle form factor dominates the scattering. However the slope of $P(q)$ is still influenced below this threshold due to a big exclusion zone. The influence on the evaluation of R_g will be discussed in detail in chapter 6.8. However, qualitatively it shall be used to explain the apparent increase of $R_{g\,app}$ and $R_{h\,app}$ from w$_{ns}$ = 0 to w$_{ns}$ = 0.7 that can be seen for all concentrations at C_s = 10^{-5} mol/L. Obviously this increase does not occur in case of C_s = 4*10^{-5} mol/L, for which the exclusion zones are way smaller due to screening as can be deduced by the much higher apparent molecular weight (Figure 6.12). Therefore one may conclude that screening of the inter particle potential increases the evaluated $R_{g\,app}$ although an increase of the salt concentration leads to a

contraction of the polyion as found by essentially all experiments and theories so far [Förster, Schmidt 1995; Beer, Schmidt, Muthukumar 1997].
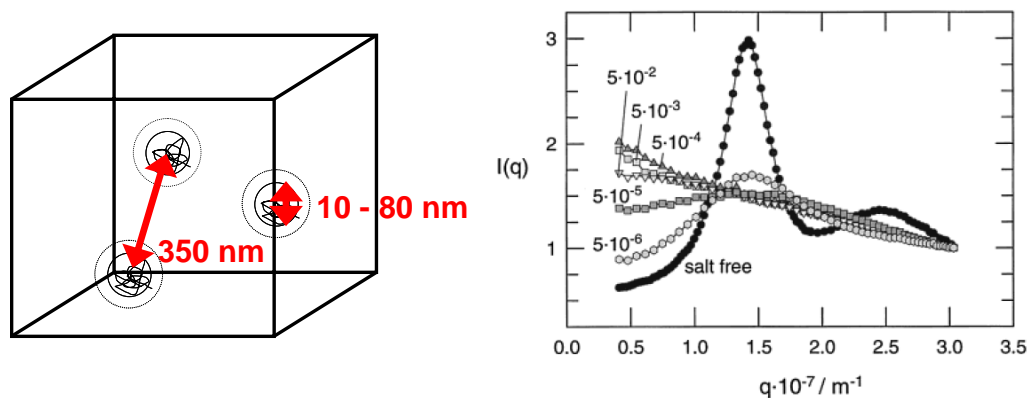

Figure 6.9 Left: The occupied space of the polyions is very small, using 12 mg/L and R_g = 10-80 nm it ranges from 0.0025 to about 2%. Right: [Gröhn, Antonietti 2000] scattering intensity for polyelectrolyte microgels: R_h = 43.5 nm; c_p = 0.375 g/L at various salt concentration (in mol/L).
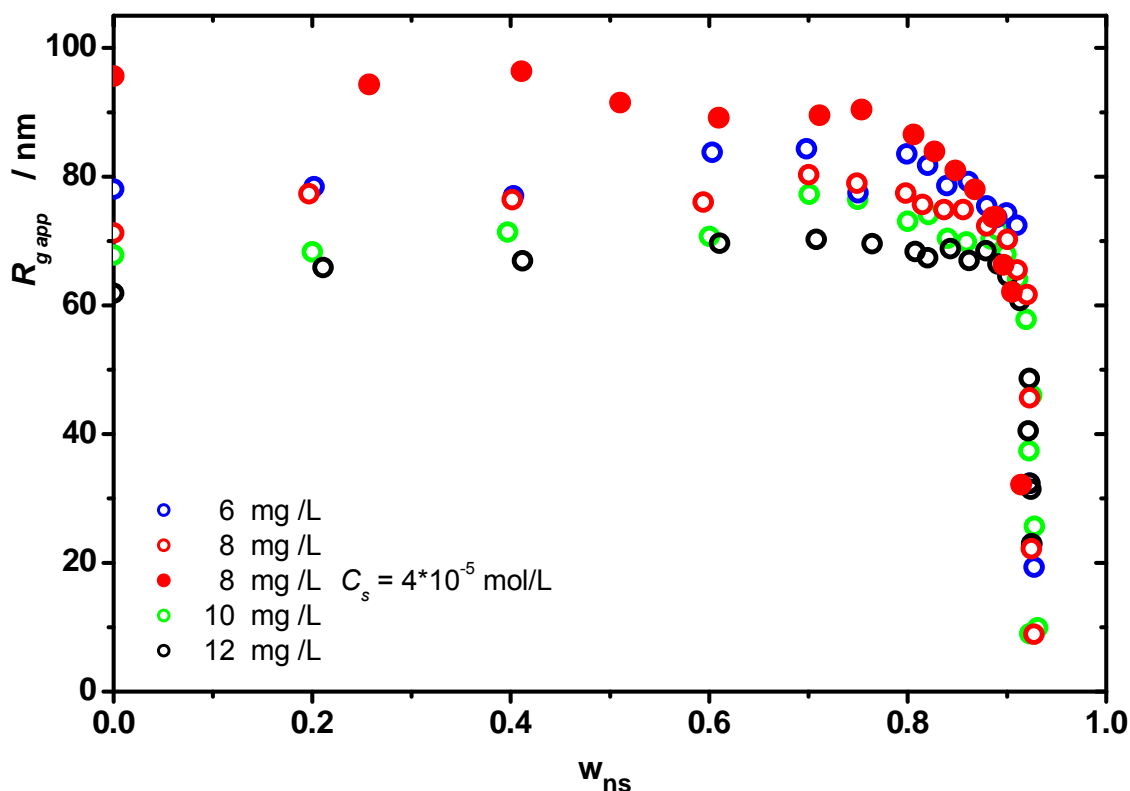
Figure 6.10 QPVP$_{20}$: Apparent radius of gyration, $R_{g\,app}$, is plotted as function of the weight fraction of non-solvent, w_{ns}.
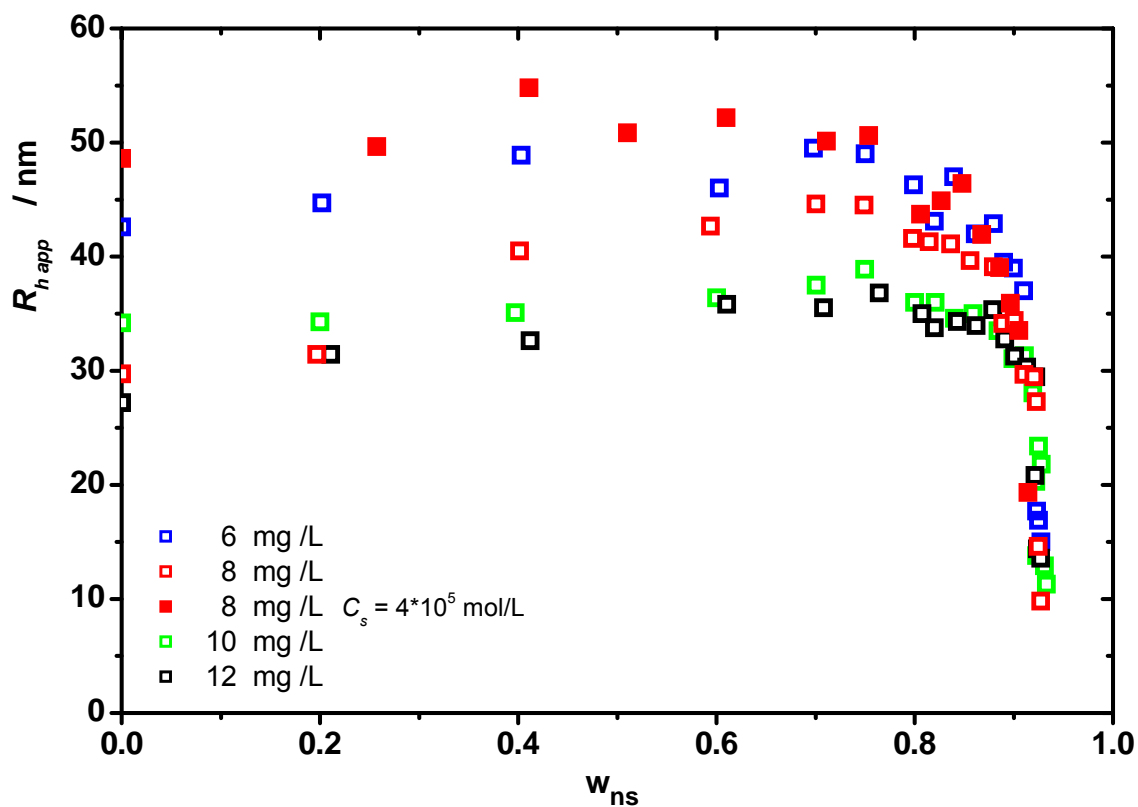
Figure 6.11 QPVP$_{20}$: Apparent hydrodynamic radius $R_{h\,app}$, is plotted as function of the weight fraction of non-solvent, w_{ns}.
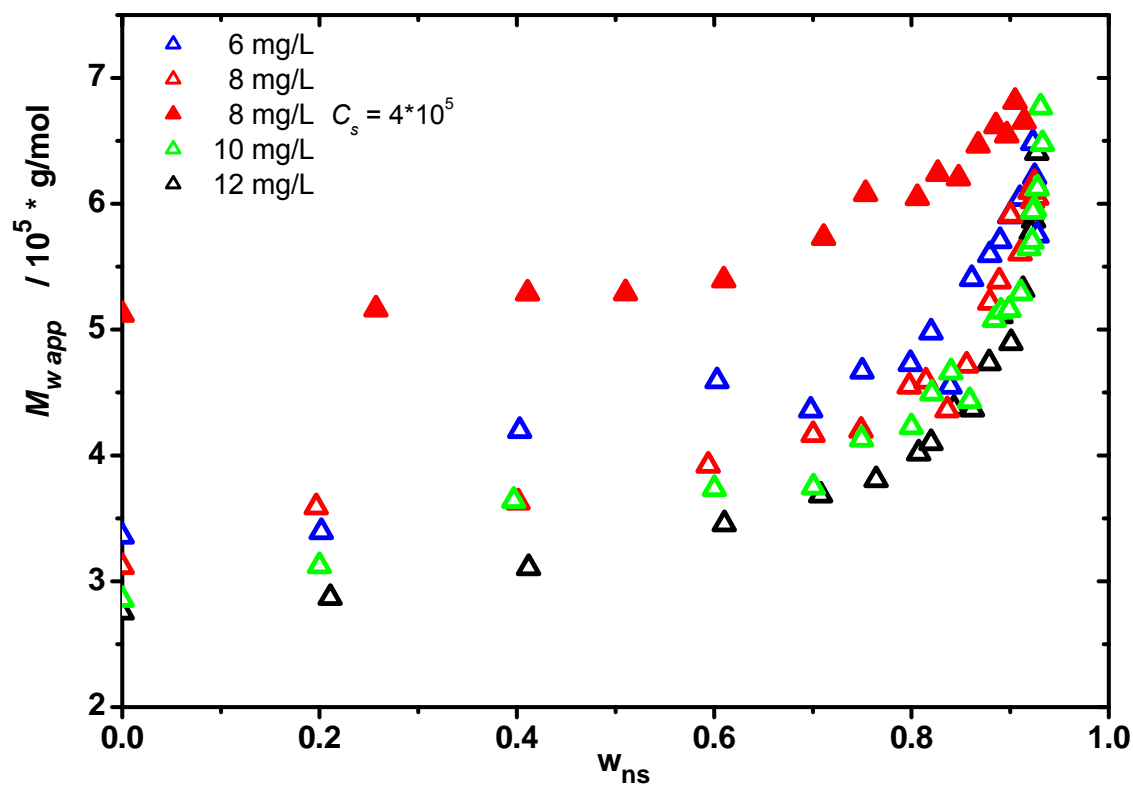
Figure 6.12 QPVP$_{20}$: Apparent molar mass, $M_{w\,app}$, is plotted as function of the weight fraction of non-solvent, w_{ns}.

6.3.2 QPVP$_{20}$ – Conductivity Data

Figure 6.13 shows the raw conductivity of the polyion solutions with c_p = 6, 8, 10 and 12 mg/L at C_s = 10^{-5} mol/L. The molar polyion equivalent concentrations are respectively C_p = 0.9, 1.3, 1.6 and 1.9 * 10^{-5} mol/L. Whereas the Walden product of QPVP$_{4.3}$ at w_{ns} = 0 and c_p = 6 mg/L is about 30 S cm^2 equiv^{-1} 10^{-3} Pa s the value of QPVP$_{20}$ is about 6 S cm^2 equiv^{-1} 10^{-3} Pa s. Therefore the effective degree of dissociation for QPVP$_{20}$is reduced. The ratio of the two degrees of quaternization is equal to the inverse of the ratio of their Walden products (4.3/20 ≈ 6/30). One might argue that QPVP$_{4.3}$ must exhibit some degree of counterion condensation, too, or at least is close to the onset of condensation, whereas condensation not necessarily means an immobilization of the counterions as originally conceived by Manning [Manning 1969]. More recent theories allow condensed counterions a certain degree of mobility [Muthukumar 2004; Vink 1990], which could be verified in experiment [Vink 1994].

The Walden product seems to increase from low to high concentration, which is the 'wrong direction' according to the Debye Hückel Onsager theory (chapter 3.2). However this feature is consistent with the systematic conductivity measurements of Vink on highly diluted polyelectrolyte solutions [Vink 1981] and will be discussed in the next chapter. The proceeding of the collapse is in agreement with the LS-data (w_{ns} = 0.93), however some conductivity seems to remain even in the collapsed state, whereas LS shows huge aggregates in this regime (that can be seen even by eye if the cuvette is inserted into the laser beam). This remaining conductivity per functional unit seems to increase with increasing concentration as indicated by the Walden product. One interpretation might be that in case of higher concentrations no single chain collapse is observed but that at a late stage of the collapse, entangled and crumpled structures might prevent a complete folding to a dense sphere, maybe in addition trapping salt ions. However LS-data does not indicate such kind of process. One may assume residual impurities from synthesis of QPVP$_{20}$ to be responsible for the remaining conductivity. If impurities lead to the final conductivity, the Walden product should exhibit equal values for all concentration series as it is divided by concentration (including the impurities). However an increase of conductivity with c_p can be observed for the Walden product as well.
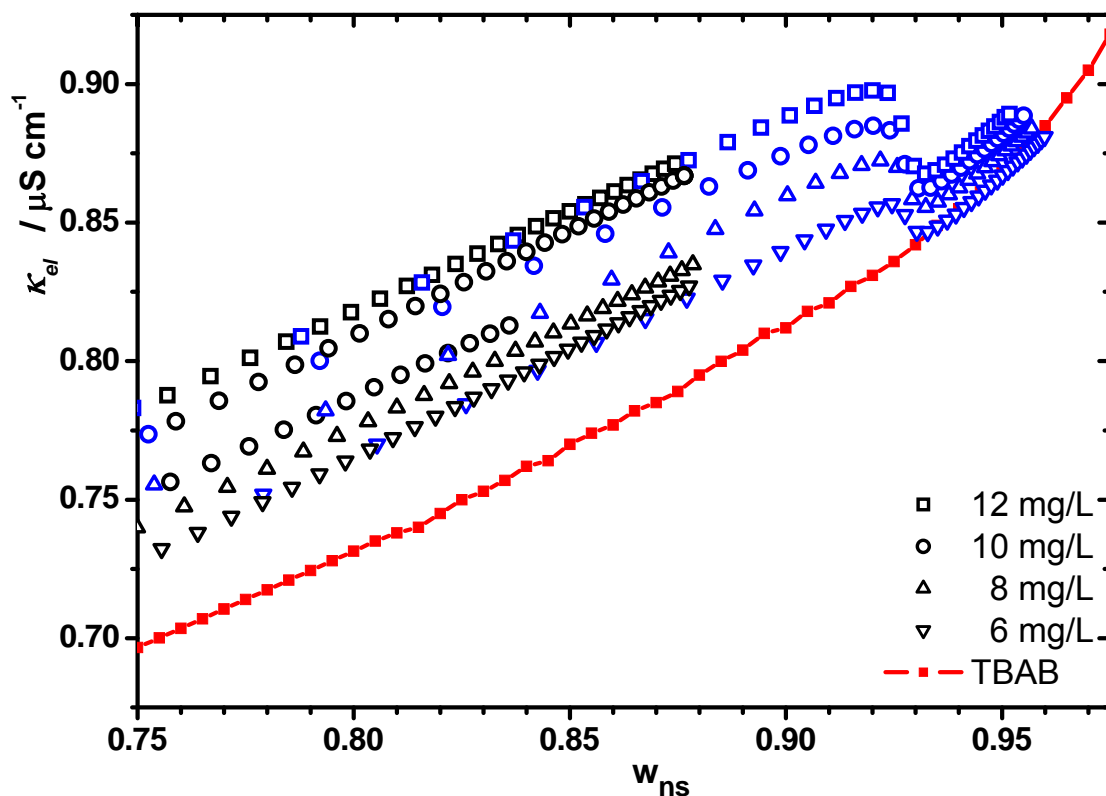
Figure 6.13 Raw conductivity data of QPVP$_{20}$ in the collapse regime. The bare salt solution is an average of many series and shown as a red curve. The different colors indicate separate series.
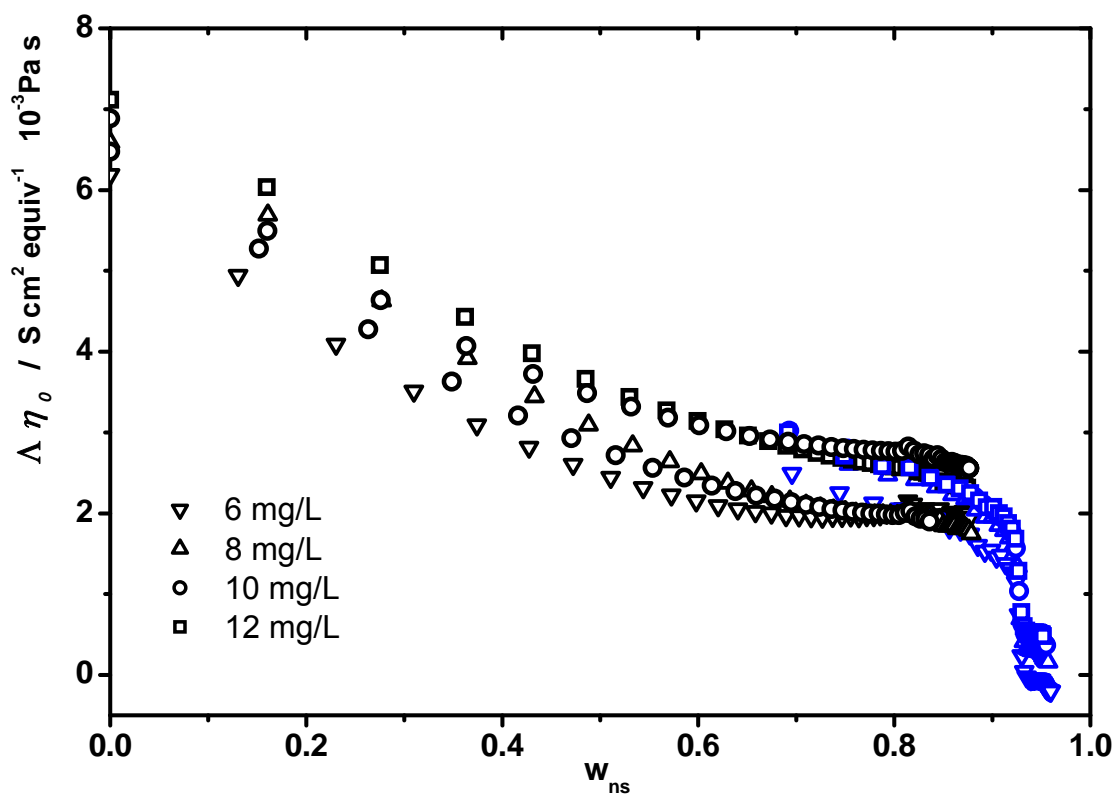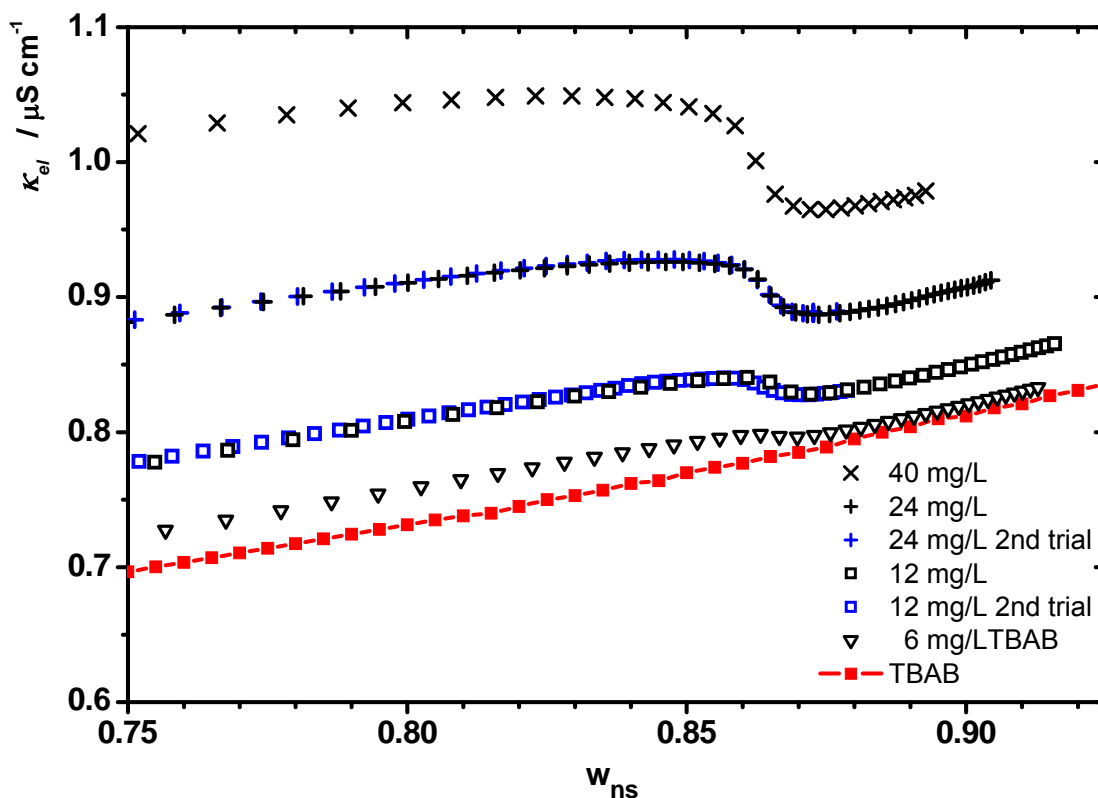

Figure 6.14 Walden product of QPVP$_{20}$, for different concentrations. The different colors indicate different dilution series.

6.4   Collapse of QPVP$_{35}$

In comparison to QPVP$_{20}$ the collapse is shifted to lower w$_{ns}$ fractions. The Manning parameter is ξ_M = 4.9, therefore QPVP$_{35}$ is expected to exhibit strong counterion condensation even in the good solvent regime. The final collapse is shifted further to a lower w$_{ns}$ value, well into the good solvent regime.

6.4.1 QPVP$_{35}$ – Light Scattering Data

The Rayleigh ratio of a test sample with c_p = 12 mg/L in pure 1-propanol showed oscillations, apparently due to a structure factor, therefore light scattering was conducted at 6 mg/L. Compared to QPVP$_{4.3}$ and QPVP$_{20}$ the QPVP$_{35}$-sample confirms the observed trend of a decreasing $R_{g\,app}$ as well as $R_{h\,app}$ with increasing degree of quaternization at equal w$_{ns}$ in the good solvent regime. $M_{w\,true}$ is now even higher: 1.16*10^6 g/mol whereas $M_{w\,app}$ still starts at very low values, however a distinction between QPVP$_{20}$ and QPVP$_{35}$ can not be made due to too poor data at c_p = 6 mg/L.
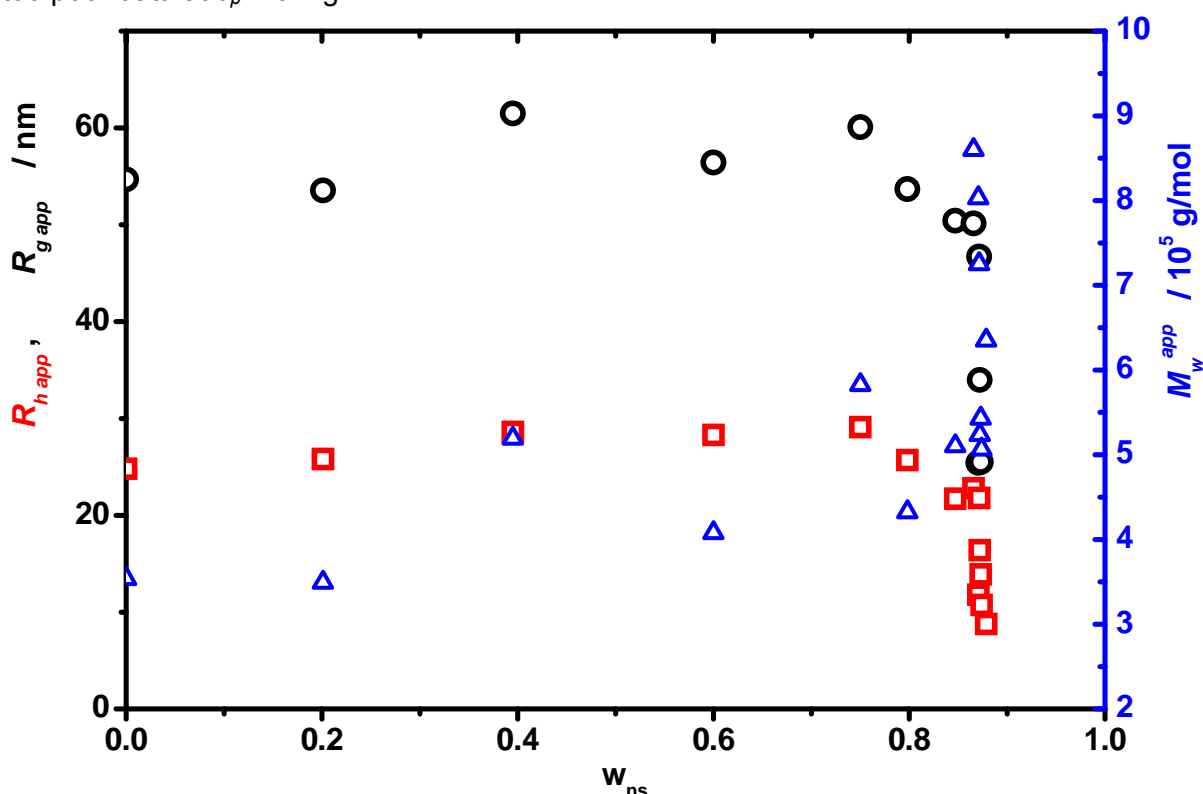
Figure 6.15 QPVP$_{35}$: Apparent radius of gyration, $R_{g\,app}$, (circles, left axis), the apparent hydrodynamic radius $R_{h\,app}$, (squares, left axis) and the apparent molar mass, $M_{w\,app}$, (crosses, right axis) are plotted as function of the weight fraction of non-solvent, w$_{ns}$.

6.4.2 QPVP$_{35}$ – Conductivity Data

The equivalent conductivity respectively the Walden product for the QPVP$_{35}$ is further reduced to about 4 'units' at w$_{ns}$ = 0; c_p = 6 mg/L. This value is higher than expected assuming linearity compared to QPVP$_{20}$, i. e. all new introduced functional units only bear condensed ions. (The ratio of the two degrees of quaternization is 35/20 therefore 35/20 * 4 'units' = 7 'units' may be expected for QPVP$_{20}$, however only 6 'units' were measured). Therefore one may deduce the absolute number of dissociated counterions per chain to have further increased in comparison

to QPVP$_{4.3}$ and QPVP$_{20.}$ Unfortunately the scattering of $M_{w\,app}$ is too big to yield an additional indication. The conductivity measurements were conducted in a higher concentration regime: 6, 12, 24 and 40 mg/L. The molar polyion equivalent concentrations are respectively C_p = 1.5, 3.0, 5.9 and 9.8 * 10^{-5} mol/L. The Walden products exhibit an increase from 6 to 24 mg/L at fixed w$_{ns}$ – value. The increase seems to level off for 40 mg/L. Vink who devoted his scientific career to polyelectrolyte conductivity, with extensive experimental work as well as applied theoretical approaches, measured the conductance of highly diluted polyelectrolyte samples in water [Vink 1981]. Figure 6.16 shows the equivalent conductivity of a highly diluted polyion (carboxy-methylated hydroxyethyl cellulose having a degree of substitution of sodium of 32%, degree of polymerization = 1900) without screening salt against the equivalent concentration C_p. Starting from C_p = 0, the first increase is counterintuitive whereas the subsequent continuous decrease is covered qualitatively by the Debye Hückel Onsager theory. Vink explained this behavior with the specific nature of water, i. e. he imagined a partial exchange of H$^+$ and Na$^+$ to be responsible. The 'starting' increase, according to Figure 6.16, is in the concentration regime of about 5*10^{-6} mol/L to 1*10^{-4} mol/L. This is in line with the concentration regime used in this dissertation, where polyions show an increase in equivalent conductivity, too (chapter 6.2 - 6.6). Wandrey conducted a detailed study on two polyelectrolytes in water (cationic and anionic) featuring various molar masses, C_p spanning over 5 decades with and without added low molecular salt [Wandrey 1999]. All measurement series showed the decrease of Λ in the same highly diluted regime. Wandrey explained the decrease with 'impurities of water and its starting self-dissociation'. However this dissertation used organic solvents of highest purity that were even further dried and redistilled and handled in a glove box, rendering the two explanations to be not convincing. One can deduce the effect to be of general kind in polyelectrolyte conductivity. A final distinction whether this behavior is due to a real polyion-conformational change or just due to general equipment limits can not be made in the framework of this dissertation (compare chapter 7.4 for further investigation).
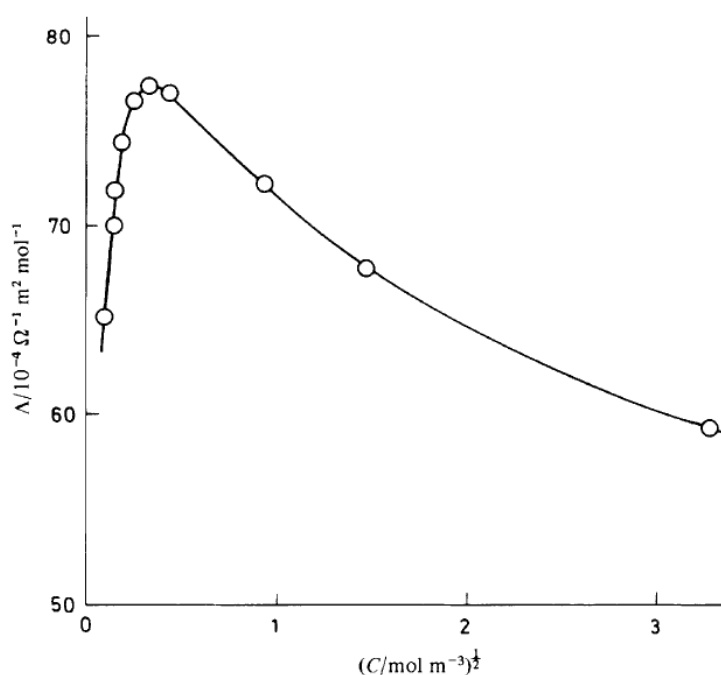
Figure 6.16 [Vink 1981] Equivalent conductivity of carboxy-methylated hydroxyethyl cellulose having a degree of substitution of sodium of 32% against the equivalent concentration C_p; without screening salt.

Figure 6.17 QPVP$_{35}$: Raw conductivity data of QPVP$_{35}$ in the collapse regime. The bare salt solution is an average of many series and shown as a red curve. The different colors indicate separate series.
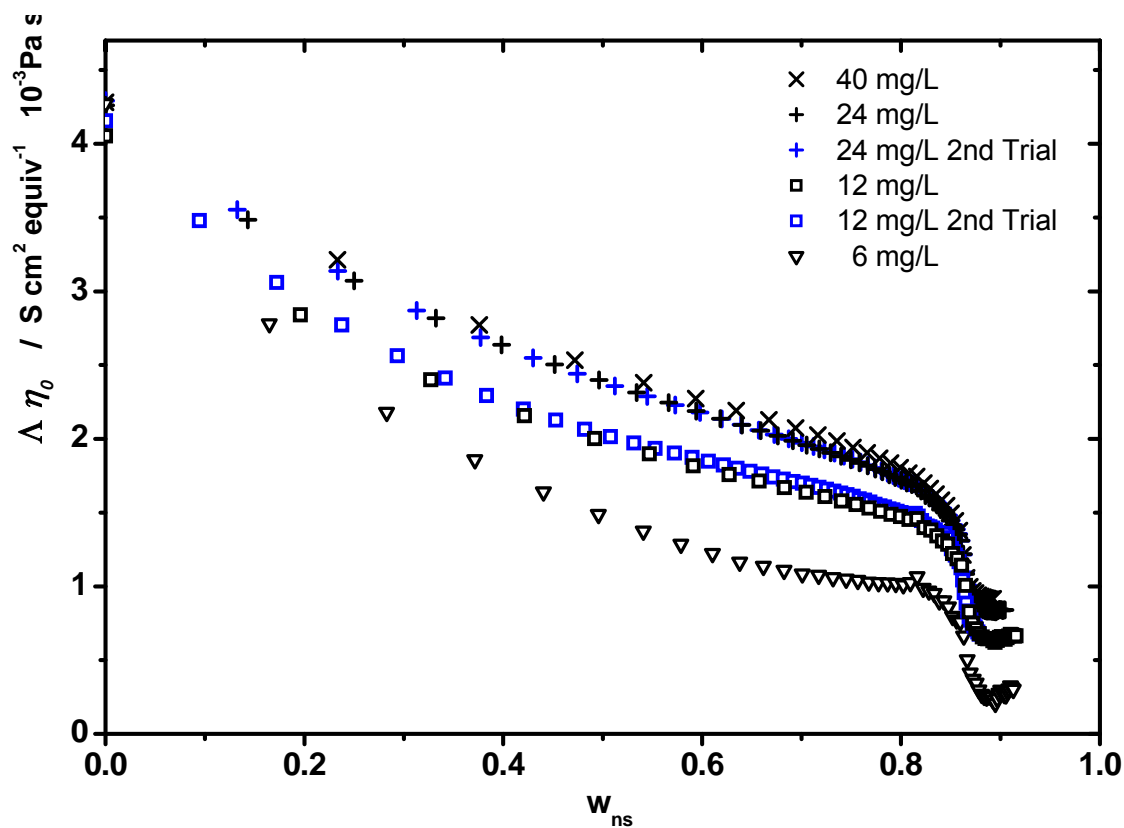

Figure 6.18 Walden product of QPVP$_{35}$, for different concentrations. The different colors indicate separate series.

6.5 Collapse of QPVP$_{2.4}$

QPVP$_{2.4}$ showed poor reproducibility in light scattering due to an aggregation tendency for $w_{ns} \geq 0.4$ (see Figure 6.20 and Appendix for more examples) in line with peculiar signatures in conductivity measurements. In contrast to the other samples, time dependent kinetics were involved as conductivity measurements suggest. Therefore data of QPVP$_{2.4}$ should be regarded as critical. The Manning parameter for QPVP$_{2.4}$ is very low: $\xi_M = 0.34$ and no counterion condensation is expected to occur at all. The concentration series investigated are 6 and 12 mg/L. In terms of equivalent concentration this is 1.3 and 2.7×10^{-6} mol/L.

6.5.1 QPVP$_{2.4}$ – Light Scattering Data

The QPVP$_{2.4}$ was monitored by light scattering at c_p = 6 mg/L. Big aggregates of various size and number were detected for $w_{ns} \geq 0.4$ as indicated by two diffusive decays in dynamic light scattering (Figure 6.20). The preparation technique was the same as for all samples in this dissertation (see chapter 5.7). The instable regime is indicated in Figure 6.19 by filled symbols. Light scattering data were acquired up to w_{ns} = 0.983. For evaluation of higher non solvent fractions a higher starting polyelectrolyte concentration in the cuvette would be necessary (see chapter 5.7), however those higher concentrations showed too many aggregates to be analyzed. Therefore the collapse could not be followed by light scattering. The apparent radii of gyration as well as the apparent hydrodynamic radii in the good solvent regime are almost equal or smaller than those of QPVP$_{4.3}$ data. The last three $R_{g\,app}$ may show the onset of the collapse. The evaluated molar mass is in the order of QPVP$_{4.3}$, however the low excess count rate at c_p = 6 mg/L makes the absolute scattering intensity scatter a lot.
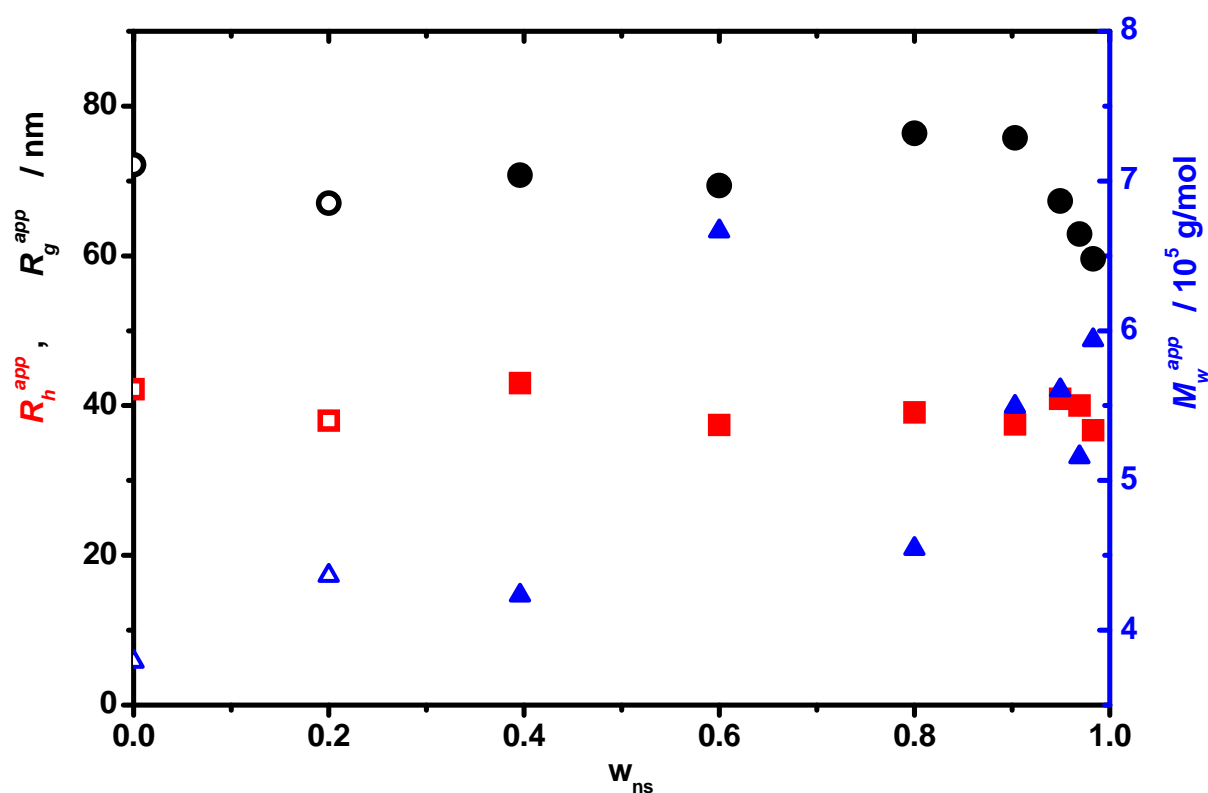

Figure 6.19 Apparent radius of gyration, $R_{g\,app}$, (circles, left axis), the apparent hydrodynamic radius $R_{h\,app}$, (squares, left axis) and the apparent molar mass, $M_{w\,app}$, (crosses, right axis) are plotted as functions of the weight fraction of non-solvent, w_{ns}. The instable regime is indicated by a change of the symbol used.
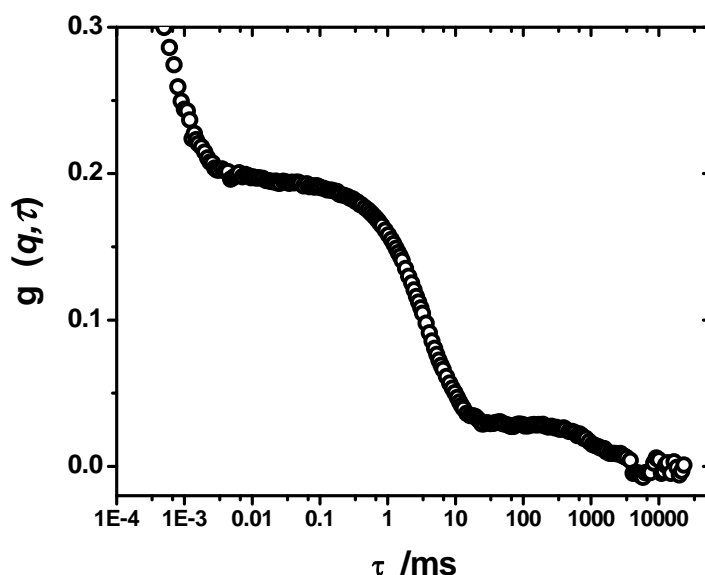
Figure 6.20 Dynamic light scattering on QPVP$_{2.4}$ at w$_{ns}$ = 0.95; correlation function measured at 17° scattering angle. The first decay corresponds to the solvent self-diffusion (see chapter 5.7.3), the second decay yields the diffusion coefficient of the polyelectrolyte whereas the third decay is the signature of aggregates. The average over all measured angles yields $R_h{}^{app}$ = 40.9 nm.

6.5.2 QPVP$_{2.4}$ – Conductivity Data

The conductivity data shows the final collapse to proceed at very high w$_{ns}$ values (w$_{ns}$ ≥ 0.996). The transition seems to be broader compared to the other samples discussed so far. This suggests kinetical processes like aggregation to be involved, obscuring single chain properties. Furthermore the Walden product highly depends on the starting w$_{ns}$ value of the series as well as the equilibration time, most likely due to time dependent aggregation kinetics as indicated by light scattering. Aggregates might be as well an explanation for the peculiar behavior of the 6 mg/L series that features a minimum at w$_{ns}$ ≈ 0.6. One should note that 6 mg/L of such a low charged polyion is very small compared to the experimental error of the salt-concentration (about 0.1%), the average of the salt-baseline as well as the error of the temperature (about ± 0.1°C). However as the excess conductivity for c_p = 6 mg/L still approaches zero one may assume to measure a signature of the polyion. The net conductivity for the last series exhibits even negative values (see Figure 6.21), this may be attributed to the non reproducibility of the salt concentration within the required accuracy. At least two observations that should not be biased by aggregates shall be emphasized: the Walden products in pure 1-propanol are reduced compared to QPVP$_{4.3}$ and within QPVP$_{2.4}$ higher polyion concentrations exhibit higher Walden products.
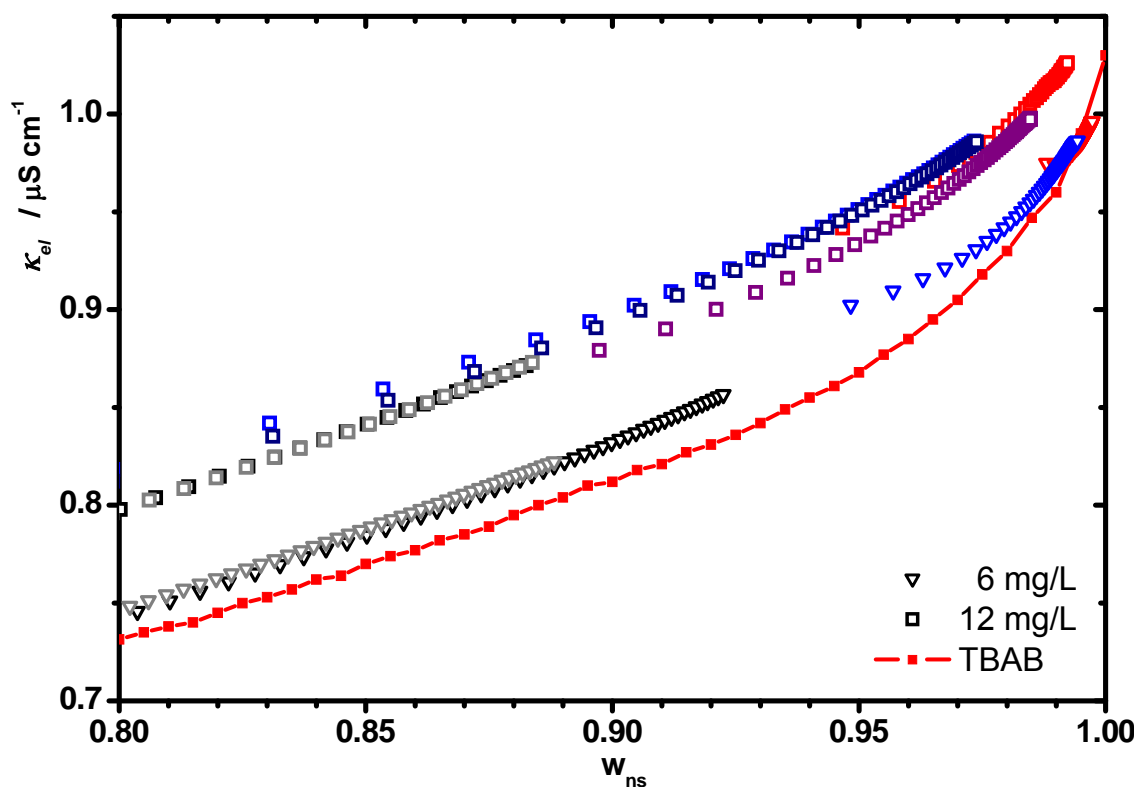
Figure 6.21 Raw conductivity data of QPVP$_{2.4}$ in the collapse regime. The different colors indicate separate series.
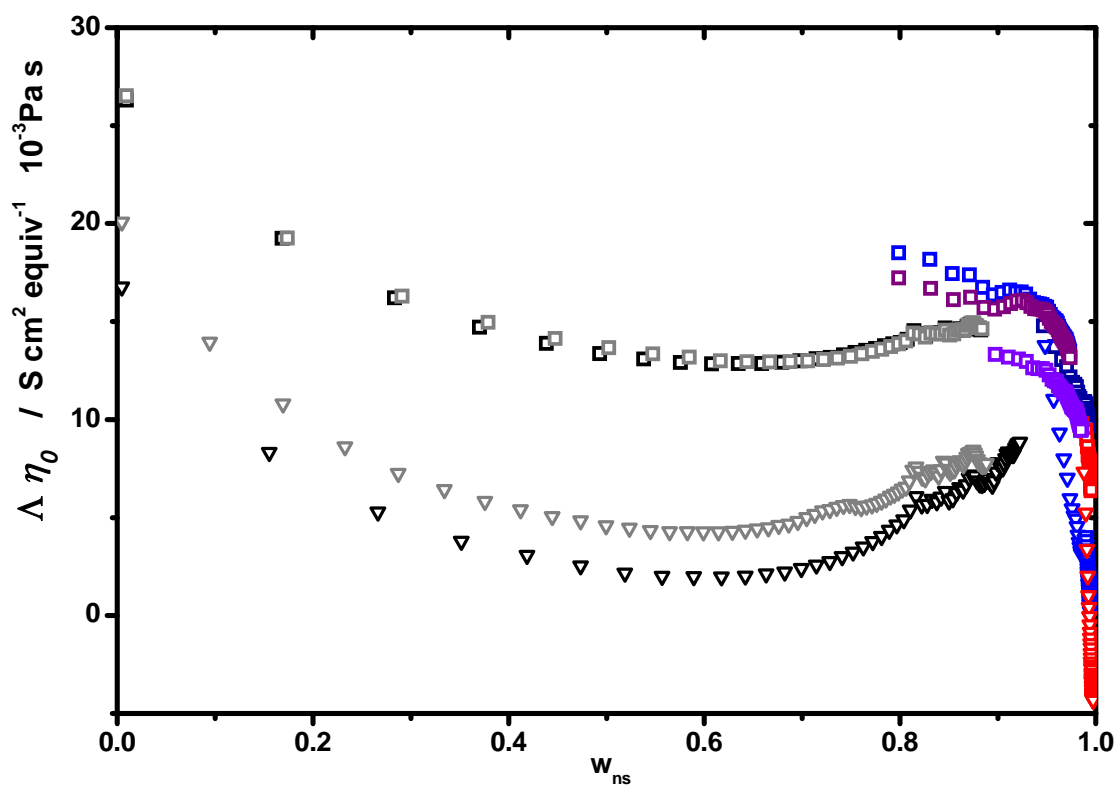

Figure 6.22 Walden product of QPVP$_{2.4}$ for different concentrations. The different colors indicate separate series.

6.6   Collapse of QPVP$_{1.2}$

QPVP$_{1.2}$ exhibited aggregates for $w_{ns} \geq 0.4$, too. However compared to QPVP$_{2.4}$ fewer aggregates were detected for QPVP$_{1.2}$ in general (see Figure 6.24 and Appendix for more examples). The Manning parameter of QPVP$_{1.2}$ is very low: $\xi_M = 0.17$ and no counterion condensation is expected to occur at all in the good solvent regime. The concentration series investigated are 6, 12 and 24 mg/L. In terms of equivalent concentration this is 0.7, 1.4 and $2.7 \cdot 10^{-6}$ mol/L. This sample is at least not stable for $w_{ns} \geq 0.4$. Light scattering shows aggregates for $w_{ns} \geq 0.4$, in line with peculiar signatures in conductivity measurements.

6.6.1 QPVP$_{1.2}$ – Light Scattering Data

The QPVP$_{1.2}$ was monitored by light scattering at $c_p = 6$ mg/L. Big aggregates of various size and number were revealed for $w_{ns} \geq 0.4$ by a biexponential decay in dynamic light scattering. The instable regime is indicated in Figure 6.23 by filled symbols. Light scattering data was acquired up to $w_{ns} = 0.97$. Higher non solvent fractions showed too many aggregates to be evaluated. Therefore the collapse could not be followed by light scattering. The apparent radii of gyration as well as the apparent hydrodynamic radii in the good solvent regime are smaller than those of QPVP$_{2.4}$. The last three $R_{g\,app}$ and $R_{h\,app}$ show the onset of the collapse in line with the conductivity data. The evaluated molar mass in the good solvent regime is the highest of all QPVP samples, which is in line with the low degree of quaternization and therefore low number of dissociated counter ions.
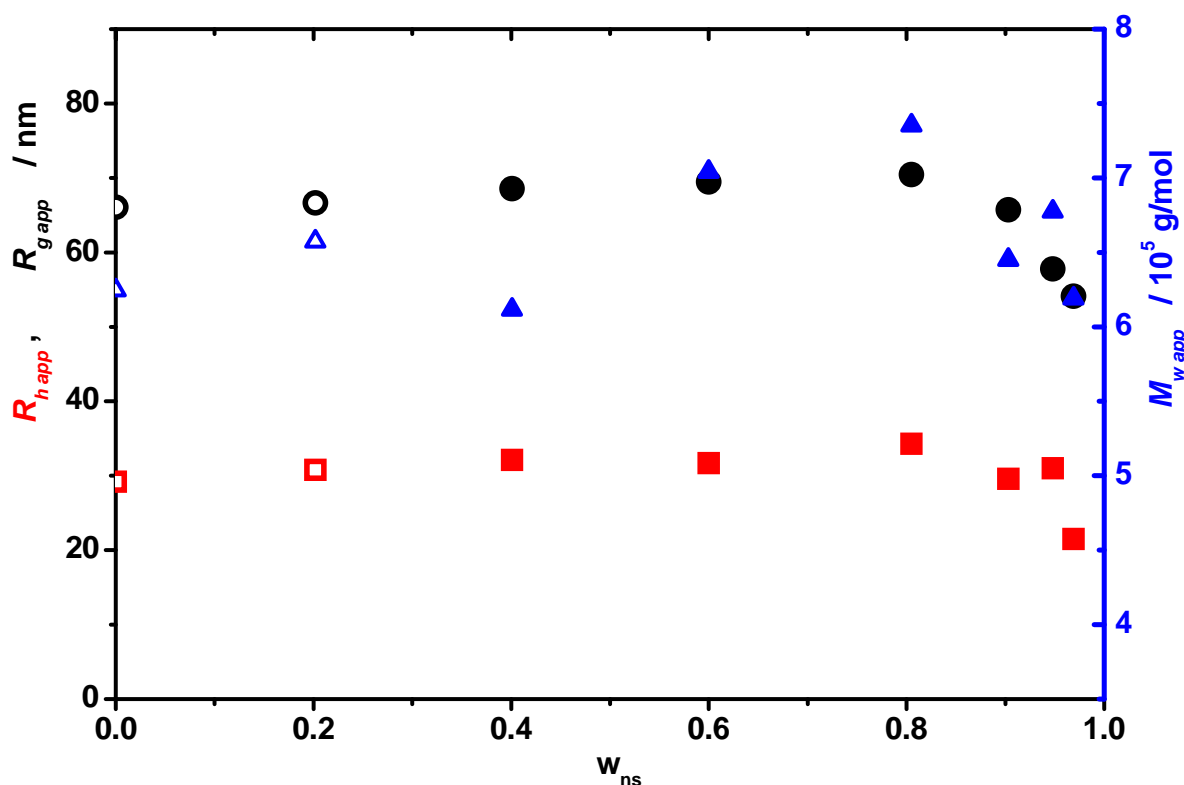

Figure 6.23 Apparent radius of gyration, $R_{g\,app}$, (circles, left axis), the apparent hydrodynamic radius $R_{h\,app}$, (squares, left axis) and the apparent molar mass, $M_{w\,app}$, (crosses, right axis) are plotted as functions of the weight fraction of non-solvent, w_{ns}. The instable regime is indicated by a change of the symbol.
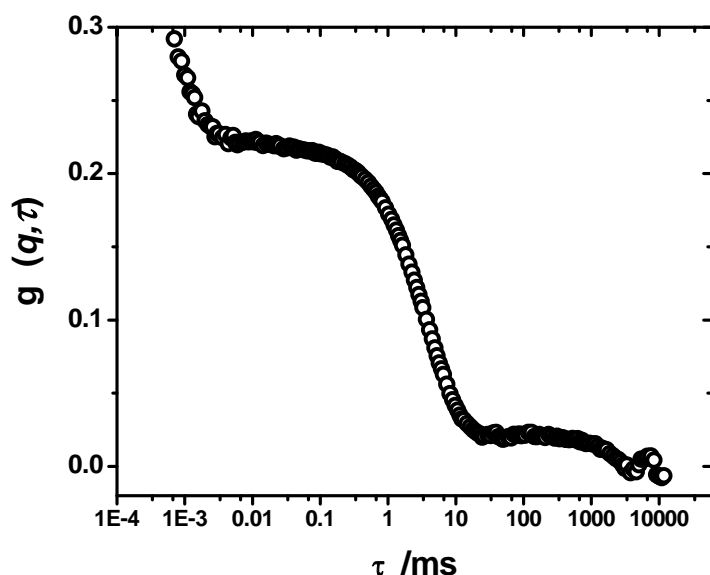
Figure 6.24 Dynamic light scattering on QPVP$_{1.2}$ at w$_{ns}$ = 0.95; correlation function measured at 17° scattering angle. The first decay corresponds to the solvent self-diffusion (see chapter 5.7.3), the second decay yields the diffusion coefficient of the polyelectrolyte whereas the third decay is the signature of aggregates. The average over all measured angles yields R_h^{app} = 30.8 nm.

6.6.2 QPVP$_{1.2}$ – Conductivity Data

The conductivity data shows the final collapse to proceed at very high w$_{ns}$ values (see Figure 6.26). The transition is quite broad. Aggregates might be an explanation for the peculiar behavior of the 6 mg/L series that features a minimum at w$_{ns}$ ≈ 0.6 which is even more pronounced compared to the QPVP$_{2.4}$ sample. One should note that 6 mg/L for such a low charged polyion is vanishing small compared to the experimental error of the salt-concentration (about ± 0.1%), the average of the salt-baseline as well as the error of the temperature (about ± 0.1°C) (see Figure 6.25). However as the excess conductivity for c_p = 6 mg/L still approaches zero one may assume to measure a signature of the polyion. If there's a trend from QPVP$_{4.3}$ over QPVP$_{2.4}$ to QPVP$_{1.2}$ the Walden product of QPVP$_{1.2}$ is supposed to be lower than that of QPVP$_{2.4}$ however it is very high and depends very much on the concentration.
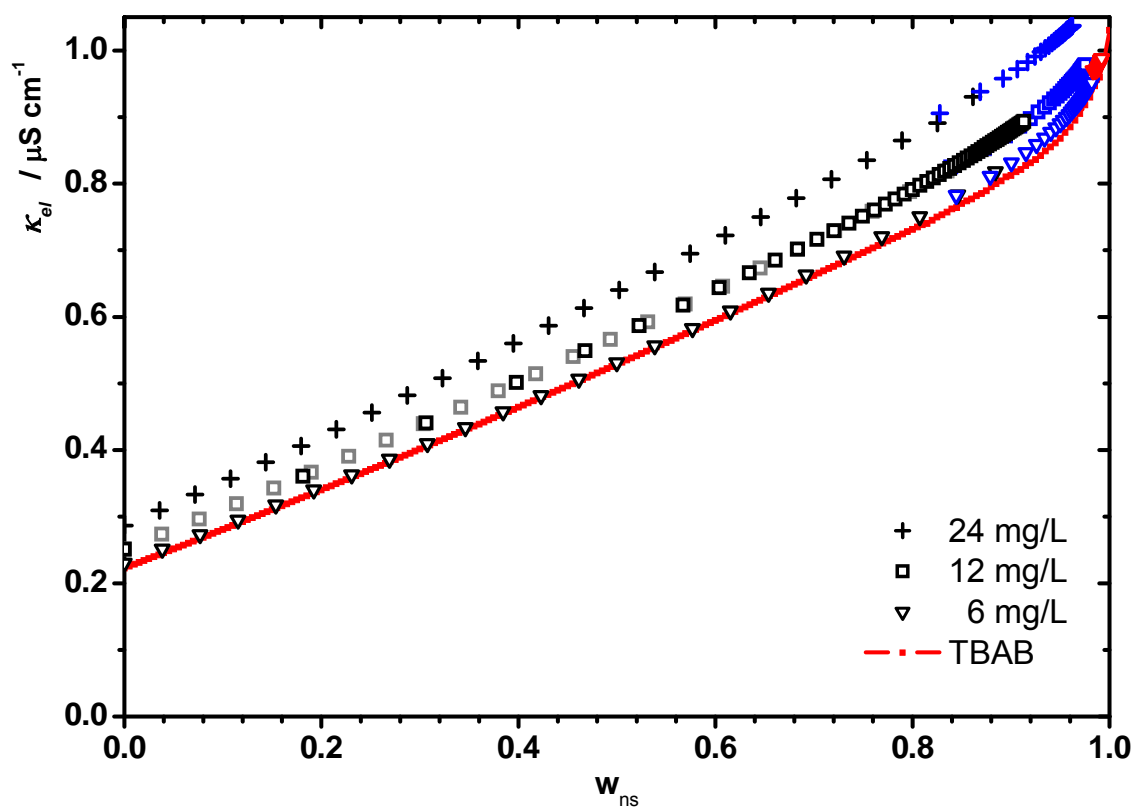
Figure 6.25 Raw conductivity data of QPVP$_{2.4}$ in the collapse regime. The different colors indicate separate series.
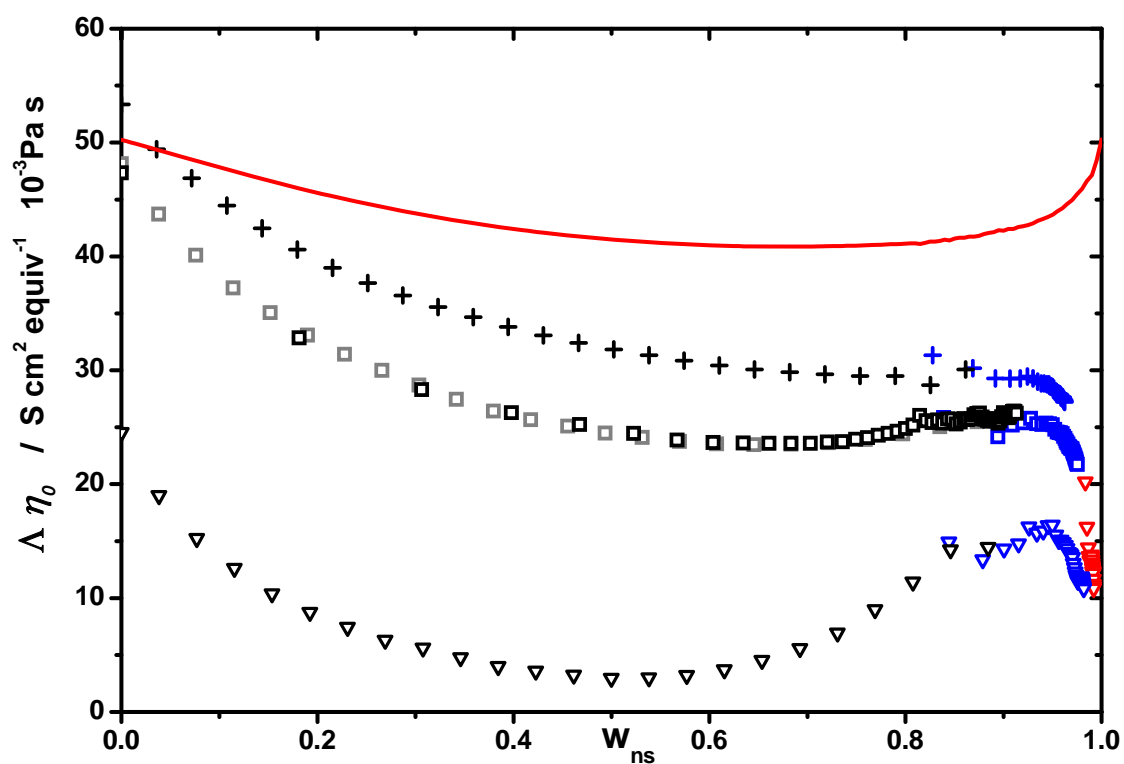
Figure 6.26 Walden product of QPVP$_{2.4}$; for different concentrations; The different colors indicate separate series.

7   Raw Light Scattering Data

Figures 7.2 and 7.3 show the apparent expansion coefficients $\alpha_g = R_{g\,app} / R_{g\,\theta}$ (respectively $R_g / R_{g\,\theta}$ in case of PVP$_{851}$) against the non-solvent fraction w$_{ns}$. Some trends can be explained by concepts of polyelectrolyte-theory (see chapter 2):

- With respect to the neutral polymer, introduction of chemical charges leads to an expansion of the coil.
- The precipitation point shifts to lower values of w$_{ns}$ from QPVP$_{4.3}$ over QPVP$_{20}$ to QPVP$_{35}$, which can be ascribed to increasing dipole-dipole attraction due to more condensed counterions (Figure 7.1). According to conductivity data QPVP$_{2.4}$ is in line with this trend and it exhibits the highest critical non-solvent fraction of all samples w$_{ns,\,c}$ $\approx$ 0.997. QPVP$_{1.2}$ shows a deviation from this trend (w$_{ns,\,c}$ $\approx$ 0.992), most likely due to the vanishing polyelectrolyte character. However reproducibility is low for QPVP$_{2.4}$ and QPVP$_{1.2}$ and aggregates may bias the two values.
- The lower the polyelectrolyte concentration of QPVP$_{20}$ at C_s = 10^{-5} mol/L, the bigger are the according apparent radii of gyration.

Some features are not in line with polyelectrolyte theories:

- QPVP$_{20}$ at c_p = 8 mg/L has been measured at C_s = 10^{-5} mol/L as well as C_s = 4*10^{-5} mol/L yielding a Debye length of about 40 respectively 20 nm (see Figure 5.10). The series with higher salt content exhibits the bigger $R_{g\,app}$ (see Figure 6.10). This is in disagreement with all polyelectrolyte concepts.
- Higher degrees of quaternization are expected to expand the coil. This is even true if the number of dissociated ions would be limited due to kind of Manning threshold. Although weaker than Coulombic repulsion the many condensed counterions increase the osmotic pressure in the vicinity of the polyion and thereby swell it. This was first described by Oosawa [Oosawa 1971], captured in equations 2.66, 2.67 and is the basis for polyelectrolyte swelling in reference [Vasilevskaya, Khokhlov, Yoshikawa 2000].
- An increase of c_p leads to a strong decrease of $R_{g\,app}$ and $R_{h\,app}$. Additional screening of the counterions is expected to reduce the polyion-size. However the effect is too big. Muthukumar's and Kundagrami's theory predict for QPVP$_{20}$ at c_p = 6 mg/L respectively c_p = 12 mg/L a decrease of α_g in the order of 6%, whereas according to Figure 6.26 the reduction is about 20%.

The QPVPs in Figures 7.2 and 7.3 exhibit a maximum of $R_{g\,app}$ vs. w$_{ns}$, whereas QPVP$_{1.2}$ and QPVP$_{2.4}$ exhibit the weakest signature if any at all. The maximum could be a result of the decreasing dielectric constant which in turn may increase the repulsion of like charges along the chain. However the χ_1 parameter counteracts the expansion with increasing w$_{ns}$ as can be seen by the uncharged PVP. Furthermore QPVP$_{20}$ and QPVP$_{35}$ exhibit a high Manning parameter with counterion condensation even in the good solvent regime. Such samples are expected to shrink with an increase of l_B, yet they show the strongest signature of a maximum. Figures 7.4 and 7.5 shows the apparent expansion coefficients $\alpha_h = R_{h\,app} / R_{h\,\theta}$ against the non-solvent fraction w$_{ns}$. All trends are in qualitative agreement with those of $R_{g\,app}$. However the influence of electrostatically motivated exclusion volumes most likely differs in its extent on R_g respectively R_h. Therefore the ratio $R_{g\,app} / R_{h\,app}$ may not be proportional to the 'true' R_g / R_h - ratio and the information about the degree of anisotropy may be biased. Keeping this uncertainty in mind the run of the ratio $R_{g\,app} / R_{h\,app}$ shows an interesting behavior as shown in Figure 7.6. Despite some significant reduction in the absolute chain dimensions the ratio $R_{g\,app} / R_{h\,app}$ remains on a high level close to 2 which lies well above the theoretical limit of neutral flexible coils in the excluded volume limit, R_g/R_h = 1.73. The samples QPVP$_{4.3}$ and QPVP$_{20}$ exhibit for w$_{ns}$ > 0.923 respectively w$_{ns}$ > 0.993 a ρ-ratio of about 1 as it is expected

for spherically collapsed coils. A similar behavior was also observed for the Ca^{2+} and Cu^{2+} induced collapse of polyacrylic acid [Huber 1993] and of polymethacrylic acid [Ikeda, Beer Schmidt 1998]. For the Ca^{2+} and Sr^{2+} induced collapse of NaPA a string of sphere collapse was postulated by SANS [Schweins, Lindner, Huber 2003] and by anomalous x-ray scattering experiments, [Goerigk, Schweins, Huber 2003] respectively. However, the divalent counterion induced collapse of polyelectrolytes has an entirely different physical origin as compared to the collapse of polyelectrolytes in a poor solvent [Kundagrami, Muthukumar 2008].

Figure 7.7 shows the apparent ρ-ratio of the quaternized samples vs. the apparent expansion coefficient of the radii of gyration $\alpha_{g\,app}$. $QPVP_{4.3}$ and $QPVP_{20}$ at $C_s = 10^{-5}$ mol/L show a comparable course. With respect to its degree of expansion $QPVP_{35}$ has a comparatively high ρ-ratio whereas $QPVP_{20}$ with high salt content has a comparatively low apparent ρ-ratio. Figure 7.8 shows some literature data of temperature induced coil to globule collapses of uncharged polymers (see figure text for details), salting out experiments on sodium-polyacrylate chains, as well as the sample $QPVP_{4.3}$. In the small $\alpha_{g\,app}$-regime the course of the apparent ρ-ratio of $QPVP_{4.3}$ does not show any distinct feature compared to the run of the ρ-ratios of the neutral polymers.
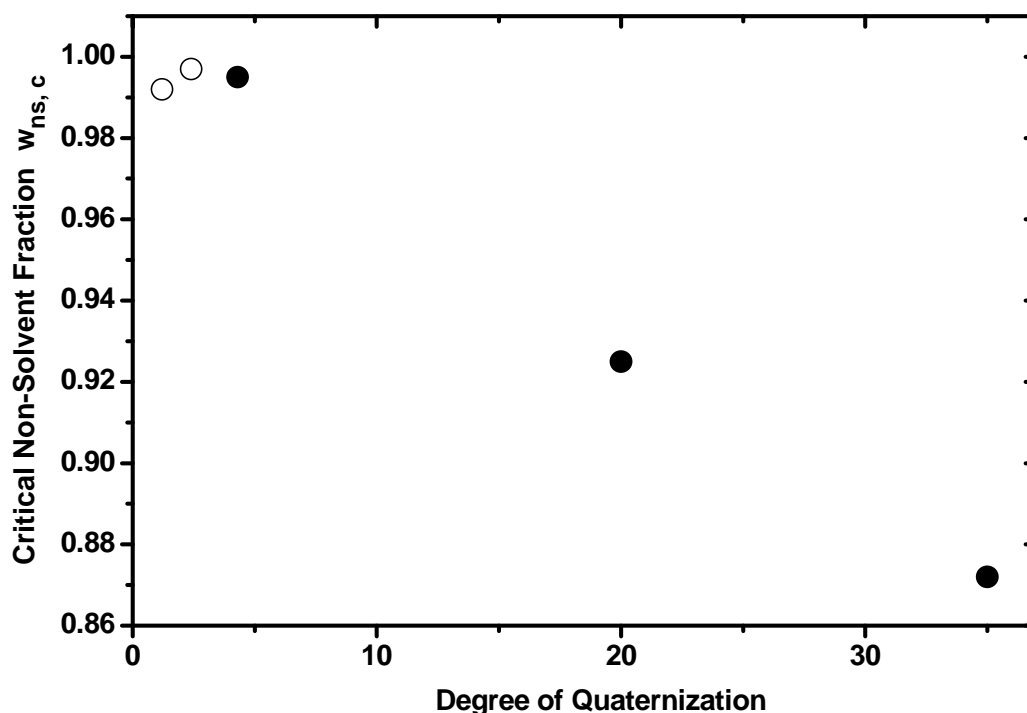

Figure 7.1 Critical non-solvent fraction $w_{ns,\,c}$ vs. the degree of quaternization. The two samples $QPVP_{1.2}$ and $QPVP_{2.4}$ exhibited aggregates (chapter 6.5 and 6.6) and feature open symbols.
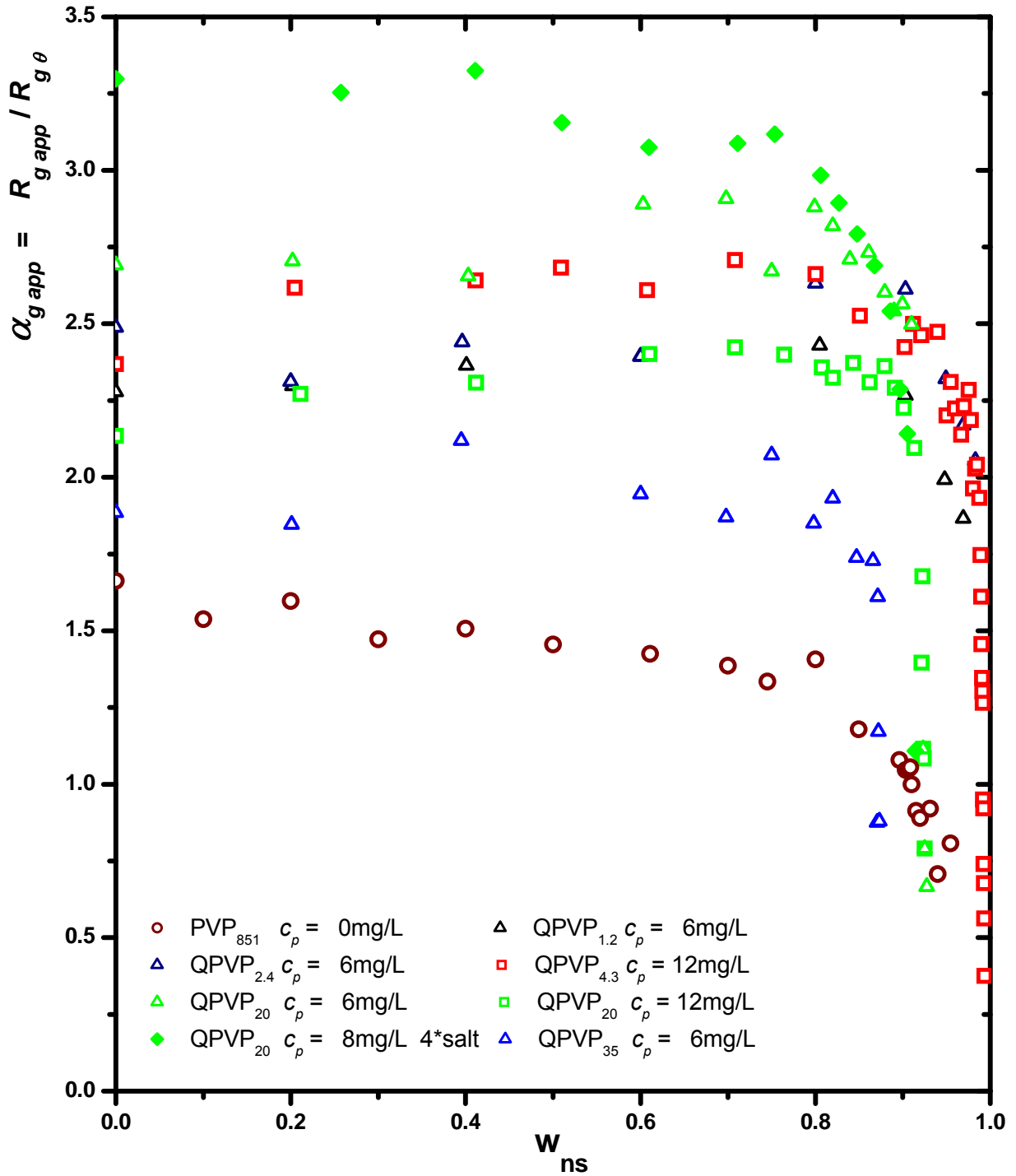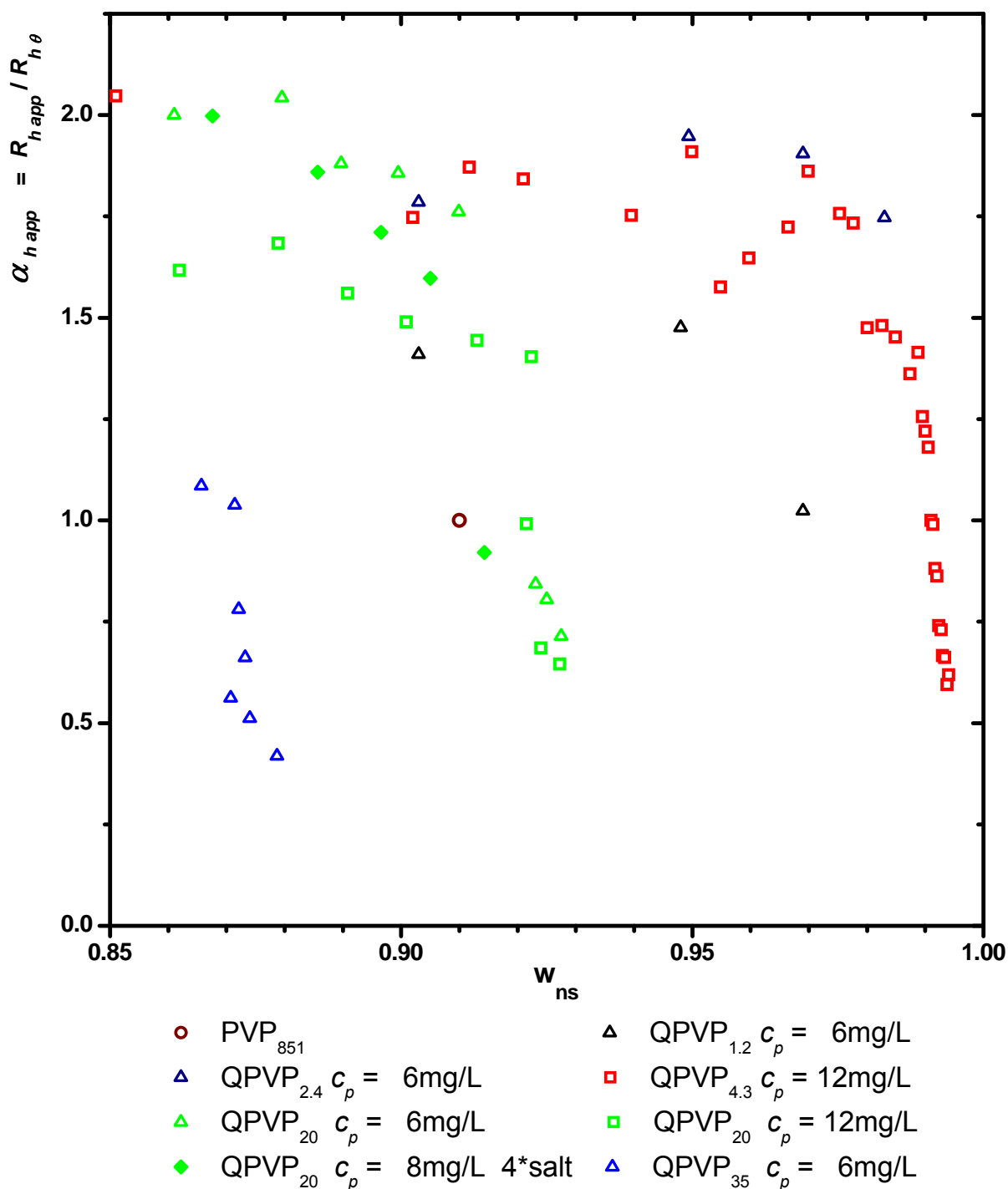
Figure 7.2 Apparent radii of gyration expansion coefficients $\alpha_{g\,app}$ are plotted as functions of w_{ns}. Different samples are indicated by different colors. Equal concentrations feature the same symbols. All measurements were conducted at $C_s = 10^{-5}$ mol/L, except QPVP$_{20}$ with $c_p = 8$ mg/L measured at $C_s = 4*10^{-5}$ mol/L.
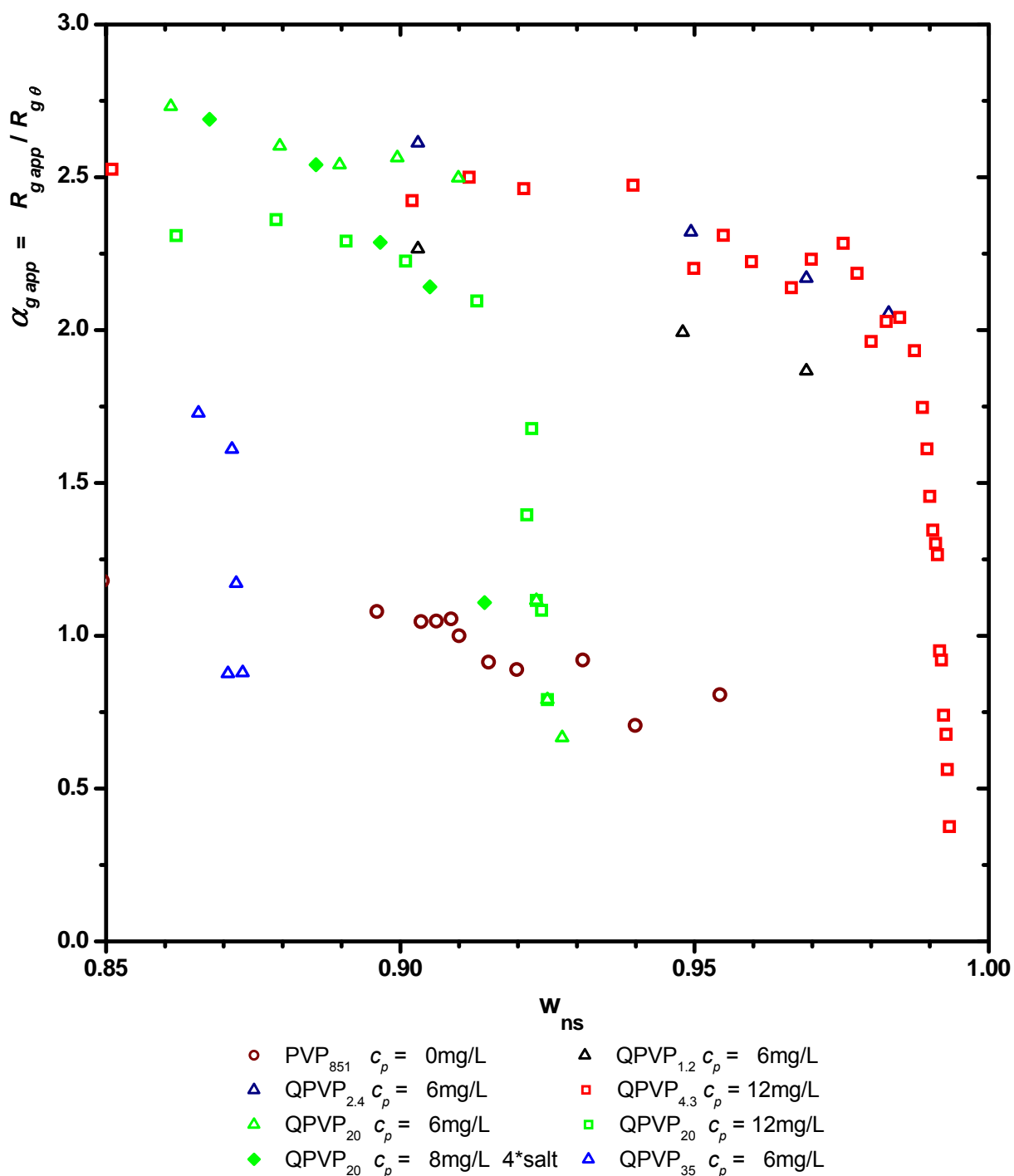
Figure 7.3 Magnification: Apparent radii of gyration expansion coefficients $\alpha_{g\,app}$ are plotted as functions of w_{ns}. Different samples are indicated by different colors. Equal concentrations feature the same symbols. All measurements were conducted at $C_s = 10^{-5}$ mol/L, except QPVP$_{20}$ with $c_p = 8$ mg/L measured at $C_s = 4*10^{-5}$ mol/L.
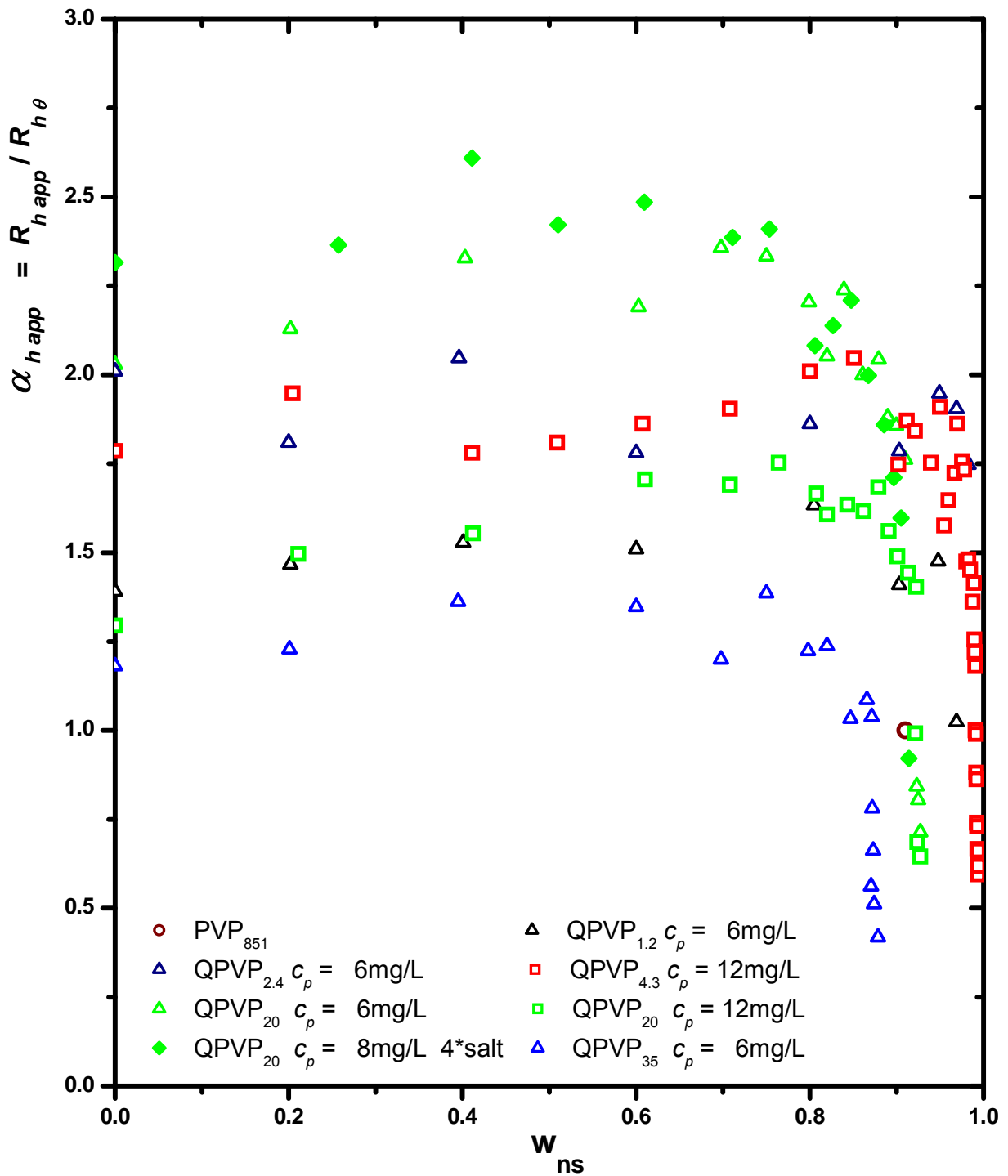
Figure 7.4 Apparent hydrodynamic radii expansion coefficients $\alpha_{h\,app}$ are plotted as functions of w_{ns}. Different samples are indicated by different colors. Equal concentrations feature the same symbols. All measurements were conducted at $C_s = 10^{-5}$ mol/L, except QPVP$_{20}$ with $c_p = 8$ mg/L at $C_s = 4*10^{-5}$ mol/L.

Figure 7.5 Magnification: Apparent hydrodynamic radii expansion coefficients $\alpha_{h\,app}$ are plotted as functions of w_{ns}. Different samples are indicated by different colors. Equal concentrations feature the same symbols. All measurements were conducted at $C_s = 10^{-5}$ mol/L, except QPVP$_{20}$ with $c_p = 8$ mg/L measured at $C_s = 4*10^{-5}$ mol/L.
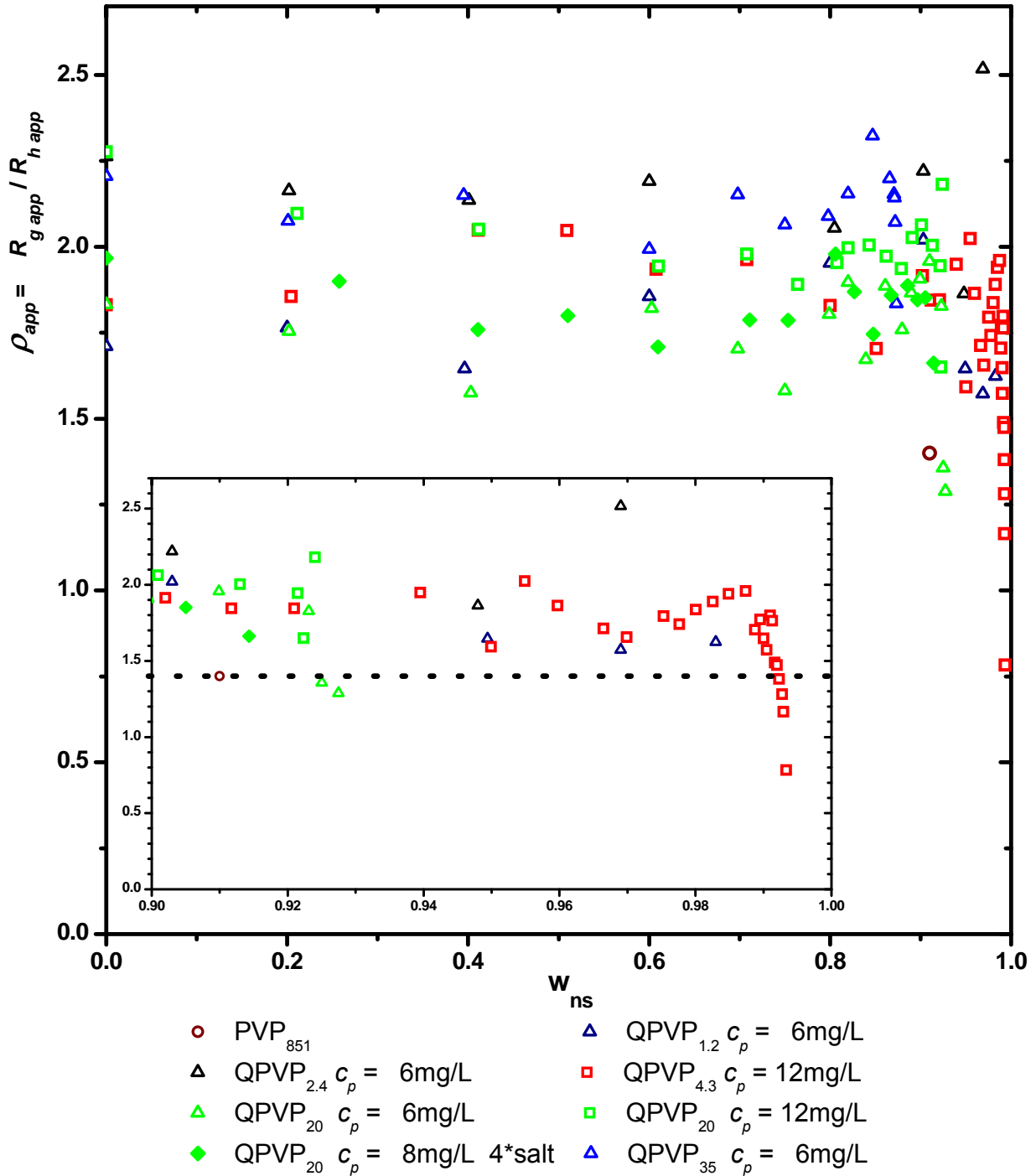
Figure 7.6 The apparent ρ_{app}-ratio $R_{g\,app}/R_{h\,app}$ is plotted vs. the fraction of non solvent w_{ns}. Different samples are indicated by different colors. Equal concentrations feature the same symbols. All measurements were conducted at $C_s = 10^{-5}$ mol/L, except $QPVP_{20}$ with $c_p = 8$ mg/L measured at $C_s = 4*10^{-5}$ mol/L. Inset: Magnification of the collapse transition with the dotted line indicating $R_{g\,app}/R_{h\,app} = 1.4$ experimentally found for the uncharged PVP at θ-condition.
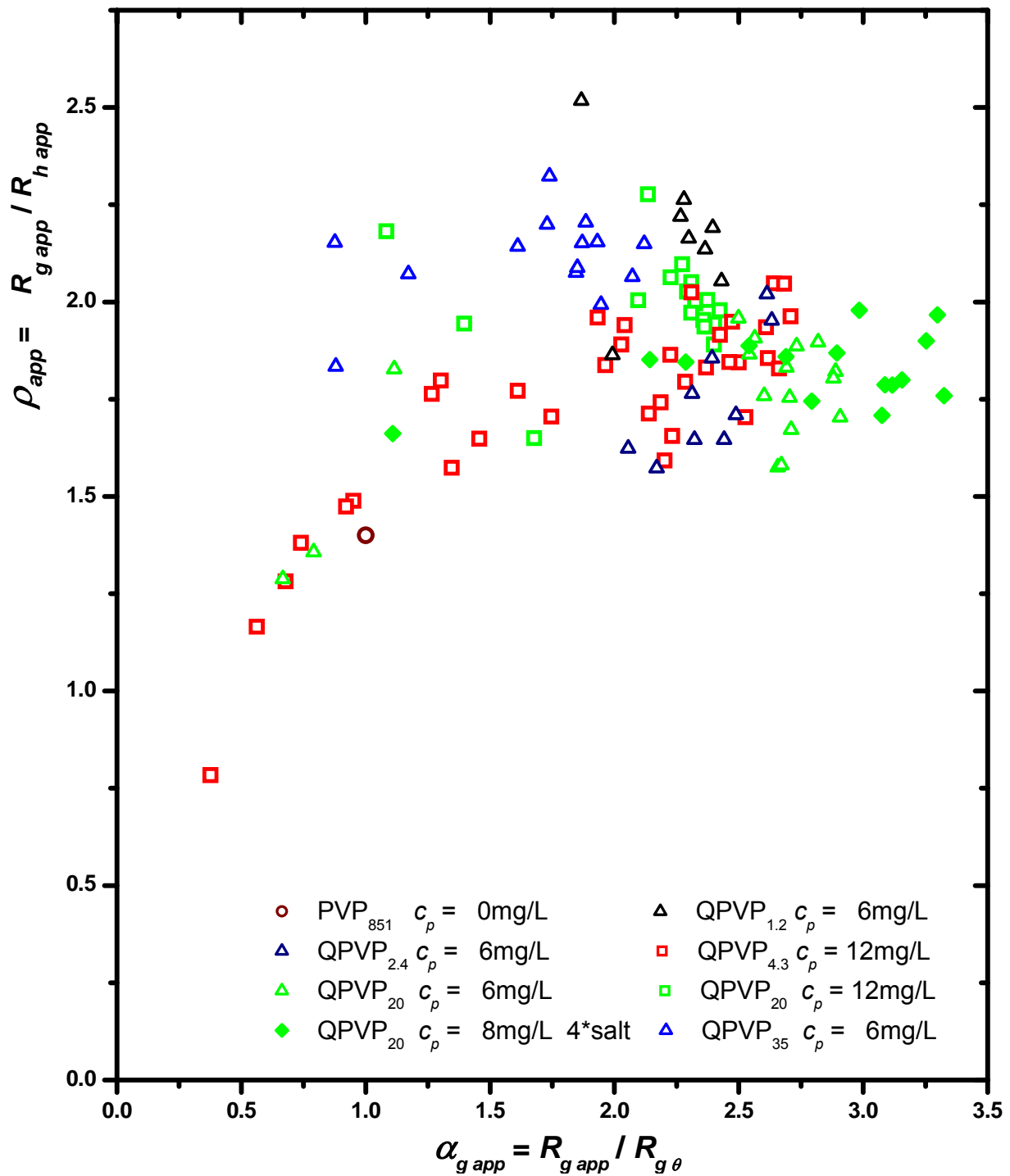
Figure 7.7 The apparent ρ_{app}-ratio $R_{g\,app}/R_{h\,app}$ is plotted vs. the apparent expansion factor $\alpha_{g\,app}$. Different samples are indicated by different colors. Equal concentrations feature the same symbols. All measurements were conducted at $C_s = 10^{-5}$ mol/L, except QPVP$_{20}$ with $c_p = 8$ mg/L measured at $C_s = 4*10^{-5}$ mol/L.
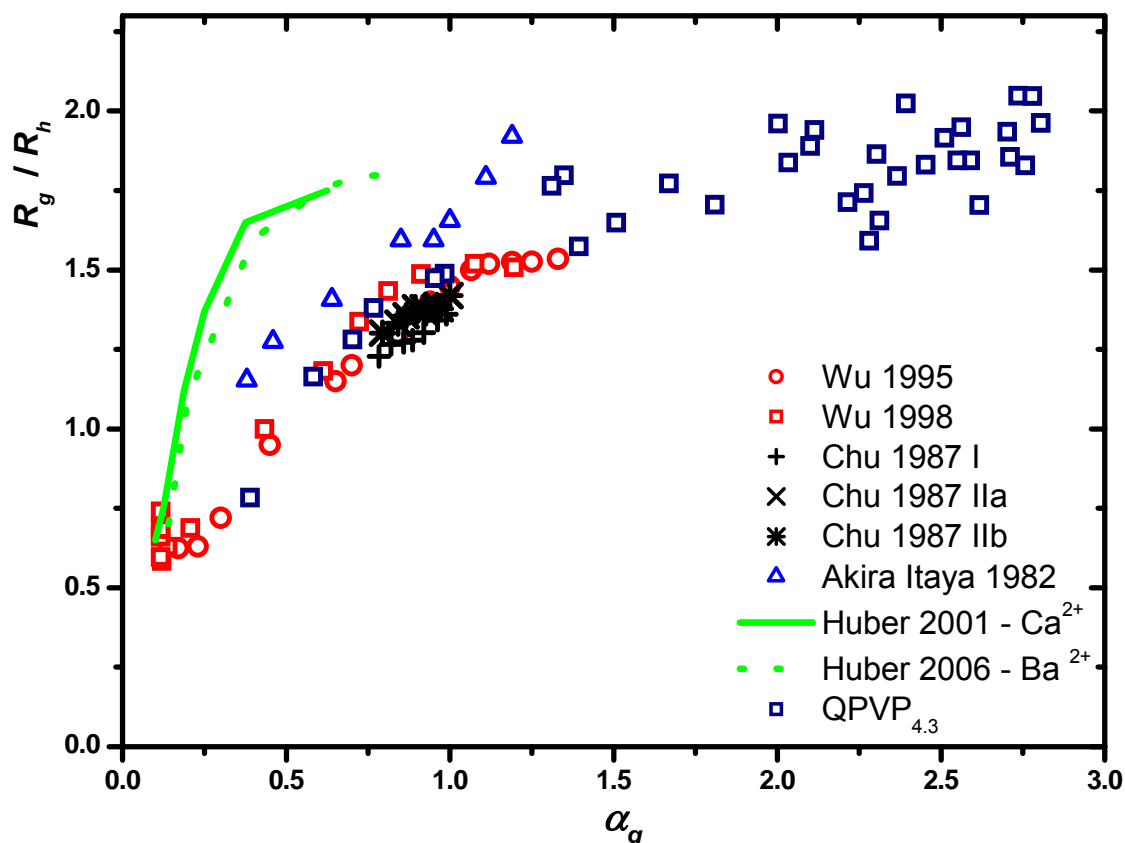
Figure 7.8 The ρ-ratio R_g / R_h is plotted vs. the apparent expansion factor α_g for uncharged polymers. The apparent course of the ρ-ratio from QPVP$_{4.3}$ is shown, too. Literature data were taken from different sources: [Itaya et al. 1982; Park Wang, Chu 1987 I,II; Wu, Zhou 1995; Wu, Wang1998; Schweins, Huber 2001; Schweins, Goerigk, Huber 2006] The 'Huber collapses' were induced by 'salting out' experiments on sodium-polyacrylate chains with Ca^{2+} respectively Ba^{2+}.

7.1 Enhanced Static Data Evaluation

The reason for the discrepancy of light scattering measurements and some predictions of polyelectrolyte models is most likely due to the influence of inter particle scattering onto the Rayleigh ratio which may be not sufficiently captured by the Zimm equation for the used low salt concentration. In case of ordered lattices, the inter particle distances respectively the oscillating signatures of a strong $S(q)$ appear on rather small q-values, whereas signatures of $P(q)$ typically appear as a monotonic decreasing function in laser light scattering. The different q-regimes of well defined $P(q)$ and $S(q)$ make them distinguishable and evaluation is possible using established techniques (Figure 4.6). In contrast uncharged polymers up to a size of about 100 nm are conveniently evaluable by the Zimm equation which covers the intraparticle structure factor by a linearization of such and inter particle interference by an angle-independent offset governed by the exclusion volume of the particles. In the intermediate regime for which a defined exclusion distance of two repelling particles happens to be in the order of the particle size, $P(q)$ and $S(q)$ are assumed to feature a strong angle dependent signature in the same q-regime. According to eq. 4.26 an extended Zimm formula with a q-dependent structure factor may yield a better approximation in a simple analytic expression.

First of all the regime of validity for the Fluctuation theory shall be discussed. Fluctuation theory for uncharged particles predicts for $\theta = 0$ [Yamakava 1971]:

$$\frac{Kc_p}{R\left(c_p, q=0\right)} = \frac{1}{RT}\frac{\partial \Pi}{\partial c_p} \tag{7.1}$$

In case of charged particles Vrij and Overbeek [Vrij, Overbeek 1962] showed that Fluctuation theory in general is only valid if:

$$\frac{2\sin\left(\theta/2\right)}{\kappa_D\lambda} \ll 1 \tag{7.2}$$

This condition is fulfilled for all samples used in this dissertation. (Furthermore Hara pointed out that eq. 7.2 is valid at $\theta = 0°$ in any case even for salt free solutions. However equations derived from fluctuation theory cannot be used at finite angles for such solutions [Hara 1995]). The discrepancy of the apparent molar mass M_{app} and the true molar mass at $q = 0$ is a measure for the magnitude of inter particle interactions. The non biased true molar mass M is already known, as it can be calculated from the molar mass of the precursor in combination with the degree of quaternization from elemental analysis. Therefore the extent of this discrepancy shall be used in the following to determine the effect onto the evaluation of R_g. Defining the apparent molar mass as $M_{app} = R\left(c_p, q=0\right)/Kc_p$ the Rayleigh ratio can be rewritten as (eq. 4.26):

$$\frac{Kc_p}{R\left(c_p, q\right)} = \frac{1}{M_{app}}\left\{1+q^2\left[\frac{R_g^{\,2}}{3}-\frac{\xi_g^{\,2}}{6}\left(1-\frac{R\left(c_p, q=0\right)}{MKc_p}\right)\right]\right\} \tag{7.3}$$

Now using eq. 7.1 and expressing Π as a power series in c_p, i. e. the common used virial series, leads to:

$$\frac{Kc_p}{R\left(c_p, q\right)} = \frac{1}{M_{app}}\left\{1+q^2\left[\frac{R_g^{\,2}}{3}-\frac{\xi_g^{\,2}}{6}\left(1-\frac{1}{1+2A_2Mc_p+3A_3Mc_p^{\,2}}\right)\right]\right\} \tag{7.4}$$

Using the data of this dissertation A_3 is positive and its maximum contribution to non ideality for all samples is about 10% (eq. 7.9). Therefore higher orders of the virial expansion will be neglected. Both parameters ξ_g and A_3 can be described using the second virial coefficient A_2 which in turn can be obtained from M_{app} in relation to M (see below). ξ_g in eq. 7.1 is the root-mean-square radius of the intermolecular excluded volume. The second virial coefficient is proportional to this exclusion volume. As a good approximation the simple radius of the exclusion sphere shall be used for ξ_g which can be evaluated from the well established relation [Higgins, Benoit 1996]:

$$\xi_g^{\,2} = \left(\frac{3M^2A_2}{16\pi N_A}\right)^{2/3} \tag{7.5}$$

The third virial coefficient A_3 for hard spheres is given by:

$$A_3 = \varepsilon_{vir}\frac{5}{8}A_2^{\,2}M \tag{7.6}$$

with $\varepsilon_{vir} = 1$. However for random coils ε_{vir} was found to range from 0.25 to 0.75, whereas for polyelectrolytes Nordmeier [Nordmeier 1995] as well as Sorci and Reed found in the law salt

regime a constant value of about 0.1 (see [Sorci, Reed 2002] on this topic) which will be used in the following. Inserting eq. 7.5 and 7.6 into eq. 7.4 yields:

$$\frac{Kc}{R\left(c_p, q\right)} = \frac{1}{M_{app}} \left\{ 1 + \frac{q^2}{3} \left[R_g^{\,2} - \frac{1}{2}\left(\frac{3M^2 A_2}{16\pi N_A}\right)^{2/3} \frac{1}{1+\left[2A_2 Mc_p\left(1+\dfrac{3}{32}A_2 Mc_p\right)\right]^{-1}} \right] \right\} \qquad (7.7)$$

This defines the true radius of gyration R_g as:

$$R_g = \left[R_{g\,app}^{\,2} + \frac{1}{2}\left(\frac{3M^2 A_2}{16\pi N_A}\right)^{2/3} \frac{1}{1+\left[2A_2 Mc_p\left(1+\dfrac{3}{32}A_2 Mc_p\right)\right]^{-1}} \right]^{0.5} \qquad (7.8)$$

A_2 can be calculated from the relation:

$$\frac{1}{M_{app}} = \frac{1}{M} + 2A_2 c_p + \frac{3}{20}A_2^{\,2} Mc_p^{\,2} \qquad (7.9)$$

The extended Zimm extrapolation is shown in Figure 7.9. Scattering of data points is increased compared to Figures 7.2 and 7.3 as the involvement of the absolute scattering intensity adds an additional error, even more as the absolute intensity scatters much more than its angle dependency (compare $M_{w\,app}$, chapter 6). However one can deduce the trends to be now in accordance with polyelectrolyte concepts (see discussion in chapter 7). One should stress that now no maximum in the course of $\alpha_{g\,app}$ vs. w_{ns} can be observed but a monotonic decreasing function. The decrease of $\alpha_{g\,app}$ within the good solvent regime seems to be stronger for the higher quaternized samples.
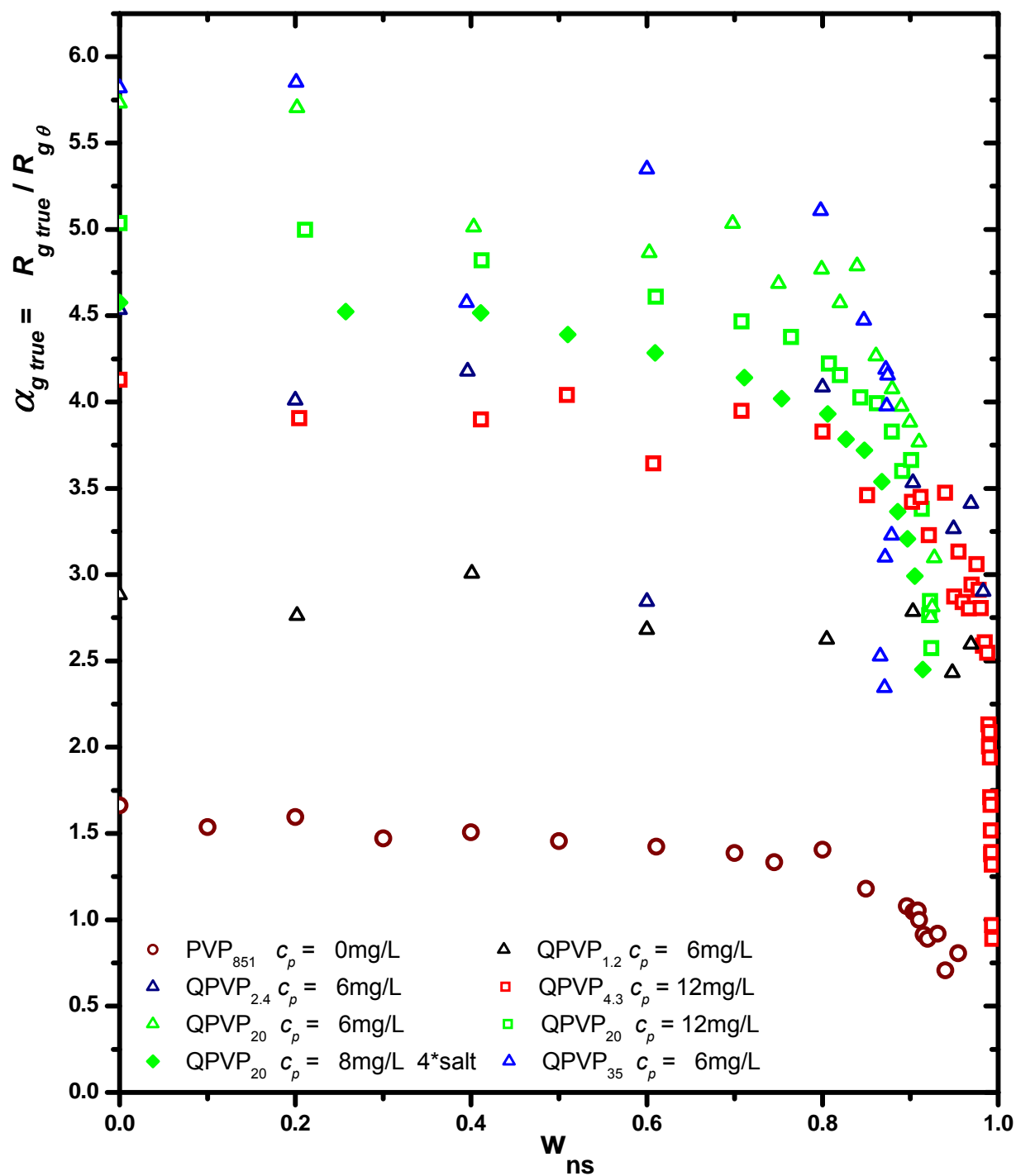
Figure 7.9 'True' radii of gyration expansion coefficients α_g are plotted as functions of w_{ns}. Different samples are indicated by different colors. Equal concentrations feature the same symbols. All measurements were conducted at $C_s = 10^{-5}$ mol/L, except QPVP$_{20}$ with $c_p = 8$ mg/L which has been measured at $C_s = 4*10^{-5}$ mol/L.

7.2 Enhanced Dynamic Data Evaluation

The apparent diffusion coefficient D_{app} is given by the generalized Stokes-Einstein relation [Yamakava 1971; Hara 1995]:

$$D_{app} = M \frac{(1 - \upsilon_p c_p)}{N_A f_p} (\partial\Pi / \partial c_p) \tag{7.10}$$

υ_p *partial specific volume of the polymer*

f_p *frictional coefficient of polyion*

For weak interactions Π as well as f_p may be expanded in terms of c_p:

$$\frac{\partial\Pi}{\partial c_p} = (1 + 2A_2 M c_p + ...) \tag{7.11}$$

$$f_p = f_p^0 (1 + k_f c_p + ...) \tag{7.12}$$

f_p^0 *frictional coefficient of polyion at infinite dilution*

k_f *polyion friction expansion coefficient*

This defines the self diffusion coefficient D_s as:

$$D_{app} = \frac{k_B T}{f_p} \left[1 + (2A_2 M - k_f - \upsilon_p) c_p + ... \right]$$

$$= D_s (1 + k_D c_p + ...) \tag{7.13}$$

which is identical to eq. 4.56 for $q = 0$ (k_D is the diffusion virial coefficient). However when interaction is strong as it is in case of low ionic strength the influence of $\partial\Pi / \partial c_p$ is much stronger than that of f_p and $(1 - \upsilon_p)$ [Pusey, Tough 1985]. Therefore the self diffusion coefficient D_s for strongly interacting solutions may be obtained according to:

$$D_s \approx \frac{D_{app} RT}{M(\partial\Pi / \partial c_p)} = \frac{D_{app}}{(M/M_{app})} \quad \hat{=} \quad R_h = R_{h,app} (M/M_{app}) \tag{7.14}$$

The enhanced diffusion coefficients respectively their corresponding hydrodynamic radii are shown in Figure 7.10. Due to involvement of absolute intensity, scattering of data points is increased compared to Figures 7.4 and 7.5. The different courses of α_h in principle resemble the run of the α_g from Figure 7.9. However the trend of increasing hydrodynamic radii with increasing degree of quaternization is broken from sample QPVP$_{20}$ to QPVP$_{35}$. With regard to the R_g/R_h-ratio this might be interpreted as a more anisotropic topology as it may occur due to strong attractive dipole-dipole interactions of condensed ions. However QPVP$_{20}$ does not show any indication of a trend towards more anisotropy compared to QPVP$_{4.3}$ rendering the effect as very abrupt if real.
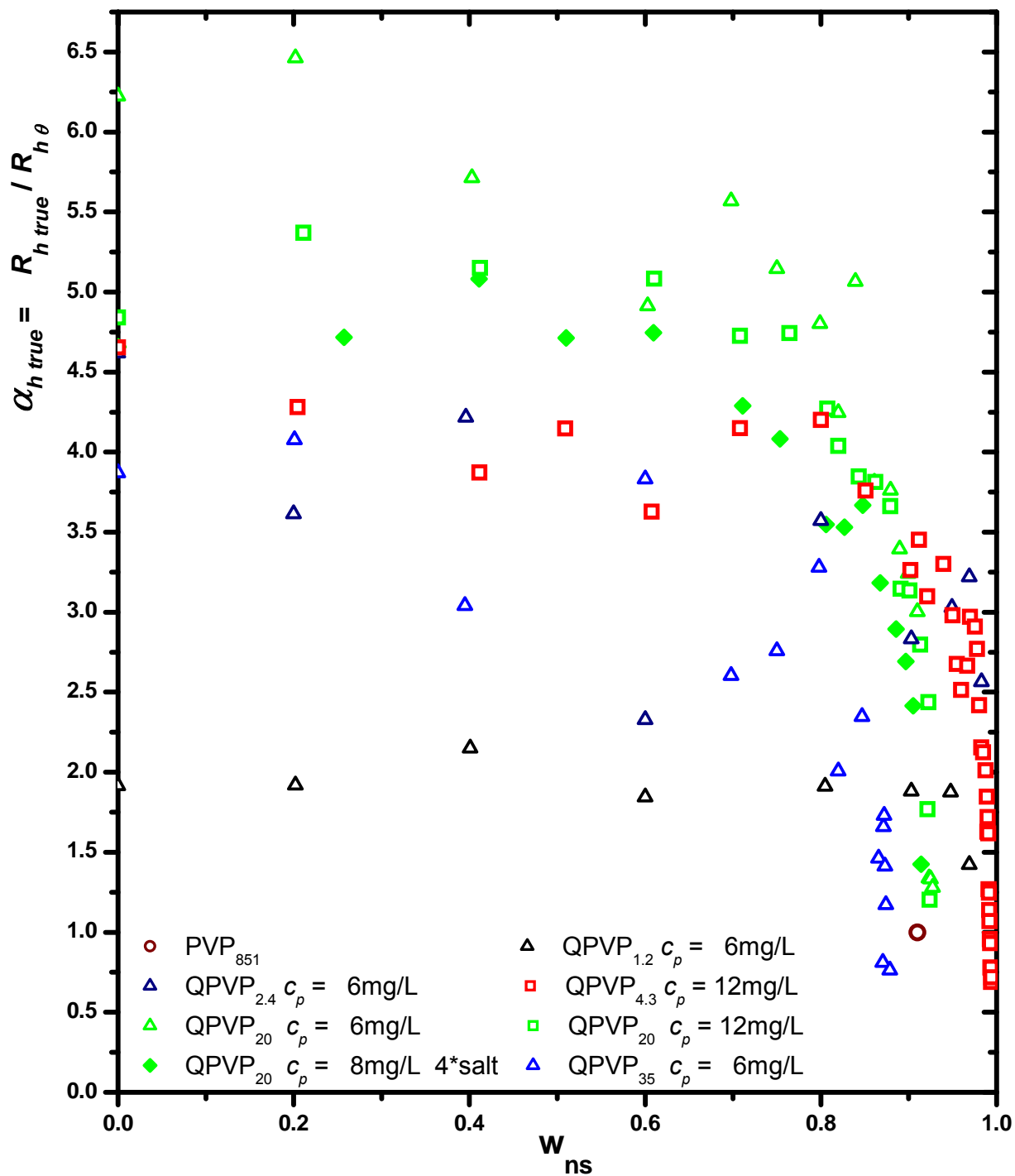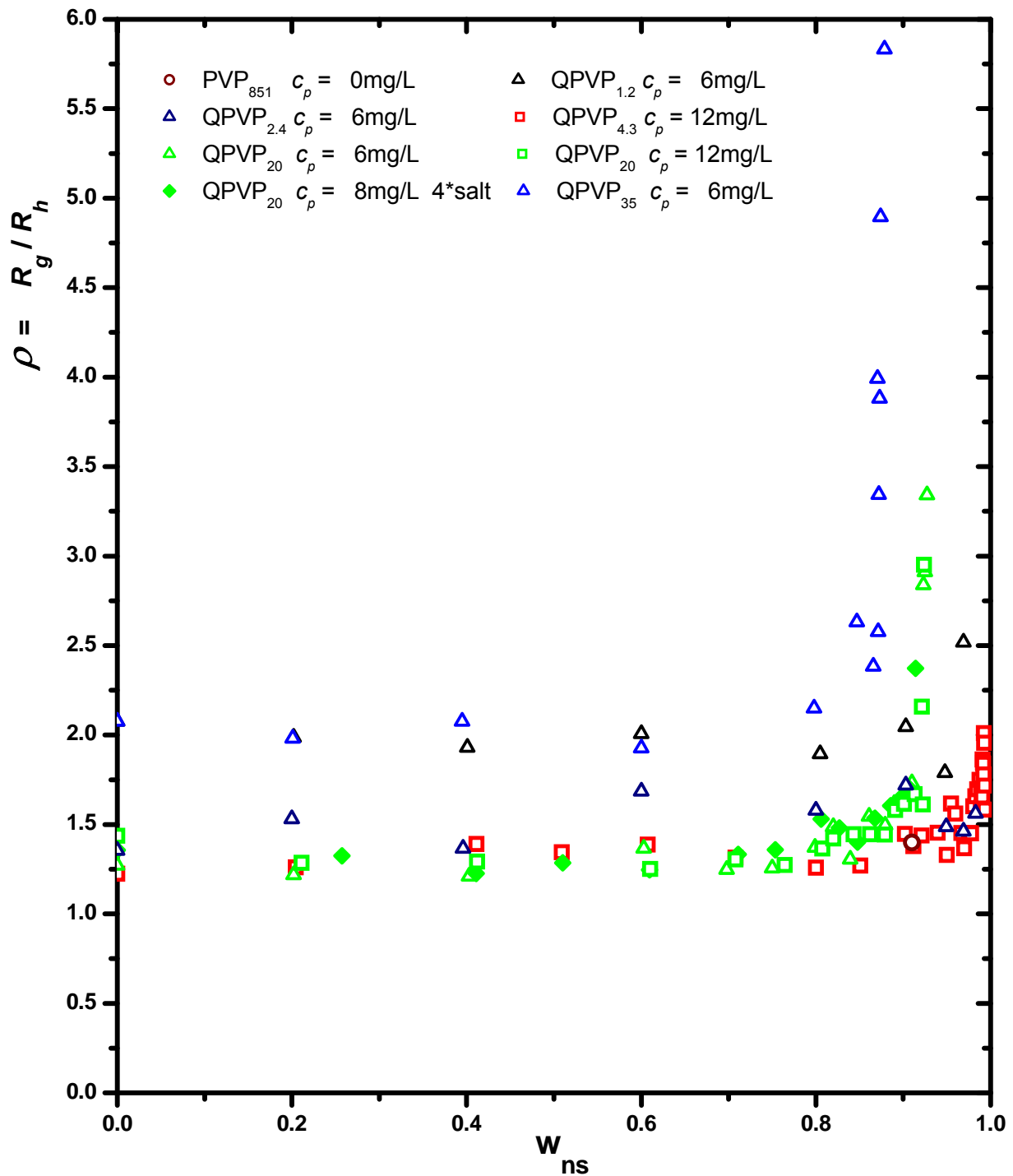
Figure 7.10 'True' hydrodynamic radii α_h are plotted as functions of w_{ns}. Different samples are indicated by different colors. Equal concentrations feature the same symbols. All measurements were conducted at $C_s = 10^{-5}$ mol/L, except QPVP$_{20}$ with $c_p = 8$ mg/L measured at $C_s = 4*10^{-5}$ mol/L.

7.3 ρ–Ratio

The ρ-ratios as calculated from the 'true' radii of gyration respectively hydrodynamic radii are plotted in Figure 7.12 respectively 7.13. The scattering of the ρ-ratios is reduced compared to Figures 7.6 and 7.7 due to the fact, that most of the error of the absolute scattering is cancelled. According to Figure 7.12 QVP$_{4.3}$ exhibits an almost constant ρ-ratio in the good solvent regime of about 1.4 that however increases in the poor solvent regime to a value of about 2 till it finally starts to decrease shortly before precipitation. A ρ-ratio of about 1.4 is a bit low compared to a value of 1.7 as expected for an expanded coil. Nevertheless in principal the course may reflect the formation of an anisotropic shape in the poor solvent regime as has been predicted by theoreticians like Dobrynin and Holm with their pearl necklace structure or Yethiraj with his sausage like structures (see Figure 7.11). The high ρ-ratio of QPVP$_{35}$ in the good solvent regime may be an indication of anisotropy in the good solvent regime as it could be mediated by the many condensed counterions. However QPVP$_{35}$ and QPVP$_{20}$ exhibit very high ρ-ratios close to their precipitation point that can not be obtained by any structure at all (compare ρ-ratio of a cylinder in Table 4.1). Therefore extrapolation of the data according to eq. 7.8 and/or 7.14 is biased at least in the poor solvent regime especially when the M_{app}/M ratio does not approach 1 'fast enough' (see $M_{w\,app}$ in chapter 6). Figure 7.13 shows the 'true' ρ- ratios as functions of the true expansion coefficient α_g. The analog plot of the apparent quantities suggests a monotonous decrease of ρ vs. α_g (Figure 7.7). In contrast the extrapolated ρ vs. α_g plot suggests a constant value in the good solvent regime with an increase at the end of the collapse stage which finally seems to decrease again for the samples QPVP$_{4.3}$ and QPVP$_{35}$. However as already stressed the extrapolated data has to be biased as ρ-ratios > 3 cannot be obtained by any physical topology.
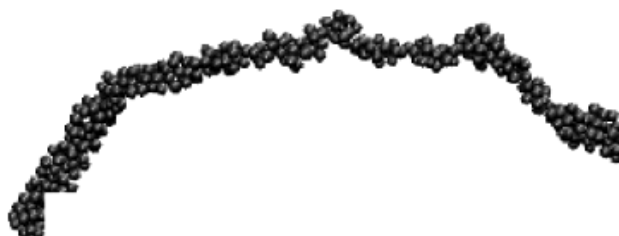

Figure 7.11 [Yethiraj 2006] Simulation snapshot in the poor solvent regime for a chain with 382 segments and a fraction of chemical units of 1/3.

Figure 7.12 'True' ρ - ratios are plotted as functions of w_{ns}. Different samples are indicated by different colors. Equal concentrations feature the same symbols. All measurements were conducted at $C_s = 10^{-5}$ mol/L, except QPVP$_{20}$ with $c_p = 8$ mg/L measured at $C_s = 4*10^{-5}$ mol/L.
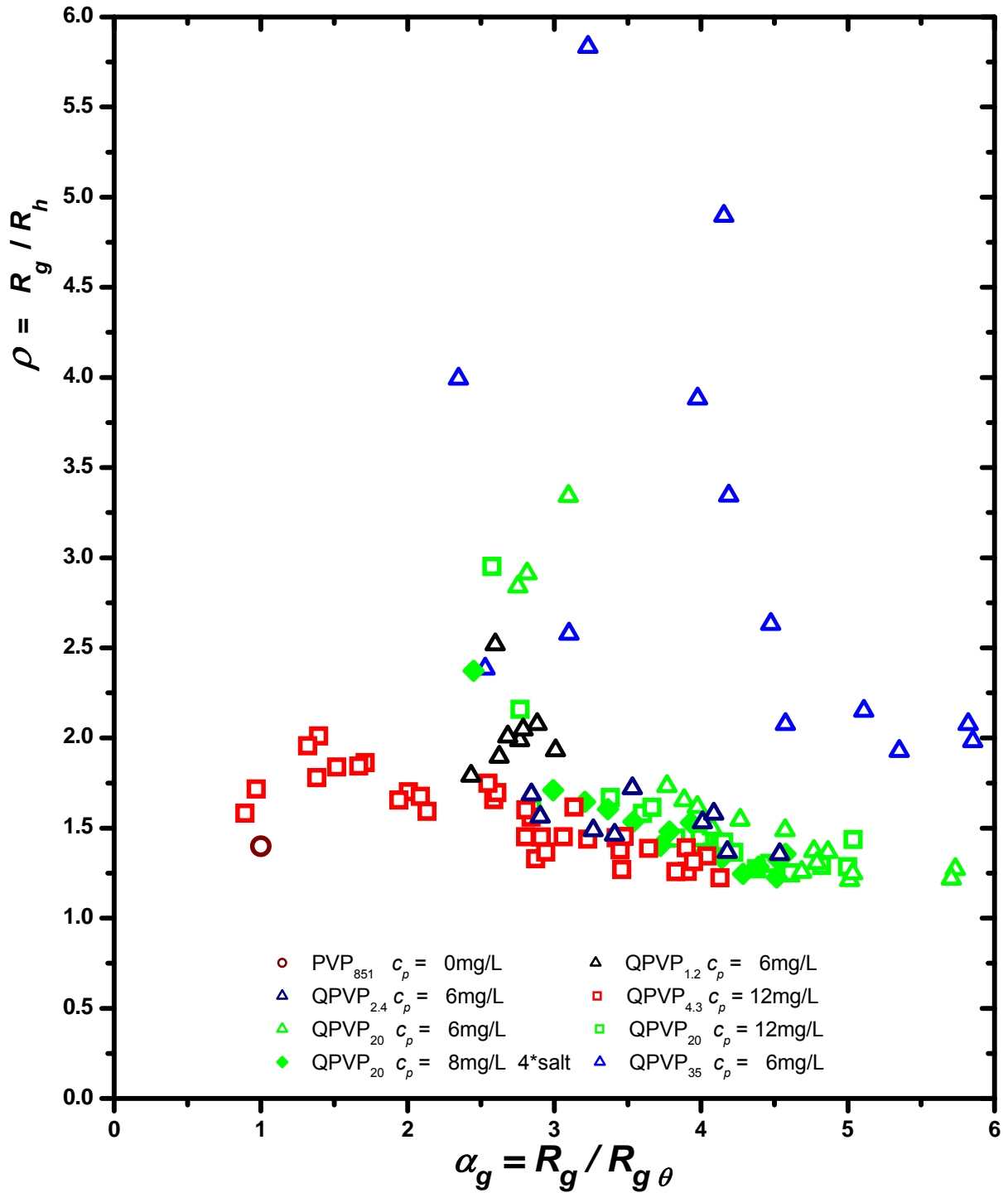
Figure 7.13 'True' ρ - ratios are plotted as functions of α_g. Different samples are indicated by different colors. Equal concentrations feature the same symbols. All measurements were conducted at $C_s = 10^{-5}$ mol/L, except QPVP$_{20}$ with $c_p = 8$ mg/L measured at $C_s = 4 \cdot 10^{-5}$ mol/L.

7.4   Degree of Dissociation

Ignoring all dynamic coupling and screening effects between polyions and counterions/salt-ions (chapter 3.24), the effective degree of dissociation γ can be determined semi-quantitatively from the equivalent conductivity Λ according to eq. 6.8. The mobility of the bromide ion can be estimated from the run of equivalent conductivity of the pure salt solution by knowing the part of the bromide ion. The fraction of the bromide conductivity of Λ was approximated by a linear increase from 53 % at w_{ns} = 0 to 62 % at w_{ns} = 1 as extensive measurements on very similar systems suggest [Evans, Gardam 1968; Evans et al 1971; de Lisi, Goffredi 1973]. The equivalent conductivity of the polyion can be calculated according to eq. 3.18 using the Stokes Einstein relation:

$$\lambda_p = \gamma z_p Fe \, / \left(6\pi\eta_0 R_h \right)$$ (7.15)

z_p	*number of chemical charges per chain*
F	*Faraday constant*
η_0	*solvent viscosity*

Inserting eq. 7.15 into 6.8 yields the following simplified expression for the equivalent conductivity of the polyion with its counterions:

$$\Lambda_p = \gamma \, \lambda_{br} \;+\; \frac{\gamma^2 z_p Fe}{6\pi\eta_0 R_h}$$ (7.16)

Therefore by combination of conductivity data and dynamic light scattering data one can approximate γ. The effective degree of dissociation changes the speed of the polyion as well as the number of its effective charges, captured by the quadratic dependence on γ. Equation 7.16 shows that a reduction of R_h increases conductivity. Therefore during the proceeding of the collapse the parameter γ must over-compensate the 'conductivity increase' due to size reduction as the run of the Walden products finally approaches zero as shown in chapter 6. One should stress that the use of friction coefficients from diffusion experiments for the determination of γ is not unique but was utilized before [Schmitt et al. 1978; Vink 1981], however not without some dispute in the community as the equality of friction coefficients can be questioned [Manning 1980]. Figure 2.2 shows the dependence of the diffusion coefficient on the C_p / C_s -ratio. The polyion-diffusion coefficients of the solutions used in this dissertation are most likely at least partly coupled to its counterions (compare chapter 7.1 and 7.3) as they exhibit C_p / C_s –ratios in the intermediate regime. The increase of the diffusion coefficient with an increase of this ratio is due to coupling of diffusive motion of counterions and polyion thereby accelerating the polyion as captured by the Coupled Mode Theory. In conductivity experiments polyions are assumed to couple with low molecular weight ions, too. However as polyions and counterions exhibit two opposite migration directions, counterion coupling should decelerate the polyion (whereas coions should accelerate it) as discussed in chapter 3.2.4 and captured by the fraction of total energy dissipation due to interionic friction β. The effect of β on the conductivity data cannot be separated ab initio, therefore friction coupling will be neglected at first but discussed later. Irrespective of interionic friction the real chain dimensions need to be used as these determine the viscous drag in directed motion as is true for electrophoretic experiments. Even if still biased the hydrodynamic radii extrapolated according to eq. 7.14 are supposed to give a much better approximation for real chain dimensions compared to the 'raw data' and were therefore used for the estimation of γ. According to eq. 7.10 - 7.13 the calculated 'true' hydrodynamic radii are upper limits (if any significant deviations occur at all), according to eq. 7.16 this translates into γ being an upper

limit, too. Figure 7.14 shows γ for the samples QPVP$_{4.3}$, QPVP$_{20}$ and QPVP$_{35}$ (QPVP$_{1.2}$ and QPVP$_{2.4}$ were not measured up to the collapse by LS, see chapter 6) as calculated by eq. 7.16. One should note that due to the involvement of the absolute scattering intensity all three measurement techniques dynamic and static lightscattering as well as conductivity were combined to obtain γ. The course of γ resembles the run of the Walden product of the respective sample with a less pronounced decrease in the good solvent regime. However the similarity is obvious and can be explained by the competing 'forces': whereas the square of γ in principal makes γ less sensitive, it 'must compensate' the reduction of R_h, thereby effectively adapting a course similar to the run of the Walden product.

QPVP$_{20}$ has been measured by light scattering for $6 < c_p < 12$ mg/L, making γ accessible for those concentrations, too. Two opposing trends on the determination of γ shall be emphasized. Its Walden products increase with increasing concentration thereby suggesting γ to increase with c_p as well. However an increase of γ is counteracted by a decrease of R_h with increasing c_p (see Figure 7.10) thereby decreasing the viscous drag, forcing γ (the only parameter) to decrease to some extent. Figure 7.14 shows the Walden product to be the dominant force.

It shall be noted that according to eq. 3.15 β is a mutual quantity depending on all ionic species in the solution. However according to eq. 6.6 - 6.8 the calculated Walden products 'assume' the low molecular weight ions to be unaffected by the polyelectrolyte species, thereby ascribing the influence of β completely to the polyion and according to 7.15 + 7.16 finally to γ. The low molecular weight ions contributions exhibit a much higher conductivity per functional charge than the polyions do. Therefore a deceleration of these due to coupling to the polyion may be expected to yield the bigger effect on the conductivity. Therefore the increase of the Walden product with c_p as observed for virtually all samples most likely should only be partly attributed to the equivalent conductivity of the polyion. Rather a deceleration of counter and coions can be assumed. This in turn would reduce the c_p-dependence of the Walden product respectively the c_p-dependence of the degree of dissociation. One may even speculate that the apparent increase of the polyion's equivalent conductivity with c_p at high dilution in this dissertation (as well as those of Vink and Wandrey, chapter 6.4.2) is due to a reduction of counterion-polyion coupling due to increased screening.

a

b
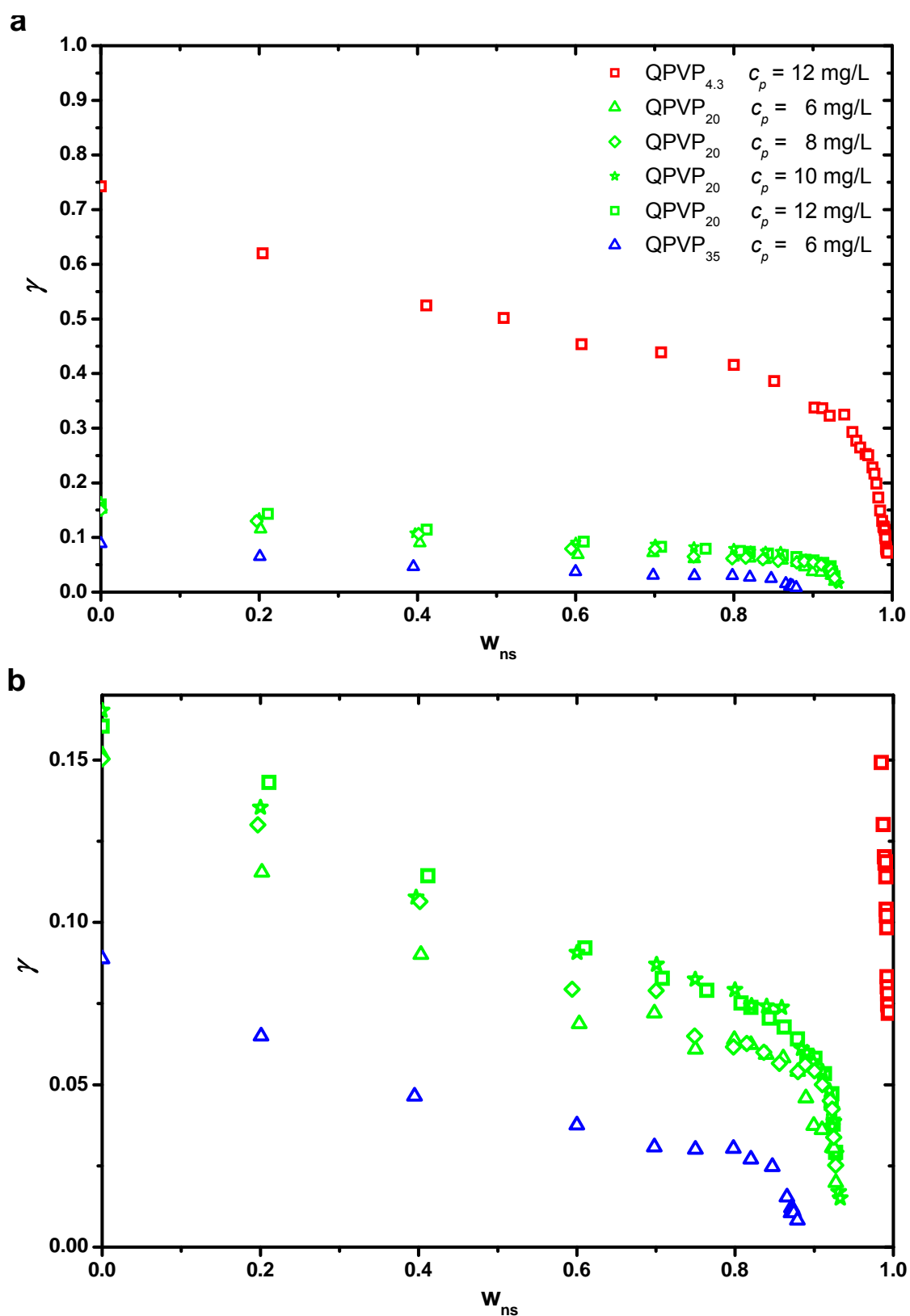
Figure 7.14 (a) The degrees of dissociation γ for $QPVP_{4.3}$, $QPVP_{20}$ and $QPVP_{35}$ at $C_s = 10^{-5}$ mol/L are plotted as functions of w_{ns}. (b) Magnification; symbols as in (a).

7.5 Comparison with Theory

In order to quantify the solvent quality of the uncharged polyvinylpyridine the radius of gyration R_g and the second virial coefficient, A_2, were measured as functions of w_{ns} (see Fig. 6.1 – 6.3). In Figure 7.15 left the expansion factor, $\alpha_g = R_g/R_{g,\theta}$, of the uncharged PVP chains is plotted against the volume fraction of the non-solvent, w_{ns} and compared to the theory (eq. 2.74) yielding the solvent quality parameter w as a function of w_{ns} (Figure 7.15 right). Note that eq. (2.74) is only valid for $w \geq 0$. For $w < 0$, values of w linearly extrapolated from its value at the θ-condition were used. θ-dimensions ($A_2 = 0$, $R_{g,\theta} = 29$ nm) were observed at $w_{ns} = 0.91$ (see Fig. 6.1 – 6.3). Below theta dimensions ternary interactions were included (the third term in eq. 2.71).
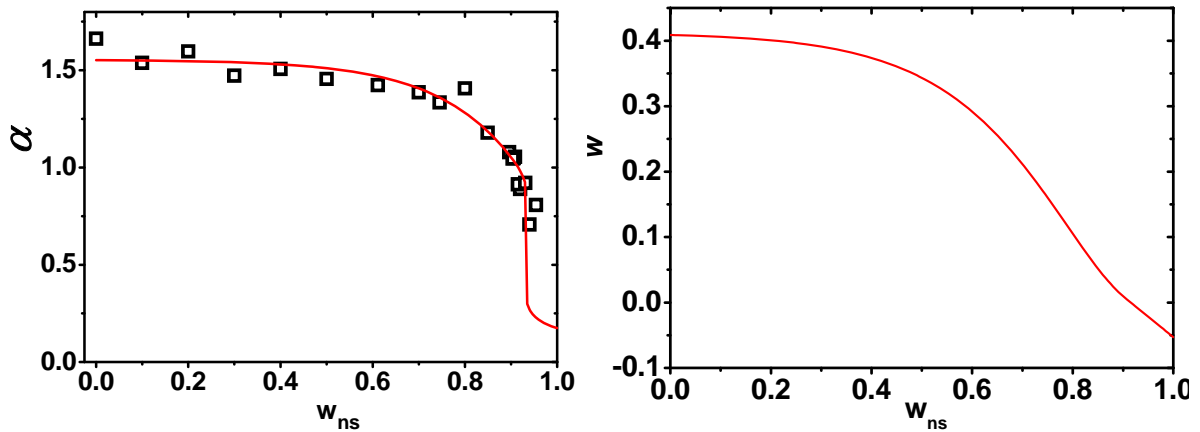
Figure 7.15 Left: The expansion factor α for the neutral polyvinylpyridine is plotted against the volume fraction of the non-solvent, w_{ns}. The red line represents the fit according to eq. 2.74 with $f = f_m = 0$ and $w_3 = 0.00165$. Right: The interaction parameter w as extracted from α according to eq. 2.74.

In Figure 7.16 the 'true' expansion factors, $\alpha_g = R_g/R_{g,\theta}$, of the polyions are plotted versus w_{ns} along with the theoretical prediction which utilize the same dependency of w on w_{ns} as obtained from the uncharged chain. In Figure 7.17 the fraction of the effective charges $\gamma = f / f_m$ derived from the conductivity data by eq. 7.16 is compared to the theoretically predicted charge density obtained through the double minimization of the free energy (eq. 2.66 - 2.71, 2.73). All three fit-pairs used the same set of parameters: $C = 0.183$ nm^{-1}, $w_1 = -0.00028$ and $w_3 = 0.00165$. Figure 7.18 shows a separate fit for QPVP$_{20}$ with $C = 0.185$ nm^{-1}, $w_1 = -0.00032$ and $w_3 = 0.00165$ for two different polyelectrolyte concentrations.

As mentioned in the theory, a non-zero positive value of w_3 was required to stabilize the chain collapse below θ-dimensions. A fixed value of $w_3 = 0.00165$ was chosen for both the uncharged and charged polymers used in the experiments.

The parameter C reflects on the local dielectric constant in the vicinity of the polyion backbone, ε_l. Since the ion-pair energy ($\tilde{l}_B \delta$) and the temperature remain constant for the entire range of the experiment. A value of 0.183 nm^{-1} for C is equivalent to $\varepsilon_l = 10.9$ if the dipole length is assumed to be 0.5 nm. This value of ε_l is in between the dielectric constant ($\varepsilon = 8.33$) of 2-ethylpyridine, which is chemically close to the chain backbone, and that of the solvent ($16 < \varepsilon < 21$). However, given the uncertainty in the dipole length d, i.e., the mean distance of the bound counterions from the respective polyion charges (which can vary from 0.3 nm to a few nm), the value for ε_l given above should not be over interpreted. Nevertheless

the value of C is remarkably close to the value $0.175\,nm^{-1}$ estimated for polymers of type sodium polystyrene sulfonate (NaPSS) in the original theory [Muthukumar 2004]. C should depend only marginally on the degree of quaternization and a fixed value for all samples should be assumed. However one should note that the fits are very sensitive to a change of C and an influence can not be ruled out.

The attractive nature of interacting dipoles is characterized by the parameter w_1. It is negative and it leads to a reduction of the excluded volume parameter w.

Qualitative agreement of experiment and theory is obtained for the shift of the precipitation point with increasing degrees of quaternization for both α_g and γ. Furthermore the trend of an increase α_g with the degree of quaternization is recovered qualitatively in the theoretical predictions as is a decrease of α_g with an increase of c_p (see Figure 7.18). However the experimental data shows a broader phase transition regime than the fits. In particular theory predicts a first-order coil-globule transition for both, size and effective charge of the polymer chain, if the excluded volume parameter w is smaller than a certain threshold value and provided that the three-body interaction parameter w_3 is also smaller than a critical value. The strength of the three-body interaction parameter is substantially lower than the critical value, and hence the theory predicts a first-order phase transition sharper than the relatively broad transition regime observed in the experiments. One should note, that polydispersity in the chain length N and in the maximum degree of ionization f_m broadens the transition due to a distribution of the threshold value of w. Whereas the chain length distribution has little effect, the variation of the number of charges per chain at constant chain length assuming a Gaussian distribution increases the transition regime slightly [Loh et al. 2008]. However a broad transition regime as shown in Figures 7.16-7.18 can not be ascribed to polydispersity effects alone. Besides possible anisotropic chain conformations, specific ion-solvation effects could also be the origin of the observed broadened width of the transition. Anyway the size and shape of the chain undergoes a drastic change at a threshold poorness of the solvent. Beyond the threshold poorness the chain collapses, and that leads it to collect its counterions as can be seen by theory as well as experiment.

A big discrepancy between theory and experiments is the insensitivity of γ according to theory, which in turn leads to a high charge on the chain. This most likely explains the much bigger increase of α_g with the degree of quaternization of the theory (Figure 7.16). Whereas conductivity measurements suggest a Manning like threshold for the effective maximum number of charges per chain (albeit it is shifted a lot), theory assumes the effective number of charges to increase linearly with the degree of quaternization for the experimental probed regime. However one should stress that Manning theory is not able to cover a change of γ due to enthalpic interactions at all (let alone a full collapse).

The 'true' expansion coefficient as evaluated according to eq. 7.8 shows a monotonous accelerating decrease from the first addition of non-solvent on. According to eq. 2.71 the chain free energy in this state is dominated by the electrostatic term, and consequently the theoretical chain dimension (corresponding to an approximately constant charge density) varies little within the good solvent regime with increasing w_{ns}. In fact a slight increase of the fits can be seen. This increase in chain size reflects a small increase in the value of Bjerrum length (with decreasing dielectric constant) that marginally enhances the intra-chain monomeric repulsion captured in the forth term of the free energy (eq. 2.71).

Within the good solvent regime the experimental γ shows a substantial even though decelerating decrease with increasing w_{ns}. However as mentioned before the Walden product of the simple salt exhibits a similar but less pronounced decrease, too (chapter 6.2.2). Therefore the decrease of γ can be explained by successive counterion binding as well as

specific ion solvation effects or changes of micro viscosity. Therefore data evaluation is based on many assumptions and the effective degree of dissociation evaluated from electrophoretic experiments maybe is not equivalent to a hypothetic degree of dissociation: $\gamma \neq f / f_m$. The theoretical charge density in the expanded state is found to be virtually constant due to the absence of variation in the effective Coulomb strength. Note that this happens despite the somewhat decreasing value of the bulk dielectric constant with increasing w_{ns}, because the Coulomb strength relevant to the ion-pair energy depends only on the local (not the bulk) dielectric constant related to the material of the polymer backbone. Again the experimental data show a broader phase transition regime.

Using a separate set of parameters for $QPVP_{20}$ the theory of uniform collapse induced by concomitant counterion binding agrees quantitatively with the location of the phase boundary, but does not properly reproduce the width of the transition as well as the absolute values of α_g and γ (see Figure 7.18 and [Loh et al. 2008]).
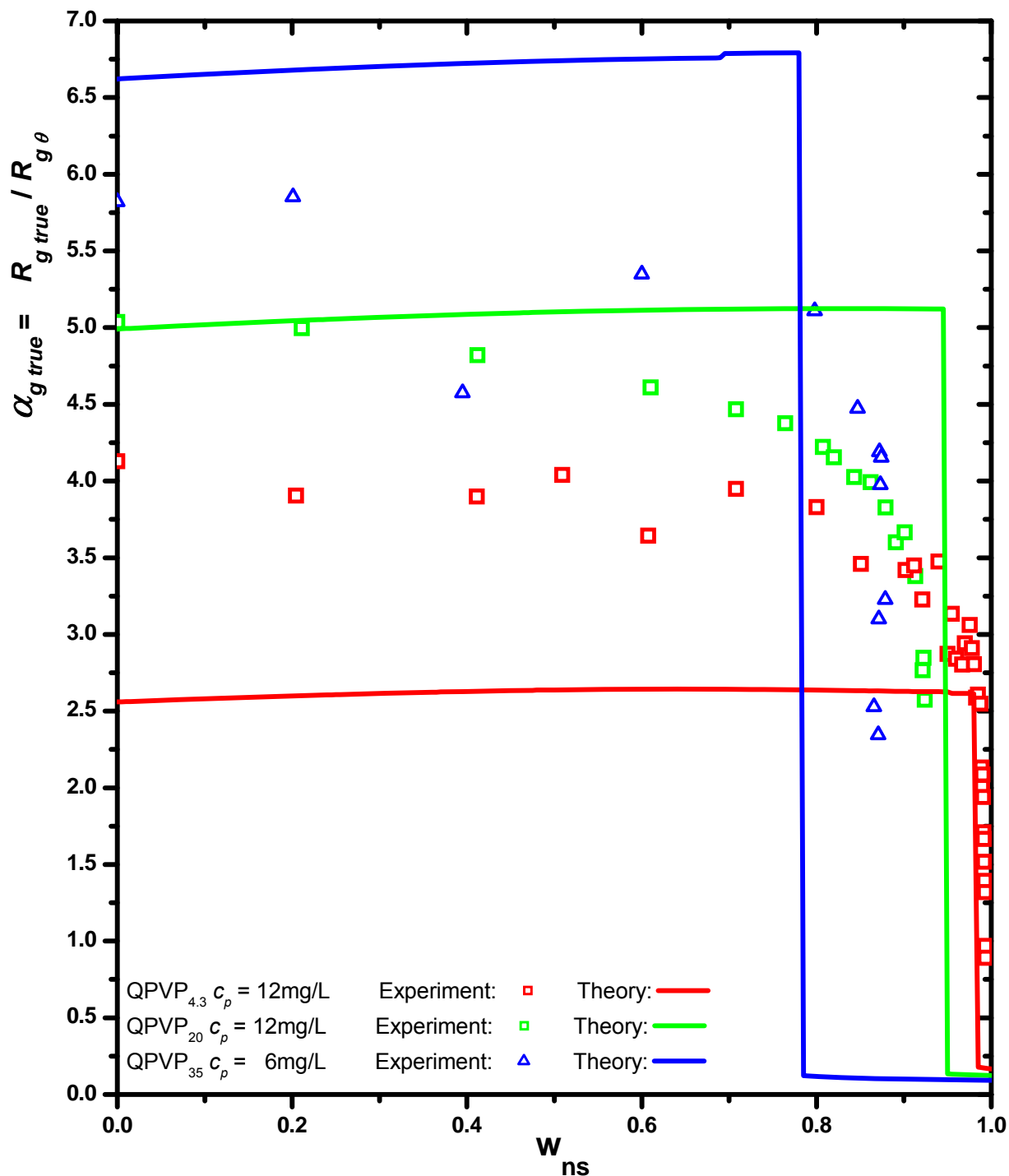
Figure 7.16 'True' radii of gyration expansion coefficients α_g for QPVP$_{4.3}$, QPVP$_{20}$ and QPVP$_{35}$ at $C_s = 10^{-5}$ mol/L are plotted as functions of w$_{ns}$. Different samples are indicated by different colors. Equal concentrations feature the same symbols. All measurements were conducted at $C_s = 10^{-5}$ mol/L, The fits were calculated by minimizing the five contributions to the free energy as described in the theoretical part with $C = 0.183$ nm^{-1}, $w_1 = -0.00028$ and $w_3 = 0.00165$.
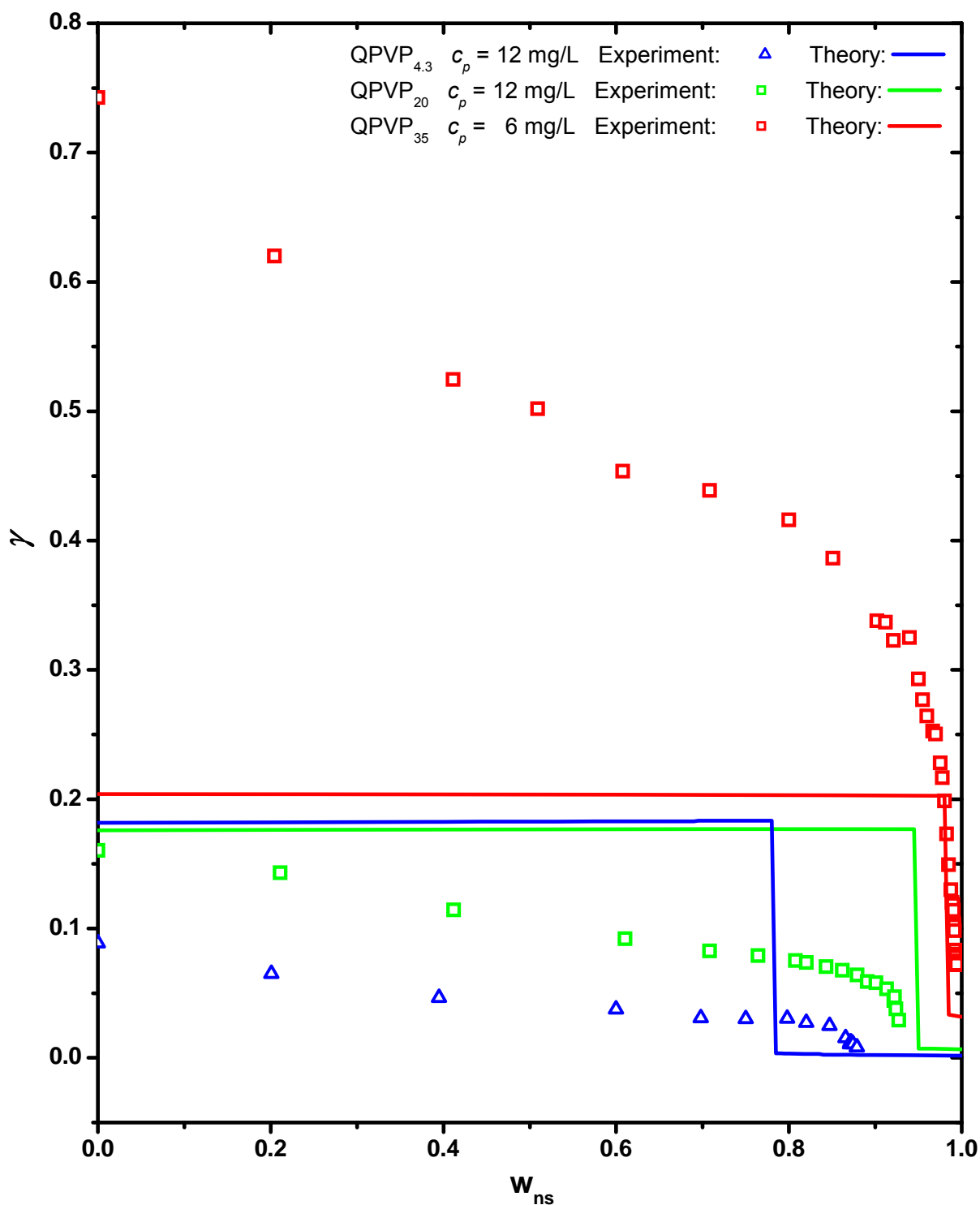
Figure 7.17 The degrees of dissociation γ for $QPVP_{4.3}$, $QPVP_{20}$ and $QPVP_{35}$ at $C_s = 10^{-5}$ mol/L are plotted as functions of w_{ns}. Different samples are indicated by different colors. Equal concentrations feature the same symbols. All measurements were conducted at $C_s = 10^{-5}$ mol/L, The fits were calculated by minimizing the five contributions to the free energy as described in the theoretical part with $C = 0.183$ nm^{-1}, $w_1 = -0.00028$ and $w_3 = 0.00165$.
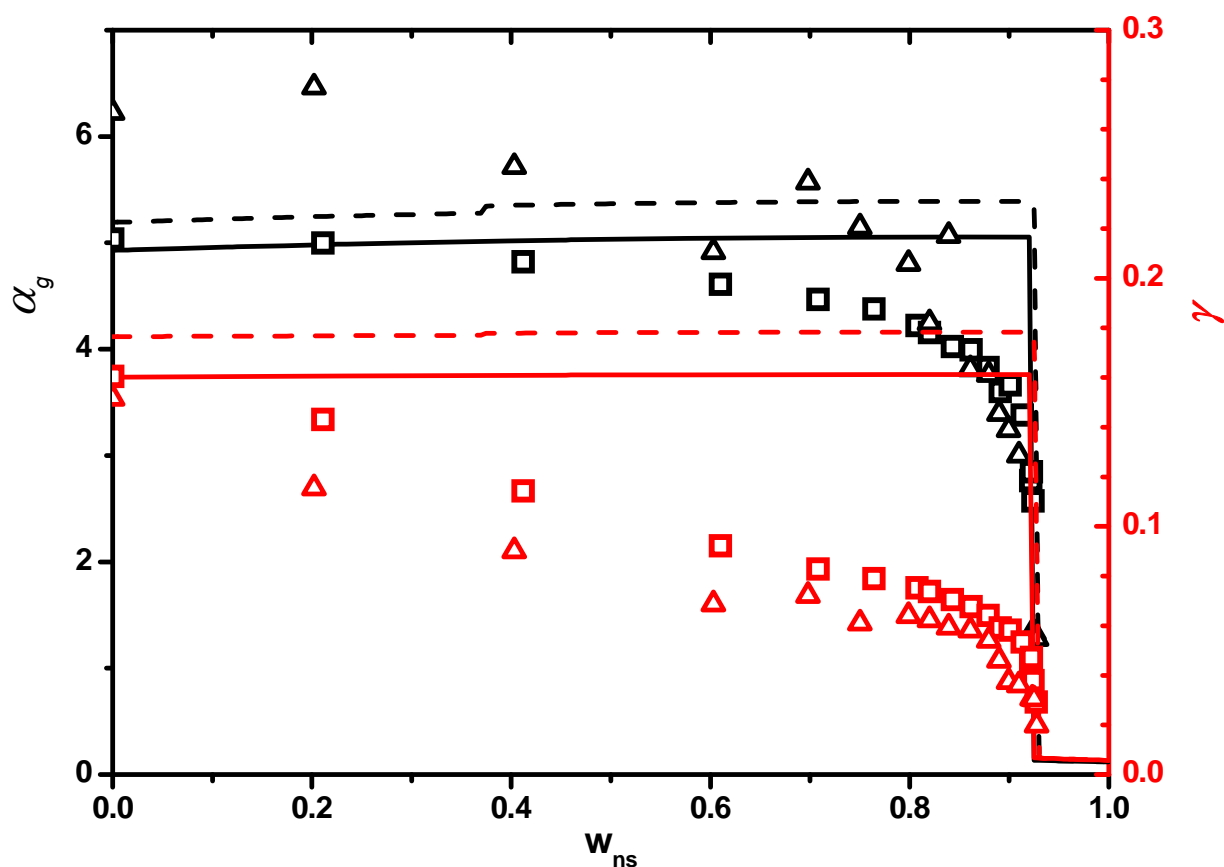
Figure 7.18 α_g for QPVP$_{20}$ at c_p = 6 mg/L (triangles up) and c_p = 12 mg/L (squares) and the according fits (dashed for c_p = 6 mg/L; solid for c_p = 12 mg/L) are plotted as functions of w$_{ns}$ (black, left axis). The degree of dissociation γ is plotted in red (right axis) with same symbols as for α_g. The fits were calculated by minimizing the five contributions to the free energy as described in the theoretical part with C = 0.185 nm^{-1}, w_1 = -0.00032 and w_3 = 0.00165.

8   Temperature Induced Collapse of QPVP$_{20}$

Besides increasing the non-solvent fraction, the collapse can be induced by utilizing a change of temperature as well. Dynamic light scattering does not need a calibration procedure like static light scattering, only the run of solvent viscosity and refractive index vs. temperature from separate measurements need to be known (see chapter 6). Using a scripting tool these parameters were automatically adjusted for the different temperatures making the measurements very convenient. As temperature equilibration needed about 2 hours a full temperature dependent measurement took about 48 hours. To reduce the loss of positively charged QPVP onto the glass surface, hydrophobized cuvettes were used (chapter 5.7.1). Due to the weak temperature sensitivity of the chosen system (unchanged: 1-propanol, 2-pentanone and the QPVP) within one measurement only a part of the collapse could be monitored and comparison of different samples is not possible. It should be stressed that temperature dependent measurements close to the precipitation point always exhibited portions of aggregates with increasing fraction the higher the temperature (see Figure 8.1). The aggregates were huge and had a diffusion coefficient of about three orders of magnitude bigger than the single chains, making a clear separation possible. These aggregates could be redissolved by reducing the temperature after measurements.

Keeping this constraint in mind a continuous collapse could be monitored with arbitrarily small step-width. Partial collapsed chains were used by choosing appropriate solvent/non-solvent fractions and the temperature was raised as the chosen system exhibits a lower critical solution temperature. The run for QPVP$_{20}$ is shown in Figure 8.2. Obviously a temperature change and change of solvent composition has essentially the same effect. A leveling off for the series with w_{ns} = 0.915 can be seen. The same data as in Figure 8.3 is plotted against a relative temperature deviation from a temperature T_c with T_c a chosen parameter to yield the best agreement for the data. A master curve is obtained using this empiric relation.
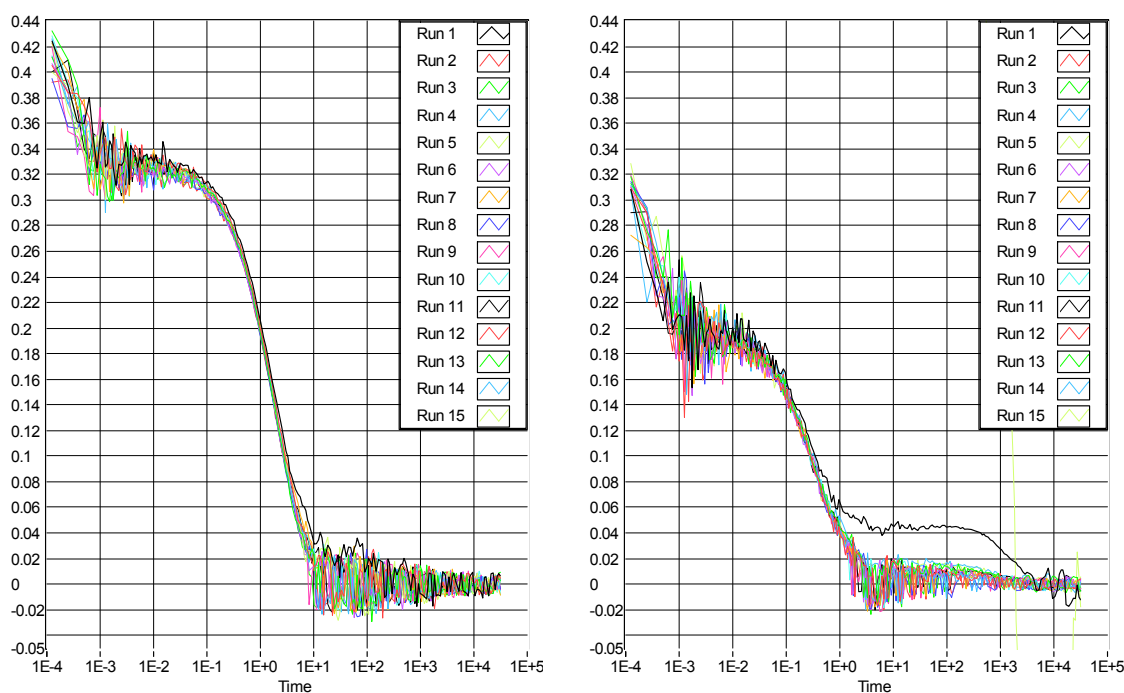
Figure 8.1 Left and right: dynamic light scattering on QPVP$_{20}$ at w_{ns} = 0.915; correlation function measured at 21.5° scattering angle; 15 runs were taken, each correlated over 90 s. Left: 20.2 °C; right: 54.9°C, the runs 1, 3 and 4 feature a second decay; run 15 is an artifact, most likely dust.
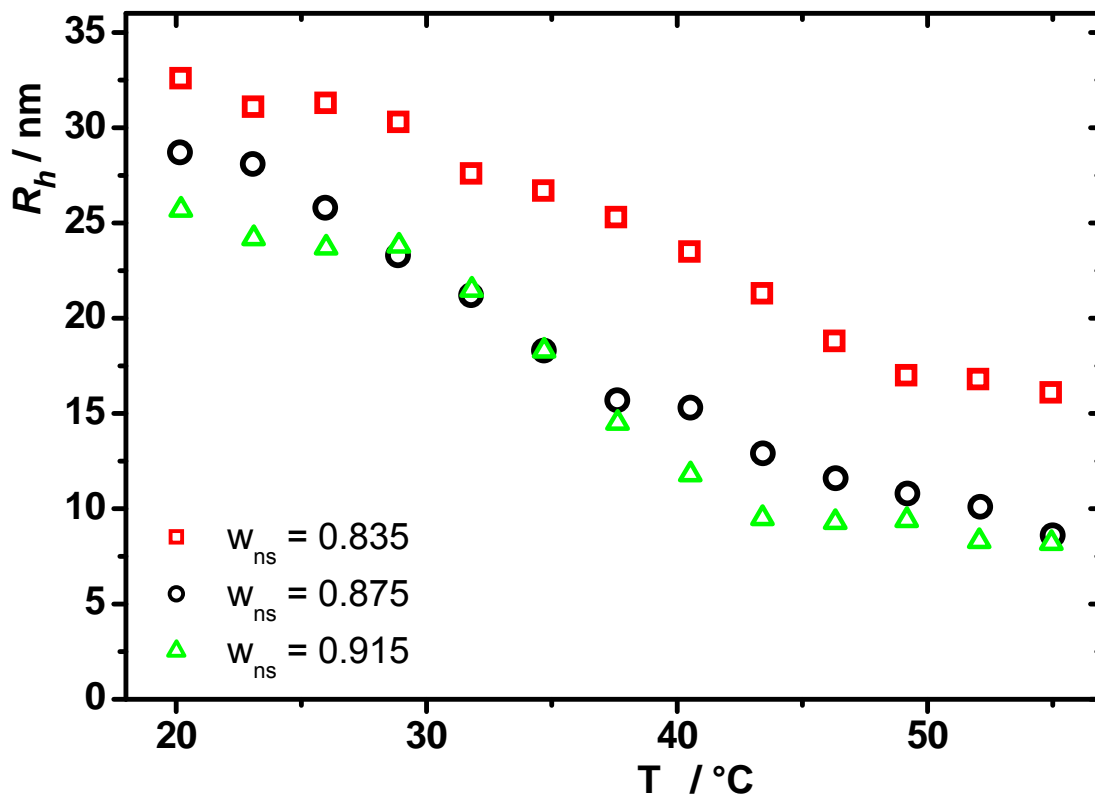
Figure 8.2 Apparent hydrodynamic radius as function of the temperature T of the QPVP$_{20}$ sample at c_p = 12 mg/L and different non-solvent fractions w$_{ns}$.
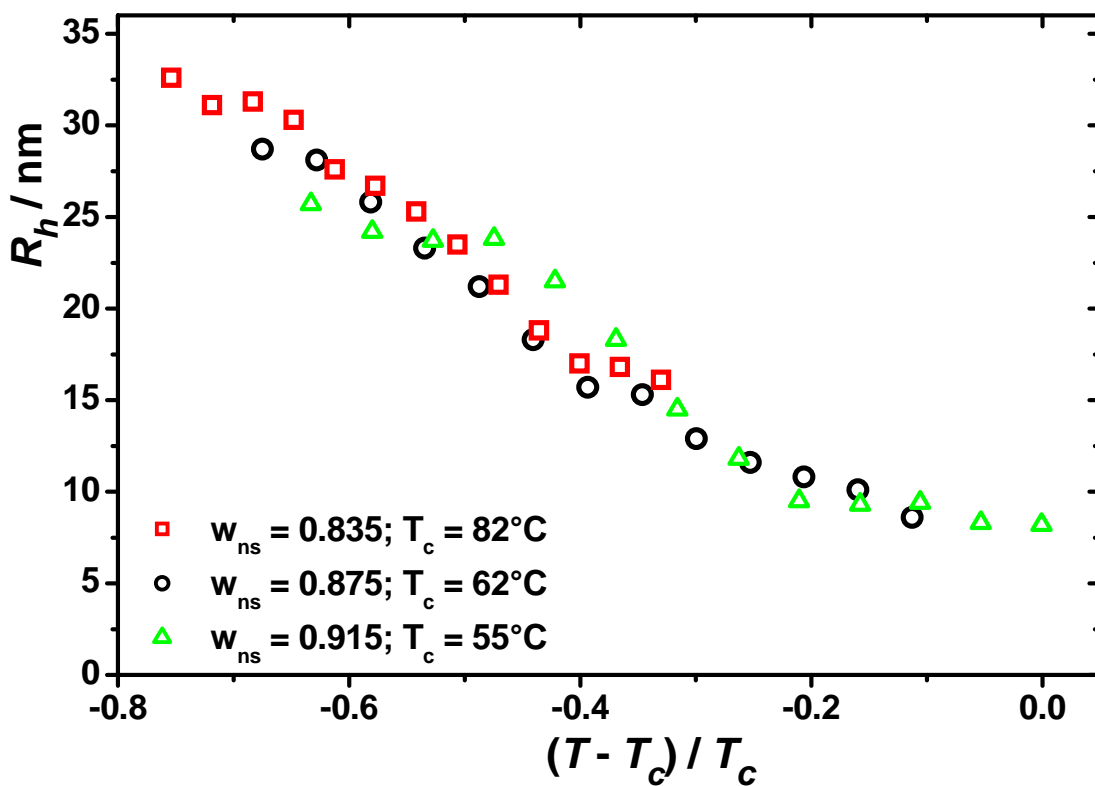
Figure 8.3 Apparent hydrodynamic radius as function of the reduced temperature $(T\text{-}T_c) / T_c$ of the QPVP$_{20}$ sample at c_p = 12 mg/L and different non-solvent fractions w$_{ns}$.

9   Summary

In this work the collapse of partially quaternized PVP's below and above the Manning limit were investigated by light scattering as well as by conductivity measurements and compared to the collapse of its uncharged precursor. The collapses were induced by an isorefractive solvent/non-solvent mixture consisting of 1-propanol and 2-pentanone, with nearly constant dielectric constant. In order to study single chain properties, measurements were performed at constant polyelectrolyte concentration at high dilution ($c_p \leq 12$ mg/L). The solvent quality of the uncharged polyion could be quantified which, for the first time, allowed the experimental investigation of the effect of electrostatic interaction prior and during polyion collapse.

To obtain high reproducibility, solvents of highest purity were further dried and distilled; all samples were prepared in a glove box with inert gas atmosphere. Light scattering measurements at high dilution were conducted close to the limit of measuring accuracy of a very precise ALV-SP86 goniometer with fiber optical detection unit. To realize conductivity measurements under inert gas conditions at this very low concentration, a new conductivity setup needed to be developed. The final setup produced very accurate data. It consisted of a container made completely out of PTFE, a stainless steel probe and attached titration units that were driven by homemade software.

In order to avoid a structure peak to be observable by light scattering, tetrabutylamonium bromide was added to the solution ($C_s = 10^{-5}$ mol/L) which causes the Debye screening length to range from 43 nm $< \lambda_D <$ 49 nm depending on the solvent composition (average polyion distance is about 350 nm). At this salt concentration intramolecular repulsion is only weakly screened.

Given that the Manning parameter ξ_M for QPVP$_{4.3}$ is as low as $l_B / c = 0.6$ (l_B the Bjerrum length and c the mean contour distance between two charges), no counterion binding should occur. However the Walden product reduces with first addition of non solvent and accelerates when the structural collapse sets in. Since the dielectric constant of the solvent remains virtually constant during the chain collapse, the counterion binding is entirely caused by the reduction in the polyion chain dimension. Remarkably the counterion binding occurs already well above the theta dimension of the polyion. The collapse is shifted to lower w_{ns} with higher degrees of quaternization as the samples QPVP$_{20}$ and QPVP$_{35}$ show ($\xi_M = 2.8$ respectively 4.9). The collapse of QPVP$_{35}$ even proceeds in the good solvent regime in agreement with recent polyelectrolyte collapse theories for highly charged polyelectrolytes.

Due to low amounts of screening salt, strong electrostatic interactions bias dynamic as well as static light scattering measurements if evaluated by a conventional Zimm analysis. An extended Zimm formula was derived to account for this interaction and to obtain the real chain dimensions. The effective degree of dissociation γ could be obtained using this extrapolated static as well as extrapolated dynamic light scattering data together with conductivity measurements. The combination of light scattering and conductivity revealed for the first time that polyion chains already collect their counter ions when the dimensions start to shrink well above the θ-dimension. One can conclude the expansion factor α_g and the effective degree of ionization of the polyion to be mutually dependent. In the good solvent regime QPVP$_{4.3}$, QPVP$_{20}$ and QPVP$_{35}$ exhibited a $\gamma < 1$. Moreover in pure propanol their ratio of degree of quaternization is almost proportional to their ratio of their degree of dissociation, suggesting a threshold for the maximum effective number of charges on the polyion. This is another strong indication for QPVP$_{4.3}$ to feature counter ion condensation in the good solvent regime. The low values of γ for QPVP$_{20}$ and QPVP$_{35}$ are assumed to be responsible for the prior collapse of the higher quaternized samples, as collapse theory predict dipole-dipole attraction to increase with the fraction of functional units along the chain.

The newly developed theory of uniform spherical collapse induced by concomitant counterion binding developed by M. Muthukumar and A. Kundagrami agrees qualitatively with the location of the phase boundary and can reproduce qualitatively the trend of an increasing expansion with an increase of the degree of quaternization. However a significant discrepancy of experiment and theory concerns the degree of dissociation. The experimental γ for the samples QPVP$_{4.3}$, QPVP$_{20}$ and QPVP$_{35}$ decreases linearly with the degree of quaternization whereas theory predicts an almost constant value. Furthermore theory does not properly reproduce the width of the transition, as well as the absolute values of α_g and γ. Besides specific ion-solvation effects and the extrapolation procedure of the light scattering data, possible anisotropic chain conformations could also be the origin of the observed discrepancy.

10 Outlook

In this work light scattering and conductivity was utilized to monitor the collapse of partially quaternized PVP at different degrees of quaternization which is certainly the most interesting parameter.

The next interesting parameter would be the salt content. Whereas a low salt content was chosen in this dissertation in order not to screen intramolecular electrostatics, higher salt concentrations could show whether the apparent quantities are consistent with those from the extrapolated data as they should agree in the high salt limit.

Due to apparent quantities in light scattering, the course of the anisotropy during the collapse, if any at all, could not be clarified. The developed extrapolation procedure certainly gives a better approximation for the dimension of the polyion, however, it is not reliable enough to yield information about the topology close to the precipitation point. More refined extrapolation procedures for R_g as well as R_h may be developed for polyelectrolyte solutions with low salt content whereas the validity could be tested with structures of fixed topology as well as computer simulations.

The resolution limit of static light scattering is about 10 nm and the collapsed dimension of the QPVP falls below this limit using the PVP-precursor with M_w = 851000 g/mol. Therefore by choosing a higher molar mass the final collapse could be monitored better and the influence of molar mass on the course of the collapse could be studied likewise.

Under the assumption that γ and λ_p are constant with respect to the counter ion species both can be experimentally determined from a second conductivity measurement via eq. 6.8, as only 2 equations with 2 unknowns remain. However as enthalpic interactions certainly have big influences in organic solvents this method may be biased.

In this dissertation the influence of the cationic part of the quaternization agent onto solubility properties is neglected. A change of the substituent could reveal an influence.

Switching to another polyelectrolyte like sodium polystyrene sulfonate might be rewarding, too. Different collapse features for an anionic polyion collapse are not expected, however it would not adsorb on glass surfaces making light scattering experiments easier.

Other measurement techniques may complement the data and help to investigate the topology, like electrophoretic light scattering or neutron scattering.

11   References

In alphabetical order by first author's last name

Aseyev, V. O.; Klenin, S. I.; Tenhu, H.; *J. Polyml. Sci.* **1998**, 36, 1107

Aseyev, V. O.; Klenin, S. I.; Tenhu, H.; *Macromolecules* **1999**, 32, 1838

Aseyev, V. O.; Klenin, S. I.; Tenhu, H.; Grillo, I.; Geissler, E. *Macromolecules* **2001**, 34, 3706

Bartsch, E. great light scattering scipt; now professor in Freiburg, Germany

Becker, A.; Schmidt, M. *Makromol. Chem., Macromol. Symp.* **1991**, 50, 249

Becker, A.; Köhler, W.; Müller, B. *Ber. Bunsen-Ges.* **1995**, 99, 600

Beer, M.; Schmidt, M.; Muthukumar, M. *Macromolecules* **1997**, 30, 8375

Berne, B. J.; Pecora, R. *Dynamic Light Scattering*, Dover Publications **2000**

Birshtein, T. M.; Pryamitsyn, V. A. *Macromolecules* **1991**, 24, 1554

Blaul, J. *PhD-Thesis* Karlsruhe **2001**

Bodycomb, J.; Hara, M. *Macromolecules* **1994**, 27, 7369

Bordi, F.; Cametti, C.; Gili, T.; Sennato, S.; Zuzzi, S.; Dou, S. and Colby, R. H. *Phys. Chem. Chem Phys.* **2006**, 8, 3653

Chu, Benjamin et al. *Macromolecules* **1987**, 20, 1965

Chu, Benjamin et al. *Macromolecules* **1987**, 20, 2833

Chang, R.; Yethiraj, A. *Macromolecules* **2006**, 39, 821

Chodanowski, P.; Stoll, S. *J. Chem. Phys* **1999**, 111, 13, 6069

Cohen J. ; Rabin, Z.; Rabin, Y. *J. Chem. Phys.* **1988**, 88, 7111

Cohen J.; Priel, Z. *Macromolecules* **1989**, 22, 2356

Cohen J.; Rabin, Z.; Rabin, Y. *Polym. Commun..* **1988**, 29, 235

Collins, K. D.; Washabaugh, M. W. *Quarterly Reviews of Biophysics* **1985**, 18/4, 323

Cowan,D.M., Jeffery,G.H., Vogel,A.I. *J. Chem. Soc.* **1940**, 171-174

Dautzenberg, H. et al *Polyelectrolytes,* Hanser Publishers **1994**

Deggelmann, M. PhD thesis, University of Konstanz, **1992**,

Dobrynin, A. V.; Rubinstein, M. *Macromolecules* **1996**, 29, 2974

Dobrynin, A. V.; Rubinstein, M. Macromolecules **1999**, 32, 915

Dobrynin, A. V.; Rubinstein, M. Macromolecules **2001**, 34, 1964

Donnan, F. G. ; *Physical Chemistry Laboratory, University College, London*, **1924**

Drifford, M. and Dalbiez, J. P. *Biopolymers* **1985**, 24, 1501

Fennell Evans, D. ; Thomas, J. ; Nadas, J. A. *J. Phys. Chem.* **1971**, 75, 1714

Fennell Evans, D.; Gardam, P. *J. Phys. Chem.* **1968**, 72, 3281

Förster, S.; Schmidt, M.; Antonietti, M. *Polymer*, **1990**, 31, 792

Förster, S.; Schmidt, M. *Adv. Polym. Sci.* **1995**, 120, 53

Govindan, B., Govindaswamy,S., Andiappan,A. *Indian Chem. Eng.* **1988**, 30, 4, 67

Goerigk, G.; Schweins, R.; Huber, K. *Europhys. Lett.* **2004**, 66, 331

Gröhn, F.; Antonietti, M. *Macromolecules* **2000**, 33, 5938

Grosberg, A. Yu.; Kuznetsov, D. V. *Macromolecules* **1992**, 25, 1970

Higgins, J. S.; Benoit, H. C. in *"Polymers and Neutron Scattering"*, Ed. Lovesey, S. W., Mitchell, E. W. J., Clarendon Press Oxford, **1996**

Huber, K. *J. Phys. Chem.* **1993**, 97, 9825

Hughes, S. R. C.; Price, D. H. *J. Chem. Soc.* A **1967**, 1093

Huie, C. W. *Electrophoresis* **2003**, 24, 1508

Ikeda, Y.; Beer, M.; Schmidt, M.; Huber, K. *Macromolecules* **1998**, 31, 728

Itaya, A. et al. *Macromolecules* **1982**, 15, 1214

Jeon, J.; Dobrynin, A. V. Macromolecules **2007**, 34, 7695

Kantor, Y.; Kardar, M. *Europhys. Lett.* **1994**, 27, 643;

Kantor, Y.; Kardar, M. *Phys. Rev. E* **1995**, 51, 1299

Katchalsky, A.; Alexandrowicz, Z.; Kedem, O. in "*Chemical Physics of Ionic Solutions*", Ed. Conway, B. E. and Barradas, R. G. Wiley, New York, **1966**.

Khokhlov, A. R. *J. Phys*. A **1980**, 13, 979

Koyama, R. *Macromolecules* **1984**, 17,1594

Koyama, R. *Macromolecules* **1986**, 19,178

Kramarenko, E. Yu.; Khokhlov, A. R.; Yoshikawa, K. *Macromolecules* **1997**, 30, 3383

Kramarenko, E. Yu.; Khokhlov, A. R.; Yoshikawa, K. *Macromol. Theory Simul.* **2000**, 9, 249

Kramarenko, E. Yu.; Erukhimovich, I. Ya. ; Khokhlov, A. R. *Macromol. Theory Simul.* **2002**, 11, 462

Kratky, O.; Porod, G. Rec. Trav. Chem., Pays-Bas. **1949**, 68, 1106

Krause, R.; Maier, E. E.; Deggelmann, M.; Hagenbückle, M.; Schulz, S. F.; Weber, R. *Physica A*, **1989**, 160, 135

Kundagrami, A.; Muthukumar, M. *J. Chem. Phys.* **2008**, 128, 244901

Lee, J. M.; Green, M. M.; Mikes, F.; Morawetz, H. *Macromolecules* **2002**, 35, 4216

Levine, I. N. "*Quantum Chemistry*", Ed. Challice, J. **2000** Prentice-Hall, New Jersey

Liao, Q.; Dobrynin, A. V.; Rubinstein, M. *Macromolecules* **2006**, 39, 1920

Liessmann,G., Schmidt,W., Reiffarth,S. data compilation of the Saechsische Olefinwerke Boehlen, Germany, **1995**

Limbach, H. J.; Holm, C. *J. Phys. Chem. B* **2003**, 107, 8041

de Lisi, R.; Goffredi, M. *Gaz. Chim. It*. **1973**, 103, 491

Liu, S.; Muthukumar, M. *J. Chem. Phys.* **2002,** 116, 9975

Liu, S.; Muthukumar, M. *J. Chem. Phys.* **2003,** 119, 1813

Loh, P.; Deen, R.; Vollmer, D.; Fischer, K.; Schmidt, M.; Kundagrami, A.; Muthukumar, M. Macromolecules **2008** ASAP

MacFarlane Jr.; R.; Fuoss, R. M. *J. Polym. Sci.* **1957**, 23, 403

Mandel, M. in "*Polyelectrolytes (Charged and Reactive Polymers)*", Ed. Selegny, E. Reidel, Dordrecht-Holland, **1974**.

Mandel, M., Varkevisser, F. A., Bloys van Treslong, *Macromolecules* C. J. **1982**, 15, 675

Mandel, M. *Polyelectrolytes. In: Encyclopedia of Polymer Science and Engineering*, 2nd Ed., Mark, F. H., Bikales, N. M., Overberger, C. G., Eds.; Wiley: New York, **1988**, Vol. 11, S. 739

Manning, G. S.; Zimm, B. H. *J. Chem. Phys.* **1965**, 43, 4250

Manning, G. S. *J. Chem. Phys.* **1969**, 51, 924

Manning, G. S. *J. Chem. Phys.* **1969**, 51, 3249

Manning, G. S. *Ann Rev. Phys. Chem.* **1972**, 23, 117

Manning, G. S. *Quart. Rev. Biophys.* **1978**, 11, 179

Manning, G. S. *J. Chem. Phys.* **1980**, 84, 1059

Manning, G. S. *J. Phys. Chem.* **1981**, 85, 1506

Manning, G. S. *Ber. Bunsenges. Phys. Chem.* **1996**, 100, 909

Manning, G. S.; Ray, J. J. *Biomol. Struct. Dyn.* **1998**, 16, 461

Manning, G. S. *Macromolecules* **2007**, 40, 8071

Marchetti,A., Preti,C., Tagliazucchi,M., Tassi,L., Tosi,G. *J. Chem. Eng. Data* **1991**, 4, 365

Marras,G., Blanco,S.T., Otin,S. *Thermochim. Acta* **1994**, 242, 1, 27

Michel, R.C.; Reed, W.F., Biopolymers **2000**, 53, 19

Muthukumar, M. *J. Chem. Phys.* **1987**, 86, 7230

Muthukumar, M. *J. Chem. Phys.* **1997**, 107, 2619

Muthukumar, M. *J. Chem. Phys.* **2004,** 120, 9343

Muthukumar, M. *J. Chem. Phys.* **2007,** 127, 244908

Nordmeier, E. *Polym. J.* **1995**, 1, 25

Odijk, T., *J. Polym. Sci., Polym. Phys. Ed.* **1977**, 15, 477

Odijk, T., *J. Polymer* **1978**, 19, 989

Oosawa, F. *Polyelectrolytes* Marcel Dekker: New York, **1971**

Öttinger, H. C.; Hütter, M.; Schurtenberger, P. Polymere II : Physik

Park, I. H., Wang, Q. W., Chu, B. *Macromolecules* **1987**, 20, 1965

Rayleigh, Lord Philos. Mag. **1882**, 14, 184

Reddy, G.; Yethiraj, A. *Macromolecules* **2006**, 39, 8536

Reed, W. F.; Peitzsch R. M., Burt, M. J. **1992**, 25, 806

Reed, W.F.; Morfin I.; Rinaudo, M.; Bosali, R.; J. Physique II **1994**, 4, 1001

Ruhong Zhou, et al. *Science* **2004**, *305*, 1605

Schiessel, H. Macromolecules **1999**, 32, 5673

Schmitt, A., Meullenet, J. P.; Varoqui, R. *Biopolymers* **1978**, 17, 1249

Schweins, R.; Huber, K. *Eur. Phys. J. E* **2001**, 5, 117

Schweins, R.; Lindner, P.; Huber, K. *Macromolecules* **2003**, 36, 9564

Schweins, R.; Huber, K. *Macromol. Symp.* **2004**, 211, 25

Schweins, R.; Goerigk, G., Huber, K. *Eur. Phys. J. E* **2006**, 21, 99

Sedlák, M. *J. Chem. Phys.* **1996**, 105, 10123

Severin, M.; *J. Chem. Phys.* **1993,** 99, 628

Skolnick, J.; Fixman, M. Macromolecules **1977**, 10, 944

Sorci, G. A.; Reed, W. F. *Macromolecules* **2002**, 35, 5218

Spiteri, M. N.; Williams, C. E.; Boue, E. *Macromolecules* **2007**, 40, 6679

Stepanek, P.; Tuzar, Z.; Kadlec, P.; Kriz, J. *Macromolecules* **2007**, 40, 2165

Stevens, M. J.; Kremer, K. *Phys. Rev. Lett.*, **1993**, 71, 2228

Stevens, M. J.; Kremer, K. *J. Chem. Phys.* **1995,** 103, 1669

Varoqui, R.; Schmitt, A. *Biopolymers* **1972**, 11, 1119

Vasilevskaya, V. V., Khokhlov, A. R.; Yoshikawa, K. *Macromol. Theory Simul.* **2000**, 9, 600

Vink, H. *J. Chem. Soc., Faraday Trans.* 1 **1981**, 77, 2439

Vink, H. *Makromol. Chem.* **1982**, 183, 2273

Vink, H. *J. Chem. Soc., Faraday Trans.* 1 **1984**, 80, 507

Vink, H. *J. Chem. Soc., Faraday Trans.* **1990**, 86(14), 2607

Vink, H. *J. of Colloid and Interface Science* **1995**, 173, 211

Volk, N; Vollmer, D.; Schmidt, M.; Oppermann W.; Huber, K.;Holm, C.; Joanny, J. F., Kremer, K.; Netz, R. R.; Reineker, P.; Seidel, C.; Vilgis, T.A.; Winkler, R. G. *Adv. Polym. Sci.* **2004**, 166, 29-111

Vrij, A.; Overbeek, J. Th. G. *J. Coll. Sci.* **1962**, 17, 570

Wandrey, C. *Langmuir* **1999**, 15, 4069

Wiener, N. *Acta Math*. **1930**, 55, 118, and Khintchine, A. *Math. Ann.* **1934**, 109, 604

Williams, C. E.; Carbajal-Tinoco, M. D. *Europhys. Lett.* **2000**, 52, 284

Williams, C. E. et al *J. Phys. Chem. B* **2002**, 106, 12165

Winkler, R. G.; Gold, M.; Reineker, P. *Phys. Rev. Lett.*, **1998**, 80, 3731

Wilcoxon, J. P. and Schurr, J. M. *J. Chem. Phys.* **1983**, 78, 3354

Wu, C.; Zhou, S. *Macromolecules* **1995**, 28, 8381

Wu, C.; Wang, X. *Phys. Rev. Lett.*, **1998**, 80, 4092

Zernicke, F.; Prins, J. *Z. Phys*. **1927**, 41, 184

Zimm, B H.. *J. Chem. Phys* **1948**, 16,12, 1093
Zhou, K. et al. Macromolecules **2008** ASAP

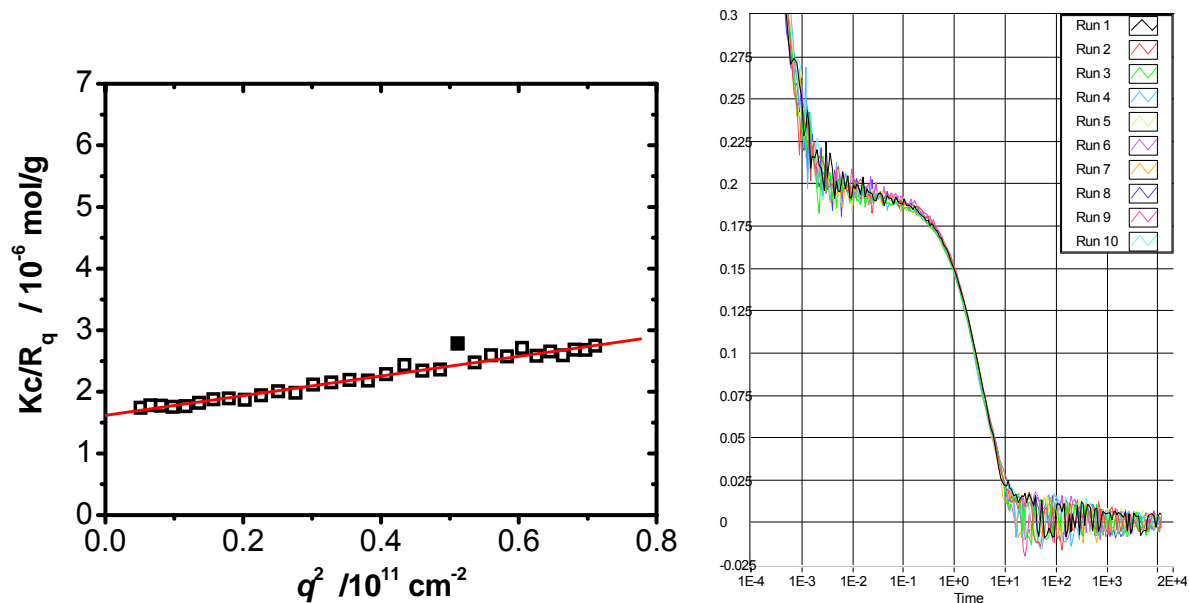**Examples for the collapse of QPVP$_{1.2}$ – monitored by light scattering**

Static and dynamic light scattering on QPVP$_{1.2}$ at w$_{ns}$ = 0, 0.4 and 0.969; Correlation functions were measured from 17° to about 30° scattering angle with at least 5 steps. Runs with no or the least amount of aggregates were averaged and the resulting second decay was fitted with a second order exponential decay.
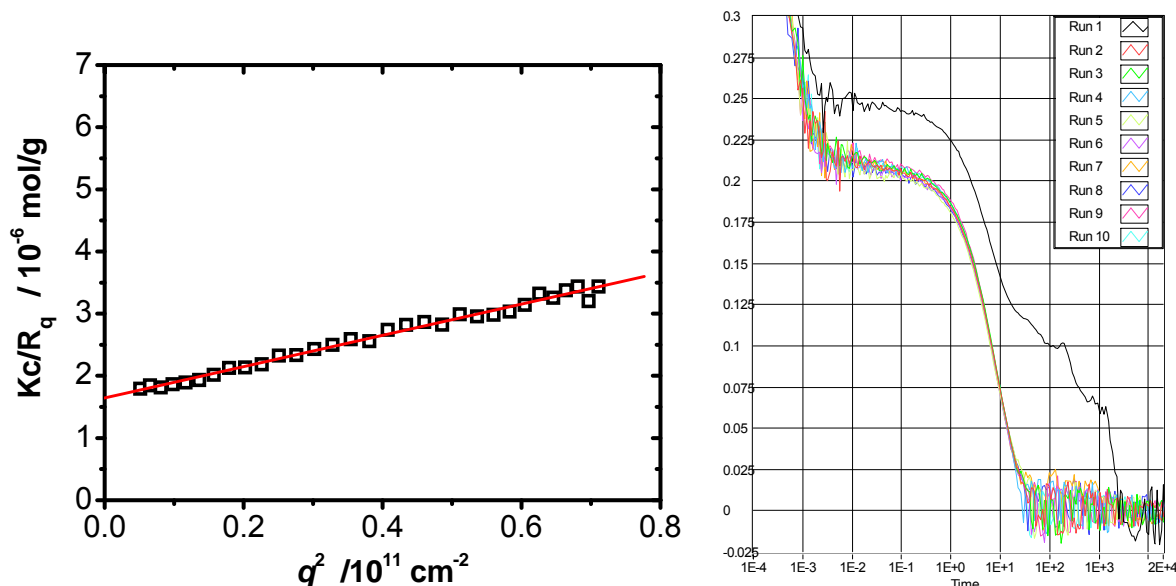
Figure A.1 w$_{ns}$ = 0; left: reduced scattering intensity vs. q^2 yielding R_g^{app} = 66.1 nm and M_w^{app} = 6.3 * 10^5 g/mol; right: correlation function at 17° scattering angle; the average over all correlation functions measured yields R_h^{app} = 29.2 nm.
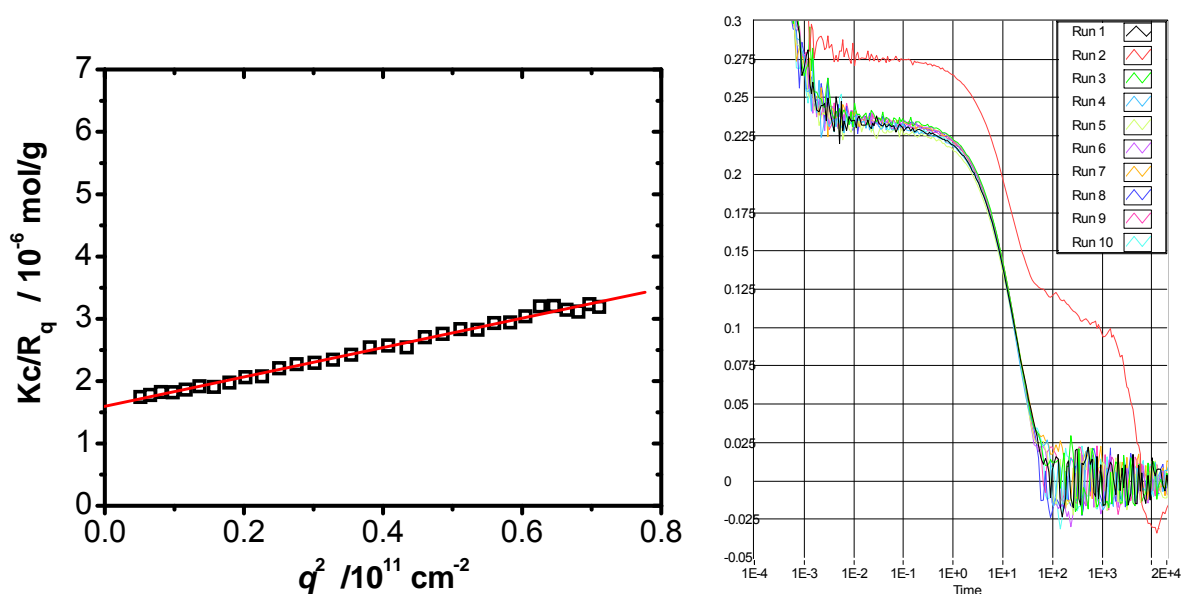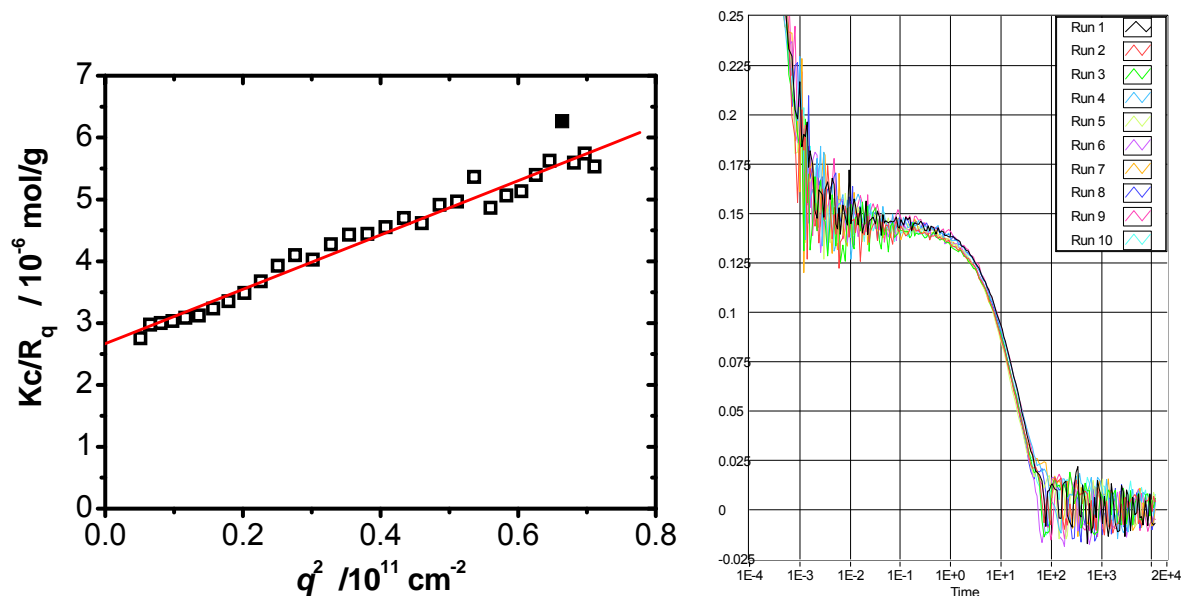

Figure A.2 w$_{ns}$ = 0.4; left: reduced scattering intensity vs. q^2 yielding R_g^{app} = 68.6 nm and M_w^{app} = 6.1 * 10^5 g/mol; right: correlation function at 17° scattering angle; the average over all correlation functions measured yields R_h^{app} = 32.1 nm.
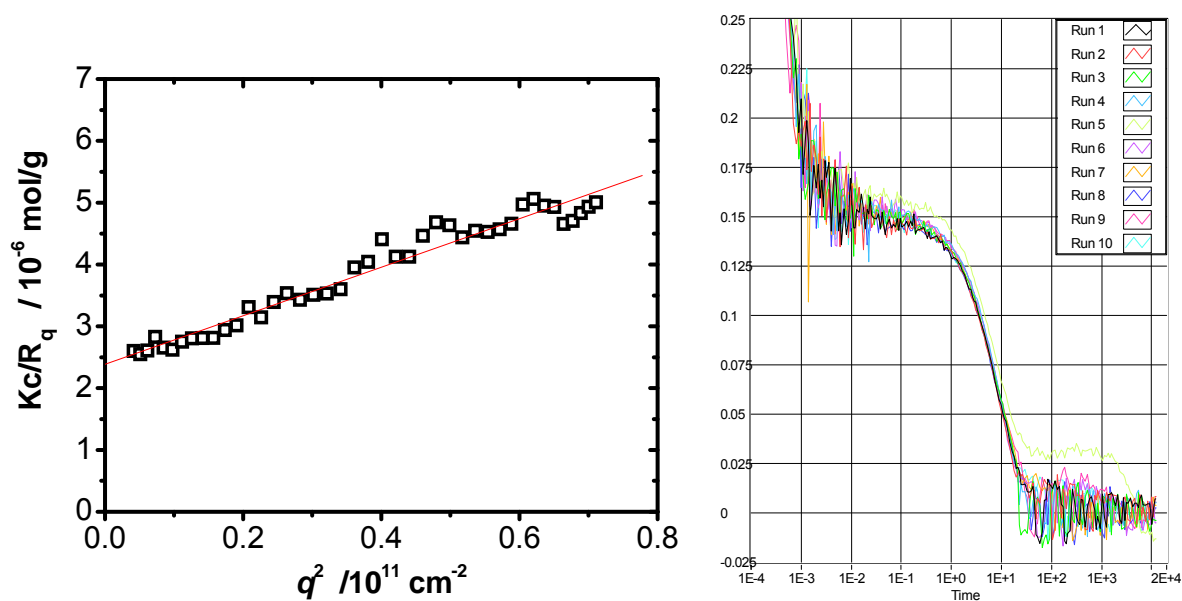
Figure A.3 w_{ns} = 0.969; left: reduced scattering intensity vs. q^2 yielding R_g^{app} = 57.8 nm and M_w^{app} = 6.2 * 10^5 g/mol; right: correlation function at 17° scattering angle; the average over all correlation functions measured yields R_h^{app} = 31.0 nm.

## Examples for the collapse of QPVP$_{2.4}$ – monitored by light scattering

Static and dynamic light scattering on QPVP$_{2.4}$ at w_{ns} = 0, 0.4 and 0.969; Correlation functions were measured from 17° to about 30° scattering angle with at least 5 steps. Runs with no or the least amount of aggregates were averaged and the resulting second decay was fitted with a second order exponential decay.

Figure A.4 w_{ns} = 0; left: reduced scattering intensity vs. q^2 yielding R_g^{app} = 72.2 nm and M_w^{app} = 3.8 * 10^5 g/mol; right: correlation function at 17° scattering angle; the average over all correlation functions measured yields R_h^{app} = 42.2 nm.

Figure A.5 w_{ns} = 0.4; left: reduced scattering intensity vs. q^2 yielding R_g^{app} = 70.8 nm and M_w^{app} = 4.2 * 10^5 g/mol; right: correlation function at 17° scattering angle; the average over all correlation functions measured yields R_h^{app} = 43.0 nm.
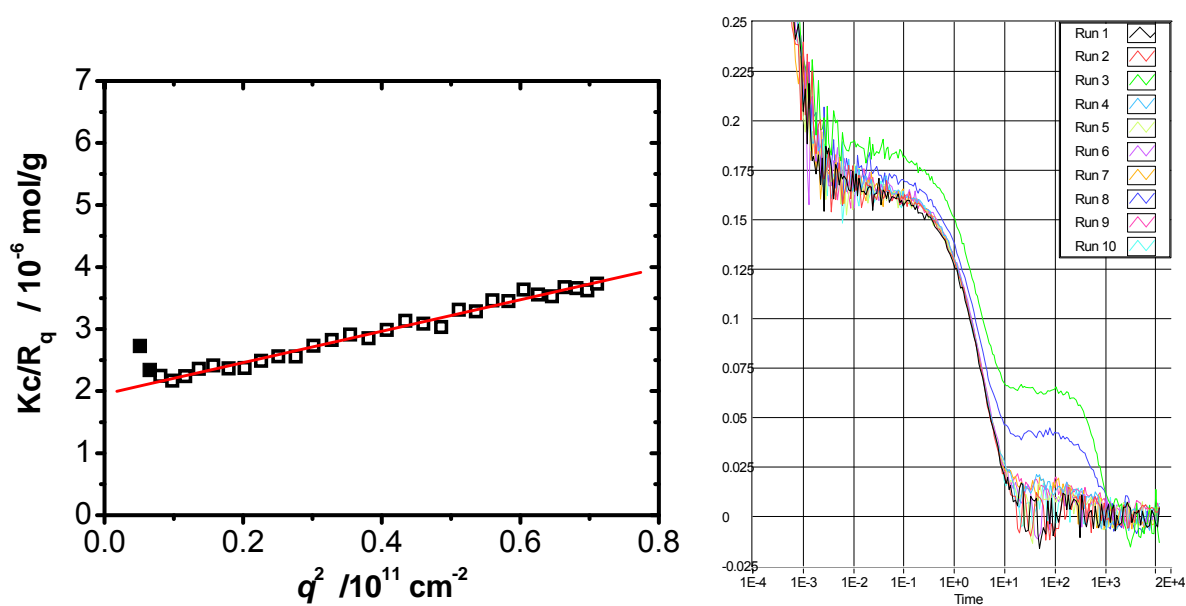
Figure A.6 w_{ns} = 0.969; left: reduced scattering intensity vs. q^2 yielding R_g^{app} = 62.9 nm and M_w^{app} = 5.2 * 10^5 g/mol; right: correlation function at 17° scattering angle; the average over all correlation functions measured yields R_h^{app} = 40.0 nm.